Visualisation and monitoring of tumour-mediated immune modulation in primary cancer and premetastatic niche establishment using S100A8/A9-specific imaging.

Eisenblaetter, Michel

Awarding institution:
King's College London

Visualisation and monitoring of tumour-mediated immune modulation in primary cancer and premetastatic niche establishment using S100A8/A9-specific imaging.

submitted by

Michel Eisenblaetter

for obtaining a

PhD in Imaging Sciences & Biomedical Engineering

Abstract

Development and spread of malignant disease are crucially dependent on the recruitment and reprogramming of various immune cells. At the primary tumour site, tumour-associated macrophages and immature myeloid cells facilitate local invasion and neoangiogenesis and promote the establishment of a tumour-permissive microenvironment. Systemic cancer spread is preceded by the establishment of a permissive microenvironment in the target tissue of metastasis – the premetastatic niche.

As crucial players in the establishment of the premetastatic niche as well as the orchestration of tumour immune evasion at primary tumour level, myeloid-derived suppressor cells (MDSC) release S100A8/A9, an exosomal protein that contributes to metastasis, angiogenesis, and immune suppression.

S100A8/A9 is a ligand for TLR4 and RAGE and acts as a chemo-attractant to myeloid cells. The local S100A8/A9 level is a sensitive indicator of immune cell activity.

Building on the development of S100A8/A9-specific optical imaging for monitoring of local inflammation, I assessed S100A8/A9 imaging for the visualisation of tumour-associated immune cell activity. I strived to establish local S100A8/A9 imaging signals to be coincident with the increased activity of tumour-promoting immune cells and therefore indicative of high malignant activity within the primary tumour and the establishment of a premetastatic niche in distant tissue.

A S100A9-targeting antibody has been labelled for optical in vivo imaging and used for fluorescence imaging of tumour-associated inflammation in an orthotopic murine breast cancer model. The local S100A9-signal could be shown to reflect the tumour-associated macrophage and MDSC abundance and activity and predict local tumour growth.

To enable systemic imaging of tumour-mediated immune cell activity, the optical tracer has been developed into a SPECT tracer for labelling with ^{111}In and tested in a well-characterised murine model of local inflammation.

In a syngeneic mouse model of metastatic breast cancer, S100A8/A9-SPECT sensitively reflected MDSC abundance and the establishment of an immunosuppressive environment in premetastatic lung tissue. A significant correlation between the S100A8/A9 imaging signal in the premetastatic lung and the subsequent metastatic tumour burden could be established. The results suggest S100A8/A9 as a potent imaging biomarker for monocyte activity, reflective of tumour-associated immune cell activity.

Table of contents

List of figures

List of tables

1 Introduction

Following cardiovascular disease and infections, cancer is still third in the ranking of causes of death, accounting for an estimated 8 million deaths per year as recently confirmed by the Global Burden of Disease study (*1, 2*).

Major progress has been made towards treatment of primary cancer. Surgery and endovascular intervention, radiotherapy and chemotherapy greatly evolved over the past decades and strongly increased the possibilities of and chances for local tumour control. The majority of cancer-related deaths are, however not caused by the local primary tumour growth and local invasion but the development of distant metastasis. Therefore, the success of cancer therapy is often determined by the stage and extent of disease at the time of diagnosis.

In breast cancer, the presence of distant metastasis at the time of diagnosis reduces the 5-year survival rate by a factor of 4 as compared to those women with localised disease – from almost 99% to less than 24% (*3*). This discrepancy is the raison d'être for all screening programs with the aim of early cancer detection. However, it also illustrates that oncology does not yet have the sufficient means for effectively treating systemic cancer spread – especially the multi-step process of metastasis is still not fully understood. Diagnostic approaches only cover some aspects of malignant disease, failing to provide vital information on other aspects of cancer (*4*) including the detection of micrometastatic disease and/or the visualisation of tumour- immune cell crosstalk.

Understanding the multi-step process of metastasis with the possibility to identify potential for intervention in the development of systemic disease and diagnostic approaches for detection and measurement of the early phases of metastasis would basically turn cancer from a fatal killer into a local, controllable disease.

By establishing a first in vivo imaging marker for tumour-mediated immune remodelling, this study is intended to provide a versatile method for further research

on tumour-mediated, premetastatic tissue priming and offer insights into the process of systemic cancer spread.

2 Background

2.1 Tumour immunology and immunotherapy

The innate immune system in vertebrates constantly monitors the body and screens for potentially pathological alterations in cells, showing as e.g. variations in cell surface markers. Aberrant cells are recognised, labelled and subsequently destroyed – a mechanism that enables the control of infection as well as premalignant lesions. The presence of certain subtypes of immune cells, CD8+ T cells, Natural killer (NK) cells and pro-inflammatory macrophages have been shown to be independent positive outcome predictors (*5*). However, preclinical and clinical data suggest that at some point during tumour development, the immune system falls under the influence of the tumour and begins to actively support disease development (*6*). This process is called tumour immunoediting. In the context of this escape from immunosurveillance, the composition and functionality of tumour-associated immune cells changes and a tumour-promoting, immunosuppressive environment is established (*7*). Only successful escape from immunosurveillance and attempted elimination guarantees establishment of manifest cancer.

Beyond changing the immediate environment through local tissue destruction, established cancer influences and modulates virtually all physiological systems of the body and drives host cells to essentially contribute to malignant development. Host cells that are recruited by the tumour support vital steps of tumour development beyond the initial lesion establishment. For example, release of pro-angiogenic factors like vascular endothelial growth factor (VEGF) activates endothelial cells and results in sprouting of new vessels, supplying oxygen and nutrients for the growing tumour (*8*); activation of phagocytes in the immediate tumour environment further supports

angiogenesis and enables degradation of extracellular matrix for tumour expansion (*9, 10*).

Although a potential crosslink between malignant disease and the immune system has been proposed more than 100 years ago already by Virchow, who observed an infiltrate of lymphocytes into solid tumours (*11*), the potential impact of tumour associated immune cells for therapy and the need of appropriate diagnostics has long been ignored. Relatively recently, the major role of tumour associated inflammation, constituted by tumour educated immune cells, in the process of cancer development and spread has been fully recognised (*12*). In particular, tumour associated inflammation, tumour immunosuppression and evasion of anti-tumour immunity have been newly called hallmarks of cancer (*13*). The current effort to establish cancer therapy that specifically targets the tumour-associated immune cells rather than the tumour cells is a clear indication of this change of paradigm (*4*).

Various immune cells accumulate in the primary tumour microenvironment in response to active tumour signalling and as secondary effect of the metabolic situation in the tumour. The tumour immune infiltrate comprises monocytes and macrophages, T cells, mast cells, fibroblasts and dendritic cells. Mature and immature variants of all these cells, especially monocytes have been found. The physiological anti-tumour immune response, elicited mainly by the tumour expression of aberrant surface molecules following proteome mutation, is driven by CD8+ T cells and NK cells

Monocytes and macrophages constitute the biggest group of immune cells in the tumour microenvironment and can account for more than 50% of the whole tumour mass. Monocytes and macrophages accumulate in response to actively secreted specific cytokines, the hypoxic metabolic state in the tumour tissue or necrosis-related cell damage associated molecular pattern (DAMP) molecules in the tumour. To roughly differentiate the various subtypes of macrophages, functional characteristics have been used to define pro-inflammatory macrophages, traditionally activated via

the complement immune system (M1) from immunomodulatory macrophages with function in tissue regeneration, wound healing and resolution of inflammation, activated via alternative pathways (M2) (*14*). Under physiological circumstances, M1 and M2 macrophages balance inflammation and tissue growth. In the tumour microenvironment, the M2 macrophage dominates over the pro-inflammatory M1 phenotype. Under the influence of IL-4, IL-13, IL-10 and M-CSF, macrophages preferentially lean towards M2 polarisation and support neoangiogenesis via secretion of VEGF, supply the tumour with growth factors and also contribute to immune remodelling by promoting the accumulation of regulatory T cells (Treg) and myeloid-derived suppressor cells (MDSC) in the tumour microenvironment. Among other functions, monocytes and terminally differentiated macrophages also support local invasion and intravasation, representing early steps of distant metastasis: it has been shown that immune cells at the active tumour margin establish reciprocal signalling loops with tumour cells. Through supply of epidermal growth factor (EGF) to the tumour cell and reception of CSF-1 in return, macrophages are virtually guiding the tumour cell towards activated vasculature (*15*). The abundance of tumour-associated macrophages (TAM) correlates with outcome and prognosis for selected cancer types (*16, 17*). In preclinical model systems, the depletion of macrophages had a positive effect on tumour development (*18*).

The physiological balance between effector T cells (CD8+) and Treg (CD4+), required to ensure tissue homeostasis and limitation of inflammatory processes is disturbed in the tumour environment. While CD8+ effector T cells are the backbone of anti-tumour immunity in the context of immunosurveillance, the tumour microenvironment is dominated by T cell subtypes that suppress cytotoxic immune activity and inhibit recognition of tumour cells as potential targets for immunity. These CD4+ Treg accumulate in the tumour microenvironment, in response to IL-2 signalling. Activated effector T cells secrete pro-inflammatory cytokines and directly attack tumour cells. Treg inhibit activation of CD8+ T cells, hampering tumour killing and accumulation of

further inflammatory cells. Regulatory T cells moreover promote M2 polarisation of TAM via a IL-10/TGFβ signalling loop and inhibit dendritic cell (DC) activity (*19*).

It has been shown that stromal cells – under the influence of Treg – actively work together to prevent direct contact between cytotoxic T cells and tumour cells (*20*).

Besides immunosuppressive Treg, immature monocytes with immunomodulatory function – MDSC are among the major effectors of the tumour-promoting microenvironment. Their accumulation and function has been associated with the expression of S100A8/A9 (*21*).

Together, tumour-induced Treg and MDSC impair the anti-tumour immune activity and promote tumour immune evasion (*22*).

One particular strategy of cancer immunotherapy is to inhibit or block Treg function to unleash the anti-tumour immune response. It has been hailed the turning point in cancer therapy in a Science Editorial in 2013 (*4*), referring to very promising results of immunomodulatory therapy even in advanced cancer, refractory to conventional therapy. This could mark a paradigm shift in cancer therapy, refocusing from the primary tumour cell towards the tumour-promoting environment. However, a significant number of patients in phase I and II clinical trials did not respond to specific immunotherapy at all – possibly because of differences in composition of the tumour microenvironment.

As the tumour microenvironment is still not fully understood with regards to components, their interplay and regulating factors, the precise mechanisms underlying the therapy effects or failure currently remain unknown. Moreover, diagnostic medicine does not currently hold means for monitoring of early immunomodulatory therapy effects. By clinically established diagnostic methodology, effects on the tumour may not be detectable for several months. This is especially devastating as response to immunomodulatory treatment is currently difficult to predict, associated with inhomogeneous outcome and relatively frequent therapy

failure. Identification of the patients who will likely respond to tumour immunotherapy will be essential to foster success of future cancer therapy.

Tumour-driven immune remodelling has also been implicated in the process of metastasis. Besides the aforementioned support of initial steps to metastasis – tumour cell migration and intravasation, variation in immune cell activity and function in distant tissue seems to precede and accompany systemic tumour spread. These tumour-mediated processes, leading to the establishment of a tumour-permissive environment in premetastatic tissue are summarised in the premetastatic niche (PN) concept.

2.1.1 The premetastatic niche

In the late 19th century, the English surgeon Stephen Paget discovered from the reevaluation of autopsy records that systemic tumour spread was not determined by physical distribution of tumour cells alone. He particularly hinted towards the discrepancy between blood supply and establishment of metastasis for instance in liver and lung (high frequency of metastasis) and spleen (low frequency of metastasis). He concluded that additional, tissue-specific factors must guide circulating tumour cells and built from that his 'seed and soil' hypothesis (*23*). Paget's hypothesis still fits with modern metastasis research, now interpreting the seed as circulating tumour cell, cancer stem cell or progenitor cell and the soil as a microenvironmental niche, comprising multiple growth factors, stromal and immune cells in a neatly regulated interplay (*24*).

The pre-metastatic niche is commonly characterised by stromal reorganisation and the infiltration of various immune cells (*25*), providing circulating tumour cells with a hospitable environment, protected from host immunity.

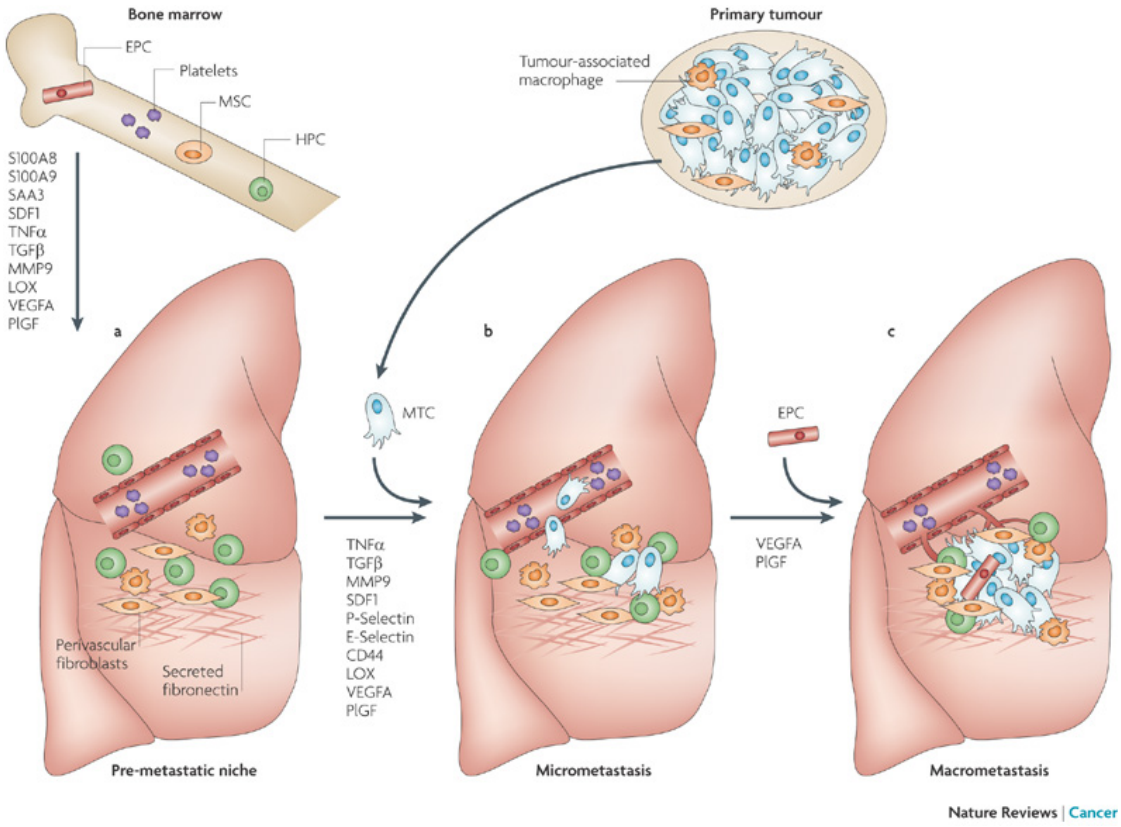

Figure 1: The premetastatic niche.

Schematic illustration of the sequence of premetastatic niche induction. In response to tumour-secreted factors, myeloid cells are mobilised from the bone marrow and colonise potential target sites of metastasis, establishing a hospitable microenvironment for circulating tumour cells. The immune and stroma cells, assembled in the premetatastic niche support establishment of manifest metastasis. Illustration adapted from (*26*)

As part of this mechanism, the entry of tumour cells into the niche is promoted by selective activation of the local vascular endothelium. After leaving the vascular space, the tumour cell is immersed in an extracellular matrix, prepared to foster tumour cell growth by supply of growth factors and growth promoting cell contacts including provision of active fibronectin. The vulnerable seed is protected from host immunity by an immunosuppressive microenvironment.

Among the first cells entering the area of future metastasis are VEGFR1+ haematopoietic progenitor cells (*27*). These cells form clusters that precede further immune cell infiltration and tumour cell seeding and begin to remodel the local

microenvironment through induction of matrix metalloproteinases (MMP; prominently MMP9) and integrins. The cell clusters have been described as heterogeneous, comprising cells of various maturation states including CD117+ progenitor cells as well as CD11b+ monocytes and mature macrophages.

The $CD11b^{+}$ myeloid cells are a heterogeneous population of immature cells with immunomodulatory capabilities – MDSC, which seem to orchestrate further formation of the premetastatic niche (*28*) and promote the immunosuppressive function. The recruitment of immature myeloid cells and endothelial progenitors to the niche is driven by toll-like receptor 4 (TLR4) signalling, a multi-ligand receptor, activated by S100A8/A9 (*29*).

Further components of the premetastatic niche include endothelial cells, driving the angiogenic switch in the metastatic lesion and mesenchymal cells, which develop into fibroblasts for the tumour (and metastasis) stroma.

It is still not clear, how the premetastatic niche is regulated and installed and whether tumour cells are specifically guided to established niches or reach them by chance and due to the enhanced entry mechanism.

Exosomes are currently being seen as a potential means of communication between the primary tumour and the target tissue of metastasis. Exosomes are small membrane vesicles, released by many cells in the human body. However, the delivery by tumour cells is vastly increased as compared to healthy cells. They contain proteins, mRNA and miRNA and have the potential to selectively alter recipient cells and the extracellular matrix in the target area.

2.1.2 The role of MDSC in primary cancer and the premetastatic niche

The tumour makes use of several mechanisms to suppress and evade the anti-tumour immune response. Immunomodulatory Treg and MDSC accumulate in the tumour and actively inhibit anti-tumour action. MDSC accumulation has been associated with numerous factors including among others VEGF, GMCSF,

S100A8/A9 and CCL2 (*30*). MDSC are not a discrete cell population but much rather comprise a variety of cells in different stages of maturation and with different backgrounds: in mice as well as in humans, MDSC of granulocytic as well as of monocytic heritage have been described (*31*). The granulocytic MDSC present a $Ly6G^{+}Ly6C^{low}$ phenotype with high intracellular levels of reactive oxygen species (ROS) but virtually no nitric oxide (NO) while the monocytic MDSC is characterised as $Ly6G^{-}Ly6C^{high}$ with high NO and undetectable ROS levels. The markers, shared across all subtypes of MDSC include Gr1 and CD11b. Various subtypes of MDSC have been described with CD115 and CD124 expression being related to immunosuppressive activity (*32*)

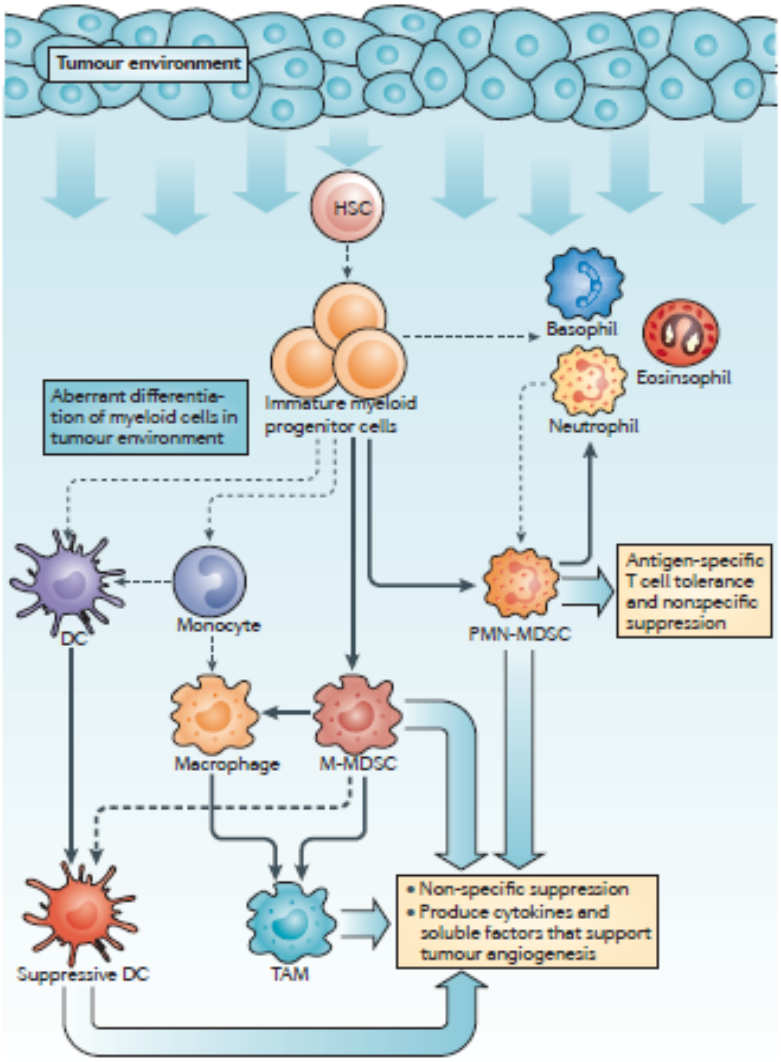

Figure 2: MDSC are immature monocytes and granulocytes

Schematic illustration of the differentiation pattern of MDSC in relation to precursors and mature cells without immunomodulatory function. Illustration from (*33*).

MDSC of all types share a common function and serve for orchestration of the immunomodulatory function in the premetastatic niche, although monocytic MDSC have been described to be generally more active than granulocytic MDSC.

MDSC have been shown to nitrate T cell receptors (TCR), preventing their activation (*34*) and to moreover interfere with TCR-CD3 signalling, crucially required for full T cell activation (*35*). They moreover exert immunosuppressive effects via production and secretion of iNOS and Arginase and differentiate into tumour-promoting TAM under the influence of the tumour microenvironment (*36*) .

MDSC accumulation in the premetastatic niche is mediated inter alia by the myeloid-related protein heterodimer S100A8/A9 (*37*), member of the S100 protein family of calcium binding proteins. S100A/A9 is actively released by monocytic cells, upon activation and during differentiation and acts as a proinflammatory, intrinsic danger signal, promoting the accumulation of specific immune cell populations. MDSC induce expansion and local accumulation of Tregs and via this detour as well as directly suppress the anti-tumour immune activity of NK cells (*38*). MDSC have been shown to accumulate in the primary tumour in response to a variety of cytokines and soluble factors including granulocyte colony stimulatory factor (G-CSF) and TGFβ, released by tumour and/or non-tumour cells within the tumour microenvironment (*39*). MDSC express receptors for S100A8/A9 and initiate an autocrine loop to increase local levels of the heterodimer (*40*), which in turn increases MDSC accumulation. Up-regulation of S100A8/A9 has moreover been found in the lung tissue of tumour-bearing animals prior to establishment of manifest metastasis (*41, 42*). S100A8/A9 is secreted by myeloid cells either directly into the interstitium or as a major component of exosomes (*43*) and promotes the recruitment of $CD11b^+$ myeloid cells to the premetastatic lungs (*41, 42*), which must be interpreted as driving premetastatic niche establishment.

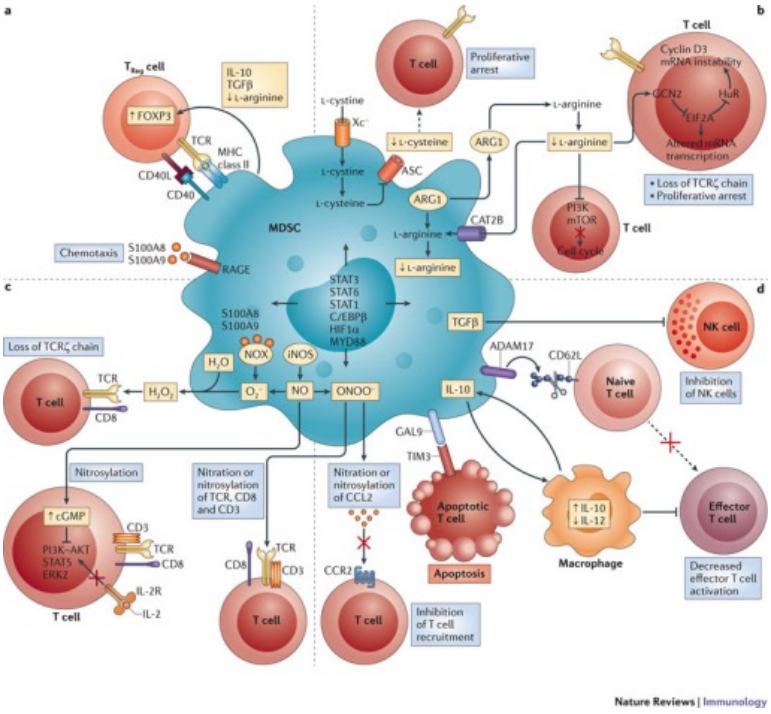

Figure 3: Immunomodulatory activity of MDSC

The illustration summarises the interaction of MDSC with T cells, macrophages and NK cells in the tumour microenvironment to promote an immunosuppressive environment, permissive for growing tumours and establishment of metastasis. Illustration adapted from (*33*)

The prominent role of MDSC in tumour-mediated immune remodelling inspired therapeutic targeting of MDSC expansion via e.g. eradication of MDSC-stimulating factors or MDSC function by inhibition of Arginase and iNOS. Moreover, promotion of MDSC differentiation into mature myeloid cells without immunosuppressive function by provision of Vitamin A or Vitamin D3 has been described (*30*).

2.2 S100A8/A9 as a marker for immune cell activity

S100A8/A9 is a heterodimer of the S100 family of calcium binding proteins, particularly released by activated phagocytes. It is involved in numerous intra- and extracellular processes (*44*) but was most prominently attributed a strong promoter of

inflammation and chemokine to immune cells, sensitively reflecting local phagocyte activity in inflammatory disorders.

The family of S100 proteins is characterised by two calcium-binding-sites per molecule and comprises more than 20 members. S100 A8 (MRP8) and S100A9 (MRP14) are specifically linked to innate immune functions by their expression in granulocytes, monocytes and early differentiation stages of macrophages. Intracellular, S100A8/A9 are involved in tubulin turnover, thereby controlling phagocyte migration (*45*). There is moreover evidence that these phagocyte specific S100 proteins are actively secreted in a tubulin dependent manner (*46*) during activation of the cell.

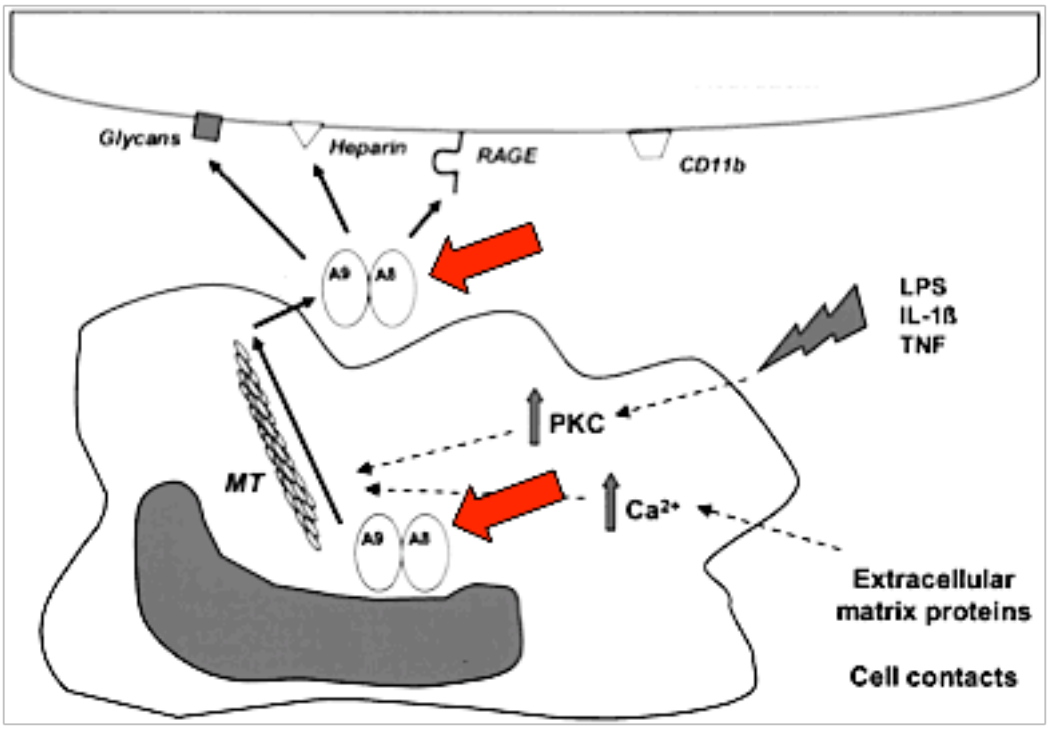

Figure 4: S100A8/A9 release and action

Schematic illustration of S100A8/A9 release upon activation of a resting monocyte by LPS, Il-1β or TNF. S100A8/A9 is actively transported to the cell surface through interaction with cytoskeleton components and released into the interstitium. Via binding of, among other receptors, RAGE and TLR-4, S100A8/A9 exerts proinflammatory effects. Illustration adapted from (*47*).

They are in this role regarded as a damage-associated molecular pattern (DAMP) molecule, exhibiting kind of a double life: as intracellular molecules they have a role in cell homeostasis; after release to the extracellular compartment either passively, due to cell damage or actively during infections or inflammation, they become danger signals which activate immune cells and vascular endothelium (*48, 49*).

Release of these molecules is specifically restricted to sites of vascular inflammation since secretion of S100A8/A9 is induced by contact of phagocytes with inflammatory activated endothelial cells. Therefore, various proinflammatory functions have been described for S100A8/A9: S100A8/A9 is an endogenous ligand for pattern recognition receptors RAGE and TLR4, binds to heparin sulfate proteoglycan and carboxylated N-glycans on endothelial cells, and induces the production of pro-inflammatory cytokines and adhesion molecules on endothelial cells (*50*).

Through the interaction with endothelial cells, S100A8/A9 stimulates the paracrine production of mediators to attract further $CD11b^+$ myeloid cells, such as serum amyloid A (SAA) 3 in the pre-metastatic lungs (*42*).

S100A8/A9 has been shown to act as endogenous ligand to TLR4, mediating the secretion of TNF and other proinflammatory, monocyte-specific cytokines (*50, 51*). They activate endothelial and immune cells; exhibit cytotoxic activities, have been described as chemotactic factors and promote adhesion and recruitment of leukocytes to sites of inflammation. S100A8/A9 are significantly overexpressed at sites of inflammation, in infections, autoimmune diseases and artherosclerotic plaques and are a sensitive marker for unstable angina pectoris. There is strong correlation of their serum concentrations to disease activity in many inflammatory disorders like Rheumatoid Arthritis (RA), Systemic Lupus erytematosus (SLE), Inflammatory Bowel Disease (IBD) or vasculitis (*50, 52-55*).

In the context of juvenile arthritis, several reports identify S100A9 as superior indicator of inflammation activity compared to established markers of inflammation – a relapse of disease under therapy or after abortion of therapy is reflected by elevated serum

levels of S100A9 as early as three to four weeks before clinical symptoms occur (*53, 56, 57*). The local tissue concentration of the S100A8/A9 complex in the area of inflammation and S100A8/A8 release has in this context been reported as up to 20-fold higher as compared to the correlating serum level (*49*).

The association between tumour development and increased immune cell activity in the tumour-supportive environment and the evidence for an involvement of S100A8/A9 in regulation of tumour-associated inflammation led to the evaluation of S100A8/A9 as a clinical tumour marker in various human cancers like prostate, gastric and colon cancer (*58*). Generally, high S100A8/A9 levels in tumour tissue or in serum seem to indicate a more rapid, aggressive course of disease (*59, 60*). Non-invasive detection and measurement of exosomal S100A8/A9 release in potential pre-metastatic sites would strongly promote the clinical utility of this marker.

Recently, S100A8/A9 has been discussed as one of the bookmarking mediators of the premetastatic niche (*61*).

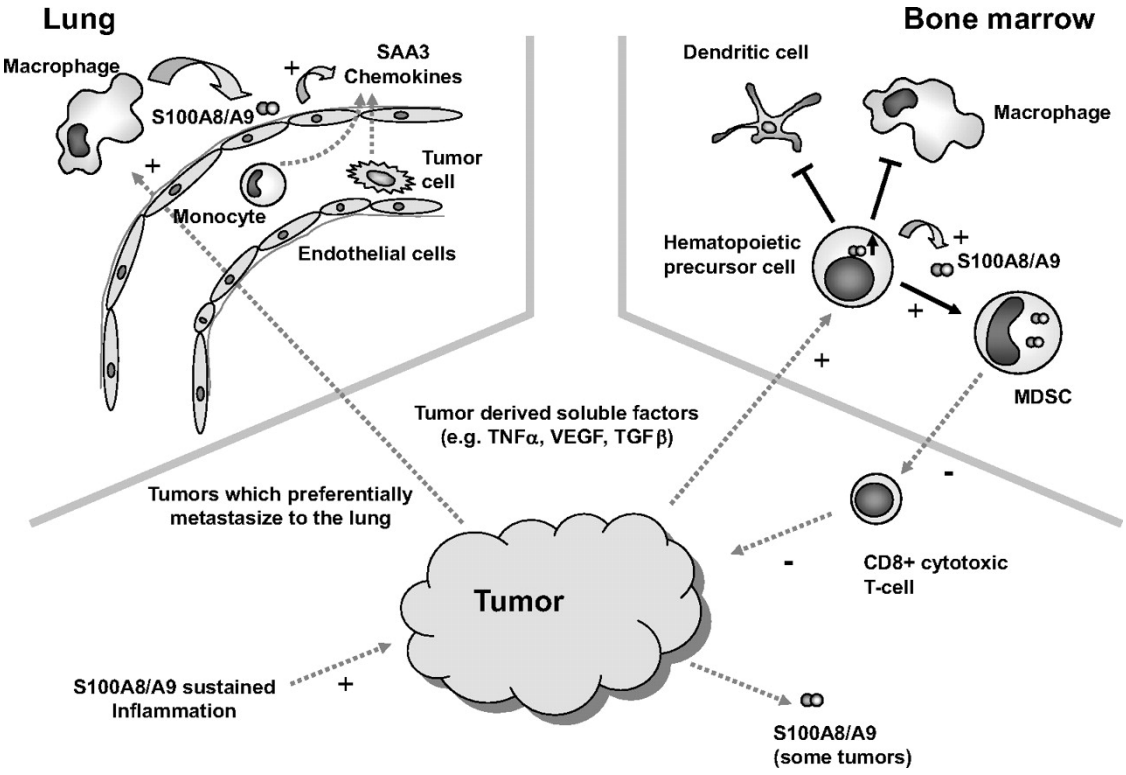

Figure 5: S100A8/A9 in the context of malignant disease

S100A8/A9 is released in the premetastatic lung environment, inducing hyperpermeability foci in the lung for easier extravasation of immune and tumour cells. It moreover acts as a chemoattractant for myeloid cells and promotes MDSC accumulation. Illustration adapted from (*50*).

Ve cadherin+ endothelial cells and Mac1+ (beta 2 integrin CD11b/CD18) myeloid cells in lung tissue of tumour bearing mice have been shown to express high amounts of S100A8/A9 in response to tumour secreted factors that could include tumour exosomes (*41*). S100A8/A9 is believed to, directly (*62*) or via promotion of soluble factors such as TNFα, TGFβ and MIP2 (*63*), activate endothelial cells and recruitment of lymphocytes (*64*). These factors in turn signal for the circulating tumour cells to leave the blood stream and to seed into the prepared niche.

The crucial role of S100A8/A9 for cancer development and spread has been underlined by recent studies, showing S100A9 knock-out mice to have significantly decreased numbers of tumour-promoting myeloid derived suppressor cells, reduced rates of metastasis and an increased overall survival (*37*) as compared to wild-type mice.

A correlation between serum S100A8/A9 and failure of tumour immune therapy response has been established in retrospective studies (*65*); in murine breast cancer models, the density of S100A8/A9+ cells in the tumour was associated with a more aggressive tumour development and reduced clinical outcome (*66*). S100A8/A9 has also been directly targeted for therapeutic purposes. The small molecule Tasquinimod binds S100A9 and induces a conformational change of the heterodimer, apparently preventing S100A8/A9 from effectively binding certain target receptors. In clinical trials, the consecutive inhibition of S100A8/A9 signalling had positive outcome effects in prostate cancer (*67*) and breast cancer (*68*), probably through revision of S100A8/A9-mediated tumour-promoting immune modulation (*69, 70*).

In both roles – as a marker for immune cell activity in inflammation and cancer as well as a therapeutic target for inhibition of pathologic immune activity, S100A8/A9 has a strong potential.

2.3 Molecular imaging

Per definition by the Society for Nuclear Medicine and Molecular Imaging, molecular imaging is “the visualisation, characterization, and measurement of biological processes at the molecular and cellular levels in humans and other living systems“ (*71*). This can be achieved via various ways and includes imaging approaches of multiple scales, ranging from microscopy systems to clinical whole body scanners. Modalities for whole body molecular imaging include magnetic resonance imaging (MRI), planar or tomographic optical imaging (OI) and radionuclide-based techniques positron emission tomography (PET) and single photon emission computed tomography (SPECT). Usually, the different imaging techniques require the use of specific contrast agents for visualisation of molecular and physiological processes.

Three major types of contrast agents can be defined by their principle of action (*72*):

1. Perfusion type contrast agents distribute with the blood pool without specifically binding target structures in tissue or the vasculature. Perfusion

type contrast agents enable measurement of perfusion and pathological variation of perfusion including hyperaemia in inflammation or highly vascularised cancer lesions. Measurement of local extravasation of perfusion type contrast agents also allows for estimation of vessel wall integrity as an indicator of pathological processes.

2. Target-specific probes are characterised by a binding moiety, specifically addressing a structure, present in the target tissue. This structure can be a cell surface marker as well as a soluble factor or extracellular matrix component. Even intracellular structures can be targeted with appropriate probes, able to penetrate the cell membrane. Target-specific probes comprise – aside from the binding moiety – a label, respective of the chosen imaging modality.
3. Activatable or smart probes are inactive and do not emit as signal, detectable by the chosen imaging modality until they interact with the target structure. Activatable probes therefore offer the highest signal-to background ratio of all probes, as the unbound contrast agent in the blood pool does not contribute to the unspecific background noise. The relatively complex chemistry behind probes with variable signal characteristics limits the use to few applications like visualisation of enzyme activity.

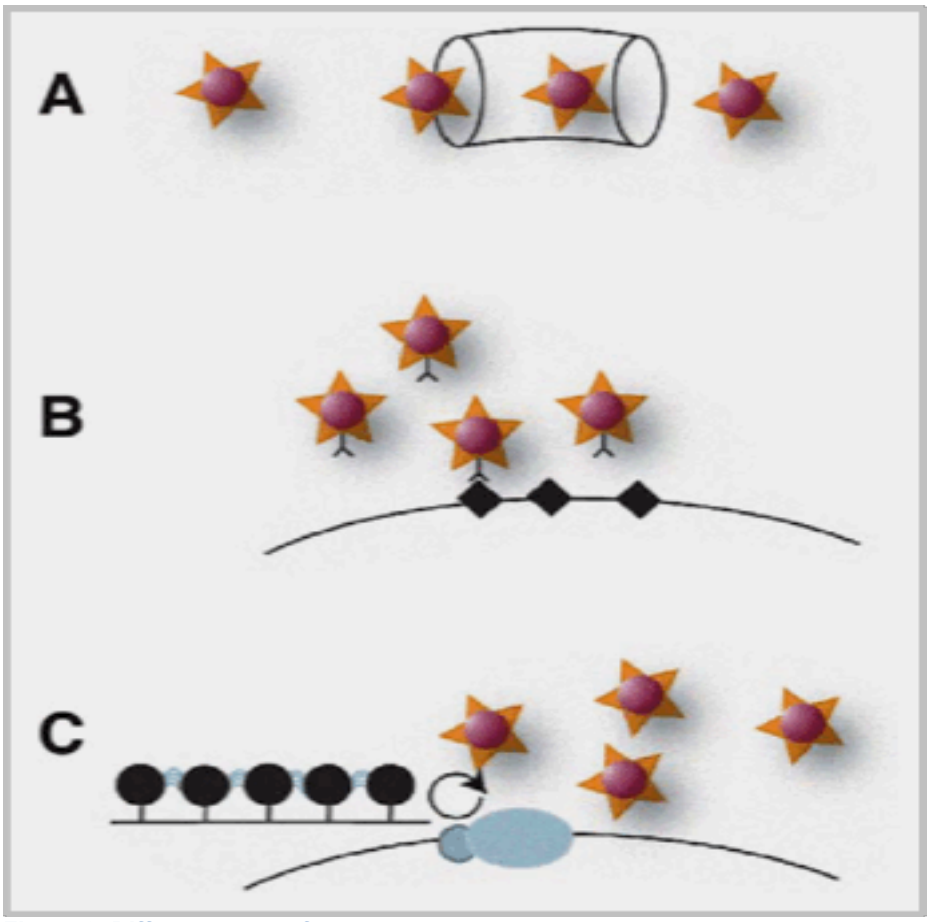

Figure 6: Different types of contrast agents.

Perfusion type contrast agents (A) distribute with the blood flow and indicate perfusion and vascular integrity without specific target binding. Target-specific contrast agents (B) comprise a binding moiety and a signalling component and specifically accumulate in areas of high target expression. A considerable unspecific background is constituted by unbound tracer. Activate-able probes (C) change their signalling capacity upon interaction with the target molecule and therefore do not exhibit unspecific background signal. Illustration modified from (*72*).

Probes of all three classes have been presented for all common imaging modalities. For specific visualisation of disease markers, targeted probes are still the most commonly used, and the chemistry behind labelling targeting molecules is well established.

In this study, we aimed for establishment of a targeted imaging technique for immune cell activity-associated markers using this straightforward technical approach.

2.3.1 Principles of target-specific imaging

Various different molecules – both natural and artificial – exhibit the potential to specifically bind target structures in biological systems, thereby qualifying in principle as the backbone of a target-specific imaging probe.

The most prominent among binding molecules certainly are antibodies of the immunoglobulin G (IgG) type. Over the past decades, the discrimination properties of antibodies have been used to establish methodology, essential for current research: ELISA, FACS and immunohistochemistry evenly rely on the specificity of antibody-target binding. Antibodies have moreover been successfully established as molecular therapeutics and – in preclinical settings – highly versatile imaging agents (*73*). IgG is widely conserved across mammals and of very similar structure even between mice and humans. A full length IgG has a size of around 150 kDa and is assembled of four subunits, two identical light chains and two identical heavy chains. The size of antibodies renders the possibility of random labelling – conjugating the antibody with a signalling molecule without changing binding affinity or in vivo distribution of the compound as compared to a naïve antibody. However, recombinant antibodies can be engineered for site-specific labelling for even easier and quicker tracer preparation. Some animals, among them camels and sharks, present with more ancient, archaic antibodies, comprising a less complex structure. The antibodies of camelidae for example do not confirm the IgG structure but lack light chains, reducing the overall size to less than 90 kDa (*74*).

From intact IgG, several fragments can be isolated and recombinantly fused. The isolated fragments, responsible for antigen binding can be as small as 15 – 20 kDa.

The size is of major importance for the tracer distribution in biological, living systems as it essentially determines the tracer ability to extravasate and penetrate stromal tissue as well as the elimination route. Smaller compounds generally show a faster tissue penetration and moreover do not require vascular integrity to be disturbed.

Bigger compounds require more time or active transport mechanisms to reach stromal, extravascular targets.

The major elimination routes from the body are the kidneys for compounds, smaller than about 30 kDa, and the liver for bigger compounds. Renal elimination is considered to be much faster, clearing circulating compounds within hours, while hepatic elimination of circulating compounds can take days or even weeks. The blood pool level of a specific contrast agent on the one hand determines the unspecific background signal, exerted by circulating tracer that has not specifically bound the target structure (yet) and on the other hand exposes the body to the label – in the case of radionuclide-driven tracers to radioactivity. A longer circulation time of bigger tracers therefore constitutes a more intensive exposure of the recipient to radioactivity with all the consecutive risks and a longer delay between tracer application and the reduction of the unspecific background signal to a level that would reasonably allow for identification of specific tracer accumulation.

For the more rapid accumulation in the target area and faster elimination from the blood pool, smaller compounds are generally regarded more favourable for in vivo application. The rapid distribution enables for examination shortly after tracer application. For some targets – especially those, located extravascular and thus more difficult to reach for circulating tracers, additional features of the targeting moiety and the label come into play – the distribution across extravascular body compartments can be influenced by the charge/polarisation as well as lipophilicity and/or hydrophilicity of the compound. Additionally, binding affinity and specificity or potential cross reactivity determine the quality of an in vivo imaging signal.

Antibodies naturally provide a high binding affinity and target specificity. Their relatively big size enables for very easy labelling approaches but also demands specifically tailored imaging approaches due to long circulation time and consecutively high unspecific background, early after administration. Ideally, a tracer would provide

the binding characteristics of an antibody with the biodistribution and elimination of a smaller molecule.

The individual choice of a tracer molecule depends on availability of high-affinity, highly specific targeting moieties and accessibility of the target structure. Depending on the tracer molecule, different labels for appropriate imaging modalities can be considered.

2.3.2 Molecular imaging modalities for target-specific imaging

Given the availability of a specific contrast agent, all in vivo imaging modalities basically qualify for in vivo molecular imaging. Some approaches, however, are more suited for particular studies than others.

In MRI, signal is generated through the interaction of electromagnetic fields with nuclei such as the protons in the water molecule. In addition, image contrast is mainly affected by relaxation processes, which can be influenced by contrast agents. However, the overall effect of contrast agents is moderate, resulting in a relatively low sensitivity to detect specifically labelled agents. Therefore a high local concentration of contrast agent is required for reliable detection, widely precluding MRI from use for targeted imaging.

Only OI and radionuclide-mediated methods offer sensitivity in the nanomolar range, enabling for detection of local tracer accumulation.

2.3.2.1 Fluorescence-mediated imaging approaches

OI relies on the use of near-infrared light as carrier of diagnostic information. As opposed to light of the visible spectrum, near-infrared (NIR) light penetrates tissue up to a couple of centimetres of depth due to lower absorption in tissue. At the same time, the autofluorescence of tissue is relatively low in the NIR range of the spectrum. Fluorescent dyes have initially been developed for fluorescence microscopy but

subsequently been used for labelling of tracer molecules for in vivo imaging applications.

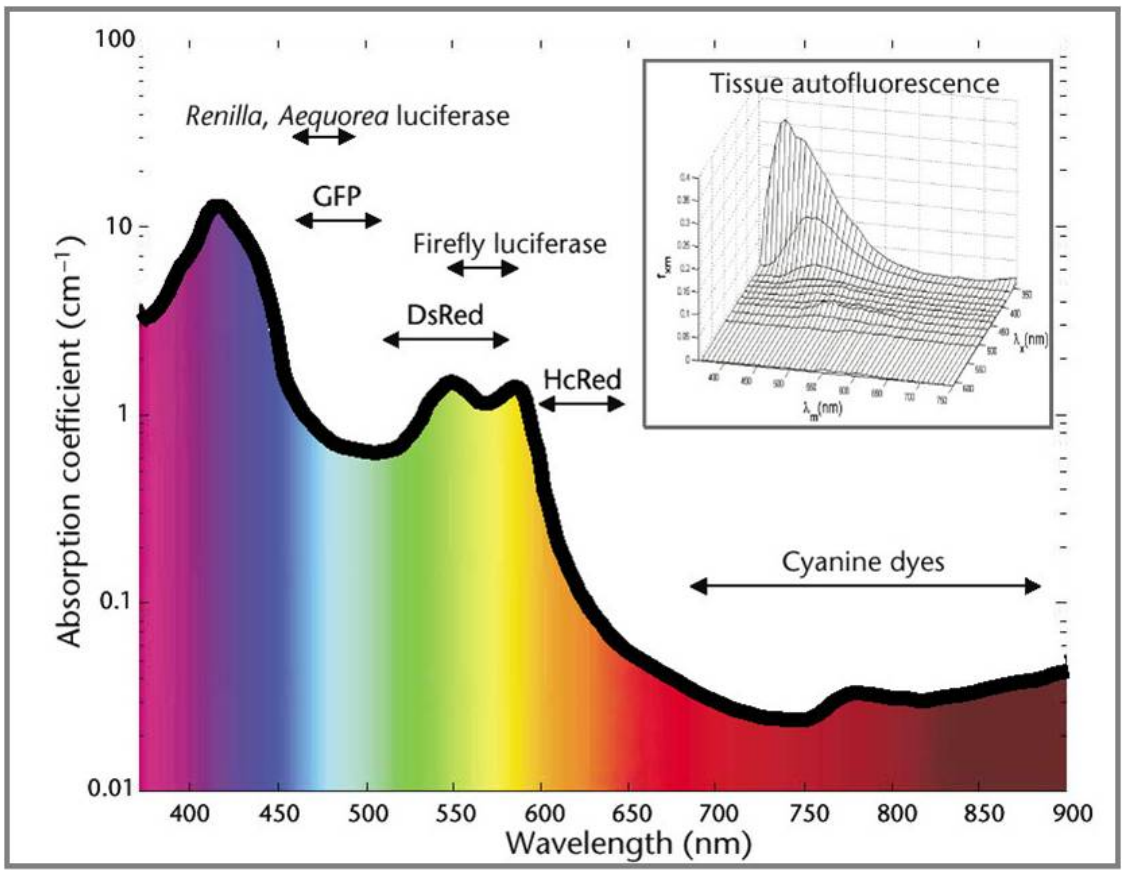

Figure 7: Absorption coefficient in relation to the optical spectrum.

The graph shows the absorption coefficient for distinct wavelengths, illustrating that light of the near-infrared range (<650 nm) faces less absorption and therefore penetrates tissue better than light of shorter wavelength. The insert shows the tissue autofluorescence. From (*75*)

Fluorescent dyes require excitation by light of discrete wavelength. The excitation light is absorbed by the dye and transformed, resulting in emission of lower energy light by the dye. This emission can be recorded at video rate by dedicated camera systems and provide sensitive high resolution imaging of the dye distribution. Fluorescence reflectance imaging (FRI) systems, combining emission light source and detector in an arrangement, similar to a camera with flash light, detect the surface signal, originating from the specimen upon excitation.

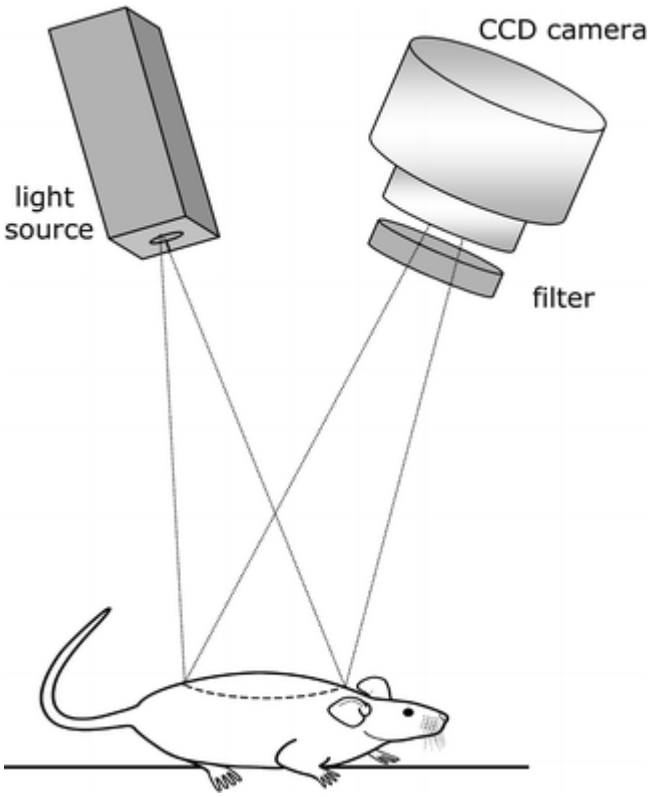

Figure 8: Principle of Fluorescence Reflectance Imaging

For FRI, a simple set up of light source and a filter-equipped camera is required. Upon illumination of the target structure, i.e. the animal, and consecutive excitation of the fluorescent dye, emitted light is collected by the camera. Specific filters ensure that only the emission of the elicited dye is collected and reduce recording of unspecific background fluorescence. Illustration from (*76*)

Due to scattering and absorption of the emitted fluorescence signal, detection by conventional camera systems is limited to a couple of millimetres of depth in living tissue. Moreover, scattering, absorption and the theoretical possibility of single signalling molecules being excited and detected multiple times hamper quantification of optical imaging signals and thorough internal controls are needed for validation of in vivo observations.

Tomographic approaches have been established to overcome these limitations. Basic fluorescence-mediated tomography (FMT) systems combine multiple excitation light sources and detectors in a gantry-like arrangement around the specimen and calculate the 3D position of a NIRF source from the signal pattern across the gantry. A mathematically more sophisticated approach uses data from near-planar, multi-

angle imaging to calculate the in vivo distribution of fluorescence tracers in a small 3D volume.

Based on phantom experiments with fluorescent light sources in defined depths of absorbing and scattering tissue, commercially available FMT systems promise full quantification for all fluorescent dyes they have been calibrated for. Although this promise has been contested recently, leading to some uncertainty as to the real potential of FMT for reliable quantification, it still is the only imaging approach for fast and easy in vivo 3D imaging of fluorescent tracer distribution in deeper tissue sections (of laboratory animals). In hybrid imaging approaches, the additional use of either CT or MRI data for image reconstruction and normalisation of the functional fluorescence data increases the image data quality. For this study however, a simple, fluorescence-only FMT system was used and to circumvent discussion on the precision and validity of quantitative FMT data has only been used for visualisation of tracer distribution in the tumour area.

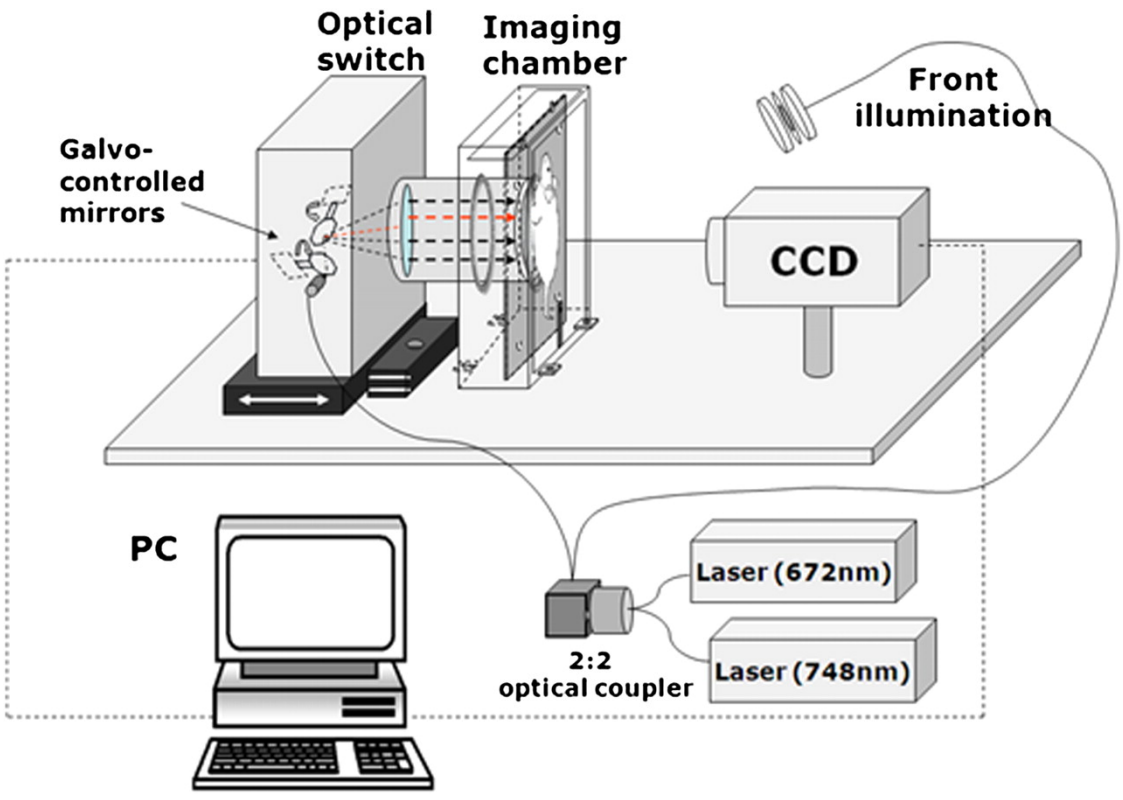

Figure 9: Exemplary set up of a Fluorescence Mediated Tomography system.

Data from a sequence of planar scans after illumination of the specimen from various angles allows for reconstruction of fluorescence dye distribution within the specimen. From (77)

Tracers for in vivo OI can usually serve as signalling molecules for Fluorescence Activated Cell Sorting (FACS) and fluorescence microscopy as well, enabling immediate correlation of in vivo imaging results.

Common dyes for NIRF imaging include cyanine dyes with excitation/emission maxima in the NIR range of the spectrum. These dyes are commercially available as active esters for quick and easy labelling of proteins or similar compounds. In contrast to other fluorescent dyes cyanine dyes do not bleach quickly, providing constant NIRF for in vivo application.

2.3.2.2 Radionuclide-mediated imaging approaches

Radionuclide-mediated imaging approaches use the energy, emitted in the context of radioactive decay for generation of image information. The two techniques, established for in vivo imaging are PET and SPECT. Both methods offer tomographic, three-dimensional information on radionuclide distribution within the specimen but differ with regards to detection method and suitable isotopes.

PET imaging is based on indirect measurement of positron-emission by isotopes that undergo β+ decay. The released positron travels for a short distance in tissue, thereby decelerating, and annihilates with an electron. The energy, released during this annihilation is emitted as a pair of annihilation γ-photons, travelling in virtually opposite (179.5°) directions. These γ-photons can be detected by a circular gantry and allow for retrospective localisation of the annihilation event, virtually identical with the localisation of the isotope. To increase the sensitivity of PET scanners scintillators potentiate each detected photon before the event is recorded by photomultipliers. Only those photons can be used for reconstruction of isotope distribution patterns that arrive the gantry in pairs, which is also called coincidence detection. The detected

events at different detector positions on a circular gantry result in projections, enabling the reconstruction of the distribution of activity. In addition, the travel time difference between the two opposite detectors can be exploited to improve image quality. Spatial and temporal resolution of PET imaging are determined by the design of the gantry and arrangement of detectors as well as the reconstruction algorithm and the energy of the radioisotope's emission protons, as higher energy protons travel further in tissue before annihilating with an electron, thereby increasing the distance between the location of the isotope/tracer and the location of the detected event.

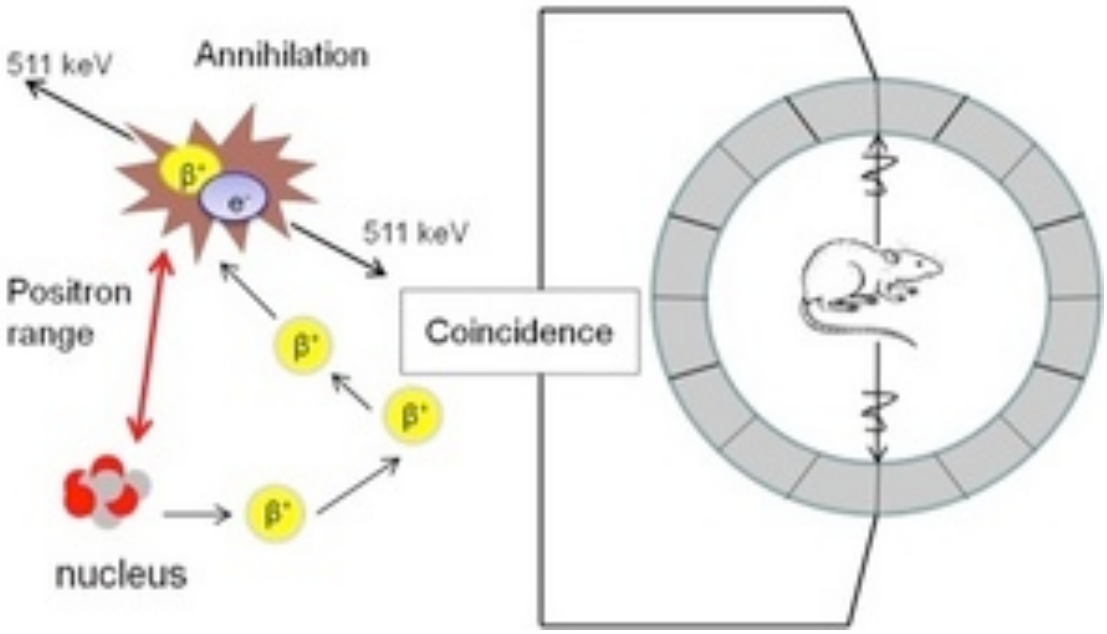

Figure 10: Principle of Positron Emission Tomography Imaging.

Upon radioactive decay of β-emitters, positrons (β^+) are released and annihilate with electrons (e^-). In result of the annihilation, two identical photons are sent out in virtually opposite direction. Recording of these photons on a circular gantry allows for reconstruction of the emitter distribution in the target volume. Image courtesy of Dr Thuy Tran, Lund University Bioimaging Center, Sweden

Radioisotopes, suitable for PET include ^{18}F, ^{11}C and ^{68}Ga. The relatively short half-life of these isotopes, ranging between around 20 min (^{11}C) and 110 min (^{18}F), demands tracer compounds of rapid biodistribution for effective imaging. Intact IgG would not have accumulated in the target area and especially have not cleared from the blood pool by the time the isotope has decayed to a degree below the detection sensitivity of PET. An exception among common PET-suitable isotopes is ^{89}Zr with a half-life of 78 h. It is increasingly used as radiolabel for antibodies in clinical immune-PET applications (*78*).

SPECT is based on direct detection of γ-rays, emitted during the decay of isotopes like ^{111}In, ^{99}Tc or ^{123}I. These isotopes are characterised by a generally longer half-life than typical PET isotopes. The half-life of ^{111}In is 67 h, enabling – just as ^{89}Zr – for labelling of e.g. intact IgG and following the tracer over several days after application.

To obtain SPECT images of γ-decay, a gamma camera is rotated around the object and planar images of γ-radiation are acquired. The gamma-camera consists of collimator in front of detector elements to measure perpendicularly arriving γ-rays. Therefore, the spatial resolution depends strongly on the set-up of the collimator and high-resolution imaging of small animals is possible. Multiple projection images are then retrospectively combined for calculation of a three-dimensional dataset, following algorithms, similar to those from computed tomography. Typically, the camera is rotated a full 360° around the specimen and images are acquired every 3-6° for ideal coverage of the object.

The sensitivity of SPECT is slightly lower than PET due to the use of a collimator.

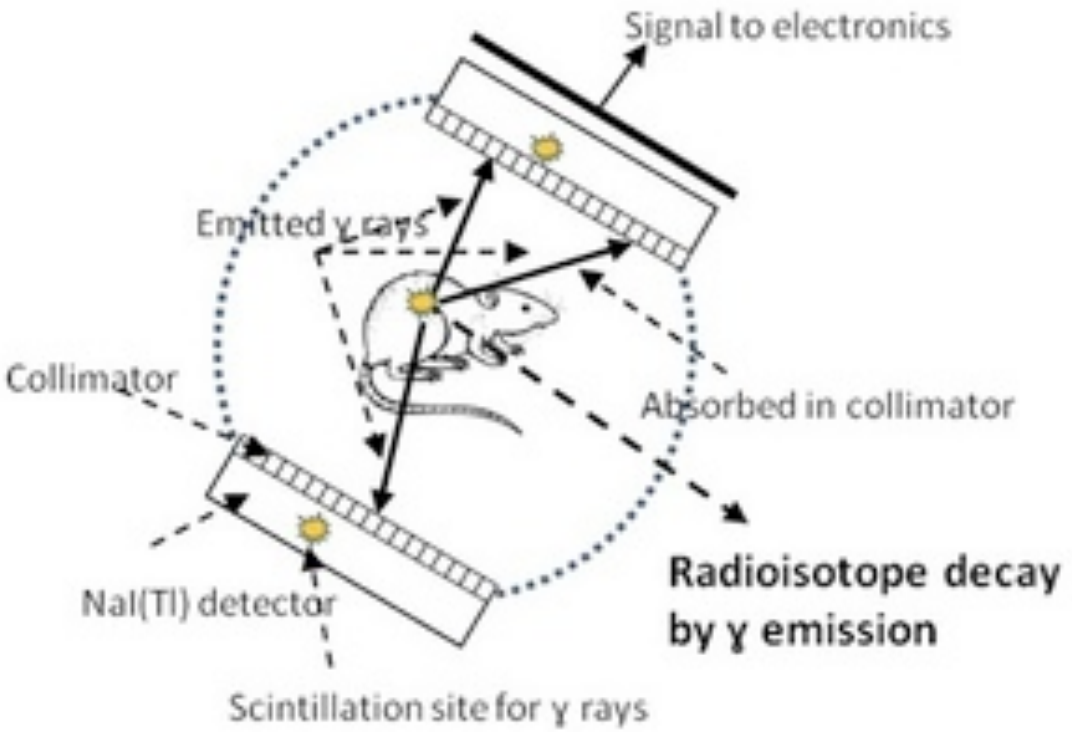

Figure 11: Principle of Single Photon Emission Computed Tomography.

Some isotopes emit γ-rays during radioactive decay. Collection and recording of these photons by a circular gantry or a circulating γ-camera allows for reconstruction of the γ-ray source distribution within the target volume. Image courtesy of Dr Thuy Tran, Lund University Bioimaging Center, Swede

2.4 Previous work on S100A8/A9 imaging

Target-specific in vivo S100A8/A9 optical imaging has recently been established for sensitive and specific monitoring of monocyte activity in local inflammation (*79*) and primary cancer lesions (*80*) using a fluorescence labelled antibody. Both publications can be found in the annex to this thesis.

Briefly, from a polyclonal antibody, targeting S100A9 (aS100A9), a fluorescent tracer has been synthesised, which has been successfully tested in vitro and in vivo. It could be shown that S100A9 is a versatile marker for inflammatory activity in exemplary models of disease, representative of different inflammatory stimuli and pathologic pathways. Specifically, the monitoring of local inflammation using S100A9 as molecular target for optical imaging has been established: We were able to show that a fluorescence labelled antibody, targeted on S100A9, allowed for specific visualisation of S100A9 release by activated immune cells in areas of inflammation. In

vivo imaging was validated using immunohistochemistry of inflamed tissue, showing S100A9 to be associated with activated monocytes in areas of inflammation. Moreover, dual injections were performed with aS100A9 and a rabbit-derived IgG (rabIgG) without relevant specificity in mice. Labelled for different excitation and emission wavelength, these dyes could be differentiated in vivo with the rabIgG representing perfusion and unspecific binding mediated background signal. Different distribution patterns suggested a specific accumulation of the S100A9-detecting tracer. We repeated the experiments in S100A9-/- mice (complete knock out). While rabIgG mediated signalling was virtually unchanged, the accumulation of aS100A9 dropped to levels, equivalent to unspecific background distribution. S100A9 in vivo imaging positively correlated with S100A9 serum levels.

In selected models of inflammation and immune activation such as arthritis and infectious disease, the predictive value of S100A8/A9 imaging could be demonstrated by establishing a correlation between in vivo imaging and disease development and outcome: Different models of arthritis have been established and examined using optical S100A9 imaging. In collagen induced arthritis in BALB/c mice, a stable, strong inflammation could be observed after challenge by clinical examination and in vivo imaging; the severity of inflammation, reflected by clinical grading, strongly correlated with in vivo S100A9 imaging. In a second step, we induced arthritis in Bl6 mice that exhibit a heterogeneous, clinically unpredictable response to the challenge. S100A9 imaging allowed for prediction of the course of disease as early as seven days after arthritis induction. In a model of local infection, S100A9 imaging at early stages after infection allowed for identification of an effective, Th1 driven immune response, representing the first in vivo marker for Th1/Th2 dichotomy.

The severity of inflammation and in vivo imaging could also be correlated for allergy, inflammatory bowel disease (*81*) and LPS induced lung inflammation.

The in vivo imaging could be shown to closely reflect local S100A8/A9 release: Serum was acquired at different time points during development of inflammation and parallel

to imaging. By ELISA, S100A9 was quantified and correlated with in vivo imaging results. Where applicable, we collected material for determination of local S100A9 levels. In models of infection, the infected hind paws were flushed and the resulting liquid was assessed for cellular infiltrate, pathogen and S100A9 (*79*). In lung inflammation, BALF was collected; in arthritis, synovial fluid was collected. Specific imaging sensitively reflected the local S100A9 levels and correlated well with systemic levels of the protein. This suggests an integrated diagnostic approach, combining an easy accessible serum test for stratification as to which patient might benefit from a specific scan to localise and differentially monitor multifocal disease (*79*).

Having used optical fluorescence imaging only, these studies were limited to superficial foci of immune cell activity such as the primary tumour lesion.

For application of S100A9 imaging to visualise the systemic influence of cancer on the immune system and the potential activity of immune cells in the context of premetastatic tissue priming, the physical limitation of optical imaging may hamper the collection of sufficient, systemic information. Moreover, imaging beyond the preclinical mouse model system would be precluded.

2.5 Purpose of this project

The aim of this thesis is to prove the suitability of S100A8/A9 to serve as a marker for tumour-associated immune remodelling in the context of primary malignant disease and systemic tumour spread.

Beginning with optical imaging of the immune cell activity in the primary tumour, methodology for visualisation of systemic tumour effects will be investigated. Building on the aforementioned optical imaging approach, S100A9-specific SPECT imaging will be developed to explore the potential of S100A9 as a translatable diagnostic imaging marker. This S100A9-specific SPECT imaging will be tested in a murine model of metastatic breast cancer to investigate *in vivo* visualisation of systemic tumour-mediated effects on monocyte activity, assessing S100A8/A9 as a surrogate

marker for tumour-mediated immunomodulation in the context of premetastatic lung tissue priming. The specific objectives of this project are

1. **To establish S100A8/A9 as a marker for local tumour-immune interaction**

   (Chapter 3)

   Optical imaging for specific detection of S100A8/A9 release will be used to identify regional changes in immune cell activity and tumour-associated inflammation in the primary tumour. Furthermore, the correlation of S100A8/A9 activity in the tumour microenvironment with tumour aggressiveness and growth will be investigated. Analysis of the cellular composition of such foci will serve for validation of the in vivo imaging results.

2. **To develop a S100A9-specific radiotracer**

   (Chapter 4)

   The fluorescent optical imaging tracer is limited to superficial, focal imaging. For evaluation of systemic S100A8/A9 release, indicative of the systemic tumour-immune interaction, a radiotracer for SPECT application will be produced.

3. **To establish systemic S100A9-specific in vivo imaging in cancer**

   (Chapter 5)

   The aforementioned S100A9-specific SPECT tracer will be used for visualisation and measurement of tumour-immune interaction in the tumour microenvironment and distant tissues. The effects of malignant disease on the immune cell activity in distant target tissue of metastasis will be examined and cellular processes, underlying the in vivo imaging signal will be identified.

4. **Understanding pre-metastatic niche establishment**

   (Chapter 5)

   The imaging methodology, established within this project, will enable studying of mediators and regulators of tumour-immune interaction and tumour-

mediated tissue priming. The effects of inhibition of the CCL2/CCR2 signalling axis will be studied exemplarily.

3 Optical S100A9 imaging in the primary tumour environment

Contents, presented in this chapter, have in part been published in the Journal of Nuclear Medicine in May 2015 under the title “Optical In Vivo Imaging of the Alarmin S100A9 in Tumour Lesions Allows for Estimation of the Individual Malignant Potential by Evaluation of Tumour-Host Cell Interaction“(*82*). The full text of the publication can be found in the Annex (9.2).

As an initial step towards understanding of tumour immune interaction and establishment of a diagnostic tool for non-invasive measurement of these processes, the aforementioned method for visualisation of local inflammation has been adapted for the visualisation of tumour-associated immune cell activity in subcutaneous tumour models.

As mentioned already, tumour-associated myeloid cells and their offspring, including immature monocytes like MDSC and macrophages are highly abundant in the tumour microenvironment. They contribute to local growth and invasion by degradation of ECM, sustenance of tumour vitality by promoting neoangiogenesis and tumour immune evasion via suppressive interaction with host immunity.

In this study, S100A8/A9 imaging is established as a tool for non-invasive visualisation and measurement of tumour-associated monocyte activity as an indicator of malignant development and growth. Due to the nature of fluorescence-mediated imaging, this preliminary study was confined to imaging of tumour immune interaction in the subcutaneous tumour lesion itself.

3.1 Material and Methods

3.1.1 Murine breast cancer model

The murine breast cancer cell lines 4T1 and 67NR share the genetic background of a common maternal cell line, derived from a Balb/c mouse, and were used for tumour induction as an established syngeneic model system of graded malignancy (*83*). The specific characteristics of the tumour cell lines include differences in the metastatic potential: While 4T1 tumours induce metastasis in lungs and bone via haematogenous dissemination and invade the local lymph nodes within weeks, 67NR cells grow only locally.

Cells were cultured and harvested according to established protocols (*83*).

Female Balb/c mice were obtained from Charles River UK and housed in a dedicated Biological Services Unit under controlled conditions (regular 12 h day/night rhythm, controlled temperature) and chow and water ad libitum. The cage bedding was extra soft paper bedding to avoid irritation of the local tumour site. After delivery, mice were allowed to rest for at least two weeks before interventional procedures were initiated.

To control for a contribution of the tumour cells to local S100A9 levels and to prove specific tracer to target binding, S100A9-/- mice with Balb/c background were inoculated with 4T1 cells accordingly and underwent the same imaging procedure. The knock out mice were developed and bred at the Institute of Immunology, University of Münster, and provided as part of a collaboration. Characteristics of the knock out mouse have been described in detail earlier (*84*).

On the day of tumour inoculation (d0), cells were harvested by trypsination, washed, resuspended in PBS and kept on ice for further use. $1.5x10^6$ cells were suspended in 50 µl PBS and implanted into mice either subcutaneously over the flank or orthotopically into the mammary fat pad. Tumour size was measured daily.

All imaging experiments were performed tumour size dependent (4 - 6 mm) to reduce the influence of differences in tumour growth between cell lines or mouse strains (*85*).

For assessment of the predictive potential of S100A9 imaging, animals were kept after in vivo imaging and the tumour growth was monitored over the following 8 - 10 days.

To control for the influence of tumour-primed MDSC on the local tumour development and potential consecutive effects on the in vivo imaging signal, splenic monocytes were harvested from tumour-bearing or healthy animals. Monocytes, including MDSC, were identified by FACS according to the expression of Gr-1 and CD11b. Mice received an i.v. injection of isolated cells from either tumour-bearing mice (tMDSC) or healthy controls (IMC) and were subsequently implanted with 4T1 tumours as described before. Imaging was performed at day 8 after tumour inoculation immediately after tracer injection and 24 h later.

3.1.2 Fluorescence tracer for S100A8/A9

A rabbit polyclonal antibody, targeting the S100A9 subunit of the S100A8/A9 heterodimer was labelled with the fluorescent dye Cy5.5 as described in detail before (*79*). The antibody addresses a specific epitope of the S100A9 protein (*86*) that is conserved across different species including mice and humans and does not interfere with the protein function. In this context, the polyclonal antibody proved different from commercially available S100A9 antibodies which did either lack specificity for human or murine S100A9 respectively, exhibited an overall reduced binding affinity or an increased cross reactivity with other S100 proteins. The identical polyclonal antibody that has been used for the in vivo imaging experiments also forms the basis of the validation experiments in ELISA, FACS and immunohistochemistry, therefore enabling for direct control of in vivo imaging data.

As a control for unspecific tracer distribution due to perfusion and e.g. $F_c\gamma$ receptor binding, a polyclonal rabbit antibody against a target, irrelevant in mice (goat serum) was used. The size of the antibodies was virtually identical, as was the genetic background of the host animals.

Briefly, the rabbit-derived antibodies addressing S100A9 or control IgG, were purified via protein G-sepharose and labelled with the fluorochromes Cy5.5 or Cy7 according to the manufacturer's instructions (GE Healthcare, Uppsala, Sweden): 5 mg of the respective antibody was dialyzed against 100 mM Na_2CO_3 buffer, pH 8.0, and a 20-fold molar excess of the fluorochrome was added for 90 min at room temperature. The resulting tracer was purified from unbound dye by size exclusion chromatography using a PD10 column. The labelling efficacy (dye/antibody ratio) was determined on the basis of UV-spectra of the purified dye-antibody-compound, using PBS as a reference buffer. The labelling for the experiments described here resulted in 2.5 – 3.0 fluorochrome molecules per antibody, irrespective of the precursors.

The tracer was stored at 4°C and protected from light to avoid bleaching. In accordance with prior experience on the use of the tracer for visualisation of local inflammation, a dose, equivalent of 2 nMol dye was administered 24 h prior to imaging. The imaging time point was chosen on the basis of prior experiments in local inflammation (*79*), where we observed the highest target-specific tracer accumulation at about 24 h after tracer administration.

3.1.3 In vivo optical imaging

Imaging studies were performed using either FRI or FMT imaging systems.

For in vivo OI, a FRI system (In-Vivo FX PRO, Bruker BioSpin, Millerica, MASS, USA) was used. Excitation light was adapted according to the dyes to 630 nm (Cy5.5) or 730 nm (Cy7) respectively. The resulting emission was recorded at 700 nm or 790 nm, using a filter-equipped, high-sensitive CCD camera. Signal acquisition time was 5 - 30 s for fluorescence images. White-light images were acquired for anatomical orientation.

FMT was used for 3D visualisation of dye distribution in the target region. The free space flat panel FMT device (In-vivo Imaging System FMT 2500, FMT 2500 Imaging Software, Vers. 1.1.1.3, both Visen Medical, now Perkin Elmer, Waltham, MASS,

USA) allowed for reconstruction of three-dimensional data from fluorescence signals at 680 and 750 nm for visualisation of Cy5.5 or Cy7 (*87, 88*). Scanning time of the tumour region was around 4 minutes.

Mice were held under inhalation-anaesthesia (2.0% Isoflurane in air) during examinations.

For image analysis, a region of interest (ROI) was placed to cover the whole tumour area as depicted on white light images. FRI data were presented as mean photon counts, normalized for the ROI area, in arbitrary units (AU). From each dataset, mean values and standard deviation were calculated.

For the treatment study, scans were performed immediately (0 h) and 24 h after tracer injection. From these values a ΔFluorescence Intensity (ΔFI) was calculated as:

ΔFI = signal from the target ROI at 24 h – signal from the target ROI at 0 h.

After in vivo imaging, animals were sacrificed and organs were harvested for correlative ex-vivo examination of dye-distribution using FRI; tumour tissue was harvested for FACS and/or histology.

3.1.4 Ex vivo validation of fluorescence imaging results

The resected tumours were divided, and equal amounts of tissue were processed for immunohistochemistry and FACS respectively. For FACS, single cell suspensions were produced from tumour tissue and stained for S100A9 and CD11b with corresponding isotype controls.

Monocyte specific staining was performed using an APC-labelled ratCD11b antibody (eBioscience, San Diego, CA, USA); S100A9 specific staining with a polyclonal S100A9 antibody and FITC labelled goat-anti-rabbit secondary antibody (Jackson Immunoresearch Europe, Newmarket, UK). Non-specific rabIgG and APC-labelled rabIgG (eBioscience) were used as controls. FACS data were gated according to size and granularity to exclude cell detritus. Isotype controls served for adjusting individual FACS measurements. All FACS measurements were conducted using a FACSCalibur

system and analysed using the CellQuest Pro software (both BD Biosciences, Franklin Lakes, NJ, USA). Data were presented as cell frequency reduced by the individual isotype control to exclude unspecific staining.

For histology, tissue was paraffin embedded and cut. Tumour sections were stained for S100A9 and F4/80 (macrophages) for direct correlation of imaging findings. All stainings were carried out according to established protocols (*49, 89*).

Moreover, lysates from resected tumours, tumour cells from tissue culture and tissue culture supernatant were analysed for S100A8/A9 using a specific, in house established enzyme linked immunosorbant assay (ELISA) (*51, 79*).

3.2 Results

3.2.1 Tumour lesions specifically retain aS100A9-Cy5.5

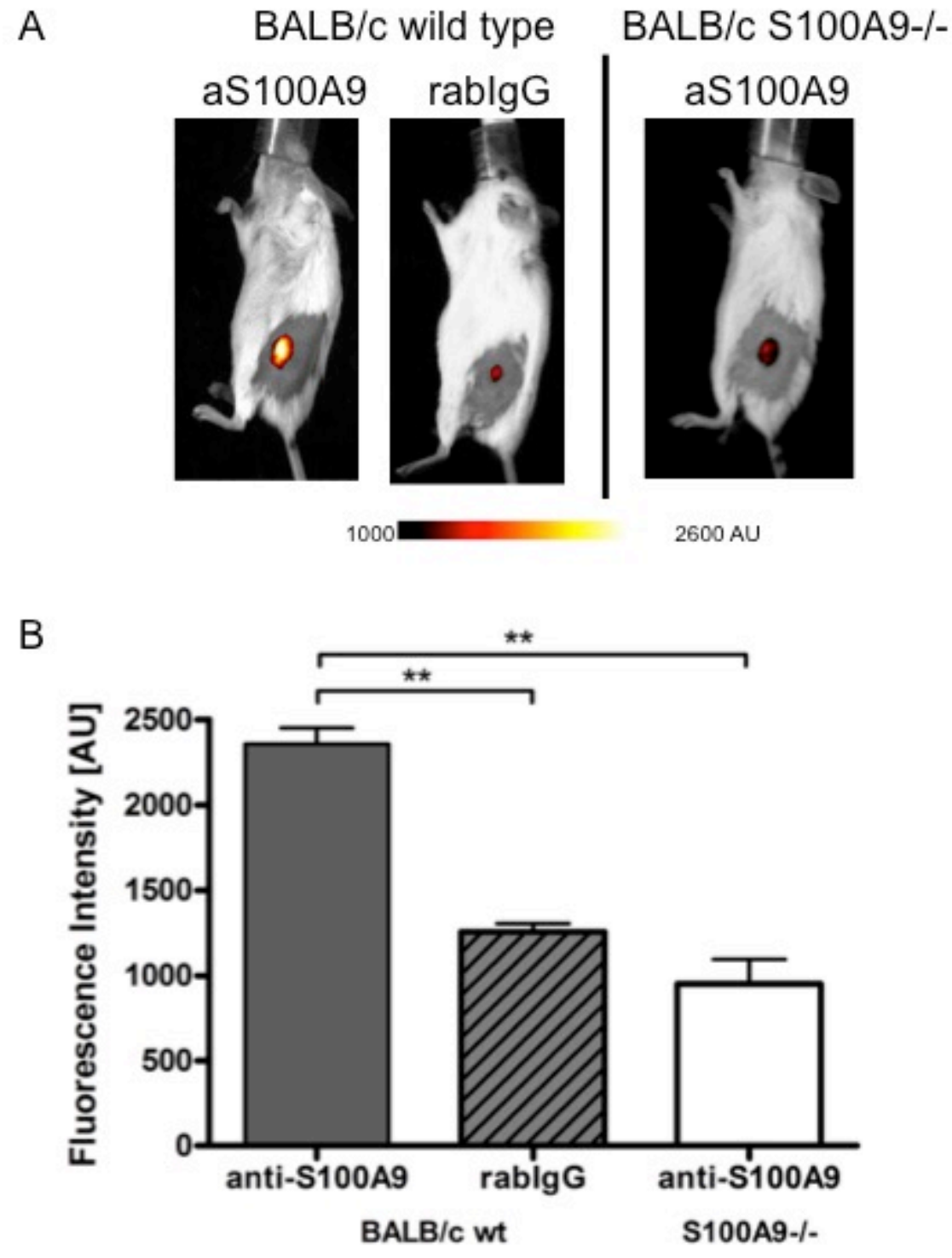

Figure 12: S100A9 optical fluorescence imaging in 4T1 tumour-bearing animals

To prove the specificity of tracer to target binding and to control for unspecific tracer accumulation (e.g. perfusion-related or $F_c\gamma R$-mediated), 4T1 tumour-bearing mice were injected with aS100A9-Cy5.5 or rabIgG-Cy5.5. Imaging experiments were conducted at a constant tumour size of 5 mm and ROI size was identical for all experiments. FRI revealed a significantly higher signal after injection of the specific probe than after injection of equal amounts of rabIgG-Cy5.5 (2430 AU vs. 1240 AU; $p < 0.001$, n = 16/12). In S100A9-/- mice, injection of aS100A9-Cy5.5 resulted in signals, comparable to the rabIgG-Cy5.5 mediated signal in wild type animals (950 AU; n = 5) . In ex vivo biodistribution studies, resected organs were analysed for fluorescence signals and a significantly higher fluorescence in the tumour after injection of aS100A9-Cy5.5 than rabIgG-Cy5.5 could be verified. Tumour to non-target tissue ratios (kidneys, muscle) were significantly higher for aS100A9-Cy5.5 than for rabIgG-Cy5.5 (aS100A9-Cy5.5 vs. rabIgG-Cy5.5 tumour/kidney: 3.2 vs. 2.1; $p \leq 0.001$; tumour/muscle: 3.76 vs. 2.4; $p \leq 0.05$).

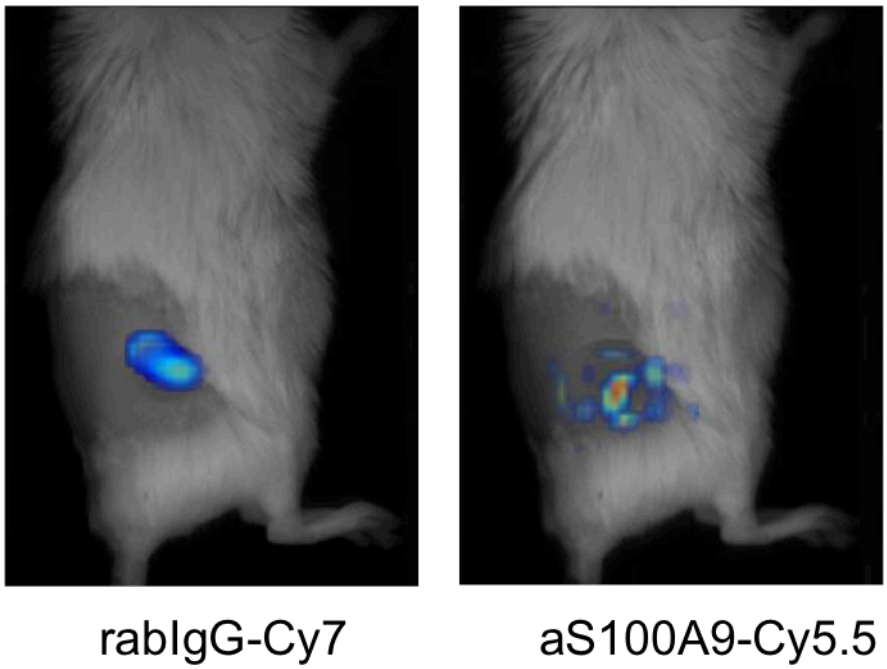

Figure 13: Fluorescence-mediated tomography imaging after parallel injection of aS100A9-Cy5.5 and rabIgG-Cy7.

The FMT scan at 750 nm for Cy7-labelled rabIgG reveals a homogeneous distribution over the subcutaneously over the flank implanted 4T1 tumour, reflecting perfusion. At the same time, aS100A9-Cy5.5 accumulates in specific tumour areas only.

After parallel injection of aS100A9-Cy5.5 and rabIgG-Cy7, FMT allowed for simultaneous evaluation of the distribution of both tracers. While rabIgG-Cy7 showed a homogeneous distribution over the whole vital tumour area, aS100A9-Cy5.5 accumulated in delineated hot-spot areas, predominantly located in the periphery of the tumour (right panel). TAMs within clusters of S100A9+ cells could accordingly be defined by histology.

3.2.3 Tumour-associated inflammation supports tumour growth

CD11b+ cells as an apparent source of S100A9 in the tumour microenvironment were isolated from the spleens of either tumour-bearing (incl. tumour primed MDSC – tMDSC) or healthy mice (naïve, immature myeloid cells – IMC) and transferred into animals, which were thereafter inoculated with 4T1 (schematic representation of the protocol in Fig 12).

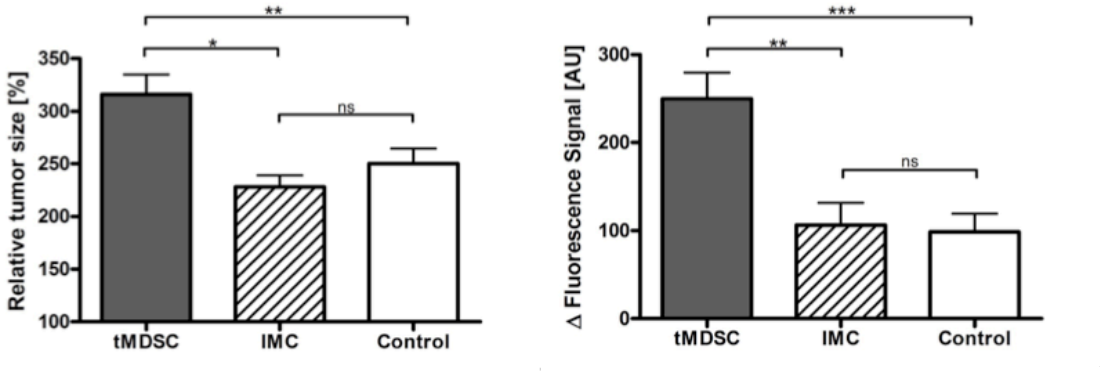

Figure 14: Growth rate and local S100A9 imaging signal in 4T1 tumour lesions after treatment with tMDSC or IMC

Mice received intravenous injections of tumour-primed MDSC (tMDSC; dark grey; n=10), isolated from tumour-bearing animals or immature myeloid cells (IMC; striped; n=10) from healthy animals or no additional cells (control; white; n=5) prior to implantation of 4T1 tumours. The growth of the tumour was monitored. When the tumours reached a diameter of 5 mm, mice were injected with aS100A9-Cy5.5 and FRI was performed immediately after tracer injection and 24 h later. The growth rate of tumours was significantly accelerated in mice that received tMDSC (*=p<0.05; **=p<0.01); application of naïve IMC had no measurable effect on the tumour growth. The accumulation of aS100A9-Cy5.5 was similarly elevated in tMDSC-treated mice as compared to controls or mice that received IMC (***=p<0.001).

The average tumour growth in animals, transferred with tumour primed CD11b+ cells including tMDSC was significantly accelerated as compared to mice after transfer of monocytes from healthy controls (average relative tumour size on day 8 as compared to day 1 tMDSC vs. IMC: 316% vs. 228%; p = 0.001). This was also reflected by in vivo imaging: S100A9 fluorescence was significantly higher in mice after transfer of

tMDSC and consecutive accelerated tumour development than in the control group (tMDSC vs. IMC: 250.2 vs. 106.6; $p < 0.01$). The transfer of IMC had no significant effect as compared to untreated mice (relative size day 8: 249%; FRI: 98.5).

3.2.4 S100A9+ cells dominate the infiltrative tumour margin

Ex vivo histology confirmed the in vivo imaging results and revealed a strongly increased infiltration of tMDSC treated tumours by S100A9+ cells as compared to IMC treated tumours.

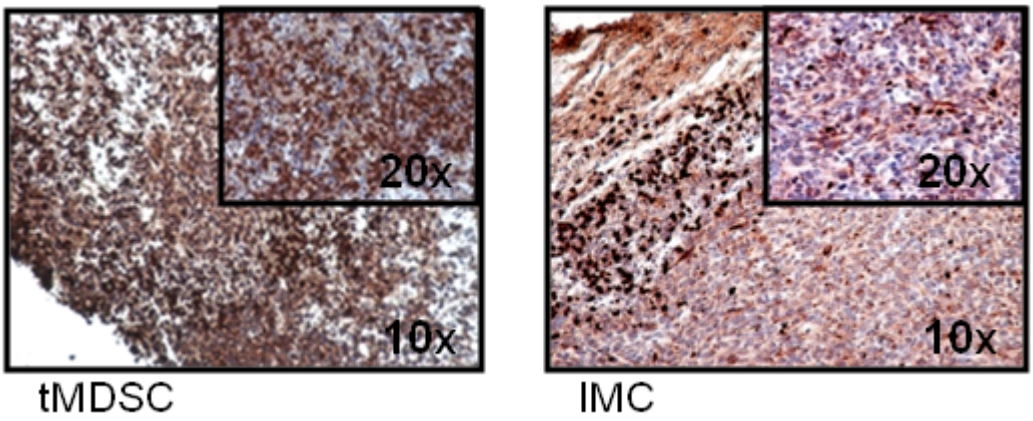

Figure 15: Immunohistochemistry for S100A9 in tumour tissue from mice that received tMDSC or IMC

After transfer of tumour-primed MDSC, tumour tissue exhibits a higher density of S100A9-positive (red/brown) monocytic cells as compared to the tissue of mice that received naïve monocytic cells from healthy control animals. In both cases, S100A9-positive cells preferentially colonise the tumour periphery.

3.2.6 The source of S100A8/A9 in the tumour microenvironment are CD11b+ monocytes

	Tissue culture supernatant		Tissue culture cell lysates		Resected tumor lysates	
Cell line	**4T1**	**67NR**	**4T1**	**67NR**	**4T1**	**67NR**
S100A8/A9 (ng/ml)	0	0	0	0	86,897	1,927
SD	na	na	na	na	50,044	1,348

Table 1: S100A9 ELISA results

ELISA of both, tissue culture supernatant and cell lysates of the different murine breast cancer cells was negative for S100A8/A9 protein expression while resected tumour samples, comprising tumour cells and the immune cell infiltrate, showed high S100A8/A9 levels. 4T1 tumour samples exhibited significantly higher protein levels than 67NR samples.

To specifically control for expression of S100A9 by tumour cells in vivo, FACS analysis of resected tumour tissue was performed. Tumour samples from 4T1 or 67NR regularly comprised less than 0.1% S100A9+ cells of other than monocytic (CD11b+) origin (Fig. 18), screening out the presence of S100A9+ tumour cells.

In summary, tumour cells did not exhibit S100A9 protein expression in vitro or in vivo; the S100A9 expression as reflected by specific imaging is virtually exclusively indicative of tumour-associated monocyte/macrophage activity.

3.2.8 S100A9 imaging predicts local tumour growth and correlates with tumour type

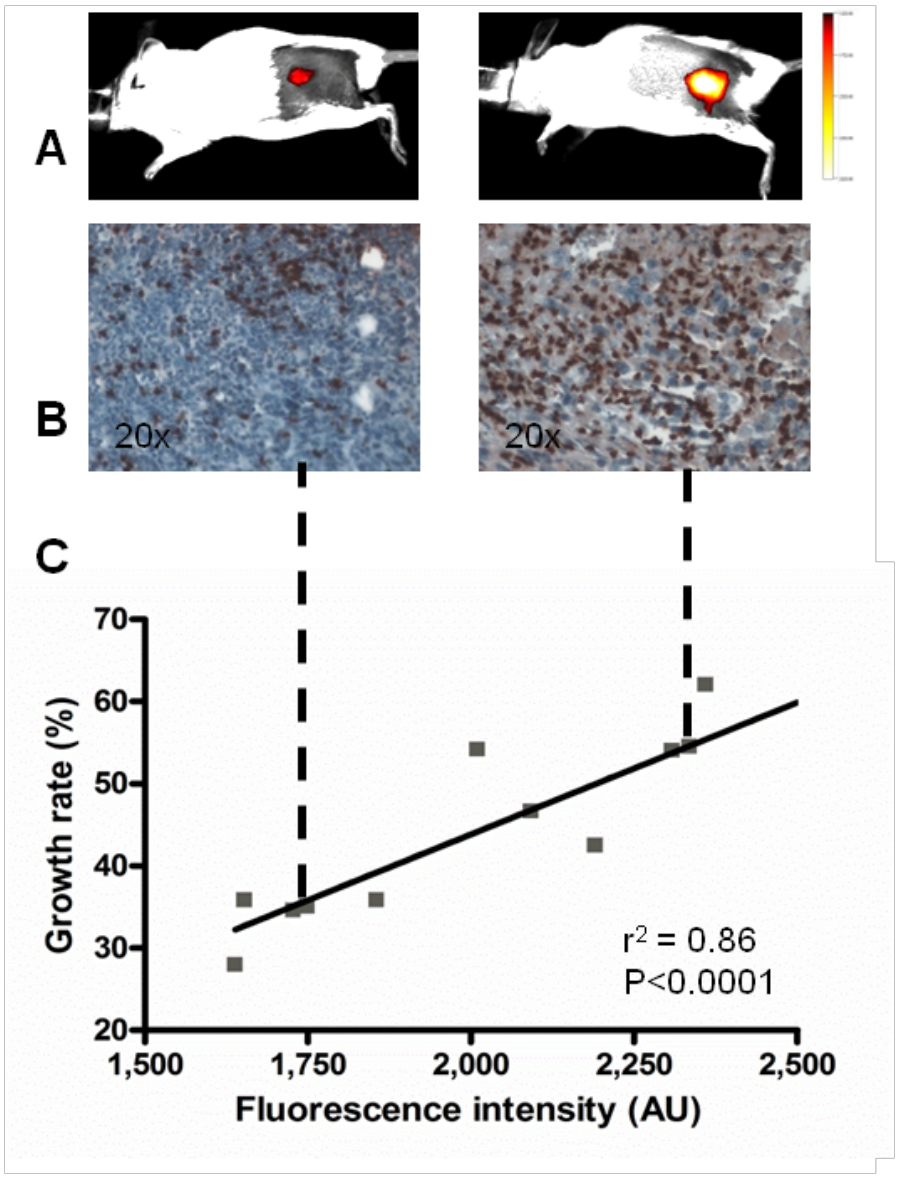

Figure 16: Correlation of S100A9-signal in primary tumour tissue and consecutive tumour growth. Mice, implanted with 4T1 tumours subcutaneously over the flank have been followed after aS100A9-Cy5.5 driven FRI. Imaging was performed at a tumour size of 5 mm, 24 h after tracer application. The growth of the tumour was followed over a period of ten days and correlated with the initial imaging signal (C; n=11). Tumour-lesions with an initially high S100A9 signal presented with a strong infiltrate of S100A9+ cells in subsequent immunohistochemistry (B). Exemplary early imaging for low and high S100A9 in vivo imaging signal in A.

The development of 4T1 tumours was assessed longitudinally over ten days, following imaging at an early stage of tumour development (tumour size < 5 mm).

A higher aS100A9-Cy5.5 signal in early FRI and the confirmatory detection of an increased presence of S100A9+ cells upon tumour resection was found in fast growing tumour lesions as compared to lesions with slower development and only mild aS100A9-accumulation. The S100A9 signal strongly correlated with the consecutive individual tumour growth ($R^2 = 0.86$; $p < 0.0001$, $n = 11$).

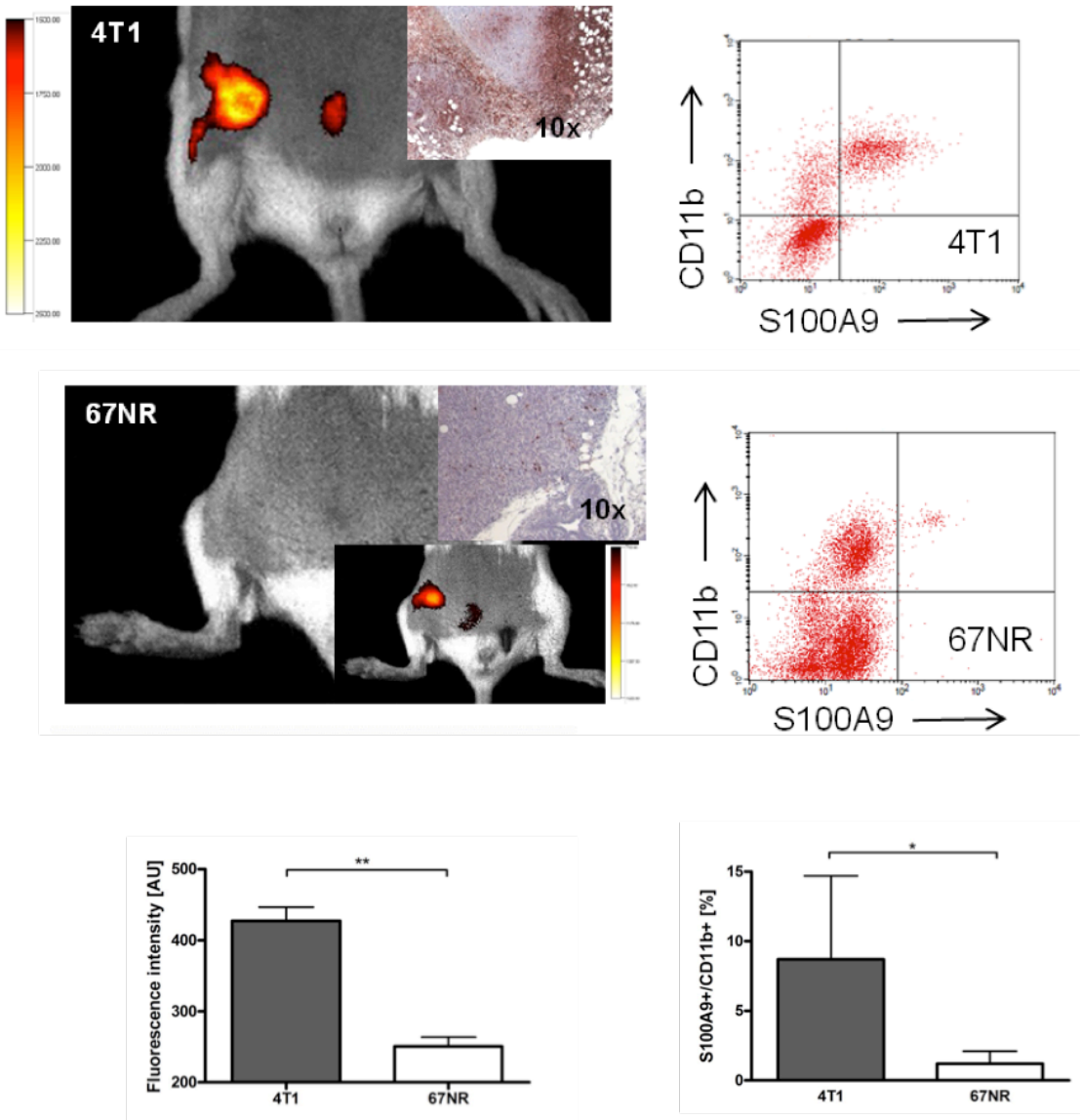

Figure 17: S100A9-specific FRI in mice bearing 4T1 or 67NR tumours.

4T1 tumour lesions (upper panel; n=10) accumulated significantly more S100A9+ monocytes as compared to 67NR tumour lesions (n=10; immunohistochemistry for S100A9 shown as inserts, representative FACS analysis on right panels). The in vivo imaging allowed for differentiation of tumour lesions according to the local S100A8/A9 release in correlation with the malignant potential (4T1 > 67NR); for visual appreciation of S100A9-distribution in the 67NR model, the scaling of the fluorescence

signal had to be adapted and the lower threshold had to be reduced by a factor of three (normal images: 1,500 – 2,500 AU; insert 500 – 1500 AU). Quantification is shown in the lower panel with *=p<0.05 and **=p<0.01.

Targeted S100A9 imaging revealed significant differences between the two tumour entities with 4T1 tumours exhibiting the highest aS100A9-accumulation (FRI signal 427.3 AU), and 67NR (250.8 AU). The ex vivo analysis of the tumour immune cell infiltrate revealed the presence of CD11b+ cells in all tumours, with the amount of S100A9+ cells among the immune cell infiltrate confirming the in vivo imaging (4T1: 8.7% of total cell infiltrate; 67NR: 1.2%) and reflecting the specific grade of malignancy.

3.3 Discussion

Tumour-associated immune cells are critical for the development of malignant disease. Numerous studies illustrated immune cells to be supportive of tumour development and spread on the one hand and the interference with the anti-tumour immune response on the other (*90*). Tumour immunotherapy, the strategy to inhibit the induction of tumour-promoting immune cells and consecutively increase the host ability to overcome the suppression of an effective anti-tumour immune response has been hailed a turning point in cancer therapy (*4*). Striking results have been reported in patients with advanced, even metastatic disease including lung, renal, prostate and breast cancer (*91*). Still, response varies largely among the selected patients and surrogate markers as to which patient might benefit from the treatment are largely elusive (*92, 93*). This specifically precludes monitoring of immunomodulatory cancer therapy as reliable diagnostic approaches for the determination of the biological activity within the tumour microenvironment are still missing. For both, clinical and preclinical applications, a method for sensitive monitoring of immune cell activity in malignant disease would be highly desirable. In clinical settings, it would enable patient stratification on the basis of tumour-mediated and -associated inflammation while in preclinical settings it would facilitate further research in tumour biology.

With the technique, presented here, a potential way to address tumour-associated inflammation is established. I used a fluorescent-labelled antibody to target and visualise the protein heterodimer S100A8/A9, reflective of local monocyte activation.

In a direct comparison of an equally sized, unspecific IgG, the S100A9-specific antibody showed a distinct distribution in selected tumour areas only (Fig. 14) and an overall higher signal intensity, reflecting the target-specific signal component as compared to perfusion/unspecific signal components only (Fig. 13). In S100A9 knock out mice, no specific signal could be induced (Fig 13).

To further specify the source of S100A8/A9 in the tumour microenvironment and assess the sensitivity of S100A9 imaging for changes of the cellular composition of

the tumour microenvironment, I modulated in tumour-bearing mice the burden with tumour-primed MDSC. A higher level of MDSC led to an accelerated tumour-growth and was accompanied by a stronger infiltration of the tumour lesion by S100A8/A9+ monocytes (Fig. 15 + 16). This was reflected by a higher in vivo imaging signal (Fig. 15) as compared to control mice. Tumour cells did not exhibit S100A8/A9 expression or release (Table 1).

The abundance of S100A9+ monocytes in the tumour reflected by a high local S100A9 imaging signal correlated with the subsequent tumour development (Fig. 17). I could show an accumulation of the specific antibody in tumour lesions to be associated with a local increase in S100A8/A9+ monocytes. The tumour cells could be excluded as a source of local S100A8/A9.

Taken together, local concentrations of S100A8/A9, as depicted by specific OI can serve as a marker for local monocyte activity in tumour-associated inflammation. This tumour-driven immune cell activity can be an indicator of the tumour ability to establish a supportive environment.

3.3.1 Alternative cell tracking approaches

Within cell tracking studies, featuring either iron oxide mediated MRI (*94, 95*) or radionuclide imaging e.g. using 64Cu liposome labels for PET (*96*), the abundance of macrophages and other phagocytes in the tumour microenvironment could already be shown. Within this study, we present an approach for visualisation of monocyte activity beyond sheer abundance in the primary tumour. With tumour-associated monocytes being discussed as prognostic indicator for tumour development (*90, 97*), this technique could provide valuable information on on-going tumour/immune cell crosstalk.

S100A8/A9 has been shown to mediate the crosstalk between tumour cells and monocytes, macrophages and MDSCs (*37, 43, 98*). Local release closely reflects the monocyte/phagocyte activity (*50*), qualifying S100A8/A9 as an imaging target for

monitoring of tumour-associated inflammation. Within this study, this has been achieved by following the principle, established for visualisation of local monocyte activity in inflammatory processes (*79*).

3.3.2 Correlation of S100A9 release and tumour development

We now utilized this approach to address crucial components of the inflammatory tumour microenvironment using S100A9 as a marker for the activity of tumour-associated monocytes.

Although endogenous S100A9-expression has been proposed for several human tumour types (*60, 99, 100*) based on elevated systemic levels (*99*) and upregulation on the RNA-level, expression on the protein level has not been well documented. The systemic levels, reported in human cancer patients and observed in tumour-bearing animals are in this context also likely to represent activated monocytes. Although further evaluation of this hypothesis will be necessary, we could safely prove that none of the tumour cell lines we used for this study shows measurable S100A9-release and thus, in these experimental tumour models, measured signals were mediated by tumour-invading monocytes.

The rabIgG-Cy5.5 mediated, unspecific background signal can be attributed to local hyperaemia and binding of the IgG to $F_c\gamma$-receptor ($F_c\gamma R$), expressed on resident and invading immune cells (*101*) as well as e.g. endothelial cells (*102*). $F_c\gamma R$ expression can equally effect on both, rabIgG and aS100A9-Cy5.5 accumulation and increase immune cell infiltration via immune complex formation (*103*). Both imaging signals are also influenced by the in vivo distribution kinetics of full length IgG – a slow clearance via the hepatic route, slow extravasation and evenly slow wash out, even in the absence of the target, leading to a high unspecific background signal, especially at early time points, up to 24 h after tracer administration. The superiority of aS100A9-Cy5.5 over the unspecific isotype control has been extensively documented (*79*). In histology, we could detect S100A9 in colocalisation with immune cells of monocytic

heritage (TAM and MDSC), indicating a mutual relationship as recently suggested (*59*). Specific sites of monocyte-activity could be identified in vivo using S100A9-driven FMT and confirmed by immunohistochemistry.

It is well established that monocytes, recruited to the tumour, support local tumour growth and invasion (*37, 50, 85, 104*). In vivo imaging of S100A9 expression allowed for stratification of tumour lesions according to the activity of tumour-associated monocytes. An established supportive microenvironment, reflected by a high S100A9 in vivo imaging signal, favours the consecutive tumour growth as suggested by our results and may be interpreted as a novel indicator of reduced prognosis.

3.3.3 Underlying/associated cellular events

Monocytes have also been reported to support the first steps towards distant metastasis at primary tumour level (*105, 106*). In a murine model of graded malignancy (*83*), the different activity of tumour-associated monocytes, potentially supporting the systemic shed of cells from the primary tumour was reflected by S100A9 imaging.

We artificially increased the number of tumour-primed MDSC in tumour-bearing animals. In tumour lesions of identical size, the transfer of tumour-educated splenic monocytes including MDSC resulted in an increased recruitment of S100A9+ cells to the tumour and significantly higher S100A9-mediated fluorescence in the tumour and stimulated a more aggressive tumour development in accordance with recent data (*37, 85*). An increase in naive monocytes however had virtually no effect on the activity of tumour-associated immune cells as reflected by S100A9 imaging and tumour growth.

Our findings support reports about the crucial importance of tumour-associated monocytes – including MDSC – for tumour development and fit with reports on them mutually promoting their respective activity and accumulation in the tumour (*9, 30*). We could demonstrate that S100A8/A9 expression as measured by in vivo imaging

reflects TAM and MDSC abundance and the malignant development in individual tumours and may thus function as a surrogate marker for the tumour's ability to recruit and activate immune cells to induce a supportive microenvironment.

Future studies will have to elucidate the relevance of S100A9 expression in the context of other tumour models and the potential for S100A8/A9 to serve as a marker for response to immunomodulatory therapy.

3.3.4 Implication for tumour staging and imaging

OI of S100A9 allows for estimation of TAM/MDSC-activity in tumours and thus enables stratification of tumour lesions with regard to local tumour-host-interactions and the potential development. For basic research, this technique will offer the opportunity to study the role of TAMs and MDSC in malignant progression in more detail. With regard to clinical cancer research, the importance of tumour-associated immune cells as promoters of malignant progression and thus as potential targets for diagnostics and therapy is emphasized and a potential route for grading tumours according to tumour-associated inflammation is suggested.

The study is however limited to the immediate tumour microenvironment, due to the methodological properties of OI. It does not allow for evaluation of potential systemic effects of the tumour such as interaction with the monocyte depots in bone marrow and spleen or the influence on potential target sites of metastasis.

To assess the importance of tumour-immune interaction in the process of metastasis and gain insight into the role of immune cells in premetastatic tissue priming, the established imaging approach needs to be adapted for whole body and deep tissue imaging.

4 Establishment of a S100A9-specific SPECT tracer

While OI is limited to superficial applications, radionuclide-driven imaging is virtually not limited by the mass of the examination sample. Retaining a sensitivity, comparable to or even superior over the sensitivity of OI, SPECT and PET qualify as systemic molecular imaging methods. As the basis for the aS100A9 tracer is a full-length IgG with consecutively long tissue and blood pool half-life, ^{111}In was chosen as a radioactive label. The half-life of ^{111}In allows for safe detection up to 48 or even 72 hours after tracer application (details on p 24).

The aim of this work was to develop a S100A8/A9-targeted SPECT tracer for systemic visualisation and measurement of S100A8/A9 release, using an ^{111}In-labelled antibody. The tracer was assessed with respect to stability under physiological conditions. In addition, the tracer was applied in vivo for biodistribution and initially tested in a model of local inflammation that has previously been characterised for S100A8/A9 expression in the area of inflammation.

4.1 Material and Methods

4.1.1 SPECT tracer for S100A8/A9

The protocol for labelling antibodies for SPECT imaging has been adapted from the protocol, established by Cooper et al (*107*).

Briefly, the full length polyclonal antibody (1-2 mg/mL), addressing the S100A9 subunit of the S100A8/A9 heterodimer, which has been used in all prior optical imaging studies (*79, 82*), was incubated with 50 mM EDTA in 0.1 M ammonium acetate for 30 min at room temperature for chelation of metal contaminations, subsequently purified and transferred to 0.1 M HEPES buffer, pH 8.5, using spin columns (molecular weight cut-off 30,000 kD; GE Healthcare UK Ltd, UK). Repetitive purification runs were performed until the antibody solution was regarded purified; at

least 30 mL HEPES buffer were used for the buffer exchange on spin columns of 1 mL volume. The concentration of the antibody solution after purification was determined using a Nanodrop and the molar content was calculated (on average in the range of 0.005 – 0.008 mM/mL).

A sufficient amount of the chelator SCN-Bz-DTPA (chemical formula $C_{22}H_{28}N_4O_{10}S$•3HCl, MW 649.9 g/Mol; Macrocyclics, Ltd., USA) was freshly dissolved in pure ethanol. On average, 1 µg chelator was dissolved in 100 µl ethanol to produce a solution of 0.015 mM concentration.

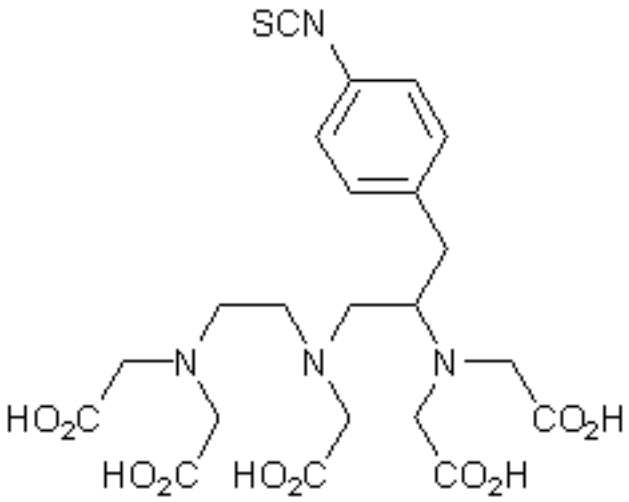

Figure 18: Chemical structure of the chelator SCN-Bz-DTPA

The purified antibody in HEPES buffer was incubated with a 20-fold molar excess of the chelator (on average around 80 µl chelator solution), at 4°C over night. The compound was thereafter purified from unconjugated precursors by ultrafiltration and resuspended in 0.1 M ammonium acetate, pH 6. The purity was determined by measuring the flow-through of the spin column for presence of light-absorbing chelator on a Nanodrop. The product was regarded sufficiently clean of unbound precursors when the measurement on the Nanodrop was 0 (no absorption).

The conjugated product – aS100A9-DTPA – was kept at 4°C until further use.

For *in vivo* imaging, the required volume (1mg in 1mL) of the labelled compound was incubated with 150 MBq ^{111}In chloride (specific activity 1.85 GBq/g In; Guy's Hospital Radiopharmacy, London, UK) for 1 h at room temperature and subsequently purified from free ^{111}In and transferred to PBS using a PD-10 desalting column (GE Healthcare UK Ltd, UK). The purity of the labelled compound was assessed using HPLC.

^{111}In-labelled aS100A9-DTPA (^{111}In-aS100A9) was injected in amounts, corresponding to around 10 MBq per animal.

As a control for unspecific label distribution due to perfusion and $F_c\gamma$ receptor binding, a rabbit-derived IgG of irrelevant specificity in mice was labelled in an analogous manner (^{111}In-rabIgG). The antibody has been raised in rabbits of identical origin as the aS100A9 in response to goat serum.

4.1.2 In vitro stability assay

To assess the stability of the antibody-chelator complex and the potential of the chelator to retain the radioactive label under physiological conditions, samples of the tracer were labelled with ^{111}In and incubated in mouse serum (SIGMA Aldrich) at 37°C for 24 or 48 h. Before incubation as well as after this time, samples were analysed using HPLC. Retention of the radioactive label and structural integrity were determined with the HPLC retention time of the compound before incubation as a reference.

4.1.3 In vivo biodistribution in healthy controls and a murine model of local inflammation

For evaluation of the in vivo distribution under normal, physiological circumstances as a reference for the distribution under pathological conditions, the tracer was initially

administered to healthy wild type mice. Healthy female Balb/c mice, aged 8 weeks, were purchased from commercial suppliers (Charles River, UK) and kept for at least ten days after delivery to allow for sufficient rest after the transport. 24 hours before SPECT/CT scanning, the mice received 10 MBq ^{111}In-aS100A9 intravenously via the tail vein. The tracer distribution was determined in vivo using SPECT/CT (see below) and ex vivo using gamma counting of isolated tissue samples, immediately after imaging.

Irritant contact dermatitis (ICD) was established for studying local inflammation and innate immunity more than two decades ago (*108-110*).

Following these protocols, ICD was induced in female Balb/c mice (age 8 weeks) by application of 1% croton oil in olive oil-acetone (1:4) to the dorsal surface of the right ear of mice for 24 h, while the left ear served as internal control. Imaging was performed at 24 and 48 hours after tracer application, corresponding to 48 and 72 h after croton oil treatment, respectively. Subsequently, mice were sacrificed and ears were snap-frozen in liquid nitrogen and transferred to immunohistochemistry.

The swelling of the affected, croton oil-treated ear can serve as a clinical marker of inflammation and correlates with established markers of inflammation. The release of S100A8/A9 has been characterized earlier to peak between 24 and 48 h after croton oil-treatment and specific S100A9-imaging in this model has been demonstrated earlier to safely reflect the inflammation activity (*79*).

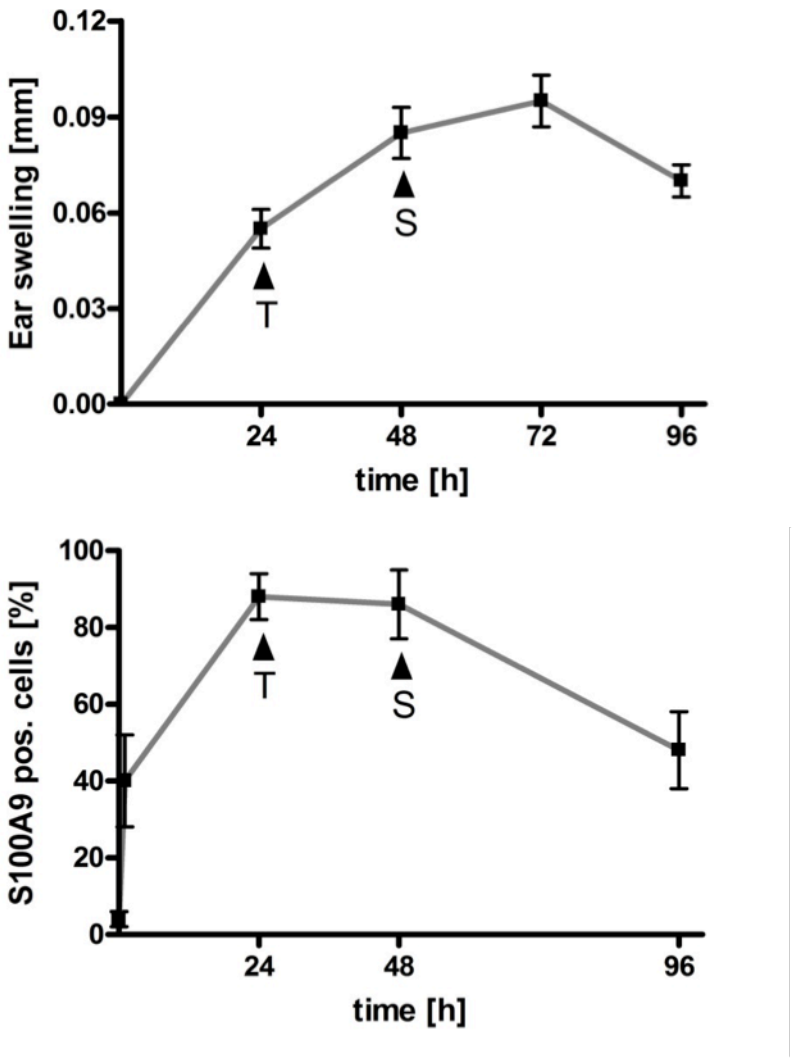

Figure 19: Kinetics and experimental design for irritant contact dermatitis

Kinetics of ear swelling as clinical sign of cutaneous inflammation and influx of S100A9+ cells into the inflamed ear as determined by immunohistochemistry. Tracer was injected 24 h after induction of inflammation (T) and 24 h prior to in vivo imaging (S).

Note that a significant ear swelling develops slower than infiltration of the site of inflammation with S100A9+ cells. The first cells, being activated in the course of local inflammation express high levels of S100A8/A9 and lead to further vascular leakage and immune cell accumulation and activation, resulting in full clinical manifestation of inflammation including the measurable ear swelling. At the time of peaking clinical inflammation, cells, representative of the acute phase of inflammation already started to differentiate into macrophages without S100A8/A9 expression.

All experimental in vivo procedures were covered by the respective project licences 70.7019, 70.7238, 70.7410, issued by the UK Home Office according to the Animals

Scientific Procedures Welfare Act. All personnel, involved in the in vivo experiments has been trained according to the King's College London regulations and obtained a personal licence, issued by the UK Home Office, to work under the respective project licences.

4.2 The preclinical SPECT/CT system

All *in vivo* imaging experiments were conducted on a dedicated small animal SPECT system (NanoSPECT/CT; Mediso Medical Imaging Systems, Hungary).

The scanner was calibrated for detection of ^{111}In-emitted β-radiation.

For imaging, a multi-pinhole collimator was installed, featuring 16 pinholes and a theoretical spatial resolution of 0.85 mm. The sensitivity, given by the manufacturer, was 7.500 cps/MBq. The system comprised a specific, heated mouse bed, which allowed for monitoring of body temperature and breathing rate of the animal during the examination. The injected dose per animal was measured and recorded before injection. Injected doses were kept consistent and the average dose, injected was around 10.0 MBq to ensure a reasonable image quality. Tracers were applied intravenously into the tail vein 24 h before in vivo imaging.

The imaging protocol comprised an orientating scout x-ray scan of the whole mouse bed for planning of the examination. On this scout image, the field of view for CT and consecutive SPECT scan was outlined. The maximum field of view, enabled by the specific mouse imaging collimators was 30 x 300 mm.

On average, the field of view for whole body mouse scans in this study was 30 x 110 mm and chosen carefully to cover the whole animal. CT scans were performed as helical scans with 240 projections. Average scan time for the CT was around 10

minutes. The SPECT scan was performed for the identical field of view with one minute frame times and an average of 50 frames per animal.

For CT and SPECT scan together, the average scan time for a whole body mouse scan was around 60 minutes. For the duration of the scan, mice were kept under Isoflurane inhalation anaesthesia (2% Isoflurane in air) on the heated dedicated mouse bed. Immediately after scanning, mice were either culled for tissue collection or returned to dedicated caging in shielded areas.

Imaging data were iteratively reconstructed and analysed using the in built VivoQuant Software (inviCRO, USA) and presented as percentage of the injected dose (%ID), based on the mean radioactivity within the ROI, normalised for the volume of the selected ROI.

For individual organ analysis, 3D ROIs were drawn on the anatomic CT images. For lung examination, a ROI was placed centrally over the whole lung area, analysing right and left lung separately and therefore excluding the mediastinum and heart, representative of the blood pool. For spleen signal analysis, the spleen was identified on coronal and axial CT images and an elliptic ROI was placed in the central organ compartment, carefully excluding any neighbouring tissues such as liver and kidneys. The ROI size was identical for all parallel experiments. From parallel experiments, mean values and standard deviation were calculated for %ID. After in vivo imaging, mice were either kept for longitudinal follow up examinations or sacrificed for tissue collection for histology and FACS.

4.2.1 Biodistribution in healthy controls

On the in vivo SPECT scans, lungs, heart, liver and spleen were individually assessed as described earlier. ROI values of the organs, normalised for the ROI size, were put in relation to the overall body activity, resulting in a comparable relative tracer dose per organ.

After scanning according to the aforementioned protocol, mice were immediately culled. The body weight and the radioactivity, contained in the whole mouse carcass, were determined. Selected tissues including blood samples were collected, separately weighed and referred to gamma counting for measurement of the specific radioactivity. From all animals, lungs, heart, liver, spleen, intestine, bone (representative sample: spine segment) and a blood sample (lancet; 20 µl) were collected.

From the sample activity, the organ weight and a dilution row of standardised amounts of the injected tracer, examined in parallel, the relative injected dose per gram tissue could be calculated as validation measure for the in vivo imaging as follows:

$$\%ID/g = Activity^{Organ}\,[CPS] \times Gradient^{dilution\ row} / Activity^{Injection}\,[MBq] \times 100 / organ\ weight\ [g]$$

4.2.2 In vivo imaging in local inflammation

24 hours after tracer injection, 48 hours after croton oil-treatment and induction of local inflammation, mice underwent SPECT/CT scanning according to the aforementioned protocol.

For image analysis, 3D ROIs were drawn to completely cover the right (affected) or left (control) ear, respectively. ROI sizes were identical for all parallel experiments.

The in vivo tracer distribution was presented as %ID, calculated as follows:

$$\%ID = Activity^{ROI}\,[CPS] / Activity^{Mouse}\,[CPS] \times 100$$

4.3 Results

4.3.1 Production of the S100A9-specific tracer

4.3.1.1 Conjugation and labelling of a polyclonal antibody against S100A9

The polyclonal antibody, targeted on the S100A9 subunit of the S100A8/A9 heterodimer was generated by Prof Johannes Roth's laboratory at the Institute of Immunology, University of Münster, Germany and characterised earlier (*86, 111*). The antibody was conjugated with a chelator (DTPA), following established standard protocols (*107*), adapted for this specific antibody.

After conjugation, the antibody-chelator construct was examined using HPLC and compared to naïve antibody to verify purity from unbound precursors.

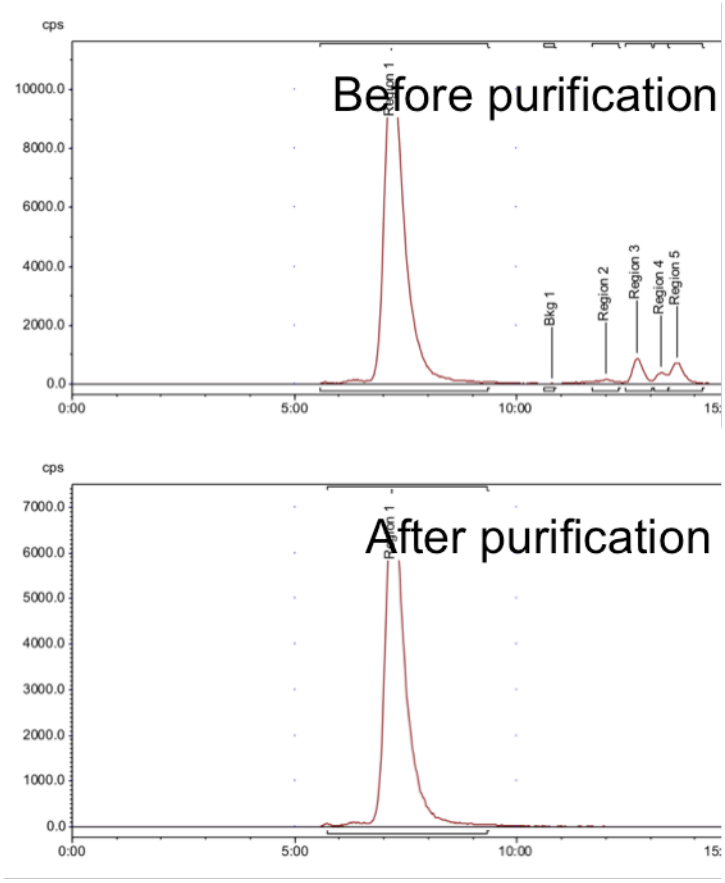

Figure 20: HPLC analysis oft he antibody-chelator compound

Minimal impurities, detectable via size exclusion HPLC before purification (upper panel), vanished completely after purification (lower panel).

The purified construct was then incubated with ^{111}In for labelling. The labelled construct was again examined using HPLC before and after incubation under physiological conditions for 24 and 48 hours.

4.3.1.2 Stability of the labelled compound

No significant impurities could be found in the construct preparations. The chelator retains the activity safely for over 48 hours and the HPLC curves do not indicate instability in the antibody-chelator construct for the observation period. An identical shape of the HPLC curves over time suggests that the compound is stable under physiological conditions in vitro.

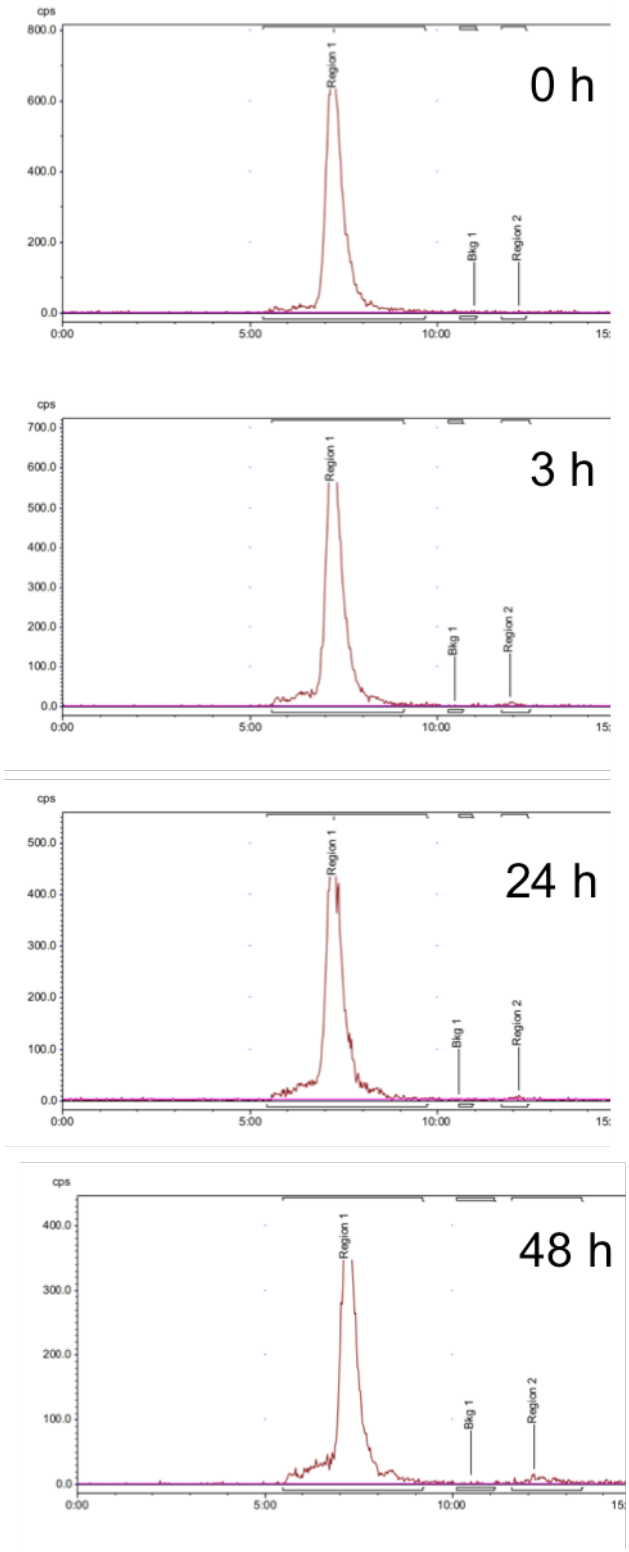

Figure 21: Stability of the compound under physiological conditions

The HPLC analysis of labelled ^{111}In-aS100A9 proves stability and label retention of the complex over up to 48 hours under physiological conditions in vitro.

4.3.2 In vivo testing in healthy animals

S100A8/A9 are released under physiological conditions at low levels in the context of multiple processes such as growth and healing as well as during inflammation and infection. The baseline level, found in serum and local tissues, increases strongly during inflammation due to activation of monocytes.

In healthy animals, no focal S100A8/A9 release should be detectable; a moderate background level should be present.

Application of ^{111}In-aS100A9 in healthy mice without foci of infection or inflammation resulted in an evenly low distribution of the probe in the mouse body as depicted by SPECT. Relatively high activity could be detected in the liver, due to the physiological route of elimination of larger proteins from the blood pool.

No specific accumulation of the tracer could be detected.

Ex vivo analysis of the tracer uptake and retention by gamma counting confirmed the in vivo imaging results.

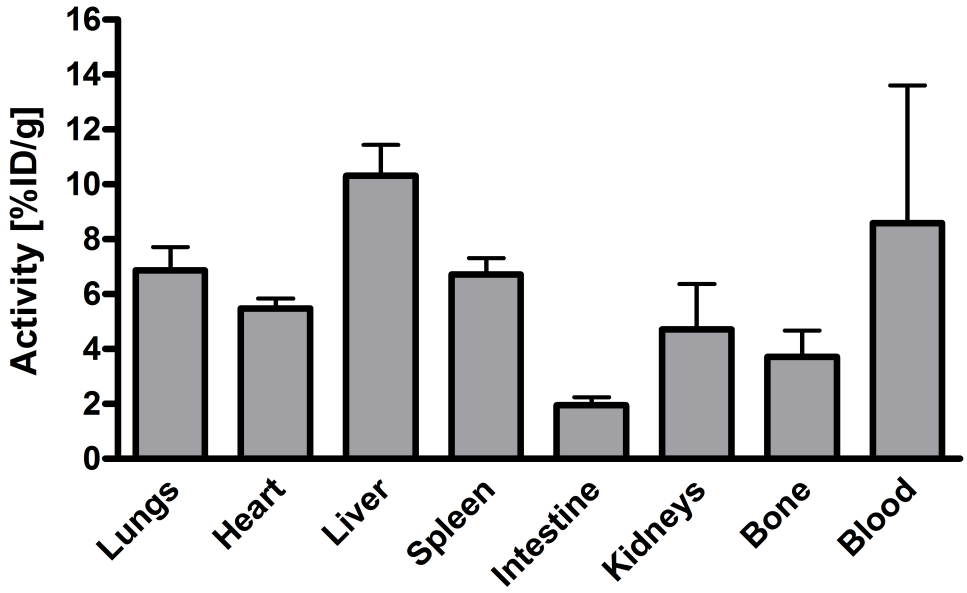

Figure 22: Biodistribution of 111In-aS100A9 in healthy controls

Relative activity per gram tissue in selected body compartments, 24 h after application of ^{111}In-aS100A9 in healthy animals (n=5; mean +/- SD).

4.3.3 In vivo testing in a model of local inflammation

To assess the specificity of ^{111}In-aS100A9 for activated immune cells, we used a model of local inflammation, well characterised for strong, local S100A8/A9 release. By application of the toxic dermal irritant croton oil to the dorsal surface of the mouse ear, an acute dermatitis is elicited. Within hours, a strong infiltrate of innate immune cells including activated monocytes locally releases S100A8/A9. The model moreover offers an ideal internal control in the form of the unaffected, healthy ear.

To control for tracer distribution, related to increased perfusion and vessel permeability in the area of inflammation, an antibody of irrelevant specificity in mice was used (rabIgG).

Animal with local inflammation received ^{111}In-aS100A9 or ^{111}In-rabIgG 24 h before SPECT imaging.

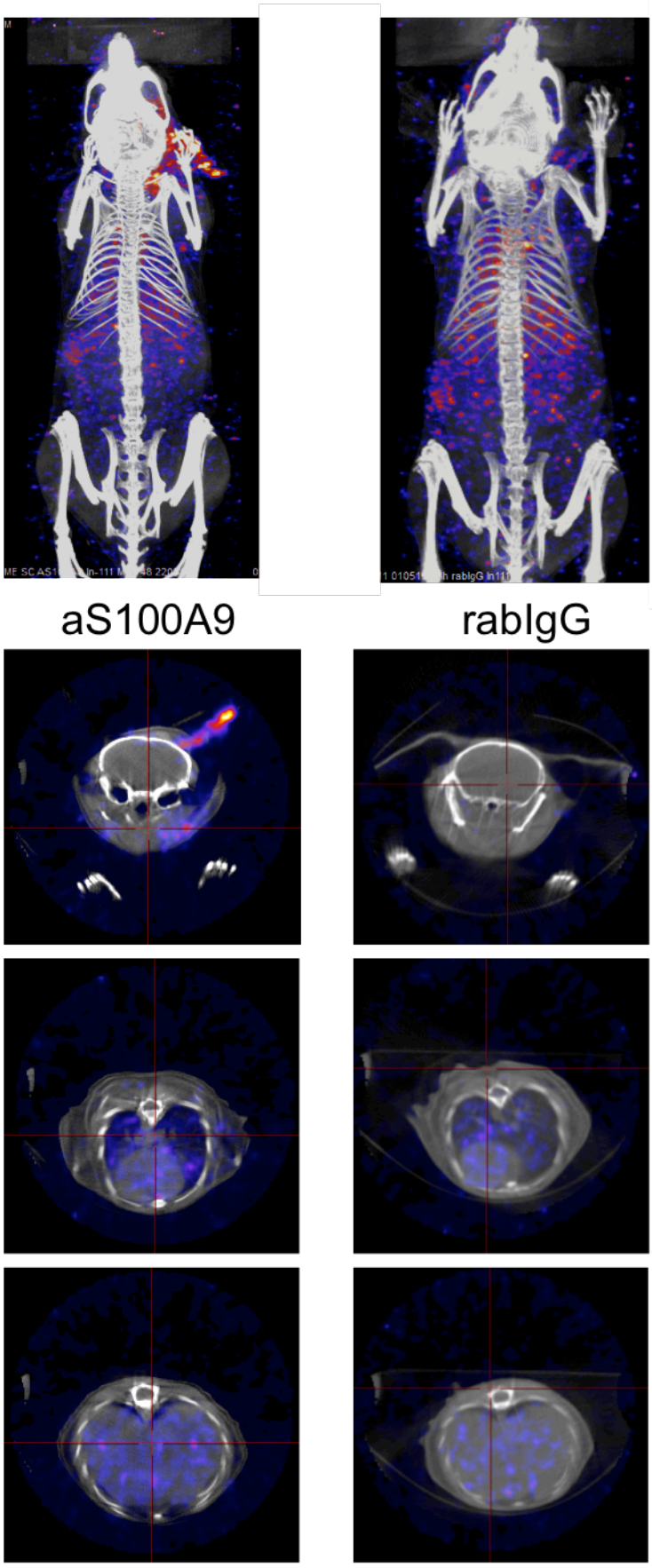

Figure 23: SPECT imaging in local inflammation

SPECT imaging 24 h after iv injection of about 10 MBq ^{111}In-aS100A9 (left) or ^{111}In-rabIgG (right). Exemplary images of a whole mouse and representative axial images of the region of inflammation, the thorax and mediastinum and the liver.

The accumulation of ^{111}In-aS100A9 in the area of inflammation is significantly higher than the accumulation of ^{111}In-rabIgG. The distribution in non-target organs, unaffected by inflammation, was virtually identical for both contrast agents.

Ex vivo biodistribution confirmed the in vivo imaging results.

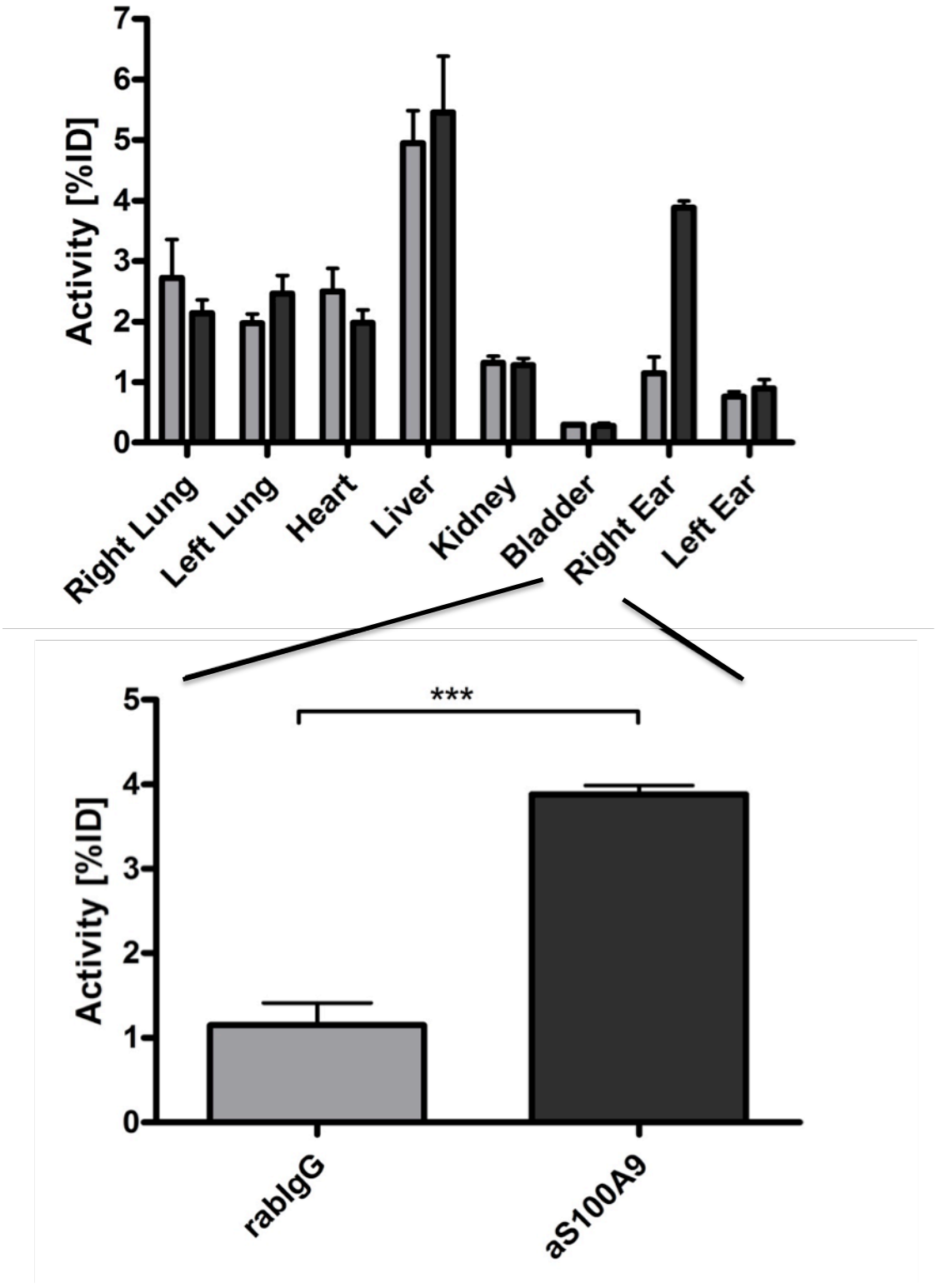

Figure 24: In vivo SPECT in local inflammation – data analysis

The distribution of ^{111}In-aS100A9 (dark grey) and ^{111}In-rabIgG (light grey) was virtually identical in non-target organs. In the area of inflammation (Right Ear), the accumulation of ^{111}In-aS100A9 was significantly higher than the accumulation of ^{111}In-rabIgG, representing hyperaemia (n=8/4; ***=p<0.001). Differences between the two tracers in the healthy control ear were not significant.

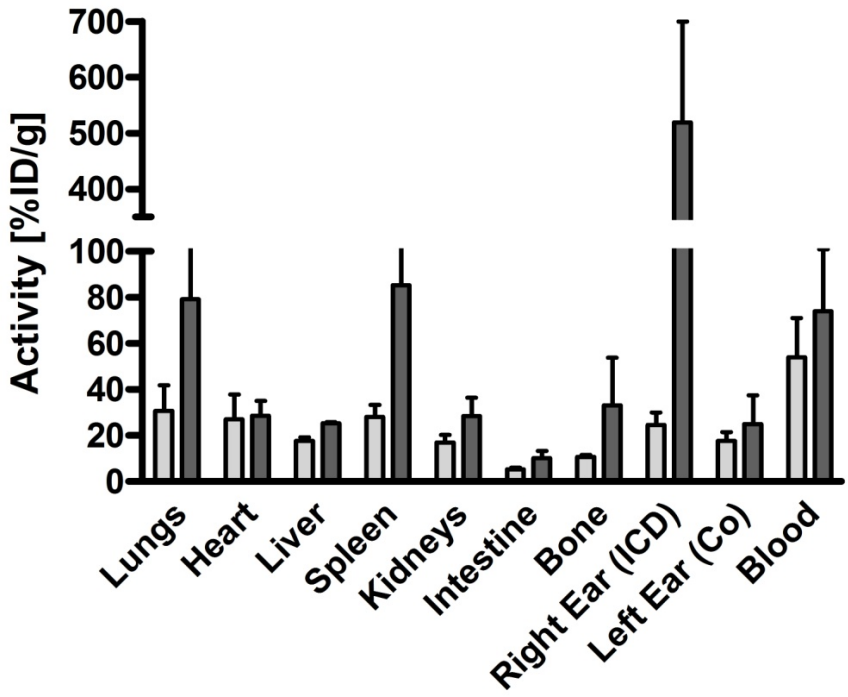

Figure 25: Ex vivo biodistribution in local inflammation.

Immediately after imaging, resected organs were weighed and the remaining activity was measured. The ex vivo biodistribution study confirms the in vivo imaging results with a strong accumulation of aS100A9 (dark grey) in the area of inflammation. In non-target organs, such as the control ear, heart and liver, accumulation of the specific tracer and rabIgG (light grey) as unspecific control was virtually identical. Notable differences could be detected in lungs and spleen, potentially representative of systemic activation of innate immune cells. Both tracers exhibited a high activity in the collected blood samples, probably due to the long circulation time, slow elimination and extravasation.

4.4 Discussion

4.4.1 Review of results

From a polyclonal antibody, targeting the S100A9 subunit of the S100A8/A9 heterodimer, the S100A9-specific tracer aS100A9-DTPA could be constructed via established conjugation chemistry. After labelling with 111In, the tracer retained – according to HPLC analyses – structural integrity and the radiolabel for over 48 h under physiological conditions in vitro (Fig. 22) and was therefore regarded suitable for in vivo application.

A signal, detected by ^{111}In-guided in vivo SPECT imaging would therefore most likely represent the specific tracer, not dissociated tracer components, which would potentially lose target specificity and potentially fall below the renal elimination threshold. Over the examination period, kidneys and especially the urine bladder were virtually void of radioactivity (Fig. 25), which would have been indicative of dissociated tracer components.

In the earlier studies, using fluorescent-labelled antibody constructs, a fluorescent signal could be detected in the bladder 24 h after tracer application. Comparing the studies, this must be attributed to impurities (unbound dye) in the fluorescent tracer solution while the conjugated antibody has been purified with more accuracy using HPLC (Fig. 21).

The antibody, used as a basis for both, the fluorescent tracer as well as the SPECT tracer has been extensively tested for specificity and binding characteristics, before this study was conceived (*86, 111*).

Having used only relatively small labels – a cyanine dye for the fluorescence imaging experiments and a DTPA variant for the SPECT imaging – the probability that labelling would fundamentally change the binding characteristics such as affinity of the antibody was quite low. We therefore abstained from testing the labelled compounds with regards to their binding affinity and concentrated on the in vivo performance including specificity of the tracer accumulation. Several factors

hampered an in vivo blocking study for further validation of the in vivo imaging data: S100A8/A9 exhibits a high and rapid turnover which would require repetitive administration of unlabelled precursors to achieve an effective blocking of the target epitope. However, the availability of the antibody was limited and having shown the target specificity in knock out studies and the sensitivity for the imaging signal for changes in target expression, we abstained from escalating the specificity testing further.

For estimation of perfusion effects due to increased permeability in the target region, a full length IgG of irrelevant specificity in mice was successfully conjugated, purified and labelled accordingly. This tracer is of similar size and allows the investigation of unspecific tracer distribution for direct comparison with the target-specific tracer.

Examination of healthy animals after injection of the probes revealed a typical distribution pattern of antibody-sized molecules: For the whole observation period, remaining tracer could be detected in the blood pool, represented in vivo by the mediastinum/heart region. The retention in the blood pool even allowed for delineation of the carotid arteries and other big vessels. At later time points, the tracer accumulated in the liver and was slowly eliminated from there. No elevated uptake or retention in the kidneys or urine bladder could be observed, confirming virtually exclusive elimination via the hepatic/biliary pathway.

In the model of local inflammation, the ^{111}In-rabIgG scan revealed increased perfusion and enhanced vessel permeability in the area of inflammation as compared to the untreated control side. However, the accumulation of the S100A9-specific probe was significantly higher in the area of inflammation with – compared to the 111In-rabIgG scan – virtually identical background signal. The difference between the two, structurally nearly identical probes, confirms the specificity of aS100A9 for inflammation activity beyond secondary signs like hyperaemia and impairment of vessel integrity.

4.4.2 Characteristics of antibody-based probes

Full length IgG antibodies usually weigh around 150 kDa and therefore exceed the upper limit for renal elimination, which is usually defined around 30 kDa. The result is a prolonged circulation time and slow elimination of unspecifically distributing tracer, constituting a potentially disturbing background signal for longitudinal studies with recurrent examinations. Moreover, the transit of large molecules from the blood pool through the vessel wall and potential further stromal tissue to finally reach a certain target structure can be hampered or at least be delayed.

As a result, the optimal imaging time point for antibody-driven imaging approaches would normally not be earlier than 24 h after tracer application (*112*). This demands the use of isotopes with long half-life to guarantee enough activity at the time of imaging. Smaller targeting molecules like antibody fragments of different size or even smaller Nano- and Affibodies have been tested to overcome this limitation. The serum half-life of Fab antibody fragments – about 50 – 55 kDa in size – has been shown to be reduced to 12 – 20 hours as compared to around one week for full length IgG (*73*). Smaller peptide structures like Nano- or Affibodies – usually smaller than 15 kDa – are eliminated even faster with a serum half-life less than one hour (*113, 114*). These tracer substances would allow for the use of isotopes with shorter half-life and therefore prospectively unlock the translational potential of target-specific imaging. Moreover, this would enable more frequent, repeated scanning without a signal overhang from previous examinations. The shorter serum half-life of smaller molecules does however usually result in a less pronounced accumulation in the target area, as the constant washout of the tracer is higher than it is for bigger molecules. It would in any case be necessary to determine the optimal imaging time point and consecutively appropriate radioisotope.

While labelling of big molecules like intact IgG can be done following relatively easy protocols for random labelling of e.g. Cysteine functions and only a comparatively small fraction of the antibody will loose specificity and binding affinity due to label

overload or obstruction of the relevant binding site, the labelling of a small tracer molecule requires a more sophisticated approach. Chelator and/or dye are relatively small as compared to an intact IgG (chelator size: around 1 kDa) with only little chance that addition of such a small structure would influence the functionality of the antibody. For small molecules however, conjugation to a chelator or dye can fundamentally change the binding affinity and ability. Site-specific labelling approaches overcome this hurdle with specifically engineered sites for label attachment, added to the targeting moiety. This requires engineering and in the case of antibody fragments or comparable peptidic tracers it would require clonal expansion of the tracer.

In summary, antibody-based probes are highly potent for preclinical research as they offer very high specificity and are easily adapted for imaging research. Direct correlation by using the identical antibody for in vivo imaging, FACS and microscopy moreover increases confidence in the reliability of research results. For translational purposes, practical reasons prompt the use of alternative targeting molecules with more favourable biodistribution patterns and the potential to use short-living isotopes.

4.4.3 Potential alternative strategies for S100A9-imaging

Despite the polyclonal antibody that has been used for this project as well as the prior work on optical imaging of inflammation and tumour-associated monocytes (*79, 82*), only very few approaches, exploring S100A8/A9 for imaging, have been published so far. In a recent study, the possibility to detect and measure S100A8/A9 using mass spectrometry has been demonstrated in isolated tissue samples (frozen biopsies) of wound healing (*115*). Although the technical process of sample preparation still strictly limits mass spectrometry to the analysis of tissue samples ex vivo, steps are being taken towards bringing mass spectrometry imaging towards in vivo application (*116*). It is unlikely that spectrometry will replace whole body in vivo imaging. It might,

though, contribute insight on target distribution on a cellular level and therefore add valuable concomitant information in combination assays.

The lack of S100A9-targeted imaging studies can not be attributed to a lack of potential tracers as even aside from the antibody construct, I have been using for this and other studies, other S100A8/A9-binding molecules exist.

Tasquinimod is a small molecule (0.4 kDa) that specifically binds and sequesters S100A9, inhibiting downstream signalling of the protein (*117*). Tasquinimod has been extensively tested in vivo and recently reached phase II clinical trials for the treatment of castration-resistant prostate cancer (*118*). Modification of the molecule to enable labelling for in vivo imaging would result in a potent, very small and therefore probably rapidly distributing imaging agent. However, due to the size of Tasquinimod, conventional labelling chemistry as used to generate aS100A9-DTPA would bear an enormous risk of interference with the binding function of the substance and site-specific labelling approaches would have to be employed. A group of chemists from the European Institute of Molecular Imaging recently published a labelled variant of Tasquinimod as a potential alternative to antibody-based tracers (*119*).

Alternative antibodies such as monoclonal murine or camel antibodies, the latter of significantly smaller size as compared to human and murine antibodies, are currently being generated and tested in the laboratories of Johannes Roth in Münster, Germany and Tony Ng/Kerry Chester, London, UK. It would be possible to isolate, from these monoclonal antibodies, small antibody fragments that could in theory combine the binding affinity and specificity of the original antibody with a more favourable biodistribution due to the reduced size.

As at the moment, the polyclonal antibody I have used for OI of inflammation and primary tumour associated immune cell activity is the only established tracer for S100A9, the study on in vivo imaging of tumour-mediated immune remodelling, was also pursued using the aforementioned compound. In the future, small targeting

molecules and alternative antibodies/antibody fragments will surely be available and tested for specific S100A9 imaging of competitive or even better quality.

5 Systemic S100A9 imaging to unravel tumour immune crosstalk

In a syngeneic, orthotopic model of metastatic breast cancer, ^{111}In-aS100A9-driven SPECT has been assessed for visualisation of tumour-mediated immune activity. Differences between tumour-bearing animals and healthy controls and high and low malignant tumours have been assessed, focussing on the spleen as the systemic monocyte depot and the lungs as target organs of metastasis.

The underlying effects on immune cell abundance and activity were evaluated and the cellular environment in premetastatic tissue was examined.

5.1 Material and Methods

5.1.1 Murine model of metastatic breast cancer

The murine (BALB/c) breast cancer cell lines 4T1.2 and 67NR represent an established model system of graded malignancy with 4T1.2 tumours rapidly inducing distant metastasis in lung and bone, while 67NR tumours grow only locally (*83*). Both cell lines originate from a spontaneous breast tumour, isolated from a Balb/c mouse in Frank Miller's laboratory at the Kormanos Cancer Center.

Tumour cells were cultivated under standard tissue culture conditions (37°C; 5% CO_2 in air; constant humidity) in Dulbecco's Modified Eagle Medium (DMEM, Sigma, Dorset, UK) complemented with 10% foetal bovine calf serum (FBS), penicillin/streptomycin and and 2mML-glutamine.

At the day of tumour inoculation, cells were harvested from tissue culture flasks by trypsination, counted and kept in phosphate buffered saline (PBS) on ice for no longer than one hour before implantation. $1x10^6$ cells were implanted orthotopically into the mammary fat pad of 8 week-old female BALB/c mice obtained from Charles River, UK.

Mice were kept under controlled conditions in the Division of Imaging Sciences BSU and tumour growth was measured daily. Temperature and day/night rhythm was constant and identical for all animals. The cages were equipped with a special soft paper bedding to prevent superficial erosion or laceration of the growing tumour lesion. Water and chow were offered ad libitum.

5.1.2 Cell labelling with viral constructs

For easier identification of tumour cells in tissue cell suspensions for FACS analyses or fluorescence microscopy of tissue samples, the experiments were performed with tumour cells lines that were engineered to stably express a membrane associated red fluorescent protein (mCherry). The viral vector for the protein was expanded in E.coli and isolated and purified using commercially available preparation kits (miniPREP, GE Healthcare UK).

Naive tumour cell lines and mCherry-positive cell lines did not differ regarding in vitro or in vivo growth or malignant behaviour including the establishment of distant metastasis.

5.2 Study Design

Purpose	**Specificity**	**Immunological Grading**			**Regulation**		**Predictive Potential**
n	12	9	15	25	9	6	15
Model	4T1.2	Controls	67NR	4T1.2	4T1.2		4T1.2 (mCherry+)
Treatment					CCL2 blocking	Isotype	
Tracer	aS100A9 / rabIgG				aS100A9		
Imaging	d10						d10
							d20
FACS		Immune cell infiltrate and function in lungs, spleen, blood, tumour tissue					
					mCherry+ metastasis		

Table 2: Experimental procedures and study design

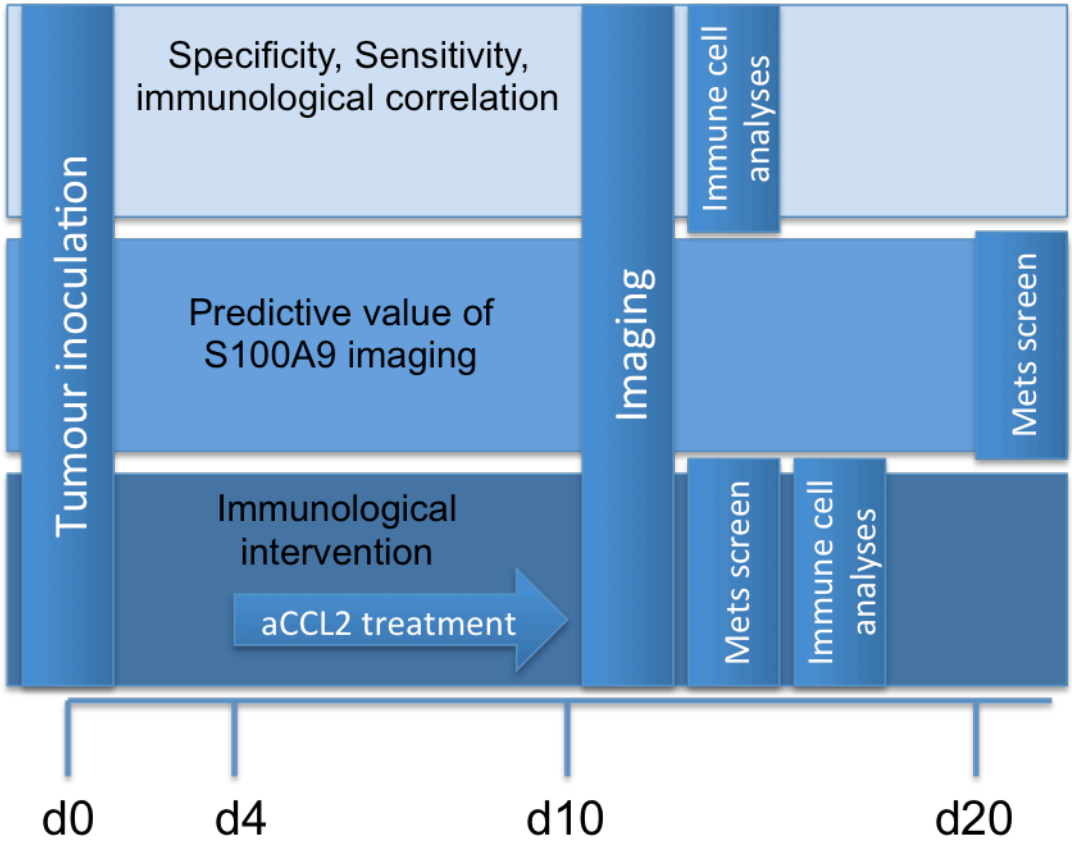

Figure 26: Graphic display of the in vivo experiments.

For all in vivo experiments, animals underwent tumour inoculation into the mammary fat pad at d 0. Depending on the experimental purpose, imaging was conducted not earlier than d 10 after tumour implantation and further analysis of tissue samples for either metastatic burden or activation and differentiation of immune cells (moncytes, NK cells, T cells) was conducted immediately after the imaging or up to 10 days later to assess the predictive value of S100A9 imaging.

5.2.1 Systemic imaging in tumour-bearing animals

At specific time points after tumour inoculation, tumour-bearing animals underwent S100A9 and rabIgG SPECT imaging as described before.

Day ten after tumour inoculation was chosen as representative of an early phase of tumour development. Average tumour size at day ten was around 5 – 8 mm. No animal, examined at day ten after tumour induction, exhibited a detectable metastatic tumour spread.

For assessment of late stage tumour effects, mice were examined at day 20 or later after tumour induction. Average tumour size at this time point was 10 mm. In some of

the animals, examined at this time point, manifest lung metastasis and enlargement of inguinal lymph nodes, indicative of tumour invasion, could be detected.

Experiments were terminated and mice were culled before tumour lesions could grow beyond a volume of 1 mL.

24 h prior to the respective imaging time point, mice received ^{111}In-aS100A9 or ^{111}In-rabIgG in amounts, corresponding to 10 MBq activity intravenously via the tail vein.

Imaging was carried out according to the aforementioned protocol for SPECT/CT imaging (p 62).

After imaging, mice were either kept in designated, shielded areas for longitudinal examination or culled immediately for collection of tissue samples for further validation.

5.2.2 Systemic S100A9 imaging under CCL2 blockade

In vivo blocking of CCL2 was performed in analogy to established protocols (*120*): 4T1.2 tumour-bearing mice received an intraperitoneal injection of 100 µg goat polyclonal anti-CCL2 antibody (R&D, Abingdon, UK) in 100 µl PBS every other day beginning on day 4 after tumour inoculation. Control mice were in parallel treated with 100 µg normal goat polyclonal serum in 100 µl PBS.

To control for the effect of CCL2 and further assess the role of the CCL2-CCR2 axis in promoting the release of S100A8/A9 from positive cells, monocytes and granulocytes of particular character (monocytes: CD11b+CD115+CCL2highCX3CR1low; granulocytes Gr1+CR2+CD115-) were isolated from spleen tissue of tumour-bearing mice by FACS, seeded into 96-well plates and treated with 50ng/ml recombinant mouse CCL2 (Invitrogen). After 48 h, the supernatant was collected and screened for S100A8 using ELISA (DuoSet, R&D systems) according to manufacturers' instructions. Samples from 4T1.2 tumour-bearing animals as well as 67NR tumour-bearing animals were examined.

5.2.3 Ex vivo validation studies and immunological function assays

5.2.3.1 Characterisation of tumour cells for S100A8/A9 release

To exclude the tumour cells as the primary source of S100A8/A9, responsible for in vivo SPECT signals, the release of S100A8/A9 by tumour cells of both, 4T1.2 and 67NR cell lines, has been assessed.

Using a S100A9-specific ELISA, established at the Institute of Immunology, University of Münster, Germany, cell culture supernatant of 4T1.2 and 67NR cultures and cell lysates of both cell lines have been screened for S100A9, as described in detail earlier (*54*).

The cell culture supernatant was left at least three to five days on the growing cells to allow for a potential titre to build up in the supernatant. For cell lysates, samples of at least $1x10^6$ cells were used, washed thoroughly after harvesting and lysed following standard protocols.

Additionally, single cell suspensions from tumour tissue, resected from mice 10 days after tumour inoculation have been examined. The cells were dually stained for CD11b and S100A9 and screened for single and double positivity.

5.2.3.2 Biodistribution studies and tissue collection for immunological studies

Mouse organs were collected immediately after scanning at either day 10 or day 20 after tumour inoculation, representative of early or late phases of malignant disease.

The mouse carcass was weighed and the overall body activity was measured. Dissections were carried out under surgical conditions. From all animals, lungs, heart, liver, spleen, kidneys, intestine, bone (representative sample of spine) and a blood sample (20 µl in lancet capillary) were collected and separately weighed. The retained radioactivity was determined by gamma counting. For each organ, the relative dose

per gram tissue was calculated from the collected data and a dilution row of the injected tracer, examined in parallel.

Representative tissue samples were at the same time separated for FACS or histology studies.

Cell suspensions were prepared from the isolated organs for flow cytometry analyses and cell sorting as described below. Tissue for consecutive FACS analysis was immersed in ice-cold DMEM immediately after resection.

Tissue samples for future histological examinations were embedded in optimum cutting temperature (OCT) compound and snap-frozen in liquid nitrogen-cooled 2-Methylbutane, immediately after resection. 4-5 mm thick sections were cut using a Bright 5030 microtome cryostat (Bright Instruments, Cambridge, UK) and stored at -80°C for further immunofluorescence staining and confocal microscopy analysis.

5.2.3.3 Analysis of immune cell activity and function

5.2.3.3.1 Reagents and antibodies

Tissue culture consumables: Dulbecco's modified eagle medium (DMEM), heat-inactivated fetal bovine serum (FBS), Dulbecco's phosphate buffered saline (DPBS) (all Gibco, UK), L-glutamine, Penicillin/Streptomycin (all GE Healthcare), 10x Trypsine and bovine serum albumin (BSA) (all PAA)

Reagents for preparation of cell suspensions: Red blood cell lysis buffer, 2-Methylbutane (all Sigma-Aldrich), Foxp3 staining kit, containing Fixation/Permeabilization concentrate, Fixation/Permeabilization diluent and 10x Permeabilization Wash Buffer (eBioscience), Live/Dead yellow (Life Technologies and Hoechst).

A list of all antibodies that were used for this project can be found in table 3.

	Name	Conjugation	Clone	Isotype	Reference	Dilution		Company
						FACS	Micros copy	
Primary antibodies	CD3	PE	500A2	Hamster IgG	12-0033	1:200		eBioscience
		PE-Cy7	145-2111	Hamster IgG	25-0031	1:100		eBioscience
		Biotin	OKT3	Mouse IgG2a		1:200		eBioscience
	CD4	APC				1:100		
		FITC	GK1.5	Rat IgG3b	100405	1:100		BioLegend
	CD5	Biotin	53-7.3	Rat IgG2a	13-0051	1:200		eBioscience
	CD8	Biotin	53-6.7	Rat IgG2a	13-0081	1:200		eBioscience
	CD11b	V450	M1/70	Rat IgG2b	48-0112	1:100		eBioscience
	CD19	Biotin	1D3	Rat IgG2a	13-0193	1:200		eBioscience
	CD25	PE	PC61.5	Rat IgG1	12-0251	1:100		eBioscience
	CD27	PE	LG.7F9	Hamster IgG	12-0271	1:100		eBioscience
	CD49b	PE-Cy7	DX5	Rat IgM	25-5971	1:100		eBioscience
	CD107	APC	1D4B	Rat IgG2a	121613	1:100		BioLegend
	CD115	-	3-4A4	Rat IgG2b	SC-02		1:10	Santa Cruz
		Biotin	AFS98	Rat IgG2a	130-101-913	1:20		MACS
	CCR2	-	N-14	Goat IgG	SC-31563		1:25	Santa Cruz
	Foxp3	V450	FJK-16s	Rat IgG2a	48-5773	1:50		eBioscience
	Ly-6G	Biotin	1A8	Rat IgG2a	130-101-884	1:20		MACS
	NK-p46	FITC	29A1.4.9	Rat IgG2a	130-102-300	1:50		MACS
		V450	29A1.4	Rat IgG2a	48-3351-82	1:50		eBioscience
	S100						1:50	
	Ter119	Biotin	TER-119	Rat IgG2b	13-5921	1:200		eBioscience
Secondary antibodies	Rat IgG	Alexa488	-	Goat IgG	A11006		1:200	Life Technologies
	Goat IgG	Cy3	-	Donkey IgG	705-165-147		1:200	Jackson/Stratech
	Rabbit IgG	Alexa647	-	Goat IgG	11-605-045		1:200	Jackson/Stratech
	Streptavidin	PerCP-Cy5.5			45-4317	1:200		eBioscience

Table 3: Summary of antibodies, used in this study

5.2.3.3.2 FACS sorting for MDSC identification

Samples from lungs, spleen and primary tumour tissue were screened for immunomodulatory MDSC and other sources of S100A8/A9, using FACS.

The isolated organs were mashed immediately after resection and put through a Falcon cell strainer (100 µm mesh size; Fisher Scientific, UK), suspended in ice-cold DMEM, to create a single cell suspension. The coarse cell suspension was then incubated with ACK lysis buffer (Thermo Fisher Scientific, UK) for 5 minutes to get rid of red blood cells. After purification, the single cell suspensions were washed and resuspended in PBS. Per well of a 96 wells plate, 500,000 cells were seeded. All steps were carried out at room temperature. The cells were washed with 200 µl PBS and incubated with 50 µl Live/Dead yellow. After 20 min, cells were washed with 200 µl PBS. Subsequently, 50 µl of the primary antibodies in MACS (1XPBS/1% FBS/2mM EDTA) were added per well and incubated for 20 min. The primary antibody mixture consisted of biotinylated lineage markers (CD3, CD5, CD8, CD19, CD115, Ter119, Ly6G) and directly conjugated NKp46 to identify NK cells, as well as directly conjugated CD4 and CD25 to distinguish Treg. See Table 3 for information on the antibodies that have been used. Thereafter, the cells were washed with 200 µl MACS and 50 µl of Streptavidin-PerCP-Cy5.5 in MACS were added, and again incubated for 20 min. Cells were washed with 200 µl MACS, followed by fixation and permeabilization with Fix/Perm for 30 min. Per well, 200 µl 1x Permeabilization wash buffer (Perm/Wash) were added to wash the cells. Next, cells were incubated for 45 min with 50 µl Foxp3 or S100A9, diluted in Perm/Wash. The cells were washed twice with 200 µl Perm/Wash, once with 200 µl MACS and finally resuspended in 200 µl MACS. Samples were measured using the BD Fortessa^{TM} cell analyser and data were processed with FlowJo 8.7 (Tree Star Inc.).

For identification of immunomodulatory MDSC, a specific gating strategy was applied during FACS analyses. The markers included Gr-1, CD115, CCR2 and CX3CR1.

Starting with gating to define live cells (Yellow Dead$^-$), sorting for single-cell populations (FSC-A vs. FSC-H plot) was applied. Gates were set according to fluorescence-minus one (FMO) controls for Gr-1 and CD115, CCR2 and CX3CR1. FMO control for intracellular staining with S100A8/A9 in this and other cell populations. For detection of Tregs, a gating strategy including markers CD4, CD25 and Foxp3, again with FMO, was applied. NK cells were identified according to negativity of other lineage markers (CD3, CD5, CD8, CD19, Ter119, CD115, Ly6G) and as NKp46$^+$CD49b$^+$; a FMO control was applied for staining with CD107 (LAMP1).

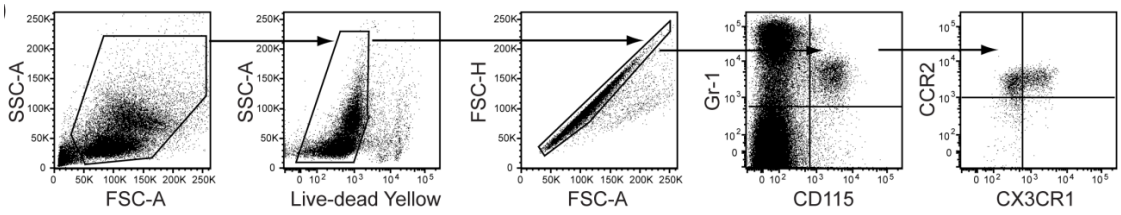

Figure 27: FACS gating strategy for identification of MDSC

Following selection of live, single cells via Life-dead staining and gating for FSC-A/H, CD115/Gr-1 double positive cells were gated and screened for CX3CR1 and CCR2.

5.2.3.3.3 Marker panel for tumour immune remodelling

In cell suspensions from lung tissue, harvested from tumour-bearing mice, the abundance and activity of Treg and NK cells was determined.

Following production of single cell suspensions and the staining principle procedures as described earlier (p 81), the markers used for this specific purpose were CD25 and Foxp3 for identification of Treg and CD107 as activity marker of NK cells.

Tissue samples were stained and sorted for all three markers in parallel to assess the association and presence of Treg and NK cells in the same tissue sample.

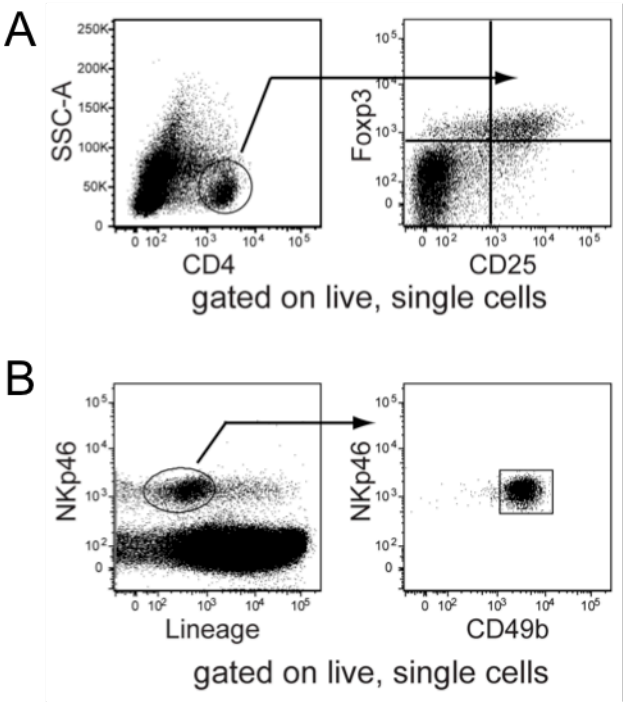

Figure 28: FACS gating strategy for identification of Treg (A) and NK cells (B).

Following identification of live, single cells as described for the MDSC already, lineage markers for Treg or NK cells were applied to identify the respective cell populations in the examined tissue samples.

5.2.3.3.4 Immunohistochemistry for validation of in vivo imaging

From all organs, examined using in vivo imaging, tissue samples were processed for histology for direct, visual verification of in vivo imaging results.

In particular, the spatial association of S100A8/A9 releasing cells, and Gr1+CD115+CCR2highCXCR1low monocytes/MDSCs was to be demonstrated.

In this context, a protocol for simultaneous staining for S100A8/A9, CD115 and CCR2 was established and executed on selected sectioned samples of lungs, spleen and primary tumour tissue of mice, bearing 4T1.2 or 67NR tumours.

All tissue samples were embedded in optimum cutting temperature compound (OCT; Sakura Finetek Europe, The Netherlands) and snap-frozen in liquid nitrogen-cooled 2-Methylbutane, immediately after resection from the animals. From these samples, 5 µm thick sections were cut using a Bright 5030 microtome cryostat (Bright

Instruments, Cambridge, UK) and stored at -80°C for immunofluorescence staining and confocal microscopy analysis.

At the time of staining, tissue was fixed in ice-cold neat acetone for 20 minutes. Slides were then labelled and a circle was drawn around each section using a hydrophobic pen (DAKO, Ely, UK) to minimise reagent use and to prevent accidental staining of adjacent sections.

All incubation steps were carried out at room temperature and in the dark, unless stated otherwise. The sections were defrosted and rehydrated for 10 min with 200 µl PBS, followed by 20 min incubation with 200 µl 3.7% PFA. Afterwards, the sections were washed five times with 200 µl PBS and the samples were blocked using 200 µl blocking solution (PBS/1% FBS/1% BSA). After 30 min, the sections were washed five times with 200 µl PBS and incubated overnight with 100 µl CD115 and CCR2 in blocking solution at 4°C. Again, sections were washed eight times with 200 µl PBS and incubated with 100 µl DαG-Cy3 in blocking solution for 1 h. Afterwards, sections were washed five times with 200 µl PBS and 100 µl goat anti-rat-Alexa488 in blocking solution was added for 1 hour. Subsequently, the samples were washed five times with 200 µl PBS, incubated with 100 µl Fix/Perm for 30 min, and washed five times with 200 µl Perm/Wash. Subsequently, the sections were incubated for 2 hours with 100 µl S100A8 in Perm/Wash, washed five times with 200 µl Perm/Wash and incubated for 1 hour with donkey anti-rabbit-Cy5 in Perm/Wash, before being washed five times with 200 µl PBS. Next, the sections were stained with 100 µl Hoechst for 20 min, washed five times with 200 µl PBS and finally mounted.

Images were acquired using the Carl Zeiss Laser Scanning Microscope 510 (LSM-510) equipped with 405, 488, 543 and 633 nm lasers and using 20x and 40x multi immersion objectives and the 63x oil immersion objective. The software used to acquire images was Zen 2009 (Carl Zeiss, Welwyn Garden City, UK).

Images were analysed using the ImageJ software (National Institute of Health).

5.3 Results

5.3.1 Biodistribution in tumour-bearing animals

Tumour-bearing animals were injected with ^{111}In-aS100A9 24 hours prior to SPECT imaging. The examination was performed on established tumours, about 14 days after tumour induction. The average lesion size was 8 mm as determined by calliper measurement.

After imaging, selected tissues were harvested for validation of in vivo imaging results by gamma counting and histology.

A strong accumulation of the S100A9-specific probe could be observed in the primary tumour, confirming the OI results (Chapter 3). As compared to healthy control animals, an increased tracer accumulation could also be observed in spleen and lungs. The retention of the tracer in the liver was virtually unaltered.

A high signal in the mediastinum/heart region hinted towards presence of the tracer in the blood pool and could not be verified ex vivo. In contrast, tracer accumulation in tumour, lungs, spleen and liver could be confirmed by gamma counting.

^{111}In-rabIgG signals in lungs and spleen did not significantly differ from signals in healthy controls; the retention in the tumour was significantly lower as compared to ^{111}In-aS100A9.

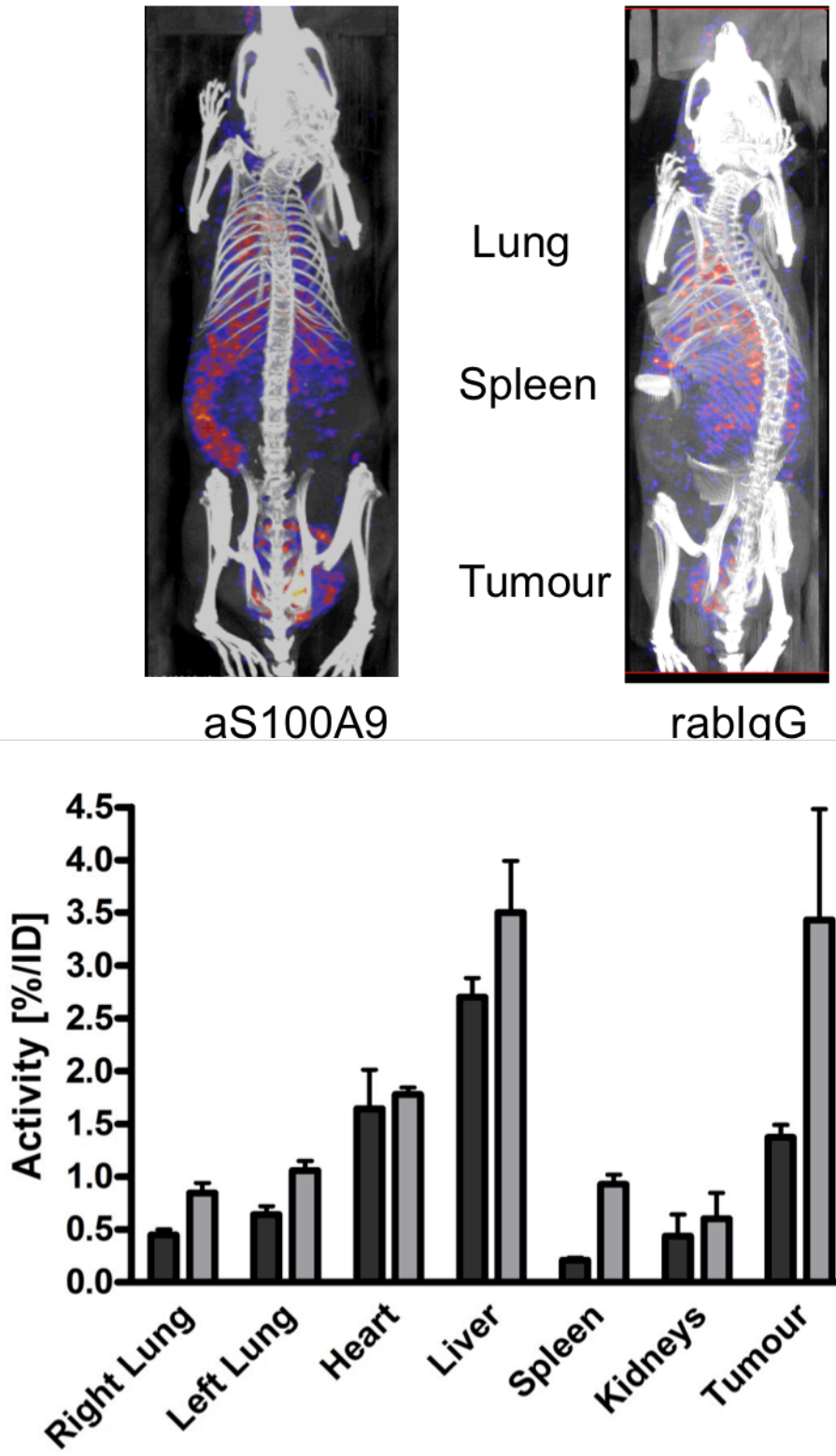

Figure 29: In vivo SPECT imaging in 4T1 tumour-bearing animals.

Exemplary images of mice, 24 h after i.v. injection of ^{111}In-aS100A9 or ^{111}In-rabIgG. Tumours (4T1) were implanted in the mammary fat pad (n=12; n=6 per tracer)

Differences in accumulation can be observed in lung tissue (0.49 %/ID vs. 0.97 %/ID), spleen (0.21 %/ID vs. 0.9 %/ID) and the primary tumour (1.4 %/ID vs. 3.4 %/ID).

5.3.2 Kinetics of S100A8/A9 release during malignant disease

We examined mice at different time points after tumour inoculation using S100A9-SPECT scanning. Imaging was performed at an early stage of tumour establishment (day 10 after inoculation) and again once the tumour was well-established, and first distant metastasis were likely to be present (day 20).

The tracer accumulation in different body compartments was compared for the different time points.

In the primary tumour, the tracer accumulation, indicative of immune cell activation, increased significantly over time. In distant tissues, however, the effects of time and continued tumour growth were less pronounced. In lung tissue, local S100A9 concentration, as depicted by targeted imaging, increased slightly albeit not significantly.

The spleen, only detectable in a few animals at day 10 after tumour induction, was clearly detectable in all animals at day 20.

Unspecific ^{111}In-rabIgG did not reveal perfusion or vessel integrity differences between the different time points for any of the examined tissues.

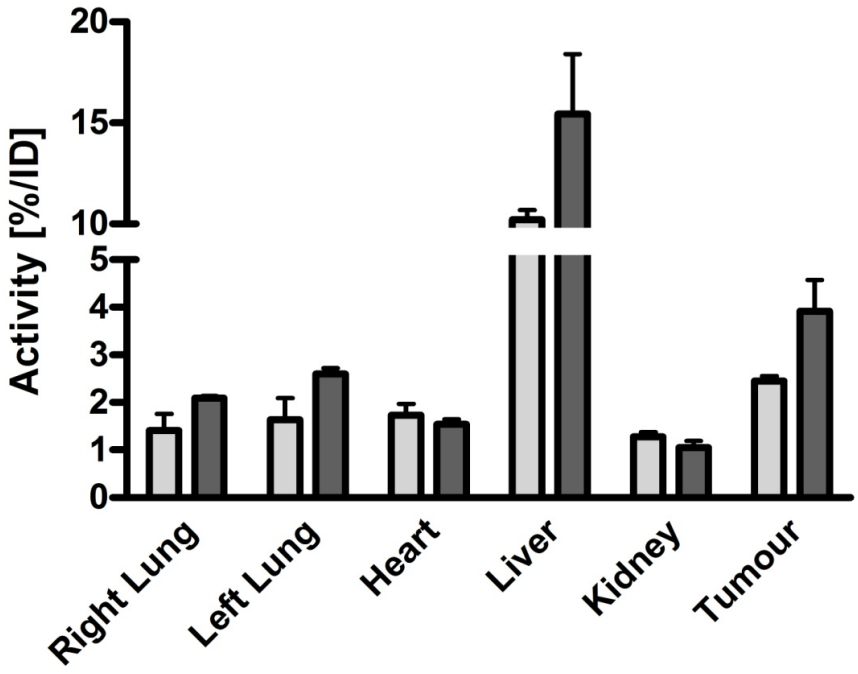

Figure 30: Development of local S100A8/A9 concentration over time.

4T1 tumour-bearing mice were examined by S100A9-SPECT on day 10 (light grey) and day 20 (dark grey) after tumour inoculation (n=15). The systemic tracer distribution was assessed using SPECT 24 h after iv injection of ^{111}In-aS100A9. The accumulation in the tumour was stronger at day 20 as compared to day 10 (3.9 %/ID vs. 2.4 %/ID). Differences in lung tissue were less pronounced (2.3 %/ID vs. 1.5 %/ID); the blood pool, represented by the heart and kidney signal was virtually identical. The strongly elevated signal in the liver on day 20 after tumour implantation can be an indicator of immune cell activity in the liver, e.g. in the context of developing liver metastasis. It would require analysis of liver tissue for changes in the cellular composition and/or accumulation of circulating tumour cells to further differentiate this finding.

5.3.3 Association of S100A8/A9 release and metastatic capability

We established a model of graded malignancy, represented by variation in the capacity to form and establish distant metastasis. The model is based on single cell clones from a spontaneous murine breast cancer, isolated from Balb/c mice. The two cell lines that have been chosen for this project are the cell lines 4T1.2 and 67NR. While 4T1.2 tumours form lung and lymph node metastasis within a few weeks of

tumour induction in orthotopic location, 67NR exhibits local growth only. The local growth characteristics of both cell lines are virtually identical.

At day 10 after tumour inoculation, mice bearing either 4T1.2 or 67NR tumours were examined using ^{111}In-aS100A9-SPECT. The tracer distribution and resulting signal were evaluated in vivo and validated ex vivo using gamma counting of harvested tissue samples.

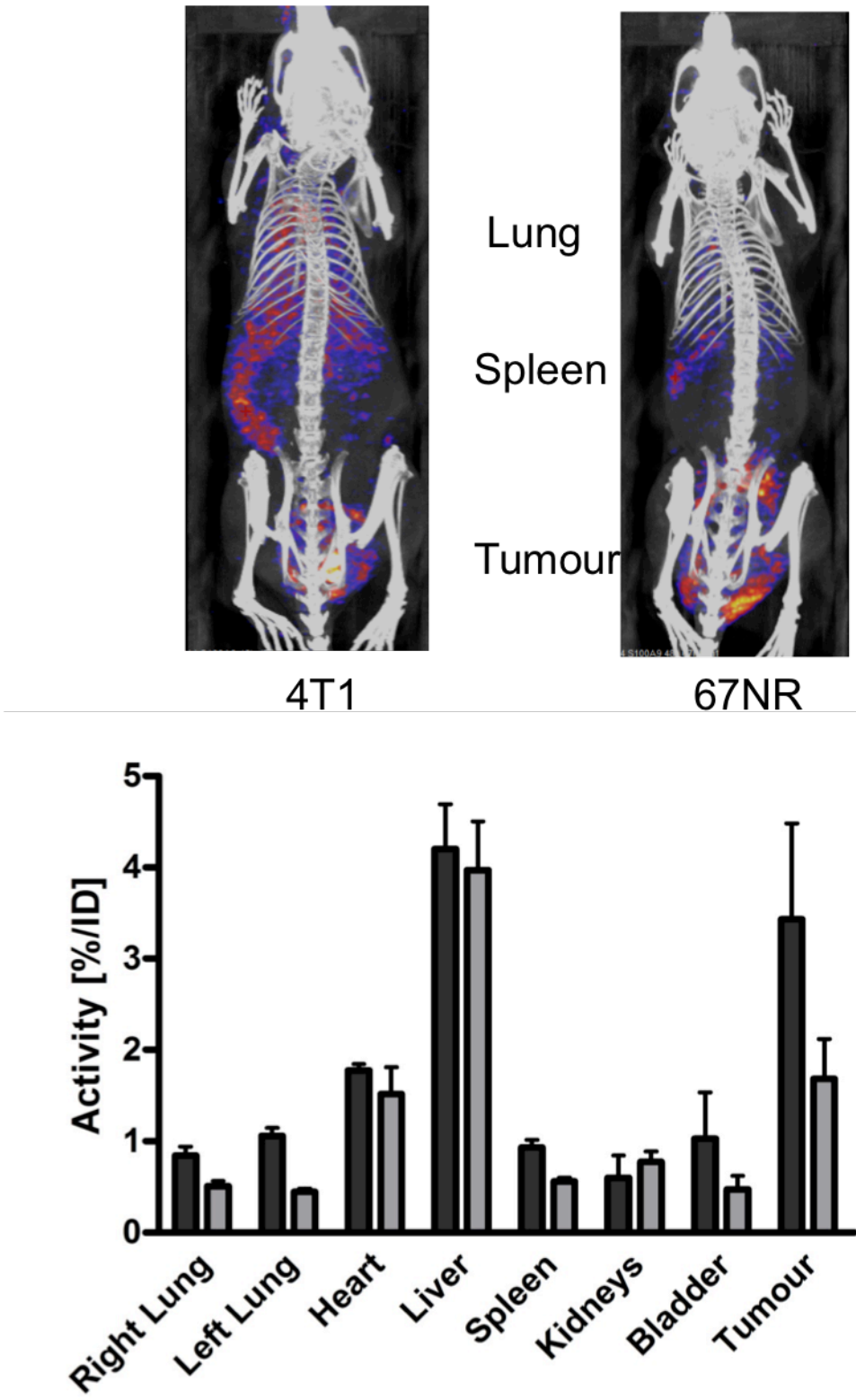

Figure 31: S100A9 SPECT imaging in 4T1 or 67NR tumour-bearing animals

Exemplary images show the difference between 4T1 (n=18) or 67NR (n=8) tumour bearing animals (tumours implanted in the mammary fat pad) in systemic S100A8/A9 distribution as depicted by SPECT imaging, 24 h after iv injection of ^{111}In-aS100A9: While in 4T1 tumour-bearing animals (dark grey) strong tracer accumulation can be observed in spleen and lung, 67NR tumour-bearing animals (light grey) do

not exhibit a similarly pronounced pattern (lungs: 0.95 %/ID vs. 0.55 %/ID; spleen: 0.93 %/ID vs. 0.6 %/ID). Tracer accumulation in target organs of metastasis and the spleen as mirror of the systemic monocyte differentiation is only slightly higher than in healthy controls. Unspecific accumulation in liver, heart (blood pool) and kidneys/bladder does not exhibit significant differences between the two tumour entities.

Separate analyses were performed for the primary tumour, spleen and lungs and ^{111}In-rabIgG-mediated SPECT served for discrimination of unspecific tracer distribution. The perfusion levels as depicted by rabIgG-SPECT were not significantly different between 4T1 and 67NR tumour-bearing animals.

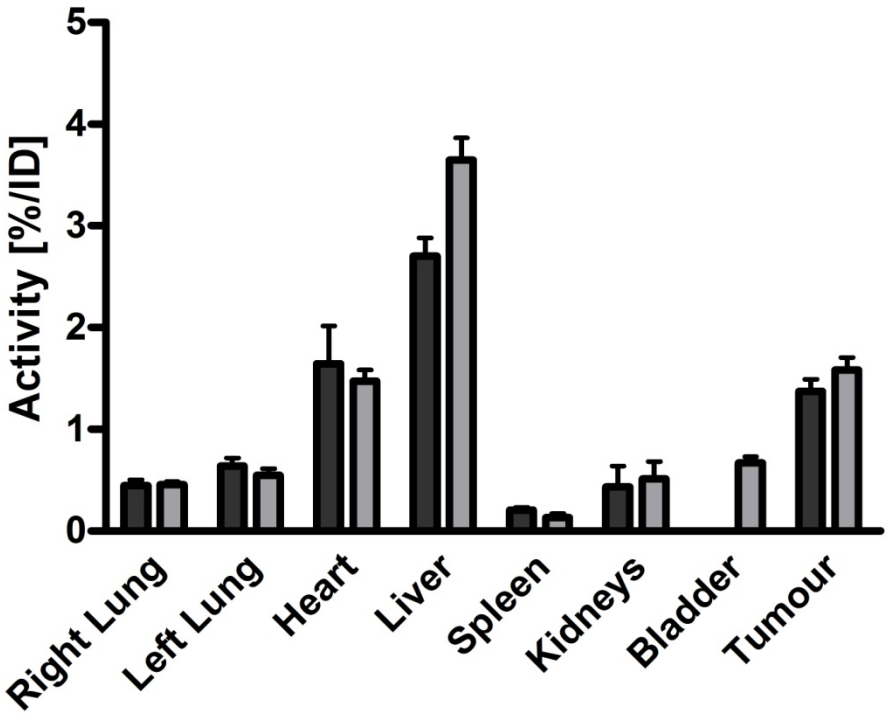

Figure 32: 111In-rabIgG-driven SPECT in animals bearing 4T1 or 67NR tumours.

No significant differences between 4T1 (dark grey; n=7) and 67NR (light grey; n=7) tumour-bearing animals (tumours implanted in the mammary fat pad) could be detected by rabIgG SPECT (iv injection 24 h prior to imaging), thereby attributing the differences, detected by S100A9 SPECT to differences in local S100A8/A9 concnetration.

In accordance with results from the fluorescence imaging experiments, the specific tracer accumulation in the tumour already was different for the two tumour entities with a higher signal in 4T1.2 tumour lesions as compared to less malignant 67NR.

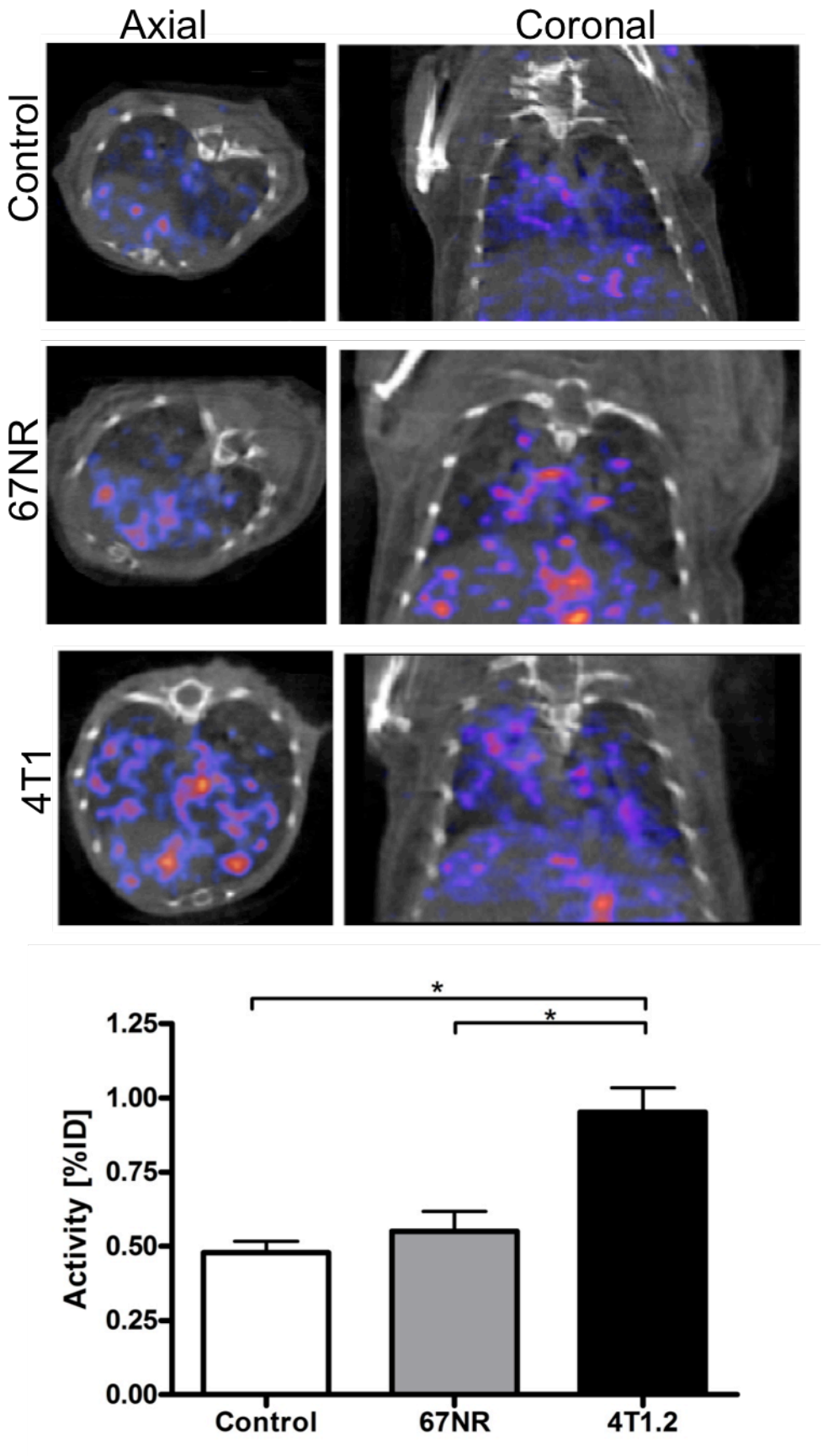

Figure 33: In vivo S100A9 SPECT – focus on the lungs.

The comparison of aS100A9 accumulation in the lungs of healthy controls (n=5), 67NR (n=8) and 4T1 (n=18) tumour-bearing animals revealed a significantly higher S100A9 concentration in the lungs of 4T1 tumour-bearing animals as compared to the two other groups (0.49 vs. 0.55 vs. 0.95 %/ID; *=p< 0.05).

Similarly, the S100A9-signal in lung tissue and spleen was higher for 4T1 tumour-bearing animals as compared to 67NR tumour-bearing littermates.

In spleen tissue, the effects of 67NR tumours were less pronounced than the effects of 4T1.2 tumours.

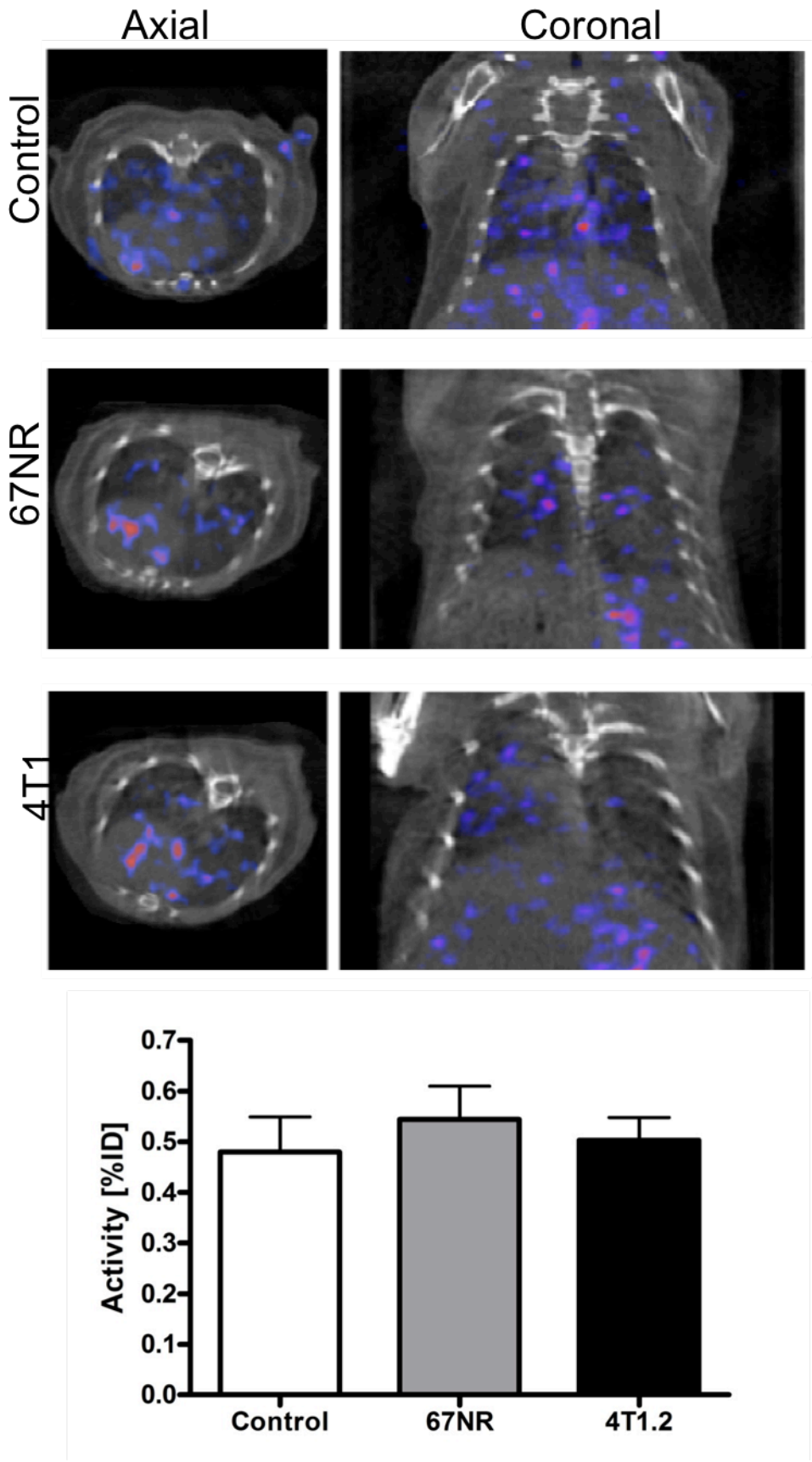

Figure 34: rabIgG SPECT to control for specificity of aS100A9-mediated in vivo imaging.

^{111}In-rabIgG did not allow for detection of physiological differences between the lungs of healthy controls (n=4) or tumour-bearing animals (67NR – n=7; 4T1 – n=7).

The ^{111}In-rabIgG-mediated signal in the lungs of 67NR tumour-bearing animals did not exceed the ^{111}In-aS100A9 signal in healthy animals.

5.3.4 Source of S100A8/A9

Tissue samples from lungs, spleen and primary tumour from both, 67NR and 4T1.2 tumour-bearing animals have been analysed for S100A8/A9 positive cells and cell populations, which were different in number as compared to healthy control animals.

Cell suspensions from tissue samples were stained for a combination of immune cell markers and analysed, using FACS. Presence and spatial association of cells in the in vivo situation were consecutively assessed and validated using fluorescence microscopy, using a combination of respective markers.

The increased S100A9 signals in the spleen of 4T1.2 and 67NR tumour-bearing animals were accompanied by splenomegaly and changes in the cellular composition of the splenic cell populations.

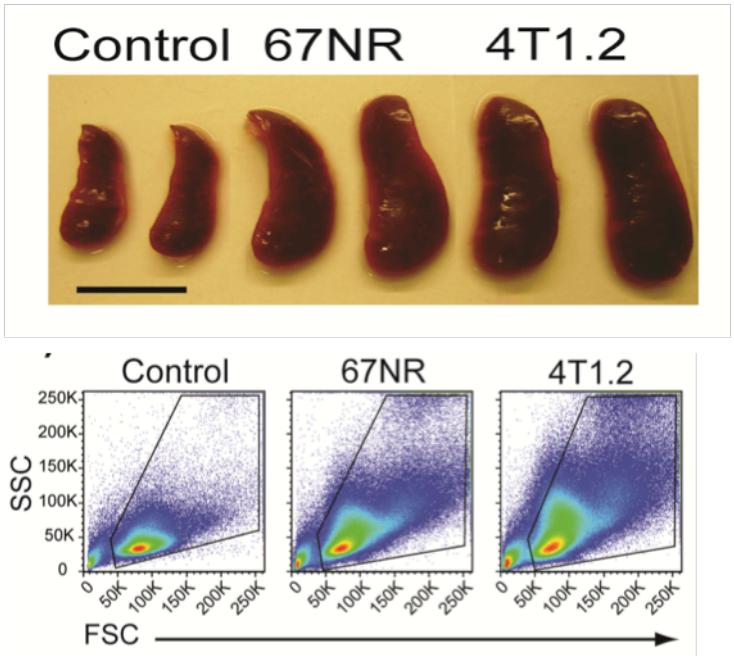

Figure 35: Examination of the spleen of healthy and tumour-bearing animals.

The tumour-induced splenomegaly is clearly visible on exemplary resected organs of tumour-bearing animals as compared to healthy controls. The FACS analysis of single cell suspensions of these organs reveals a strongly increased and aberrant cellularity.

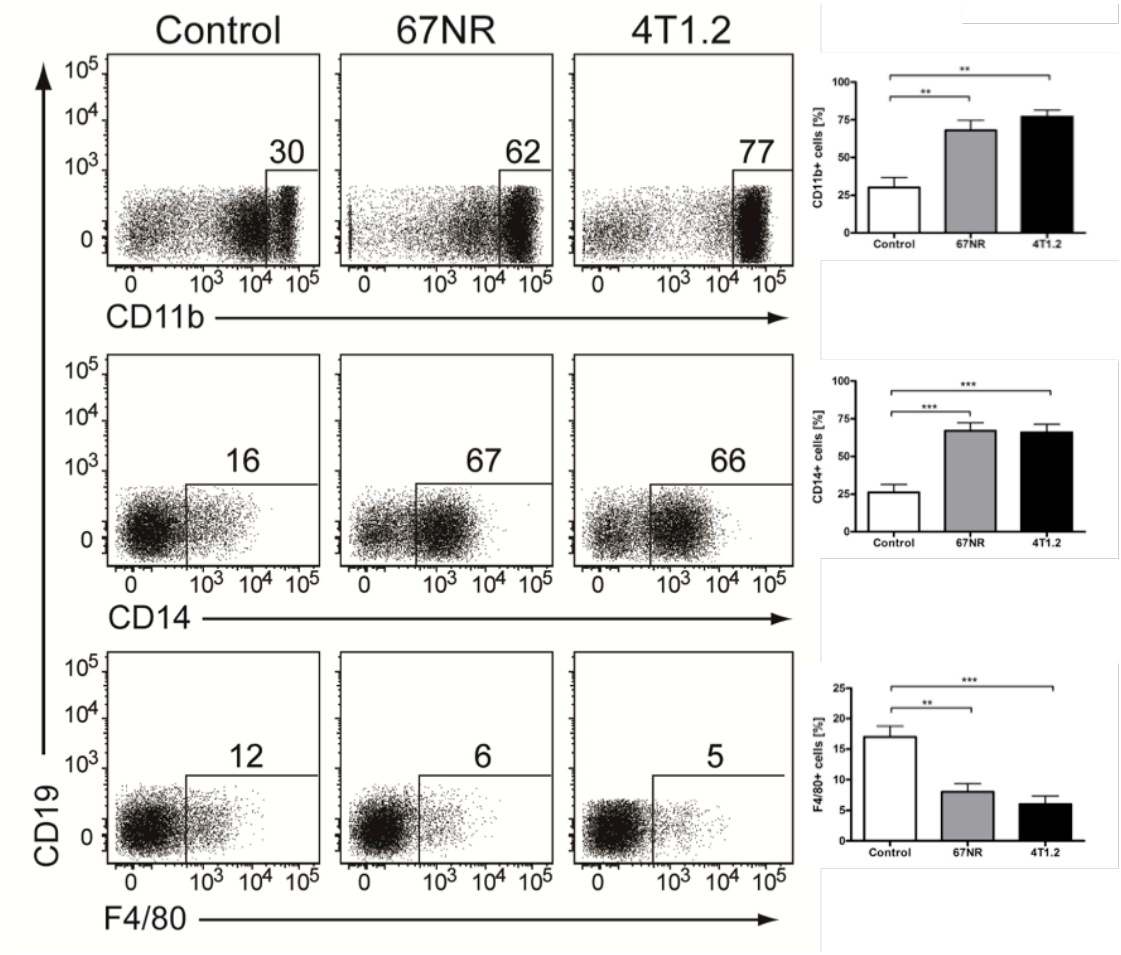

Figure 36: Phenotypic analyses of spleen tissue.

Comparing the CD3- CD19- population (non T-cells, non B-cells) in healthy controls (white; n=9), 67NR tumour-bearing animals (light grey; n=15) and 4T1 tumour-bearing animals (black; n=25) with regards to the abundance of different immune cell markers, a more than two-fold increase in the number of CD11b+ (monocytic) cells could be detected (upper panel). Fostering this impression, CD14 is overexpressed in this population as well (middle panel). The expression of F4/80 as a marker for mature macrophages however, is significantly reduced (bottom panel).

**=p<0.01; ***=p<0.001

A significant increase in the frequency of $CD3^{-}CD19^{-}CD11b^{+}CD14^{+}$monocytes could be observed in 67NR and 4T1.2 tumour-bearing mice at day ten after tumour inoculation. Monocytes in tumour-bearing mice were on average less differentiated as

judged by the decreased frequency of F4/80^{+} cells as compared to respective controls.

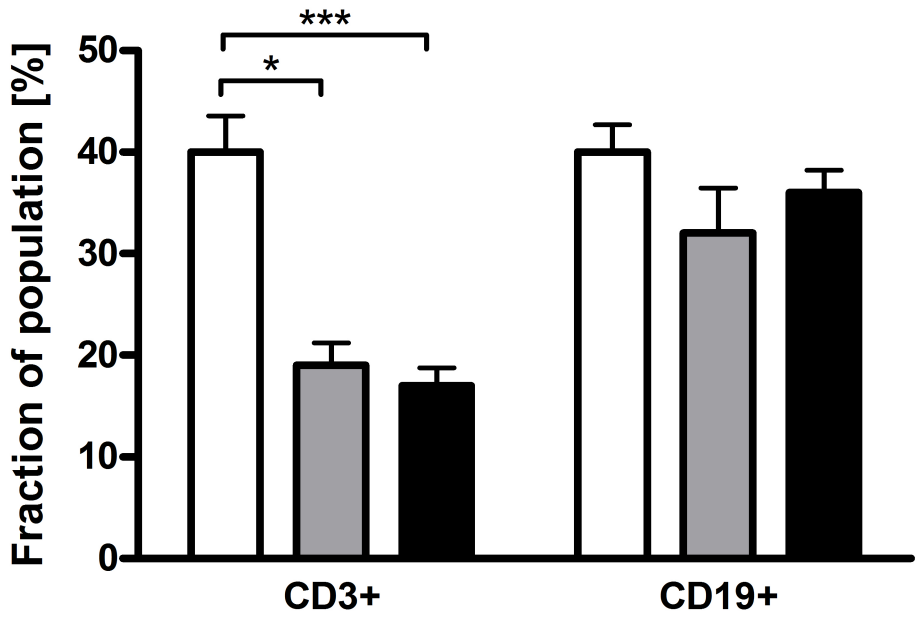

Figure 37:FACS analysis of splenic cells in tumour-bearing mice – T- and B-cells.

The CD3+ population of T cells was reduced by a factor of around two (40% vs. 19% vs. 17%; *=p<0.05; ***=p<0.001) in 67NR (grey; n=15) or 4T1 (black; n=25) tumour-bearing animals as compared to healthy controls (white; n=9) while the CD19+ B-cell population did not show a significant variation (40% vs. 32% vs. 36%).

Similarly representative of a less differentiated phenotype of myeloid cells, splenocytes in tumour-bearing mice showed an increased expression of CD80 and a reduced expression of MHC II as compared to healthy controls (*40*).

We further characterised the phenotype and function of the monocyte population that we found increased in association with elevated S100A8/A9 tracer levels in SPECT. We harvested spleens from tumour-bearing animals and analysed the cellular infiltrate in comparison to tissue samples from healthy controls. FACS staining for several cell surface markers allowed us to define a subset of the increased monocyte (CD3^{-}CD19^{-}

$CD11b^{+}CD14^{+}$) population first in the spleens of tumour-bearing animals and consecutively also in the premetastatic lung tissue.

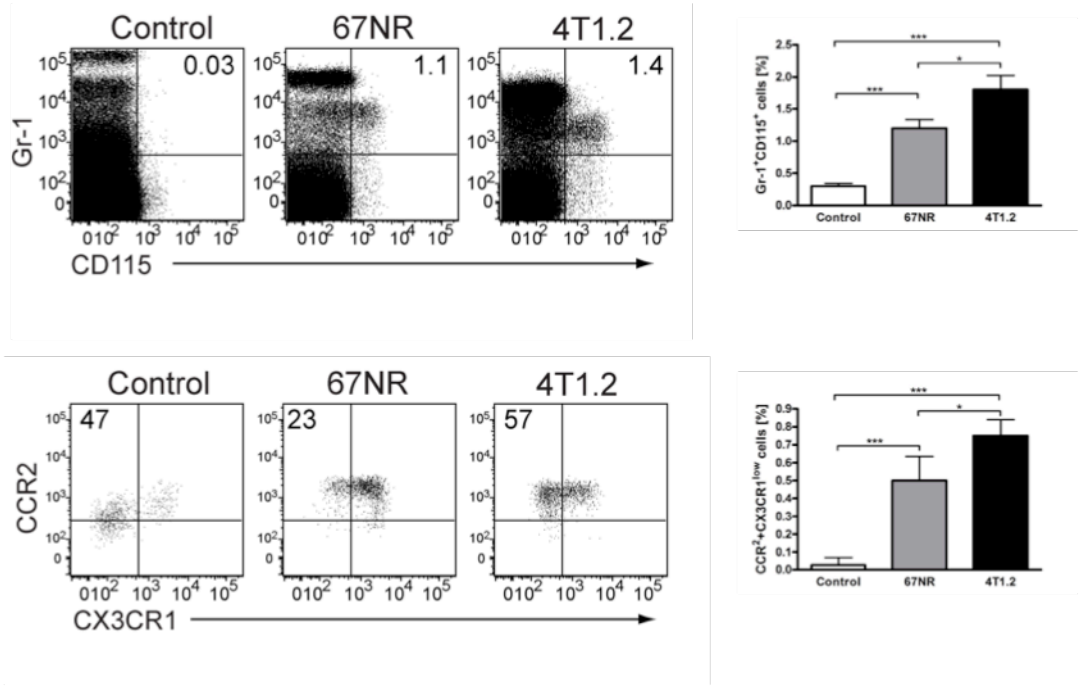

Figure 38: Characterisation of tumour-induced monocytes in spleen tissue.

Among all live cells in the spleen, a population of Gr-1+ CD115+ cells (upper right quadant in FACS plots) was significantly increased in tumour-bearing, as compared to healthy animals (upper panel; 0.3 vs. 1.2 vs. 1.8 %). In this population, cells with the phenotype CCR2+ CX3CR1low were significantly more abundant in tumour-bearing animals than in healthy controls and moreover more abundant in animals, bearing highly malignant 4T1 tumours (0.025 vs. 0.5 vs. 0.75 %).

*=p<0.05; ***=p>0.001

Presence of this specific cell population was different in 67NR as compared to more metastatic 4T1.2 tumour-bearing animals and provided an immunological correlate for the differences in in vivo imaging between the two models. This particular monocyte population, increased in tumour-bearing animals as compared to healthy controls was positive for Gr-1 and CD115 – defining a monocyte before full differentiation. The cells moreover expressed a phenotype including high expression of CCR2 and low positivity for CX3CR1, defining pro-inflammatory monocytes (*121*). Further markers, found in this population included CD62L, CD49d, CD11b and interleukin-4 (IL-4)

receptor. In summary, the marker combination suggested them to be part of or at least associated with the heterogeneous family of MDSCs (*122*).

This Gr-1^{+}CD115^{+}CCR2^{high}CX3CR1^{low}monocyte population was also positive for S100A8/A9 by intracellular FACS staining. Complementary confocal microscopy analysis of frozen spleen sections showed intracellular and extracellular S100A8/A9 in areas surrounding CD115^{+}CCR2^{+} cells.

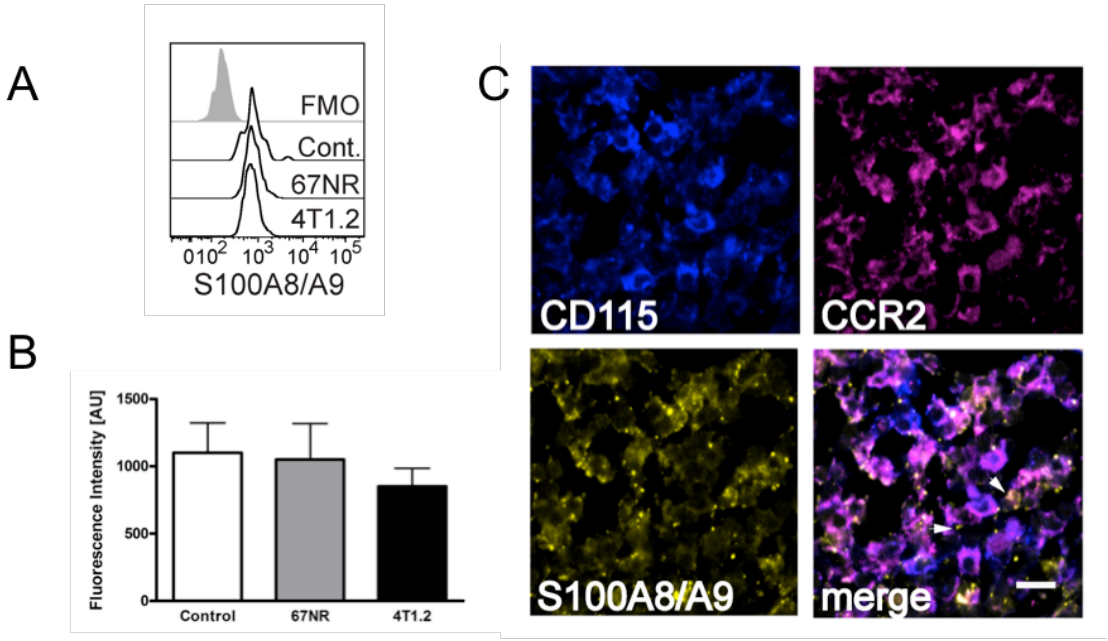

Figure 39: Tumour-induced monocytes are S100A8/A9 positive and release S100A8/A9.

Within the aforementioned Gr-1^{+}CD115^{+}CCR2^{high}CX3CR1^{low} monocyte population, a strong positivity for intracellular S100A8/A9 could be detected (exemplary plot in A; quantification in B for control/67NR/4T1 n=9/15/25). The amount of intracellular S100A8/A9, as reflected by the mean fluorescence intensity, was not significantly different for monocytes from healthy controls or tumour-bearing animals. A slightly lower signal in those cells, isolated from 4T1.2 tumour-bearing animals could reflect a higher S100A8/A9 release in those animals. Confocal microscopy revealed extracellular S100A8/A9 (yellow) in the vicinity of CD11b+CCR2+ cell clusters.

5.3.5 Association of S100A9 imaging and MDSC abundance

The frequency of $Gr1^{+}CD115^{+}CCR2^{high}CX3CR1^{low}$ monocytes in lungs, spleen and tumour tissue correlated with the respective metastatic potential of the underlying model: monocyte levels in tumour tissue as well as the periphery were significantly higher in the highly malignant 4T1.2 tumours as compared to non-metastatic 67NR tumours.

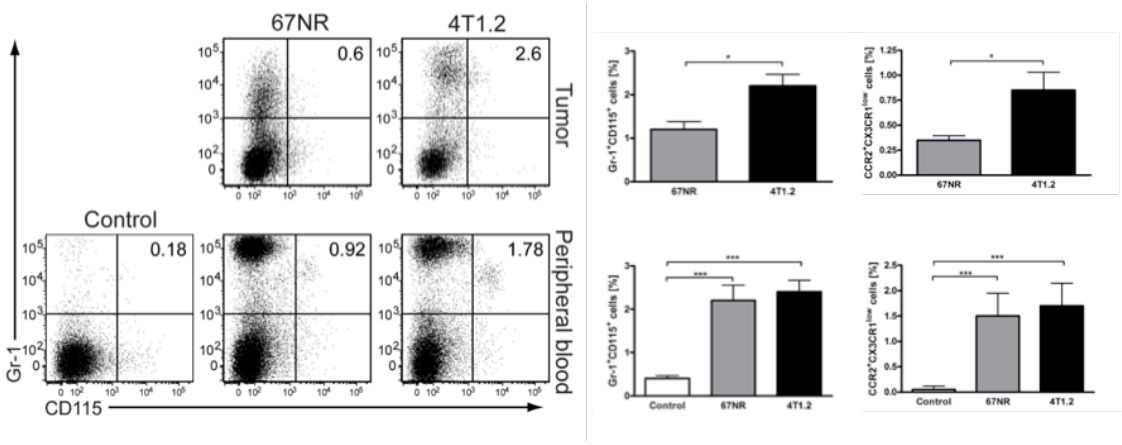

Figure 40: Gr1+CD115+CCR2highCX3CR1low monocytes in tumour tissue and peripheral blood.

FACS analyses of samples from primary tumour tissue as well as peripheral blood reveal $Gr1^{+}CD115^{+}CCR2^{high}CX3CR1^{low}$ monocytes in higher numbers in 4T1.2 tumours (n=18) as compared to 67NR tumours (n=8; =p<0.05), confirming the in vivo imaging results and in the blood of tumour-bearing as compared to healthy control animals (n=9). Although the exemplary FACS plots suggest a strong difference between the two tumour entities, no significant difference between the MDSC abundance in peripheral blood could be detected between 67NR and 4T1.2 in the final, comprehensive analysis (***=p<0.001).

In vivo S100A9-SPECT imaging showed a significantly higher tracer uptake in the lungs of 4T1.2-tumour bearing mice as compared to 67NR-tumour-bearing mice and controls (fig. 34), reflecting the increased MDSC abundance.

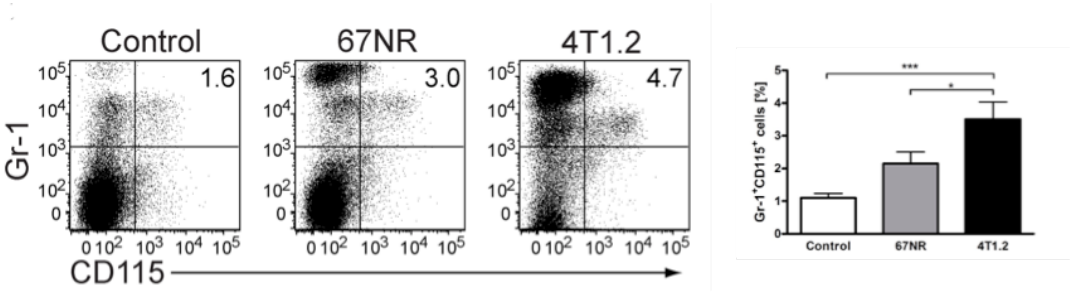

Figure 41: Abundance of Gr1+CD115+CCR2highCX3CR1low monocytes in premetastatic lung tissue

Resembling the analysis of spleen tissue, MDSC can be found in significantly higher amounts in premetastatic lung tissue of tumour bearing animals (67NR: 2.2% of live cells; 4T1.2: 3.5%; n=8/18; $p<0.05$) as compared to the lungs of healthy controls (1.1%; n=9; $p<0.001$). Metastatic 4T1.2 tumours induce a higher infiltration of lungs by MDSC than non-metastatic 67NR.

Confocal microscopy of frozen lung sections revealed intra- and extracellular S100A9 in areas of $CCR2^{+}CD115^{+}$ monocyte accumulation. As compared to tissue samples of healthy controls or 67NR tumour-bearing mice, samples of 4T1.2 tumour-bearing animals exhibited an increased staining for extracellular S100A9, confirming the *in vivo* imaging findings.

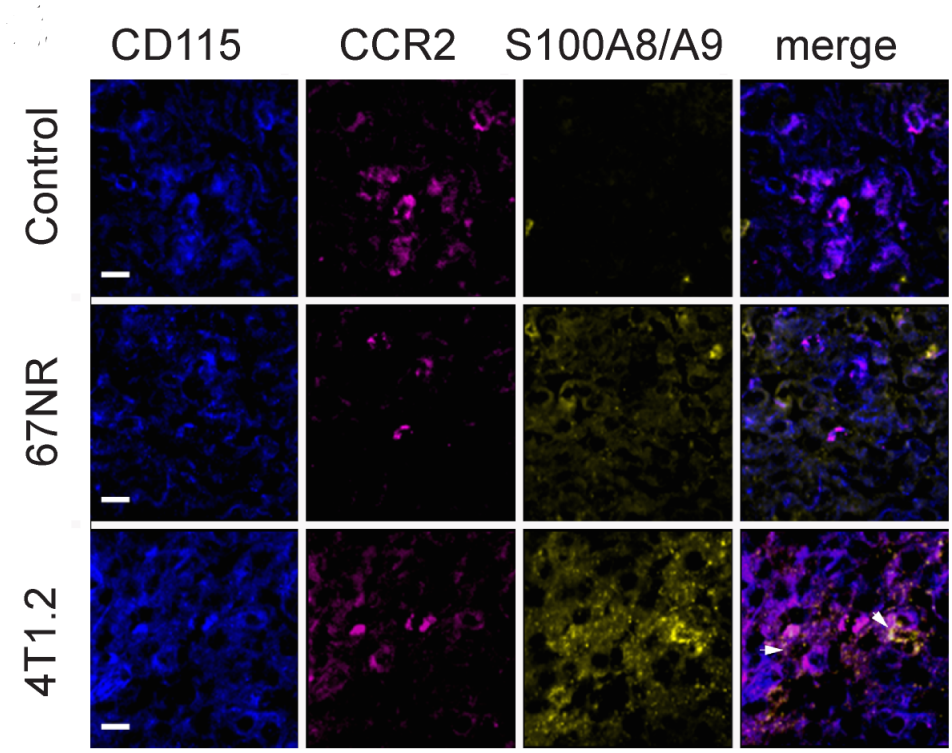

Figure 42: Confocal microscopy of premetastatic lung tissue.

In the lungs of tumour-bearing mice, clusters of CD115+CCR2+ cells could be detected in colocalisation with released S100A8/A9. The abundance of such clusters was higher in highly malignant tumour-bearing animals than in controls, confirming the in vivo SPECT imaging results.

5.3.6 Changes under CCL2 blocking

The CCR2-CCL2 signalling axis has previously been implicated in metastatic breast cancer cell seeding in the lungs (*123*). In response to CCR2-mediated signalling, tumour-associated monocytes accumulate in the primary tumour microenvironment as well as at metastatic sites (*124*). The blockade of CCR2-binding seems to inhibit the initialisation of a premetastic niche (*125*). With established effects on metastatic tumour cell seeding and established blocking procedures to adapt for this study, the CCL2-CCR2 signalling axis was an ideal target to assess S100A9-imaging for visualisation of the effects of therapy and intervention.

Upon in vitro stimulation with recombinant CCL2, monocytes (Gr-1^{+}CD115^{+}CCR2^{high}CX3CR1^{low}), derived from spleens of 4T1 tumour-bearing mice, secreted a significantly higher amount of S100A8/A9 in comparison to cells, derived from 67NR tumour-bearing mice. Matched samples of granulocytes (Gr-1^{+}CR2^{+}CD115^{-}) did not increase secretion of S100A8/A9 in response to CCL2 stimulation.

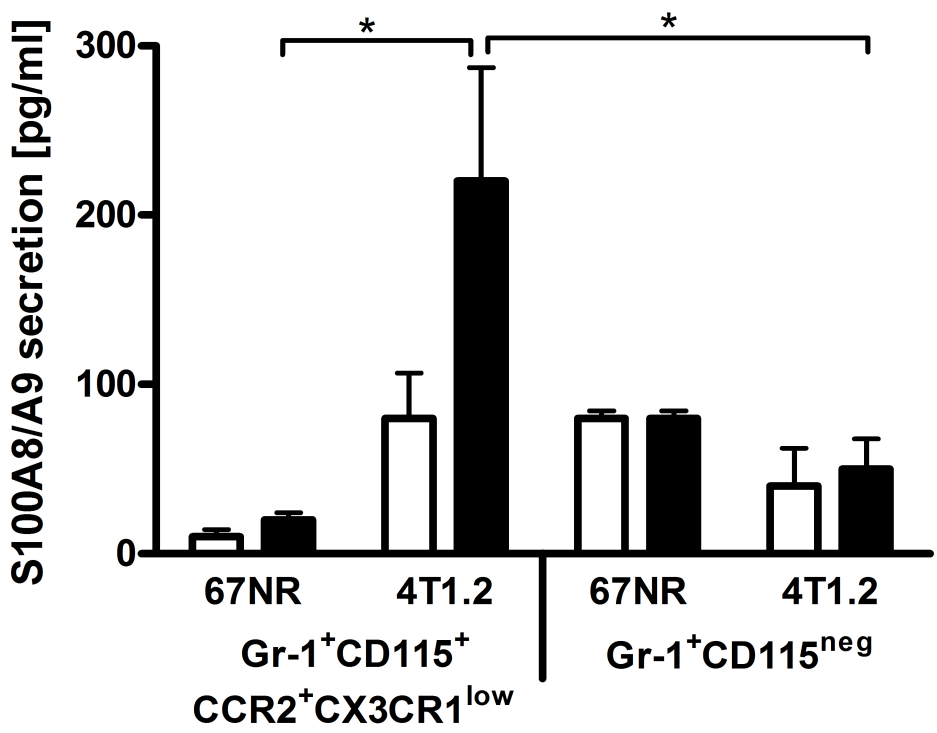

Figure 43: S100A8/A9 release upon CCL2/CCR2 stimulation.

Cells, isolated from either 67NR or 4T1.2 tumour-bearing animals were stimulated with CCL2 (black bars) or examined without further treatment (white bars). The resulting release of S100A8/A9 was determined by ELISA. CCL2-stimulation resulted in strong S100A8/A9 release from Gr-1^{+}CD115^{+}CCR2^{+}CX3CR1^{low} monocytic cells, while no significant increase in the release of S100A8/A9 could be observed from granulocytic (CD115^{-}) cells or MDSC from 67NR animals (*=p<0.05)

It has been shown earlier, that CCL2 acts as a chemo-attractant for MDSC (*126*). In this context, blockade of the CCL2-CCR2 signalling axis should decrease the recruitment of Gr-1^{+}CD115^{+}CCR2^{high}CX3CR1^{low}monocytes to premetastatic lung tissue as well as the SPECT-detectable S100A8/A9 in vivo imaging signal.

CCL2-blocking with blocking antibodies according to established treatment protocols indeed induced a significant reduction of the specific tracer accumulation in spleens and lungs of 4T1.2 tumour-bearing animals as depicted by in vivo SPECT imaging.

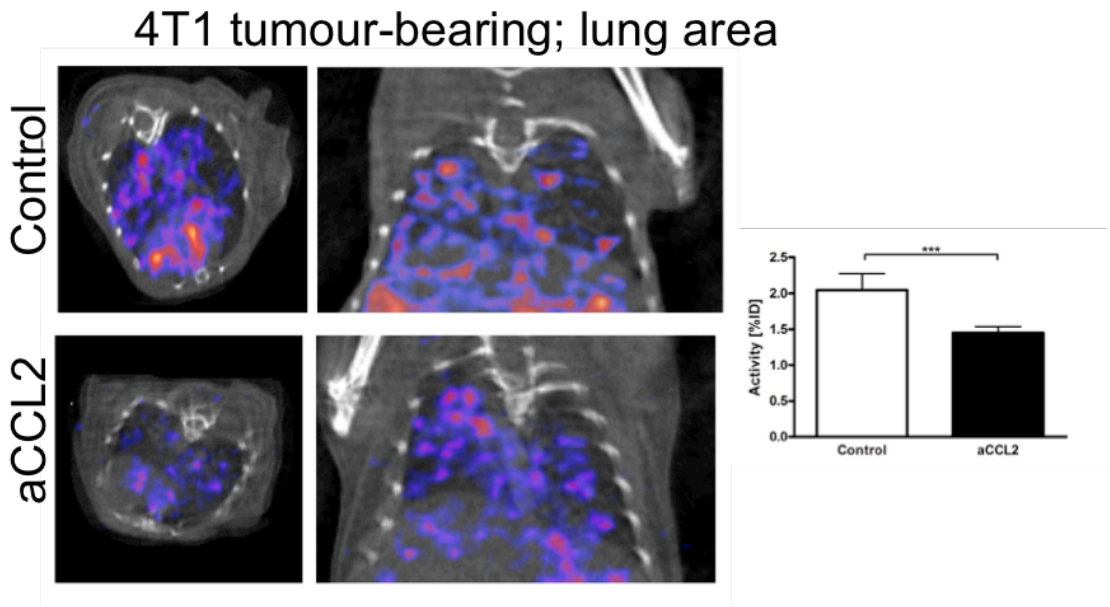

Figure 44: In vivo S100A9 SPECT imaging under CCL2/CCR2 blockade – lung tissue

In the lung tissue of 4T1 tumour-bearing animals, the treatment with aCCL2 (bottom panel; black bar on graph; n=9) significantly reduced S100A8/A9 release, as depicted by specific SPECT, as compared to controls, treated with unspecific IgG (upper panel; white bar on graph; n=6; 2.1 vs. 1.45 %/ID; p< 0.001).

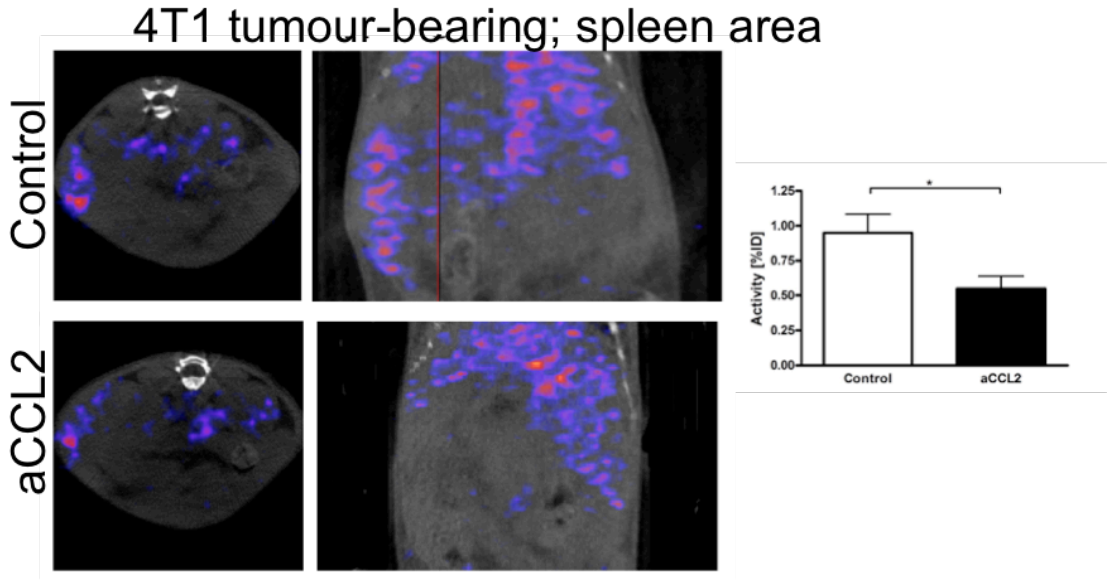

Figure 45: In vivo S100A9 SPECT imaging under CCL2/CCR2 blockade – spleen tissue.

Confirming the in vivo imaging results, presented before, a reduction of S100A8/A9 release under CCL2/CCR2 blockade was also detectable in the spleens of tumour-bearing animals (n=9/6; 0.95 vs. 0.55 %/ID; p<0.05).

The concomitant FACS analyses of tissue samples confirmed the in vivo imaging results and revealed a significant reduction of $Gr1^{+}CD115^{+}CCR2^{high}CX3CR1^{low}$ monocytes as compared to those animals, which received an ineffective control treatment only.

5.3.7 The cellular microenvironment, effects on Treg and NK cells

The increased frequency of Gr-1^{+}CD115^{+}CCR2^{high}CX3CR1^{low}monocytes in the lung tissue of tumour-bearing mice was associated with an increased presence of CD25^{+}Foxp3^{+}Treg cells. Compared to healthy controls, the increase was more pronounced in 4T1.2 tumour-bearing mice, while an only limited effect on the pulmonary Treg population could be observed in 67NR tumour-bearing animals.

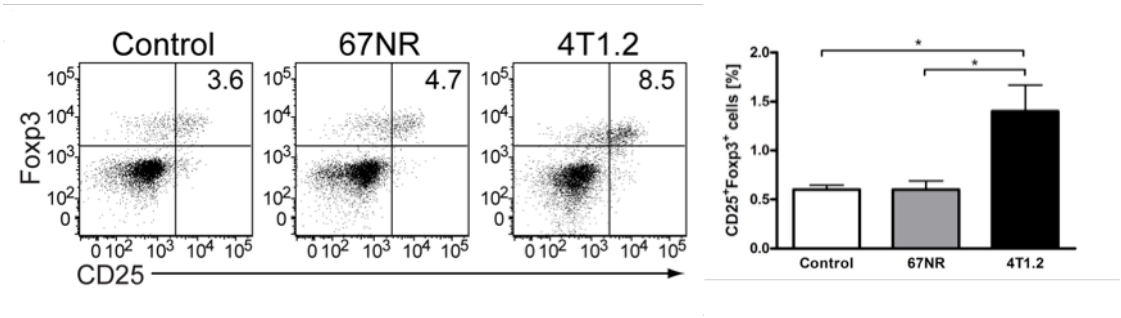

Figure 46: Treg in lung tissue of healthy and tumour-bearing mice.

Exemplary FACS plots for CD25+Foxp3+ cells in lung tissue from healthy control animals (n=9), 67NR (n=8) and 4T1.2 (n=18) tumour-bearing animals reveal a significant, almost two-fold increase in Treg in the lungs of those animals, bearing highly malignant tumours, as compared to controls and low-malignancy tumours (*=p<0.05).

Tregs play a pivotal role in controlling inflammation by inhibiting the proliferation and cytotoxic activity of NK cells (*127, 128*). To assess the activity of NK cells under the influence of MDSC and Treg in the premetastatic microenvironment, the frequency and degranulation of NK cells, isolated from lung tissue of tumour-bearing and healthy control mice, was assessed. Inversely mirroring the increase in immunosuppressive Treg activity in the pre-metastatic lung tissue was a concomitant decrease in the number of NK cells. Although the differentiation state of NK cells was not affected, their activation state, as indicated by staining for CD107 (LAMP1) as a measure for degranulation function (*129*), was significantly impaired in the presence of Treg and Gr-1^{+}CD115^{+}CCR2^{high}CX3CR1^{low}monocytes.

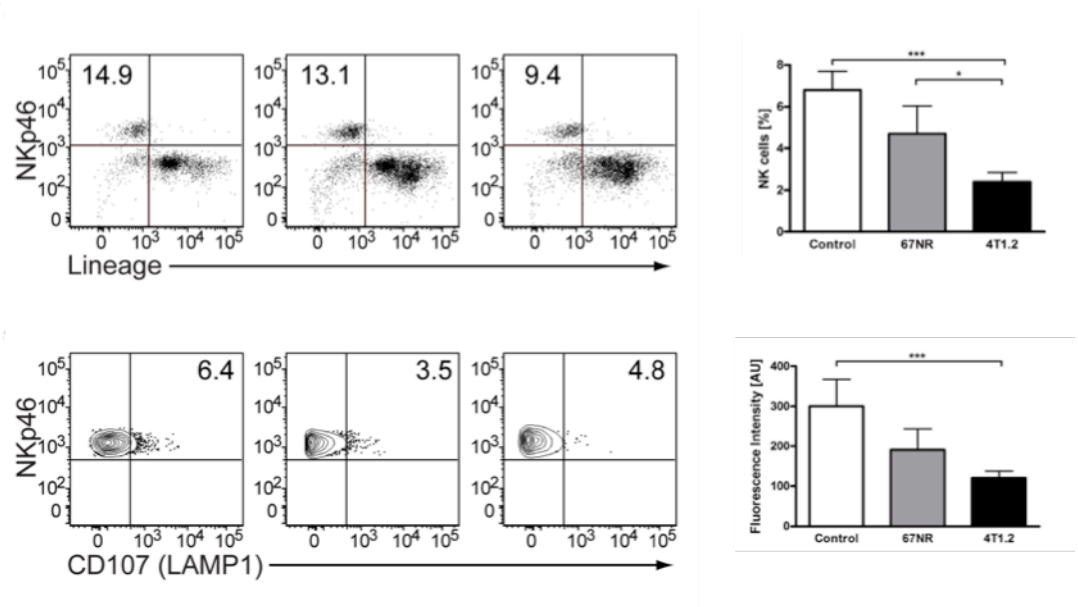

Figure 47: NK cell abundance and function in premetastatic lung tissue

The number of NK cells in the lung tissue of 67NR (n=8) or 4T1 (n=18) tumour-bearing mice was significantly reduced as compared to healthy controls (n=9; upper panel; *=p<0.05; ***=p<0.001). Those cells, present, exhibited a limited function (bottom panel), as reflected by the expression of NK cell activity marker LAMP1.

These results are supported by earlier work from Huang et al and others, showing a direct correlation between the accumulation of monocytes/MDSC in tumour tissue and the consecutive development of a Treg-mediated immunomodulatory environment that impairs potential anti-tumour immune activity (*130*).

5.3.8 Correlation of S100A9 in vivo imaging and metastatic burden

To assess the predictive and prognostic potential of S100A8/A9 imaging, a representative group of mice, bearing 4T1.2 tumours, was followed after initial in vivo imaging at day 10 and re-examined at day 20 after tumour inoculation.

Tissue samples from the lungs were screened for mCherry-positive tumour cells, confirming metastatic spread. FACS sorting of cell suspensions from the tissue samples enabled for quantification of the metastatic deposit.

At the time of in vivo imaging, 10 days after tumour inoculation, screening of tissue samples from 4T1.2 tumour-bearing animals for mCherry-positive tumour cells confirmed the premetastatic state of malignant disease: no tumour cells, representative of a local metastatic deposit, could be detected in any of the samples: the mCherry+ fraction in lung tissue was <0.1% for both, healthy controls and tumour-bearing animals. At the second investigated time point (day 20), mCherry-positive 4T1.2 tumour cells were clearly detectable in equivalent tissue samples (>0.4%; p <0.0001).

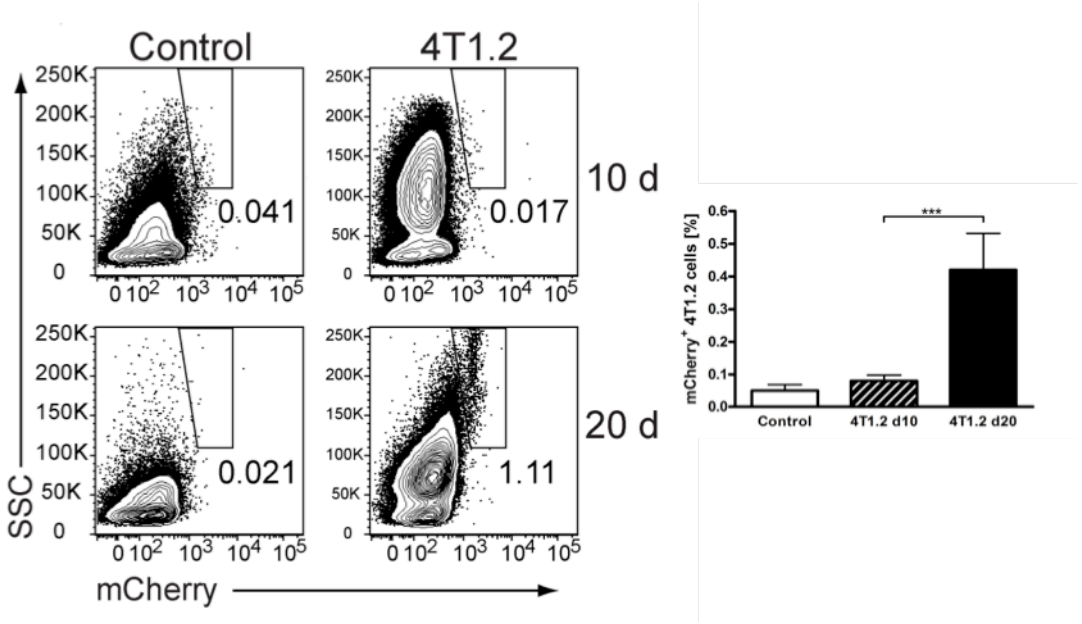

Figure 48: FACS screen for tumour cells in lung tissue.

In the lungs of 4T1 tumour-bearing mice, the FACS screen for mCherry+ tumour cells was negative at day 10 after tumour inoculation (0.08% of live cells; healthy control: 0.05%; n=4), confirming that this time

point represents a premetastatic phase of malignant disease. In contrast, a measurable colonisation of the lungs by tumour cells was evident at day 20 after tumour induction (0.42% of live cells; n=11; p<0.001).

Comparison of the in vivo imaging data from day 10 with the quantitative data on the individual metastatic burden revealed, that increased S100A9-levels, as depicted by SPECT imaging at day 10 after tumour implantation, were indicative of the tumour-mediated immune remodelling and correlated significantly with the consecutive tumour cell seeding into the lung (r^2 = 0.79; p<0.0001).

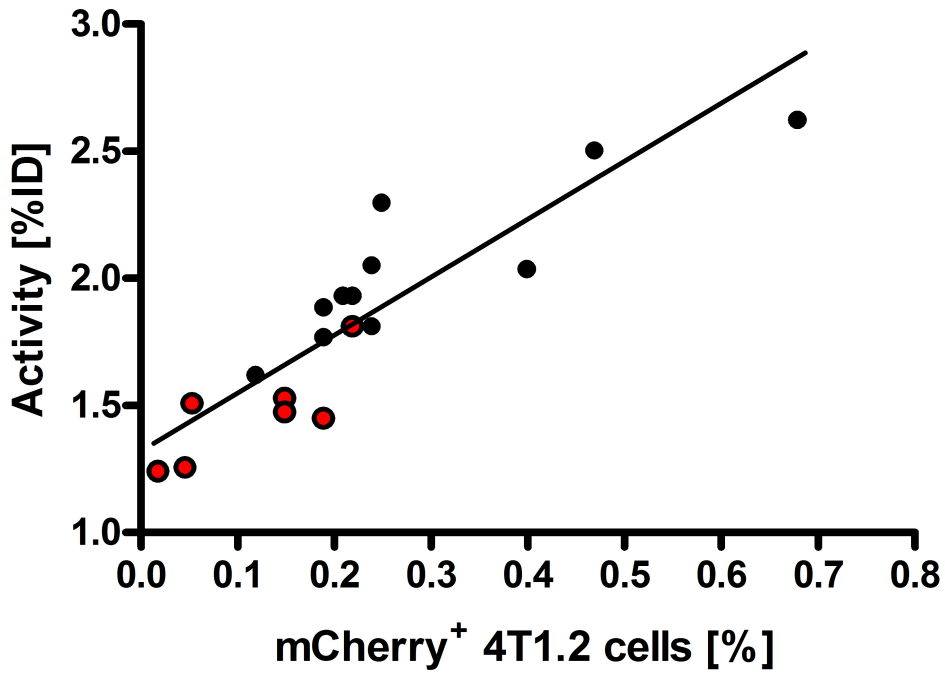

Figure 49: Correlation of S100A9 SPECT and metastatic development.

The aS100A9-driven SPECT , obtained in the premetastatic phase of disease at day 10 after tumour induction, correlated with the consecutive metastatic burden as represented by the number of mCherry+ cells in the lung tissue (n=11; r^2= 0.79; p<0.0001). To increase variation and assess the sensitivity of aS100A9 imaging, seven aCCL2-treated animals (red dots) have been included in the analysis.

Local release and concentration of S100A8/A9, as a marker of premetastatic tissue priming, is indicative of immune cell activity in premetastatic lung tissue that favours and drives colonisation of lung tissue by circulating tumour cells.

5.4 Discussion

5.4.1 Review of Results

A syngeneic, orthotopic model system for metastatic breast cancer has been established, using tumour cell lines with a common genetic background. The two cell lines 4T1.2 and 67NR represent high and low grade breast cancer respectively (*83*). The comparison of data from the two models allows for an estimation of the results that are to be expected in heterogeneous spontaneous disease. Engineering of the cell lines for expression of mCherry allowed for retrospective confirmation of the absence of metastasis/tumour cell deposits in distant tissue at day 10, and estimation of the metastatic burden at day 20 after tumour inoculation (Fig. 49).

Both, 4T1.2 and 67NR tumours, exhibited effects on the immune system of tumour-bearing animals. Splenomegaly and a change in spleen cellularity occurred in both tumour entities, although the effects were significantly more pronounced in 4T1.2 tumour-bearing animals (Fig. 36).

A specific population of monocytes, with the phenotype Gr1+CD115+CCR2highCX3CR1low was distinctly increased in tumour-bearing animals in spleen and lungs at day 10 after tumour inoculation already (Figs. 39, 42). The monocyte was positive for S100A8/A9 and released the heterodimer upon stimulation with CCL2. Release was higher in cells, isolated from 4T1.2 tumour-bearing animals than from 67NR tumour-bearing animals or controls (Figs. 40, 44).

The presence of this particular cell type was associated with an increased presence of Treg (Fig. 47) and a reduced activity of NK cells (Fig. 48), defining an immunosuppressive, tumour-permissive microenvironment.

S100A9-specific SPECT imaging in tumour-bearing animals allowed for visualisation and measurement of S100A9-release in lungs (Fig. 34), spleen and primary tumour. The signal was significantly higher in 4T1.2 tumour-bearing animals than in 67NR tumour-bearing animals or healthy controls (Fig. 32). The S100A9 signal reflected the local MDSC accumulation and correlated with the local abundance of Treg as well as

the activity impairment in NK cells, therefore providing a non-invasive readout of tumour-mediated immune remodelling in distant, premetastatic tissue.

CCL2 blockade inhibited MDSC and consecutive Treg accumulation and hampered establishment of the described immunosuppressive environment. In vivo S100A9 SPECT clearly reflected the effects of CCL2 blockade (Figs. 45, 46).

S100A9 imaging at day 10 after tumour inoculation individually correlated with the metastatic burden in lung tissue at day 20 (Fig. 50).

5.4.2 Project results in the context of the premetastatic niche concept

As pointed out in the introduction already, the idea of tissue priming by the primary tumour, preceding metastasis, is not actually new. New are the insights into the paramount role of tumour-driven immune remodelling to provide growing tumours and metastasis with support and protection in various ways. However, the current models of premetastatic niche establishment are largely based on histological analysis of tissue samples and therefore lack information on temporal development or correlation of initial stages of the metastatic process with the actual outcome.

Means for non-invasive in vivo visualisation of tumour-mediated immune activity were missing so far and therefore, information about the kinetics of premetastatic niche establishment have not been available.

S100A8/A9 as an important marker for immunomodulatory myeloid cells like MDSC has been established as an indicator of premetastatic niche establishment before. In a series of experimental studies, Hiratsuka et al discovered the association of S100A8/A9 with premetastatic tissue priming (*42, 131*). They could demonstrate that S100A8/A9, CCL2 and serum amyloid A 3 (SAA3) were upregulated and increasingly expressed in lung tissue of extra-pulmonary tumour-bearing mice as well as in cancer patient lung tissue samples. Examinations in CCL2 knock out animals led them to the conclusion that S100A8/A9 release was in part mediated by the CCL2-CCR2 axis.

They have moreover shown S100A8/A9 to stimulate SAA3-mediated MDSC recruitment and induction of vascular hyperpemability. The observations, Hiratsuka et al describe, match the finding that CCL2 blockade consecutively reduces tumour-induced S100A8/A9 release in target tissue of metastasis. In return and exceeding the results, presented by Hiratsuka et al, a direct and dynamic effect of CCL2 blockade on initiation of premetastatic niche foci and more importantly the consecutive tumour cell seeding and survival could be demonstrated.

S100A8/A9 exerts immunomodulatory effects also via toll-like receptor 4 (TLR-4), which stimulates MDSC accumulation. In the hypoxic primary tumour environment, MDSC express HIF-1α, promoting the generation of tumour-associated macrophages and driving neoangiogenesis (*132*). In the premetastatic niche, S100A8/A9-driven recruitment of MDSC exerts effects on cytotoxic T cells and NK cells, dampening the anti-tumour immune response that could hamper tumour cell seeding (*41*). Moreover, MDSC express a variety of growth factors that stimulate tumour cell establishment (*105*). Within this study, a possible way to visualise these processes to foster the understanding of premetastatic tissue priming has been demonstrated. Additionally, a specific population of monocytes within the heterogeneous group of MDSC has been characterised in detail. The cells could be confirmed as a source of S100A8/A9 in tumour-primed tissue. The local presence of this cell type could be correlated with the establishment of the premetastaic niche in the form of impaired immune function and expression of bookmarking proteins.

An association between premetastatic niche establishment – as reflected by S100A8/A9 imaging – and the colonisation of primed tissue by circulating tumour cells could be demonstrated.

The established in vivo imaging allowed for determination of local S100A8/A9 release in vivo without disturbing the premetastatic system and thus enabled assessment of the prognostic potential of S100A8/A9 for the development of metastasis.

5.4.3 Potential impact for imaging research, alternative targets/methodology

The crosstalk between tumour and immune cells has been recognised to be of major importance for tumour spread and development. Current assessment of tumour-mediated immune cell regulation is based on the quantification of different cell subsets in biopsies or surgical excisions (*133*). Diagnostic markers that allow for non-invasive, continuous monitoring of tumour-mediated inflammation and tumour-immune cell crosstalk are elusive. This precludes optimisation of and selection for cancer immunotherapy (*4*) and moreover hampers further understanding of the temporal correlation between different immune-mediated cellular events, preceding the establishment of metastasis.

This study provides the first evidence that S100A8/A9 can be used as a non-invasive imaging marker for the establishment of a tumour-permissive, immunosuppressive environment in target organs of metastasis. S100A8/A9 release was evident and detectable at an early stage of the metastatic process, before tumour cells seeded in the lungs of 4T1.2 tumour-bearing mice. Examining this premetastatic niche environment, we found an increased number of Treg along with an increase of MDSC-like cells in correlation with the in vivo imaging data. Our results are supported by studies, showing that MDSCs mediate the development of tumour-induced $Foxp3^+$ Treg (*130*), which are required for the establishment of metastasis (*134*). One well-characterised function of MDSCs is their ability to induce anergy and suppress the proliferation of effector T cells, either directly or indirectly through the induction of Tregs. The combined action of these two cell types could explain our observation of a decrease in number and activity of NK cells (*135*).

We found a $Gr1^+CD115^+CCR2^{high}CX3CR1^{low}$ monocyte population as a local source of S100A8/A9 under regulation of the CCL2-CCR2 pathway.

It has been shown that CCL2 is highly expressed in various murine breast cancer models including 4T1 and 67NR (*136*) as well as the tumour-associated stroma. Lim et al summarise in their recent review (*137*) the extensive research on the role of CCL2-CCR2 signalling in breast cancer development and spread. CCL2 directly stimulates tumour cell mobility and acts as a potent chemoattractant for MDSC (*138*) and TAM (*139*). Under the influence of CCL2, CCR2+ monocytes were driven to aid tumour cell extravasation (*123*). The blockade of CCL2-CCR2 signalling exerted effects on both, the primary tumour and metastasis, reducing tumour growth (*140*) and the abundance of distant metastasis (*136*). In contrast to the experimental research results and consecutive expectations, reproduction of the effect of CCL2-CCR2 blockade in initial clinical trials failed (*137*). For my study however, the results presented are in perfect agreement with prior work on the role of CCL2-CCR2 signalling in murine breast cancer with the dual effect of CCL2-CCR2 blockade on the tumour cell as well as associated immune cells as a potential explanation for the drastic effect on metastatic spread.

Our data suggest a correlation between malignant potential of the tumour (the more metastatic 4T1.2 vs the non-metastatic variant 67NR), abundance of the aforementioned $Gr1^{+}CD115^{+}CCR2^{high}CX3CR1^{low}$ monocyte population in pre-metastatic lungs and spleen, as well as the levels of released, SPECT-detectable S100A8/A9 in these organs.

The relevance of S100A8/A9 in malignant disease has also been highlighted by studies of Cheng et al, who have shown that S100-deficient animals present a reduced generation of Gr-1+CD11b+ MDSCs, resulting in a decreased growth of lymphomas and sarcomas (*37*). The important role for S100A8/A9 in priming organs such as the brain and lung for metastatic predisposition has been demonstrated in murine breast cancer models (*41, 141*). In addition, clinical studies of patients with high grade and invasive breast tumours have shown that S100A8/A9 can serve as marker of poor prognosis (*100, 142*). Despite the lack of a signal peptide sequence,

S100A8/A9 is actively delivered to the tumour microenvironment and distant tissues via exosomes that are secreted by tumour-associated immune cells such as MDSC (*43*). Upon release, S100A8/A9 promotes the accumulation of MDSC (*40*), thereby orchestrating an immunosuppressive microenvironment in premetastatic tissue, optimal for tumour cell deposition and growth (*41, 42*). In agreement with these previous studies, we demonstrated by in vivo SPECT imaging, supplemented by FACS analyses and histology, increased S100A8/A9 levels in pre-metastatic lung tissue, and a concomitant accumulation of MDSC-like pro-inflammatory monocytes, followed by an infiltration of the lung by circulating tumour cells. Taken together, the S100A9 specific imaging proved indicative of tumour-mediated immune cell activity in premetastatic tissue and correlated with the subsequent metastatic tumour burden at an individual animal level. Further studies will be necessary to assess which factors influence the S100A8/A9 expression in premetastatic tissue, and moreover assess additional effects on the local immune infiltrate and tumour cell seeding and growth in the premetastatic niche. So far, S100A8/A9 imaging can only serve as an indicator of tumour-induced inflammation, coincident with systemic tumour spread. It will be future work to establish the immediate link and test S100A8/A9 as a predictive marker for systemic tumour spread.

Previously, markers Gr-1, CD11b and CD115 have been used to identify tumour-induced MDSCs (*123, 143*). We have further specified this phenotype. The use of additional markers CCR2 and CX3CR1 allowed us to define a specific MDSC-like monocyte population, induced in our tumour model and to give a hint towards possible regulation. The cell type we found increased in accordance with the malignant potential of induced tumours shares surface markers of active, pro-inflammatory monocytes, but lacks markers for mature macrophages. In fact, we find the ratio of immature to mature cells of monocytic origin shifted towards immature phenotypes – in line with reports that tumours promote an arrest of certain cell types in immature stages (*144*), including MDSC.

In addition to S100 proteins (including family members 1, 2 4, 7, 8, 9, and 11), chemokines and chemokine receptors are among the soluble factors that contribute to lung metastasis in cancer. Hiratsuka et al., have recently shown that primary tumours are able to induce changes in vascular permeability, preparing homing sites for circulating, metastatic tumour cells (*131*). The CCL2-CCR2 axis seems to be crucial in this process. CCL2, secreted by tumour-associated fibroblasts induces the attraction of monocytes and monocyte-like cells, the mobilisation of bone marrow-derived myeloid cells (*123, 131*) and tumour-associated fibroblasts (*126, 145*). We show that Gr-1^{+}CD115^{+}CCR2^{high}CX3CR1^{low} monocytes secrete S100A8/A9 upon stimulation with recombinant CCL2, highlighting another potential pro-metastatic function of CCL2. There are probably other producer cells for S100A8/A9 in the tumour microenvironment but we have previously excluded tumour cells as the source, by analysis of cell lysates and tissue culture supernatants, and by FACS which showed virtually all S100A9^{+} cells found in the 4T1.2 model, to be CD11b$^{+(80)}$. Metastatic breast cancer is known to secrete CCL2 (*146*), which can stimulate MDSC-like pro-inflammatory monocytes and trigger S100A8/A9 release. This would establish a positive cooperativity between S100A8/A9 and the CCL2-CCR2 pathway. Exosomal S100A8/A9, released upon CCL2 stimulation in the primary tumour, can be delivered systemically to the pre-metastatic lung endothelium, and potentially stimulate the paracrine production of mediators such as serum amyloid A 3 (SAA3), attracting further CD11b^{+} myeloid cells to the lung niche (*42*). The effects of *in vivo* blocking of CCL2 activity highlighted the importance of this positive cooperativity in our model. Treatment with CCL2 blocking antibodies resulted in reduced S100A8/A9 expression and a significantly decreased number of pro-inflammatory monocytes in both spleen and lungs of 4T1.2-tumour bearing mice. Clinically, blocking antibodies to CCL2 such as Carlumab (Johnson & Johnson, New Brunswick, NJ, USA), are now being tested in clinical trials; treatment was well tolerated and preliminary anti-tumour activity of this approach in advanced cancer patients could be observed (*147, 148*).

The way of delivery of S100A8/A9 to the premetastatic niche is still to be determined. Analyses of the content of exosomes from tumour patients show S100A8/A9 as one of the major components, present in much higher concentrations than in exosomes from healthy controls (*43, 149*). Integrating these findings, it is reasonable to believe that, together with other biologically active proteins and DNA/RNA fragments, S100A8/A9 is systemically distributed from the primary tumour environment to potential sites of metastasis encased in exosomes. It will be future work to evaluate this hypothesis and assess the role of exosomes in mediating tumour-associated inflammation and tumour-induced immune cell activity in premetastatic tissue.

The use of S100A8/A9 as a clinical marker for cancer immune modulation and translation of a specific imaging approach will depend in part on further development of the tracer. Since the S100A8/A9 molecular target is extracellular, full-length antibodies are expected to have good access to it. Nevertheless, full-length antibodies are only slowly eliminated from the blood pool, leading to a long period between tracer application and imaging with reasonable contrast to unspecific background signal requiring isotopes with a long half-life. Smaller targeting compounds – either antibody fragments or non-peptidic small molecules should in this context be evaluated. A small molecule, binding S100A8/A9, would potentially exhibit a more rapid clearance from the blood pool and faster accumulation in the target tissue, hence enabling for the use of short-lived isotopes for clinical PET imaging. As an example, the small molecule Tasquinimod (MW 406 g/Mol), binding S100A8/A9 and inducing a conformational change of the heterodimer, is almost completely eliminated from plasma as well as liver and kidneys within 24 hours after application (*150*). Labelling of such compounds for other imaging modalities for clinical or preclinical use would also be conceivable. Moreover, a correlation with conventional tumour grading and serum markers for tumour development would foster the clinical use of S100A8/A9 as a marker for patient stratification and a prognostic potential as indicated by our results.

For cancer therapy, experimental cancer research and drug development, an opportunity to follow immune cell activity in a specific way over time will have a significant impact. For instance, despite the success and exciting potential of new therapeutic agents, such as monoclonal anti-PD1 or anti-CTLA-4 blocking-antibodies (*4*), response varies greatly (*92*) and non-invasive tools for monitoring of the conditioning of micrometastatic niches are needed to further optimise therapy and to sustain survival benefits in patients. As a paradigm for such future work, we suggest S100A8/A9 *in vivo* imaging as a first approach to non-invasively address tumour immune crosstalk. Clinical establishment of this technique could fundamentally change how patients are selected for and monitored during therapy.

6 Conclusion

S100A8/A9 has been described as a marker for immune cell activity in inflammation and cancer and a crucial player in tumour-mediated immune remodelling. Using S100A8/A9 release in vivo as readout for tumour-driven recruitment of immune cells, the activity of directly tumour-associated immune cells as well as the processes in premetastatic tissue can be observed. As S100A8/A9 is a mediator of MDSC-driven immunosuppression, it can also serve as an indicator for the consecutive immune modulation, effecting T- and NK cells. By establishing S100A9 imaging in the primary tumour microenvironment using OI and systemically, using SPECT, a first method for continuous monitoring of tumour-mediated immune cell activity is suggested.

The objectives of this study, as formulated in the introductory chapter, were

1. **To establish S100A8/A9 as a marker for local tumour immune interaction**

   It could be shown that the local concentration of S100A8/A9 closely reflects the local abundance of immunomodulatory monocyte derivatives including MDSC in e.g. the primary tumour microenvironment. The potential of a tumour

lesion to attract and activate immunomodulatory monocytes (67NR vs. 4T1: 1.2% vs. 8.7% activated monocytes) was coincident with the cell line specific malignant potential and was reflected by S100A9-specific OI (67NR vs. 4T1: 250.8 vs. 427.3 AU; $p<0.05$). The individual S100A9 imaging signal as an indicator of local immune cell activity correlated with the individual tumour development ($r2=0.86$; $p<0.0001$).

2. To develop a S100A9-specific radiotracer

A radiotracer for labelling with ^{111}In has been produced from the established fluorescent optical tracer version, described earlier (*79, 82*). The tracer has been tested for stability under physiological conditions in vitro and in vivo performance in a murine model of inflammation before application in models of malignant disease (inflammatory focus: ^{111}In-aS100A9 vs. ^{111}In-rabIgG: 3.9 vs. 1.1 %/ID; $p<0.001$; healthy control: 0.76 vs. 0.89 %/ID; not significant).

3. To establish systemic S100A9-specific in vivo imaging in cancer

^{111}In-aS100A9 has been successfully used for visualisation of systemic S100A8/A9 release in tumour-bearing animals. The tracer distribution was reflective of disease-related alteration of immune cell variety and activity in tumour, lungs and spleen of tumour-bearing animals (see chapter 5 for details on the malignant microenvironment). S100A9-specific SPECT imaging proved indicative of the establishment of an immunosuppressive microenvironment in premetastatic lung tissue (healthy lung vs. 67NR vs. 4T1.2: 0.49 vs. 0.55 vs. 0.95 %/ID; $p< 0.05$), constituted by an increased accumulation of MDSC (1.1% vs. 2.2% vs. 3.5% of live cells) and Treg (0.6% vs. 0.6% vs. 1.4%) and a reduction in number and activity of anti-tumour NK cells (6.8% vs. 4.7% vs. 2.4%; activity: 300 vs. 190 vs. 120 MFI for CD107 staining).

4. **Understanding pre-metastatic niche establishment**

   The precise system of regulatory mechanisms behind premetastatic tissue priming and the major regulators of premetastatic niche establishment are still widely unknown. Within this study however, we could ascertain that the CCL2/CCR2 signalling axis is one of potentially several regulatory pathways that can be addressed for interference with tumour-associated immune activity and tissue priming and that S100A9 imaging allows for visualisation of the effects of this intervention (CCL2 blockade vs. untreated control: 1.45 vs. 2.1 %/ID; $p< 0.05$). With S100A9-imaging being indicative of metastatic development on the basis of premetastatic niche establishment (correlation S100A9 signal vs. metastatic burden: $r2=0.79$ $p<0.0001$), this method holds the potential for future evaluation of regulators of tumour spread.

The imaging methodology, established within this project, will enable studying of further mediators and regulators of tumour-immune interaction and tumour-mediated tissue priming. S100A8/A9 is a potent marker for monocyte activity and in this context the activity and abundance of major effectors of tumour-associated inflammation (e.g. MDSC) and can serve as readout for intervention and knock-out studies.

So far, we have assessed 100A9-specific imaging for visualisation of tumour-associated inflammation in primary tumour lesions and tumour-induced immune cell activity in distant tissue. The individual, local S100A9 imaging signal allowed for estimation of tumour growth and metastatic development in a selected, syngeneic model of metastatic breast cancer in mice. Although this model – due to the syngeneic character and performance in wild type animals – is considered better suited to represent the situation in humans than for example tumour models that require immunocompromised animals, further studies will be required to foster S100A9 imaging as a potentially translatable biomarker for the human system. One aspect that needs further clarification in this context is the role of specific immune cell

populations and whether or not these roles are comparable between mice and humans: While in mice the granulocytic MDSC dominates the tumour microenvironment, the monocytic MDSC is more abundant in humans. Whether this fact has an influence on the induction and maintenance of an immunosuppressive, tumour-permissive environment needs to be addressed.

We could show that the S100A9 imaging signal reflects changes of the immunosuppressive microenvironment, constituted by blockade of the CCL2/CCR2 signalling cascade. Future work will haver to cover other important signalling routes that have already been explored for therapy but not diagnostic purposes. It needs to be answered whether S100A8/A9 in tumour tissue and/or the target tissue of metastasis is suited as a marker for immunomodulatory therapy on a broad basis. Moreover, different stages of therapy response need to be assessed separately to control for adverse effects on the S100A8/A9 expression by, for example, inflammatory cells, reacting to increased cell death in the successfully treated tumour.
On the cellular level, consecutive studies will examine whether blockade of signalling cascades that promote the establishment of the premetastatic niche also inhibit tumour cell shedding from the primary tumour and whether or not the phenotype of monocytic and T cells recovers under therapy.
S100A9 imaging can play a pivotal role in research on metastatic tumour growth and provide an important tool for future studies: In searching for the mediators and communication pathways between the tumour and the target tissue of metastasis, S100A9 imaging can provide a read out for biological effects on tumour-associated immune cells. In consecutive studies, potential means of tumour-tissue communication can be assessed for their effect on S100A8/A9 release as depicted by target-specific imaging.

The importance of premetastatic tissue priming and the potential of S100A8/A9-imaging as a diagnostic tool are underlined by the observation that processes, preceding metastasis (immune cell infiltration and activation in lung tissue) predict the consecutive extent of disease. In patients, a comparable tool would enable for identification of patients, prone for metastatic development and therefore in need of closer monitoring and specific therapy.

7 References

1. T. W. H. Organization, The World Health Report 2004: changing history. Statistical Annex (2004).
2. R. Lozano, M. Naghavi, K. Foreman, S. Lim, K. Shibuya, V. Aboyans, J. Abraham, T. Adair, R. Aggarwal, S. Y. Ahn, M. Alvarado, H. R. Anderson, L. M. Anderson, K. G. Andrews, C. Atkinson, L. M. Baddour, S. Barker-Collo, D. H. Bartels, M. L. Bell, E. J. Benjamin, D. Bennett, K. Bhalla, B. Bikbov, A. Bin Abdulhak, G. Birbeck, F. Blyth, I. Bolliger, S. Boufous, C. Bucello, M. Burch, P. Burney, J. Carapetis, H. Chen, D. Chou, S. S. Chugh, L. E. Coffeng, S. D. Colan, S. Colquhoun, K. E. Colson, J. Condon, M. D. Connor, L. T. Cooper, M. Corriere, M. Cortinovis, K. C. de Vaccaro, W. Couser, B. C. Cowie, M. H. Criqui, M. Cross, K. C. Dabhadkar, N. Dahodwala, D. De Leo, L. Degenhardt, A. Delossantos, J. Denenberg, D. C. Des Jarlais, S. D. Dharmaratne, E. R. Dorsey, T. Driscoll, H. Duber, B. Ebel, P. J. Erwin, P. Espindola, M. Ezzati, V. Feigin, A. D. Flaxman, M. H. Forouzanfar, F. G. Fowkes, R. Franklin, M. Fransen, M. K. Freeman, S. E. Gabriel, E. Gakidou, F. Gaspari, R. F. Gillum, D. Gonzalez-Medina, Y. A. Halasa, D. Haring, J. E. Harrison, R. Havmoeller, R. J. Hay, B. Hoen, P. J. Hotez, D. Hoy, K. H. Jacobsen, S. L. James, R. Jasrasaria, S. Jayaraman, N. Johns, G. Karthikeyan, N. Kassebaum, A. Keren, J. P. Khoo, L. M. Knowlton, O. Kobusingye, A. Koranteng, R. Krishnamurthi, M. Lipnick, S. E. Lipshultz, S. L. Ohno, J. Mabweijano, M. F. MacIntyre, L. Mallinger, L. March, G. B. Marks, R. Marks, A. Matsumori, R. Matzopoulos, B. M. Mayosi, J. H. McAnulty, M. M. McDermott, J. McGrath, G. A. Mensah, T. R. Merriman, C. Michaud, M. Miller, T. R. Miller, C. Mock, A. O. Mocumbi, A. A. Mokdad, A. Moran, K. Mulholland, M. N. Nair, L. Naldi, K. M. Narayan, K. Nasseri, P. Norman, M. O'Donnell, S. B. Omer, K. Ortblad, R. Osborne, D. Ozgediz, B. Pahari, J. D. Pandian, A. P. Rivero, R. P. Padilla, F. Perez-Ruiz, N. Perico, D. Phillips, K. Pierce, C. A. Pope, 3rd, E. Porrini, F. Pourmalek, M. Raju, D. Ranganathan, J. T. Rehm, D. B. Rein, G. Remuzzi, F. P. Rivara, T. Roberts, F. R. De Leon, L. C. Rosenfeld, L. Rushton, R. L. Sacco, J. A. Salomon, U. Sampson, E. Sanman, D. C. Schwebel, M. Segui-Gomez, D. S. Shepard, D. Singh, J. Singleton, K. Sliwa, E. Smith, A. Steer, J. A. Taylor, B. Thomas, I. M. Tleyjeh, J. A. Towbin, T. Truelsen, E. A. Undurraga, N. Venketasubramanian, L. Vijayakumar, T. Vos, G. R. Wagner, M. Wang, W. Wang, K. Watt, M. A. Weinstock, R. Weintraub, J. D. Wilkinson, A. D. Woolf, S. Wulf, P. H. Yeh, P. Yip, A. Zabetian, Z. J. Zheng, A. D. Lopez, C. J. Murray, M. A. AlMazroa, Z. A. Memish, Global and regional mortality from 235 causes of death for 20 age groups in 1990 and 2010: a systematic analysis for the Global Burden of Disease Study 2010. *Lancet* **380**, 2095-2128 (2012).
3. SEER Program (National Cancer Institute (U.S.)), National Center for Health Statistics (U.S.), National Cancer Institute (U.S.). Surveillance Program., National Cancer Institute (U.S.). Cancer Statistics Branch., National Cancer Institute (U.S.). Cancer Control Research Program., in *NIH publication*. (U.S. Dept. of Health and Human Services, Public Health Service, National Institutes of Health, National Cancer Institute, Bethesda, Md., 2010), pp. v.
4. J. Couzin-Frankel, Breakthrough of the year 2013. Cancer immunotherapy. *Science* **342**, 1432-1433 (2013).

5. R. J. Prestwich, F. Errington, P. Hatfield, A. E. Merrick, E. J. Ilett, P. J. Selby, A. A. Melcher, The immune system--is it relevant to cancer development, progression and treatment? *Clin Oncol (R Coll Radiol)* **20**, 101-112 (2008).
6. G. P. Dunn, A. T. Bruce, H. Ikeda, L. J. Old, R. D. Schreiber, Cancer immunoediting: from immunosurveillance to tumor escape. *Nat Immunol* **3**, 991-998 (2002).
7. L. Zitvogel, A. Tesniere, G. Kroemer, Cancer despite immunosurveillance: immunoselection and immunosubversion. *Nat Rev Immunol* **6**, 715-727 (2006).
8. J. Folkman, Role of angiogenesis in tumor growth and metastasis. *Semin Oncol* **29**, 15-18 (2002).
9. A. Mantovani, T. Schioppa, C. Porta, P. Allavena, A. Sica, Role of tumor-associated macrophages in tumor progression and invasion. *Cancer Metastasis Rev* **25**, 315-322 (2006).
10. E. Y. Lin, J. W. Pollard, Tumor-associated macrophages press the angiogenic switch in breast cancer. *Cancer Res* **67**, 5064-5066 (2007).
11. F. Balkwill, A. Mantovani, Inflammation and cancer: back to Virchow? *Lancet* **357**, 539-545 (2001).
12. G. Solinas, F. Marchesi, C. Garlanda, A. Mantovani, P. Allavena, Inflammation-mediated promotion of invasion and metastasis. *Cancer Metastasis Rev* **29**, 243-248 (2010).
13. D. Hanahan, R. A. Weinberg, Hallmarks of cancer: the next generation. *Cell* **144**, 646-674 (2011).
14. A. Sica, A. Mantovani, Macrophage plasticity and polarization: in vivo veritas. *J Clin Invest* **122**, 787-795 (2012).
15. B. Z. Qian, J. W. Pollard, Macrophage diversity enhances tumor progression and metastasis. *Cell* **141**, 39-51 (2010).
16. F. Marchesi, M. Cirillo, A. Bianchi, M. Gately, O. M. Olimpieri, E. Cerchiara, D. Renzi, A. Micera, B. O. Balzamino, S. Bonini, A. Onetti Muda, G. Avvisati, High density of CD68+/CD163+ tumour-associated macrophages (M2-TAM) at diagnosis is significantly correlated to unfavorable prognostic factors and to poor clinical outcomes in patients with diffuse large B-cell lymphoma. *Hematol Oncol* **33**, 110-112 (2015).
17. L. Xu, Y. Zhu, L. Chen, H. An, W. Zhang, G. Wang, Z. Lin, J. Xu, Prognostic value of diametrically polarized tumor-associated macrophages in renal cell carcinoma. *Ann Surg Oncol* **21**, 3142-3150 (2014).
18. X. Zhan, L. Jia, Y. Niu, H. Qi, X. Chen, Q. Zhang, J. Zhang, Y. Wang, L. Dong, C. Wang, Targeted depletion of tumour-associated macrophages by an alendronate-glucomannan conjugate for cancer immunotherapy. *Biomaterials* **35**, 10046-10057 (2014).
19. R. Roychoudhuri, R. L. Eil, N. P. Restifo, The interplay of effector and regulatory T cells in cancer. *Curr Opin Immunol* **33**, 101-111 (2015).
20. J. A. Joyce, D. T. Fearon, T cell exclusion, immune privilege, and the tumor microenvironment. *Science* **348**, 74-80 (2015).
21. F. Zhao, B. Hoechst, A. Duffy, J. Gamrekelashvili, S. Fioravanti, M. P. Manns, T. F. Greten, F. Korangy, S100A9 a new marker for monocytic human myeloid-derived suppressor cells. *Immunology* **136**, 176-183 (2012).
22. S. Ostrand-Rosenberg, P. Sinha, Myeloid-derived suppressor cells: linking inflammation and cancer. *J Immunol* **182**, 4499-4506 (2009).

23. S. Paget, The distribution of secondary growths in cancer of the breast. 1889. *Cancer Metastasis Rev* **8**, 98-101 (1989).
24. J. E. Talmadge, I. J. Fidler, AACR centennial series: the biology of cancer metastasis: historical perspective. *Cancer Res* **70**, 5649-5669 (2010).
25. R. N. Kaplan, S. Rafii, D. Lyden, Preparing the "soil": the premetastatic niche. *Cancer Res* **66**, 11089-11093 (2006).
26. B. Psaila, D. Lyden, The metastatic niche: adapting the foreign soil. *Nat Rev Cancer* **9**, 285-293 (2009).
27. R. N. Kaplan, R. D. Riba, S. Zacharoulis, A. H. Bramley, L. Vincent, C. Costa, D. D. MacDonald, D. K. Jin, K. Shido, S. A. Kerns, Z. Zhu, D. Hicklin, Y. Wu, J. L. Port, N. Altorki, E. R. Port, D. Ruggero, S. V. Shmelkov, K. K. Jensen, S. Rafii, D. Lyden, VEGFR1-positive haematopoietic bone marrow progenitors initiate the pre-metastatic niche. *Nature* **438**, 820-827 (2005).
28. A. A. Keskinov, M. R. Shurin, Myeloid regulatory cells in tumor spreading and metastasis. *Immunobiology* **220**, 236-242 (2015).
29. S. Ran, The Role of TLR4 in Chemotherapy-Driven Metastasis. *Cancer Res* **75**, 2405-2410 (2015).
30. D. I. Gabrilovich, S. Nagaraj, Myeloid-derived suppressor cells as regulators of the immune system. *Nat Rev Immunol* **9**, 162-174 (2009).
31. P. Serafini, I. Borrello, V. Bronte, Myeloid suppressor cells in cancer: recruitment, phenotype, properties, and mechanisms of immune suppression. *Semin Cancer Biol* **16**, 53-65 (2006).
32. J. I. Youn, S. Nagaraj, M. Collazo, D. I. Gabrilovich, Subsets of myeloid-derived suppressor cells in tumor-bearing mice. *J Immunol* **181**, 5791-5802 (2008).
33. D. I. Gabrilovich, S. Ostrand-Rosenberg, V. Bronte, Coordinated regulation of myeloid cells by tumours. *Nat Rev Immunol* **12**, 253-268 (2012).
34. S. Nagaraj, K. Gupta, V. Pisarev, L. Kinarsky, S. Sherman, L. Kang, D. L. Herber, J. Schneck, D. I. Gabrilovich, Altered recognition of antigen is a mechanism of CD8+ T cell tolerance in cancer. *Nat Med* **13**, 828-835 (2007).
35. S. Nagaraj, A. G. Schrum, H. I. Cho, E. Celis, D. I. Gabrilovich, Mechanism of T cell tolerance induced by myeloid-derived suppressor cells. *J Immunol* **184**, 3106-3116 (2010).
36. S. Kusmartsev, D. I. Gabrilovich, STAT1 signaling regulates tumor-associated macrophage-mediated T cell deletion. *J Immunol* **174**, 4880-4891 (2005).
37. P. Cheng, C. A. Corzo, N. Luetteke, B. Yu, S. Nagaraj, M. M. Bui, M. Ortiz, W. Nacken, C. Sorg, T. Vogl, J. Roth, D. I. Gabrilovich, Inhibition of dendritic cell differentiation and accumulation of myeloid-derived suppressor cells in cancer is regulated by S100A9 protein. *J Exp Med* **205**, 2235-2249 (2008).
38. D. Lindau, P. Gielen, M. Kroesen, P. Wesseling, G. J. Adema, The immunosuppressive tumour network: myeloid-derived suppressor cells, regulatory T cells and natural killer T cells. *Immunology* **138**, 105-115 (2012).
39. S. Brandau, K. Moses, S. Lang, The kinship of neutrophils and granulocytic myeloid-derived suppressor cells in cancer: cousins, siblings or twins? *Seminars in cancer biology* **23**, 171-182 (2013).

40. P. Sinha, C. Okoro, D. Foell, H. H. Freeze, S. Ostrand-Rosenberg, G. Srikrishna, Proinflammatory S100 proteins regulate the accumulation of myeloid-derived suppressor cells. *J Immunol* **181**, 4666-4675 (2008).
41. S. Hiratsuka, A. Watanabe, H. Aburatani, Y. Maru, Tumour-mediated upregulation of chemoattractants and recruitment of myeloid cells predetermines lung metastasis. *Nat Cell Biol* **8**, 1369-1375 (2006).
42. S. Hiratsuka, A. Watanabe, Y. Sakurai, S. Akashi-Takamura, S. Ishibashi, K. Miyake, M. Shibuya, S. Akira, H. Aburatani, Y. Maru, The S100A8-serum amyloid A3-TLR4 paracrine cascade establishes a pre-metastatic phase. *Nat Cell Biol* **10**, 1349-1355 (2008).
43. M. Burke, W. Choksawangkarn, N. Edwards, S. Ostrand-Rosenberg, C. Fenselau, Exosomes from myeloid-derived suppressor cells carry biologically active proteins. *J Proteome Res* **13**, 836-843 (2014).
44. S. Ghavami, S. Chitayat, M. Hashemi, M. Eshraghi, W. J. Chazin, A. J. Halayko, C. Kerkhoff, S100A8/A9: a Janus-faced molecule in cancer therapy and tumorgenesis. *Eur J Pharmacol* **625**, 73-83 (2009).
45. T. Vogl, S. Ludwig, M. Goebeler, A. Strey, I. S. Thorey, R. Reichelt, D. Foell, V. Gerke, M. P. Manitz, W. Nacken, S. Werner, C. Sorg, J. Roth, MRP8 and MRP14 control microtubule reorganization during transendothelial migration of phagocytes. *Blood* **104**, 4260-4268 (2004).
46. A. Rammes, J. Roth, M. Goebeler, M. Klempt, M. Hartmann, C. Sorg, Myeloid-related protein (MRP) 8 and MRP14, calcium-binding proteins of the S100 family, are secreted by activated monocytes via a novel, tubulin-dependent pathway. *J Biol Chem* **272**, 9496-9502 (1997).
47. D. Foell, J. Roth, Proinflammatory S100 proteins in arthritis and autoimmune disease. *Arthritis Rheum* **50**, 3762-3771 (2004).
48. D. Foell, H. Wittkowski, T. Vogl, J. Roth, S100 proteins expressed in phagocytes: a novel group of damage-associated molecular pattern molecules. *J Leukoc Biol* **81**, 28-37 (2007).
49. M. Frosch, A. Strey, T. Vogl, N. M. Wulffraat, W. Kuis, C. Sunderkotter, E. Harms, C. Sorg, J. Roth, Myeloid-related proteins 8 and 14 are specifically secreted during interaction of phagocytes and activated endothelium and are useful markers for monitoring disease activity in pauciarticular-onset juvenile rheumatoid arthritis. *Arthritis Rheum* **43**, 628-637 (2000).
50. J. M. Ehrchen, C. Sunderkotter, D. Foell, T. Vogl, J. Roth, The endogenous Toll-like receptor 4 agonist S100A8/S100A9 (calprotectin) as innate amplifier of infection, autoimmunity, and cancer. *J Leukoc Biol* **86**, 557-566 (2009).
51. T. Vogl, K. Tenbrock, S. Ludwig, N. Leukert, C. Ehrhardt, M. A. van Zoelen, W. Nacken, D. Foell, T. van der Poll, C. Sorg, J. Roth, Mrp8 and Mrp14 are endogenous activators of Toll-like receptor 4, promoting lethal, endotoxin-induced shock. *Nat Med* **13**, 1042-1049 (2007).
52. D. Foell, H. Wittkowski, Z. Ren, J. Turton, G. Pang, J. Daebritz, J. Ehrchen, J. Heidemann, T. Borody, J. Roth, R. Clancy, Phagocyte-specific S100 proteins are released from affected mucosa and promote immune responses during inflammatory bowel disease. *J Pathol* **216**, 183-192 (2008).
53. M. Frosch, J. Roth, New insights in systemic juvenile idiopathic arthritis--from pathophysiology to treatment. *Rheumatology (Oxford)* **47**, 121-125 (2008).

54. P. L. van Lent, L. Grevers, A. B. Blom, A. Sloetjes, J. S. Mort, T. Vogl, W. Nacken, W. B. van den Berg, J. Roth, Myeloid-related proteins S100A8/S100A9 regulate joint inflammation and cartilage destruction during antigen-induced arthritis. *Ann Rheum Dis* **67**, 1750-1758 (2008).
55. P. L. van Lent, L. C. Grevers, A. B. Blom, O. J. Arntz, F. A. van de Loo, P. van der Kraan, S. Abdollahi-Roodsaz, G. Srikrishna, H. Freeze, A. Sloetjes, W. Nacken, T. Vogl, J. Roth, W. B. van den Berg, Stimulation of chondrocyte-mediated cartilage destruction by S100A8 in experimental murine arthritis. *Arthritis Rheum* **58**, 3776-3787 (2008).
56. M. Frosch, M. Ahlmann, T. Vogl, H. Wittkowski, N. Wulffraat, D. Foell, J. Roth, The myeloid-related proteins 8 and 14 complex, a novel ligand of toll-like receptor 4, and interleukin-1beta form a positive feedback mechanism in systemic-onset juvenile idiopathic arthritis. *Arthritis Rheum* **60**, 883-891 (2009).
57. N. M. Wulffraat, P. J. Haas, M. Frosch, I. M. De Kleer, T. Vogl, D. M. Brinkman, P. Quartier, J. Roth, W. Kuis, Myeloid related protein 8 and 14 secretion reflects phagocyte activation and correlates with disease activity in juvenile idiopathic arthritis treated with autologous stem cell transplantation. *Ann Rheum Dis* **62**, 236-241 (2003).
58. G. Srikrishna, S100A8 and S100A9: new insights into their roles in malignancy. *J Innate Immun* **4**, 31-40 (2012).
59. S. Grebhardt, K. Muller-Decker, F. Bestvater, M. Hershfinkel, D. Mayer, Impact of S100A8/A9 expression on prostate cancer progression in vitro and in vivo. *J Cell Physiol* **229**, 661-671 (2014).
60. M. Ichikawa, R. Williams, L. Wang, T. Vogl, G. Srikrishna, S100A8/A9 activate key genes and pathways in colon tumor progression. *Mol Cancer Res* **9**, 133-148 (2011).
61. S. Rafii, D. Lyden, S100 chemokines mediate bookmarking of premetastatic niches. *Nat Cell Biol* **8**, 1321-1323 (2006).
62. A. Saha, Y. C. Lee, Z. Zhang, G. Chandra, S. B. Su, A. B. Mukherjee, Lack of an endogenous anti-inflammatory protein in mice enhances colonization of B16F10 melanoma cells in the lungs. *J Biol Chem* **285**, 10822-10831 (2010).
63. C. L. Chaffer, R. A. Weinberg, A perspective on cancer cell metastasis. *Science* **331**, 1559-1564 (2011).
64. P. J. Neeson, P. J. Thurlow, G. P. Jamieson, C. Bradley, Lymphocyte-facilitated tumour cell adhesion to endothelial cells: the role of high affinity leucocyte integrins. *Pathology* **35**, 50-55 (2003).
65. C. Gebhardt, A. Sevko, H. Jiang, R. Lichtenberger, M. Reith, K. Tarnanidis, T. Holland-Letz, L. Umansky, P. Beckhove, A. Sucker, D. Schadendorf, J. Utikal, V. Umansky, Myeloid Cells and Related Chronic Inflammatory Factors as Novel Predictive Markers in Melanoma Treatment with Ipilimumab. *Clin Cancer Res*, (2015).
66. K. Drews-Elger, E. Iorns, A. Dias, P. Miller, T. M. Ward, S. Dean, J. Clarke, A. Campion-Flora, D. N. Rodrigues, J. S. Reis-Filho, J. M. Rae, D. Thomas, D. Berry, D. El-Ashry, M. E. Lippman, Infiltrating S100A8+ myeloid cells promote metastatic spread of human breast cancer and predict poor clinical outcome. *Breast Cancer Res Treat* **148**, 41-59 (2014).

67. L. U. Magnusson, M. Hagberg Thulin, P. Plas, A. Olsson, J. E. Damber, K. Welen, Tasquinimod inhibits prostate cancer growth in bone through alterations in the bone microenvironment. *Prostate*, (2015).
68. R. Rodriguez-Barrueco, J. Yu, L. P. Saucedo-Cuevas, M. Olivan, D. Llobet-Navas, P. Putcha, V. Castro, E. M. Murga-Penas, A. Collazo-Lorduy, M. Castillo-Martin, M. Alvarez, C. Cordon-Cardo, K. Kalinsky, M. Maurer, A. Califano, J. M. Silva, Inhibition of the autocrine IL-6-JAK2-STAT3-calprotectin axis as targeted therapy for HR-/HER2+ breast cancers. *Genes Dev* **29**, 1631-1648 (2015).
69. A. Olsson, J. Nakhle, A. Sundstedt, P. Plas, A. L. Bauchet, V. Pierron, L. Bruetschy, A. Deronic, M. Torngren, D. Liberg, F. Schmidlin, T. Leanderson, Tasquinimod triggers an early change in the polarization of tumor associated macrophages in the tumor microenvironment. *J Immunother Cancer* **3**, 53 (2015).
70. L. Shen, A. Sundstedt, M. Ciesielski, K. M. Miles, M. Celander, R. Adelaiye, A. Orillion, E. Ciamporcero, S. Ramakrishnan, L. Ellis, R. Fenstermaker, S. I. Abrams, H. Eriksson, T. Leanderson, A. Olsson, R. Pili, Tasquinimod modulates suppressive myeloid cells and enhances cancer immunotherapies in murine models. *Cancer Immunol Res* **3**, 136-148 (2015).
71. D. A. Mankoff, A definition of molecular imaging. *J Nucl Med* **48**, 18N, 21N (2007).
72. C. Bremer, V. Ntziachristos, R. Weissleder, Optical-based molecular imaging: contrast agents and potential medical applications. *Eur Radiol* **13**, 231-243 (2003).
73. A. C. Freise, A. M. Wu, In vivo imaging with antibodies and engineered fragments. *Mol Immunol* **67**, 142-152 (2015).
74. A. Mujic-Delic, R. H. de Wit, F. Verkaar, M. J. Smit, GPCR-targeting nanobodies: attractive research tools, diagnostics, and therapeutics. *Trends Pharmacol Sci* **35**, 247-255 (2014).
75. R. Weissleder, V. Ntziachristos, Shedding light onto live molecular targets. *Nat Med* **9**, 123-128 (2003).
76. V. Ntziachristos, C. Bremer, R. Weissleder, Fluorescence imaging with near-infrared light: new technological advances that enable in vivo molecular imaging. *Eur Radiol* **13**, 195-208 (2003).
77. V. Ntziachristos, Optical imaging of molecular signatures in pulmonary inflammation. *Proc Am Thorac Soc* **6**, 416-418 (2009).
78. F. C. van de Watering, M. Rijpkema, L. Perk, U. Brinkmann, W. J. Oyen, O. C. Boerman, Zirconium-89 labeled antibodies: a new tool for molecular imaging in cancer patients. *Biomed Res Int* **2014**, 203601 (2014).
79. T. Vogl, M. Eisenblätter, T. Völler, S. Zenker, S. Hermann, P. van Lent, A. Faust, C. Geyer, B. Petersen, K. Roebrock, M. Schäfers, C. Bremer, J. Roth, Alarmin S100A8/S100A9 as a biomarker for molecular imaging of local inflammatory activity. *Nat Commun* **5**, (2014).
80. A. Becker, N. G. Hokamp, S. Zenker, F. Flores-Borja, K. Barzcyk, G. Varga, J. Roth, C. Geyer, W. Heindel, C. Bremer, T. Vogl, M. Eisenblaetter, Optical In Vivo Imaging of the Alarmin S100A9 in Tumor Lesions Allows for Estimation of the Individual Malignant Potential by Evaluation of Tumor–Host Cell Interaction. *Journal of Nuclear Medicine* **56**, 450-456 (2015).

81. D. Bettenworth, M. Eisenblätter, F. Hasenberg, T. Nowacki, C. Bremer, T. Vogl, A. Lügering, Non-invasive measurement and visualisation of experimental colitis and therapeutic response by targeting Myeloid-related proteins 8 and 14. *Eur J Nucl Med Mol Imaging*, (manuscript in revision).
82. A. Becker, N. G. Hokamp, S. Zenker, F. Flores-Borja, K. Barzcyk, G. Varga, J. Roth, C. Geyer, W. Heindel, C. Bremer, T. Vogl, M. Eisenblaetter, Optical In Vivo Imaging of the Alarmin S100A9 in Tumor Lesions Allows for Estimation of the Individual Malignant Potential by Evaluation of Tumor-Host Cell Interaction. *J Nucl Med* **56**, 450-456 (2015).
83. C. J. Aslakson, F. R. Miller, Selective events in the metastatic process defined by analysis of the sequential dissemination of subpopulations of a mouse mammary tumor. *Cancer Res* **52**, 1399-1405 (1992).
84. M. P. Manitz, B. Horst, S. Seeliger, A. Strey, B. V. Skryabin, M. Gunzer, W. Frings, F. Schonlau, J. Roth, C. Sorg, W. Nacken, Loss of S100A9 (MRP14) results in reduced interleukin-8-induced CD11b surface expression, a polarized microfilament system, and diminished responsiveness to chemoattractants in vitro. *Mol Cell Biol* **23**, 1034-1043 (2003).
85. E. Kallberg, T. Vogl, D. Liberg, A. Olsson, P. Bjork, P. Wikstrom, A. Bergh, J. Roth, F. Ivars, T. Leanderson, S100A9 interaction with TLR4 promotes tumor growth. *PLoS One* **7**, e34207 (2012).
86. M. Goebeler, J. Roth, S. Teigelkamp, C. Sorg, The monoclonal antibody MAC387 detects an epitope on the calcium-binding protein MRP14. *J Leukoc Biol* **55**, 259-261 (1994).
87. V. Ntziachristos, C. H. Tung, C. Bremer, R. Weissleder, Fluorescence molecular tomography resolves protease activity in vivo. *Nat Med* **8**, 757-760 (2002).
88. A. Soubret, J. Ripoll, V. Ntziachristos, Accuracy of fluorescent tomography in the presence of heterogeneities: study of the normalized Born ratio. *IEEE Trans Med Imaging* **24**, 1377-1386 (2005).
89. D. Foell, N. Wulffraat, L. R. Wedderburn, H. Wittkowski, M. Frosch, J. Gerss, V. Stanevicha, D. Mihaylova, V. Ferriani, F. K. Tsakalidou, I. Foeldvari, R. Cuttica, B. Gonzalez, A. Ravelli, R. Khubchandani, S. Oliveira, W. Armbrust, S. Garay, J. Vojinovic, X. Norambuena, M. L. Gamir, J. Garcia-Consuegra, L. Lepore, G. Susic, F. Corona, P. Dolezalova, A. Pistorio, A. Martini, N. Ruperto, J. Roth, Methotrexate withdrawal at 6 vs 12 months in juvenile idiopathic arthritis in remission: a randomized clinical trial. *JAMA* **303**, 1266-1273 (2010).
90. P. Allavena, A. Mantovani, Immunology in the clinic review series; focus on cancer: tumour-associated macrophages: undisputed stars of the inflammatory tumour microenvironment. *Clin Exp Immunol* **167**, 195-205 (2012).
91. J. R. Brahmer, S. S. Tykodi, L. Q. Chow, W. J. Hwu, S. L. Topalian, P. Hwu, C. G. Drake, L. H. Camacho, J. Kauh, K. Odunsi, H. C. Pitot, O. Hamid, S. Bhatia, R. Martins, K. Eaton, S. Chen, T. M. Salay, S. Alaparthy, J. F. Grosso, A. J. Korman, S. M. Parker, S. Agrawal, S. M. Goldberg, D. M. Pardoll, A. Gupta, J. M. Wigginton, Safety and activity of anti-PD-L1 antibody in patients with advanced cancer. *N Engl J Med* **366**, 2455-2465 (2012).

92. B. Merelli, D. Massi, L. Cattaneo, M. Mandala, Targeting the PD1/PD-L1 axis in melanoma: biological rationale, clinical challenges and opportunities. *Crit Rev Oncol Hematol* **89**, 140-165 (2014).
93. E. Simeone, P. A. Ascierto, Immunomodulating antibodies in the treatment of metastatic melanoma: the experience with anti-CTLA-4, anti-CD137, and anti-PD1. *J Immunotoxicol* **9**, 241-247 (2012).
94. H. E. Daldrup-Link, D. Golovko, B. Ruffell, D. G. Denardo, R. Castaneda, C. Ansari, J. Rao, G. A. Tikhomirov, M. F. Wendland, C. Corot, L. M. Coussens, MRI of tumor-associated macrophages with clinically applicable iron oxide nanoparticles. *Clin Cancer Res* **17**, 5695-5704 (2011).
95. Q. Shi, L. J. Pisani, Y. K. Lee, S. Messing, C. Ansari, S. Bhaumik, L. Lowery, B. D. Lee, D. E. Meyer, H. E. Daldrup-Link, Evaluation of the novel USPIO GEH121333 for MR imaging of cancer immune responses. *Contrast Media Mol Imaging* **8**, 281-288 (2013).
96. L. W. Locke, M. W. Mayo, A. D. Yoo, M. B. Williams, S. S. Berr, PET imaging of tumor associated macrophages using mannose coated 64Cu liposomes. *Biomaterials* **33**, 7785-7793 (2012).
97. E. Obeid, R. Nanda, Y. X. Fu, O. I. Olopade, The role of tumor-associated macrophages in breast cancer progression (review). *Int J Oncol* **43**, 5-12 (2013).
98. H. Chen, C. Xu, Q. Jin, Z. Liu, S100 protein family in human cancer. *Am J Cancer Res* **4**, 89-115 (2014).
99. H. Kawai, Y. Minamiya, N. Takahashi, Prognostic impact of S100A9 overexpression in non-small cell lung cancer. *Tumour Biol* **32**, 641-646 (2011).
100. E. McKiernan, E. W. McDermott, D. Evoy, J. Crown, M. J. Duffy, The role of S100 genes in breast cancer progression. *Tumour Biol* **32**, 441-450 (2011).
101. P. M. Hogarth, J. C. Anania, B. D. Wines, The FcgammaR of humans and non-human primates and their interaction with IgG: implications for induction of inflammation, resistance to infection and the use of therapeutic monoclonal antibodies. *Curr Top Microbiol Immunol* **382**, 321-352 (2014).
102. U. S. Ryan, The endothelial surface and responses to injury. *Fed Proc* **45**, 101-108 (1986).
103. B. Heyman, Regulation of antibody responses via antibodies, complement, and Fc receptors. *Annu Rev Immunol* **18**, 709-737 (2000).
104. F. Balkwill, K. A. Charles, A. Mantovani, Smoldering and polarized inflammation in the initiation and promotion of malignant disease. *Cancer Cell* **7**, 211-217 (2005).
105. D. F. Quail, J. A. Joyce, Microenvironmental regulation of tumor progression and metastasis. *Nat Med* **19**, 1423-1437 (2013).
106. D. G. DeNardo, M. Johansson, L. M. Coussens, Immune cells as mediators of solid tumor metastasis. *Cancer Metastasis Rev* **27**, 11-18 (2008).
107. M. S. Cooper, E. Sabbah, S. J. Mather, Conjugation of chelating agents to proteins and radiolabeling with trivalent metallic isotopes. *Nat Protoc* **1**, 314-317 (2006).
108. M. Goebeler, J. Gutwald, J. Roth, C. Sorg, The severity of irritant contact dermatitis in various strains of mice correlates with endothelial expression of migration inhibitory factor (MIF). *Arch Dermatol Res* **283**, 246-250 (1991).

109. G. Kolde, J. Knop, Different cellular reaction patterns of epidermal Langerhans cells after application of contact sensitizing, toxic, and tolerogenic compounds. A comparative ultrastructural and morphometric time-course analysis. *J Invest Dermatol* **89**, 19-23 (1987).
110. U. Malorny, M. Goebeler, J. Gutwald, J. Roth, C. Sorg, Differences in migration inhibitory factor production by C57Bl/6 and BALB/c mice in allergic and irritant contact dermatitis. *Int Arch Allergy Appl Immunol* **92**, 356-360 (1990).
111. M. Goebeler, J. Roth, F. Burwinkel, E. Vollmer, W. Bocker, C. Sorg, Expression and complex formation of S100-like proteins MRP8 and MRP14 by macrophages during renal allograft rejection. *Transplantation* **58**, 355-361 (1994).
112. J. M. Warram, E. de Boer, A. G. Sorace, T. K. Chung, H. Kim, R. G. Pleijhuis, G. M. van Dam, E. L. Rosenthal, Antibody-based imaging strategies for cancer. *Cancer Metastasis Rev* **33**, 809-822 (2014).
113. P. Bannas, L. Well, A. Lenz, B. Rissiek, F. Haag, J. Schmid, K. Hochgrafe, M. Trepel, G. Adam, H. Ittrich, F. Koch-Nolte, In vivo near-infrared fluorescence targeting of T cells: comparison of nanobodies and conventional monoclonal antibodies. *Contrast Media Mol Imaging* **9**, 135-142 (2014).
114. J. Strand, Z. Varasteh, O. Eriksson, L. Abrahmsen, A. Orlova, V. Tolmachev, Gallium-68-labeled affibody molecule for PET imaging of PDGFRbeta expression in vivo. *Mol Pharm* **11**, 3957-3964 (2014).
115. D. Taverna, A. C. Pollins, G. Sindona, R. M. Caprioli, L. B. Nanney, Imaging mass spectrometry for assessing cutaneous wound healing: analysis of pressure ulcers. *J Proteome Res* **14**, 986-996 (2015).
116. P. K. So, B. Hu, Z. P. Yao, Mass spectrometry: towards in vivo analysis of biological systems. *Mol Biosyst* **9**, 915-929 (2013).
117. E. Raymond, A. Dalgleish, J. E. Damber, M. Smith, R. Pili, Mechanisms of action of tasquinimod on the tumour microenvironment. *Cancer Chemother Pharmacol* **73**, 1-8 (2014).
118. A. J. Armstrong, M. Haggman, W. M. Stadler, J. R. Gingrich, V. Assikis, J. Polikoff, J. E. Damber, L. Belkoff, O. Nordle, G. Forsberg, M. A. Carducci, R. Pili, Long-term survival and biomarker correlates of tasquinimod efficacy in a multicenter randomized study of men with minimally symptomatic metastatic castration-resistant prostate cancer. *Clin Cancer Res* **19**, 6891-6901 (2013).
119. A. Faust, T. Voller, F. Busch, M. Schafers, J. Roth, S. Hermann, T. Vogl, Development and evaluation of a non-peptidic ligand for the molecular imaging of inflammatory processes using S100A9 (MRP14) as a novel target. *Chem Commun (Camb)* **51**, 15637-15640 (2015).
120. Y. Martinez de la Torre, C. Buracchi, E. M. Borroni, J. Dupor, R. Bonecchi, M. Nebuloni, F. Pasqualini, A. Doni, E. Lauri, C. Agostinis, R. Bulla, D. N. Cook, B. Haribabu, P. Meroni, D. Rukavina, L. Vago, F. Tedesco, A. Vecchi, S. A. Lira, M. Locati, A. Mantovani, Protection against inflammation- and autoantibody-caused fetal loss by the chemokine decoy receptor D6. *Proc Natl Acad Sci U S A* **104**, 2319-2324 (2007).
121. F. Geissmann, S. Jung, D. R. Littman, Blood monocytes consist of two principal subsets with distinct migratory properties. *Immunity* **19**, 71-82 (2003).

122. S. Mandruzzato, S. Solito, E. Falisi, S. Francescato, V. Chiarion-Sileni, S. Mocellin, A. Zanon, C. R. Rossi, D. Nitti, V. Bronte, P. Zanovello, IL4Ralpha+ myeloid-derived suppressor cell expansion in cancer patients. *J Immunol* **182**, 6562-6568 (2009).
123. B. Z. Qian, J. Li, H. Zhang, T. Kitamura, J. Zhang, L. R. Campion, E. A. Kaiser, L. A. Snyder, J. W. Pollard, CCL2 recruits inflammatory monocytes to facilitate breast-tumour metastasis. *Nature* **475**, 222-225 (2011).
124. T. Kitamura, B. Z. Qian, D. Soong, L. Cassetta, R. Noy, G. Sugano, Y. Kato, J. Li, J. W. Pollard, CCL2-induced chemokine cascade promotes breast cancer metastasis by enhancing retention of metastasis-associated macrophages. *J Exp Med* **212**, 1043-1059 (2015).
125. M. Roblek, M. Calin, M. Schlesinger, D. Stan, R. Zeisig, M. Simionescu, G. Bendas, L. Borsig, Targeted delivery of CCR2 antagonist to activated pulmonary endothelium prevents metastasis. *J Control Release* **220**, 341-347 (2015).
126. J. Zhang, L. Patel, K. J. Pienta, CC chemokine ligand 2 (CCL2) promotes prostate cancer tumorigenesis and metastasis. *Cytokine Growth Factor Rev* **21**, 41-48 (2010).
127. F. Ghiringhelli, C. Ménard, M. Terme, C. Flament, J. Taieb, N. Chaput, P. E. Puig, S. Novault, B. Escudier, E. Vivier, A. Lecesne, C. Robert, J.-Y. Blay, J. Bernard, S. Caillat-Zucman, A. Freitas, T. Tursz, O. Wagner-Ballon, C. Capron, W. Vainchencker, F. Martin, L. Zitvogel, CD4+CD25+ regulatory T cells inhibit natural killer cell functions in a transforming growth factor–β–dependent manner. *The Journal of Experimental Medicine* **202**, 1075-1085 (2005).
128. M. J. Smyth, M. W. L. Teng, J. Swann, K. Kyparissoudis, D. I. Godfrey, Y. Hayakawa, CD4+CD25+ T Regulatory Cells Suppress NK Cell-Mediated Immunotherapy of Cancer. *The Journal of Immunology* **176**, 1582-1587 (2006).
129. I. Lisovsky, G. Isitman, J. Bruneau, N. F. Bernard, Functional analysis of NK cell subsets activated by 721.221 and K562 HLA-null cells. *J Leukoc Biol* **97**, 761-767 (2015).
130. B. Huang, P.-Y. Pan, Q. Li, A. I. Sato, D. E. Levy, J. Bromberg, C. M. Divino, S.-H. Chen, Gr-1+CD115+ Immature Myeloid Suppressor Cells Mediate the Development of Tumor-Induced T Regulatory Cells and T-Cell Anergy in Tumor-Bearing Host. *Cancer Research* **66**, 1123-1131 (2006).
131. S. Hiratsuka, S. Ishibashi, T. Tomita, A. Watanabe, S. Akashi-Takamura, M. Murakami, H. Kijima, K. Miyake, H. Aburatani, Y. Maru, Primary tumours modulate innate immune signalling to create pre-metastatic vascular hyperpermeability foci. *Nat Commun* **4**, 1853 (2013).
132. S. C. Williamson, A. E. Hartley, R. Heer, A review of tasquinimod in the treatment of advanced prostate cancer. *Drug Des Devel Ther* **7**, 167-174 (2013).
133. W. H. Fridman, F. Pages, C. Sautes-Fridman, J. Galon, The immune contexture in human tumours: impact on clinical outcome. *Nat Rev Cancer* **12**, 298-306 (2012).
134. P. B. Olkhanud, D. Baatar, M. Bodogai, F. Hakim, R. Gress, R. L. Anderson, J. Deng, M. Xu, S. Briest, A. Biragyn, Breast cancer lung metastasis requires expression of chemokine receptor CCR4 and regulatory T cells. *Cancer Res* **69**, 5996-6004 (2009).

135. C. Liu, S. Yu, J. Kappes, J. Wang, W. E. Grizzle, K. R. Zinn, H. G. Zhang, Expansion of spleen myeloid suppressor cells represses NK cell cytotoxicity in tumor-bearing host. *Blood* **109**, 4336-4342 (2007).
136. T. Yoshimura, O. M. Howard, T. Ito, M. Kuwabara, A. Matsukawa, K. Chen, Y. Liu, M. Liu, J. J. Oppenheim, J. M. Wang, Monocyte chemoattractant protein-1/CCL2 produced by stromal cells promotes lung metastasis of 4T1 murine breast cancer cells. *PLoS One* **8**, e58791 (2013).
137. S. Y. Lim, A. E. Yuzhalin, A. N. Gordon-Weeks, R. J. Muschel, Targeting the CCL2-CCR2 signaling axis in cancer metastasis. *Oncotarget* **7**, 28697-28710 (2016).
138. L. Zhao, S. Y. Lim, A. N. Gordon-Weeks, T. T. Tapmeier, J. H. Im, Y. Cao, J. Beech, D. Allen, S. Smart, R. J. Muschel, Recruitment of a myeloid cell subset (CD11b/Gr1 mid) via CCL2/CCR2 promotes the development of colorectal cancer liver metastasis. *Hepatology* **57**, 829-839 (2013).
139. H. Saji, M. Koike, T. Yamori, S. Saji, M. Seiki, K. Matsushima, M. Toi, Significant correlation of monocyte chemoattractant protein-1 expression with neovascularization and progression of breast carcinoma. *Cancer* **92**, 1085-1091 (2001).
140. H. Fujimoto, T. Sangai, G. Ishii, A. Ikehara, T. Nagashima, M. Miyazaki, A. Ochiai, Stromal MCP-1 in mammary tumors induces tumor-associated macrophage infiltration and contributes to tumor progression. *Int J Cancer* **125**, 1276-1284 (2009).
141. Y. Liu, A. Kosaka, M. Ikeura, G. Kohanbash, W. Fellows-Mayle, L. A. Snyder, H. Okada, Premetastatic soil and prevention of breast cancer brain metastasis. *Neuro Oncol* **15**, 891-903 (2013).
142. K. Arai, S. Takano, T. Teratani, Y. Ito, T. Yamada, R. Nozawa, S100A8 and S100A9 overexpression is associated with poor pathological parameters in invasive ductal carcinoma of the breast. *Curr Cancer Drug Targets* **8**, 243-252 (2008).
143. B. Huang, P. Y. Pan, Q. Li, A. I. Sato, D. E. Levy, J. Bromberg, C. M. Divino, S. H. Chen, Gr-1+CD115+ immature myeloid suppressor cells mediate the development of tumor-induced T regulatory cells and T-cell anergy in tumor-bearing host. *Cancer Res* **66**, 1123-1131 (2006).
144. G. Gallina, L. Dolcetti, P. Serafini, C. D. Santo, I. Marigo, M. P. Colombo, G. Basso, F. Brombacher, I. Borrello, P. Zanovello, S. Bicciato, V. Bronte, Tumors induce a subset of inflammatory monocytes with immunosuppressive activity on CD8+ T cells. *The Journal of Clinical Investigation* **116**, 2777-2790 (2006).
145. H. W. van Deventer, D. A. Palmieri, Q. P. Wu, E. C. McCook, J. S. Serody, Circulating fibrocytes prepare the lung for cancer metastasis by recruiting Ly-6C+ monocytes via CCL2. *J Immunol* **190**, 4861-4867 (2013).
146. L. Bonapace, M. M. Coissieux, J. Wyckoff, K. D. Mertz, Z. Varga, T. Junt, M. Bentires-Alj, Cessation of CCL2 inhibition accelerates breast cancer metastasis by promoting angiogenesis. *Nature* **515**, 130-133 (2014).
147. K. J. Pienta, J. P. Machiels, D. Schrijvers, B. Alekseev, M. Shkolnik, S. J. Crabb, S. Li, S. Seetharam, T. A. Puchalski, C. Takimoto, Y. Elsayed, F. Dawkins, J. S. de Bono, Phase 2 study of carlumab (CNTO 888), a human monoclonal antibody against CC-chemokine ligand 2 (CCL2), in metastatic castration-resistant prostate cancer. *Investigational new drugs* **31**, 760-768 (2013).

148. S. K. Sandhu, K. Papadopoulos, P. C. Fong, A. Patnaik, C. Messiou, D. Olmos, G. Wang, B. J. Tromp, T. A. Puchalski, F. Balkwill, B. Berns, S. Seetharam, J. S. de Bono, A. W. Tolcher, A first-in-human, first-in-class, phase I study of carlumab (CNTO 888), a human monoclonal antibody against CC-chemokine ligand 2 in patients with solid tumors. *Cancer chemotherapy and pharmacology* **71**, 1041-1050 (2013).
149. H. Ji, D. W. Greening, T. W. Barnes, J. W. Lim, B. J. Tauro, A. Rai, R. Xu, C. Adda, S. Mathivanan, W. Zhao, Y. Xue, T. Xu, H. J. Zhu, R. J. Simpson, Proteome profiling of exosomes derived from human primary and metastatic colorectal cancer cells reveal differential expression of key metastatic factors and signal transduction components. *Proteomics* **13**, 1672-1686 (2013).
150. J. T. Isaacs, S. L. Dalrymple, D. M. Rosen, H. Hammers, A. Olsson, T. Leanderson, Anti-cancer potency of tasquinimod is enhanced via albumin-binding facilitating increased uptake in the tumor microenvironment. *Oncotarget* **5**, 8093-8106 (2014).

8 Acknowledgments

This project has been supported by funding from the King's College London & UCL Comprehensive Cancer Imaging Centre through a one year pump priming and a Cancer Research UK Clinical Research Fellowship for Michel Eisenblaetter, the Medical Research Council through award of a Clinical Research Training Fellowship to Michel Eisenblaetter and the German Research Foundation through provision of a project grant to Michel Eisenblaetter.

This project could not have been realised without the amazing support by the staff at the King's College London Division of Imaging Sciences, namely Dr Kavitha Sunnassee and David Thackor and their team. Moreover, Prof Reza Razavi deserves my gratitude for the opportunity to work with the great team at his division and his very personal, outright support in all aspects of my work.

Numerous people have been strongly involved at various stages of this project and helped a lot to realise it. I want to express my special thanks for tireless help, support, advice and inspiration to Dr Fabian Flores-Borja, Prof Thomas Vogl and Prof Johannes Roth, Anne Becker MD and Nils Große Hokamp MD, Dr Gilbert Fruhwirth, Dr Rebekka Hueting and Prof Christoph Bremer.

For their patience, advice, motivation, encouragement and unreserved support, I want to thank my two supervisors Prof Tobias Schaeffter and Prof Tony Ng.

Finally, I want to thank my family - my parents and my girlfriend Julia for their encouragement and support and all the strength, they gave me.

9 Abbreviations

ACK	Ammonium-Chloride-Potassium
APC	Allophycocyanin
AU	Arbitrary units
BSA	Bovine serum albumin
BSU	Biological services unit
CD	Cluster of differentiation
CSF	Colony stimulating factor
CT	Computed tomography
DAMP	Damage associated molecular pattern
DC	Dendritic cell
DMEM	Dulbecco's modified Eagle medium
ECM	Extracellular matrix
EDTA	Ethylenediaminetetraacetic acid
EGF	Epidermal growth factor
ELISA	Enzyme linked immunosorbant assay
FACS	Fluorescence activated cell sorting
FBS	Fetal bovine calf serum
FMO	Fluorescence minus one
FMT	Fluorescence mediated tomography
FRI	Fluorescence reflectance imaging
GMCSF	Granulocyte monocyte colony stimulating factor
HEPES	4-(2-hydroxyethyl)-1-piperazineethanesulfonic acid
HIF	Hypoxia-inducible factor
HPLC	High performance liquid chromatography

IBD	Inflammatory bowel disease
ICD	Irritant contact dermatitis
ID	Injected dose
IgG	Immunoglobin G
IL	Interleukin
IMC	Immature myeloid cell
M-CSF	Macrophage-colony stimulating factor
MACS	Magnetic activated cell sorter
MDSC	Myeloid derived suppressor cell
MHC	Major histocompatibility complex
MIP	Macrophage inflammatory protein
miRNA	Micro ribonucleic acid
MMP	Matrix metallopreoteinase
MRI	Magnetic resonance tomography
mRNA	Messenger ribonucleic acid
MRP	Myeloid related protein
MW	Molecular weight
NIR	Near-infrared
NIRF	Near-infrared fluorescence
NK cells	Natural killer cells
NO	Nitric oxide
OCT	Optimum cutting temperature compound
OI	Optical imaging
PBS	Phosphate buffered saline
PET	Positron emission tomography
PN	Premetastatic niche
RA	Rheumatoid arthritis

rab	Rabbit
ROI	Region of interest
ROS	Reactive oxygen species
SAA	Serum amyloid A
SLE	Systemic lupus erythematosus
SPECT	Single photon emission computed tomography
TAM	Tumour associated macrophage
TCR	T cell receptor
TGF	Tumour growth factor
TLR	Toll-like receptor
TNF	Tumour necrosis factor
Treg	Regulatory T cell (CD4+)
VEGF	Vascular endothelial growth factor
VEGFR	Vascular endothelial growth factor receptor

10 Annex

10.1 Publication I – Vogl, Eisenblätter et al

Alarmin S100A8/S100A9 as a biomarker for molecular imaging of local inflammatory activity

Vogl T*, **Eisenblätter M***, Völler T, Zenker S, Hermann S, van Lent P, Faust A, Geyer C, Petersen B, Roebrock K, Schäfers M, Bremer C, Roth J

Nature communications 2014 Aug 6;5:4593

nature COMMUNICATIONS

ARTICLE

Received 7 May 2014 | Accepted 3 Jul 2014 | Published 6 Aug 2014

DOI: 10.1038/ncomms5593 OPEN

Alarmin S100A8/S100A9 as a biomarker for molecular imaging of local inflammatory activity

Thomas Vogl[1,2,*], Michel Eisenblätter[3,4,*], Tom Völler[1], Stefanie Zenker[1], Sven Hermann[2,5], Peter van Lent[6], Andreas Faust[5], Christiane Geyer[2,4], Beatrix Petersen[1], Kirsten Roebrock[1,2], Michael Schäfers[5,7], Christoph Bremer[2,8] & Johannes Roth[1,2,7]

Inflammation has a key role in the pathogenesis of various human diseases. The early detection, localization and monitoring of inflammation are crucial for tailoring individual therapies. However, reliable biomarkers to detect local inflammatory activities and to predict disease outcome are still missing. Alarmins, which are locally released during cellular stress, are early amplifiers of inflammation. Here, using optical molecular imaging, we demonstrate that the alarmin S100A8/S100A9 serves as a sensitive local and systemic marker for the detection of even sub-clinical disease activity in inflammatory and immunological processes like irritative and allergic contact dermatitis. In a model of collagen-induced arthritis, we use S100A8/S100A9 imaging to predict the development of disease activity. Furthermore, S100A8/S100A9 can act as a very early and sensitive biomarker in experimental leishmaniasis for phagocyte activation linked to an effective Th1-response. In conclusion, the alarmin S100A8/S100A9 is a valuable and sensitive molecular target for novel imaging approaches to monitor clinically relevant inflammatory disorders on a molecular level.

[1] Institute of Immunology, University of Münster, 48149 Münster, Germany. [2] Interdisciplinary Centre for Clinical Research, University of Münster, 48149 Münster, Germany. [3] Division of Imaging Sciences and Biomedical Engineering, King's College London, London SE1 7EH, UK. [4] Department of Clinical Radiology, University of Münster, 48149 Münster, Germany. [5] European Institute for Molecular Imaging, University of Münster, 48149 Münster, Germany. [6] Department of Rheumatology, Radboud University Medical Centre, 6500 HB Nijmegen, The Netherlands. [7] Cluster of Excellence EXC 1003 'Cells in Motion - CiM', University of Münster, 48149 Münster, Germany. [8] Department of Radiology, St Franziskus Hospital Münster, 48145 Münster, Germany. * These authors contributed equally to this work. Correspondence and requests for materials should be addressed to Th.V. (email: vogl@uni-muenster.de).

Inflammation is the driving force in a vast spectrum of clinically relevant disorders, among others recognized as a major pathological mechanism in malignant and degenerative diseases, infection and autoimmunity. Current imaging markers mostly reflect either metabolism or secondary effects of inflammatory reactions, such as increased perfusion or vessel permeability, or are only suitable for a very specific subset of diseases. In addition, all currently established biomarkers widely lack a proven prognostic potential. With biomedical research increasingly discovering the molecular and cellular basis of diseases and highly specific molecular therapies at the same time, both approaches do not provide sufficient diagnostic information. As a result, individually adapted therapy to manage chronic inflammatory diseases remains widely elusive despite significant therapeutic improvements[1].

Numerous imaging approaches have been designed to address this issue. *In vivo* visualization of local inflammation has been performed, for example, using F-18-fluorodeoxyglucose (^{18}F-FDG)-positron emission tomography (PET) or magnetic resonance imaging (MRI) with or without contrast enhancement[2]. Although these methods have proven diagnostic value, their implication in clinical practice has not fostered personalized therapy, mostly due to a lack of either desirable specificity (PET) or sensitivity (MRI).

Targeted imaging approaches to overcome these limitations would ideally address a biomarker with high expression/release or accumulation locally at the site of inflammation, representative of early inflammatory processes and residual disease activity or a prediction of flare-ups of disease in remitting-relapsing courses of chronic inflammation. In preclinical animal models, non-invasive molecular imaging methods would allow for local and longitudinal assessment of biomarkers in individual subjects. In the long-term, such biomarkers would facilitate individual adaptation of medication and would lead to a significant step forward in the concept of personalized medicine.

In recent years, the concept of alarmins or 'danger-associated molecular pattern molecules' (DAMPs) has emerged as a novel mechanism for initiating and promoting inflammation and has more recently been recognized as capable of resolving inflammation[3–6]. Expressed and released during tissue damage or cellular stress reactions, members of this protein family have been shown to be early players in the development of inflammatory processes. S100A8 and S100A9, two members of the DAMP-family, are highly expressed in early infiltrating phagocytes. During the activation of these cells, S100A8/S100A9 complexes are locally released in virtually all inflammatory disorders that are associated with phagocyte activation, like autoimmune diseases, rheumatoid arthritis, allergies, cardiovascular diseases, or local and systemic infections and tumours[7], whereas virtually no expression can be found in healthy tissue. We have previously shown that S100A8 and S100A9 promote inflammation via the activation of Toll-like receptor-4 (refs 8–11). Serum concentrations of S100A8/S100A9 complexes have been shown to be superior over conventional biomarkers for the monitoring of inflammatory disorders, especially in the detection of residual disease activity and in the prediction of relapse in arthritis[12].

However, biomarkers measured in the blood only reflect the systemic state, which is strongly affected by factors like metabolism or blood clearance, limiting the specificity and sensitivity of these approaches. In contrast to systemic measurements, non-invasive imaging should be able to detect the expression of alarmins even at the local site of inflammation. Using fluorescence reflectance imaging (FRI), we now provide the first evidence that molecular imaging allows for the reliable detection of S100A8 and S100A9 in preclinical models, locally expressed during disease, and that visualization of these proteins in conjunction with further laboratory analysis enables the monitoring of local inflammation with unique sensitivity, even allowing for the detection of sub-clinical, residual disease activity. In autoimmune arthritis, we can simultaneously monitor multiple disease foci by *in vivo* S100A9 imaging and the extent of disease could be determined with high precision and even prognostic value for disease development in independent foci of the same animal. Moreover, by imaging S100A9 expression, we have demonstrated the first biomarker detecting subclinical differences in phagocyte activation linked to disease outcome in a model of Th1/Th2-dichotomy in response to leishmania infection. We provide evidence that S100A9 may serve as a novel potent biomarker for monitoring local inflammatory processes by molecular imaging. The broad applicability and consecutive potential impact on clinical practice is illustrated by assessing the performance of our integrated approach in exemplary models of innate and adaptive immunity, autoimmunity and infection, thus covering representative relevant pathomechanisms of inflammatory disorders.

Results

Cy5.5-coupled aS100A9 accumulates at sites of inflammation. To evaluate the feasibility of monitoring S100A9 expression by optical imaging, we employed irritant contact dermatitis (ICD) as an inflammatory model, exclusively driven by innate immunity, independent of the adaptive immune system. ICD was induced in Balb/c mice by the local application of croton oil towards the ear skin[13]. ^{18}F-FDG-PET, as a clinically established imaging technique to assess inflammatory activity[14], was used to visualize elevated glucose metabolism in areas of inflammation during ICD. Although inflammation can be clearly depicted by the maximum intensity PET image (Fig. 1a, red arrow), as well as in the co-registered PET/ computed tomography (CT; Fig. 1b, axial CT slice), the resulting contrast-to-noise ratio (CNR) is low due to ^{18}F-FDG being taken up by all glucose-consuming cells (Fig. 1a).

Figure 1 | *In vivo* fluorescence reflectance imaging of mice during ICD. (**a**) ^{18}F-FDG-PET image and the fused PET/CT (axial CT slice) (**b**) of ICD in mice treated with croton oil on the right ear. The area of inflammation (red arrows) can be depicted in the maximum intensity PET image (**a**, whole body) with the axial CT slice showing the swelling of the inflamed tissue and the local uptake of FDG (ratio inflamed ear versus healthy ear = 4.8; **b**). (**c**) After the application of a-S100A9-Cy5.5 to Balb/c mice 24 h after elicitation of ICD, optical imaging (OI) was performed at the time points indicated. Strong fluorescence intensities were detected only at sites of inflammation for up to 96 h. (**d**) Quantification of CNR shows significant changes in the affected ears over the observed time period from 24 to 96 h (baseline = time point 0). Data are from three independent experiments (each $n = 5$, mean ± s.d., $^{*}P<0.05$, $^{**}P<0.01$, $^{***}P<0.001$; *P* values calculated using Student's *t*-test). (**e**) S100A8/S100A9 serum concentrations 48 h after croton oil application. Data are from five mice per group (mean ± s.d., $^{***}P<0.001$; Student's *t*-test). (**f**) Cryosections of treated and control ears were stained for S100A9-expression. The figure shows representative ear sections of an untreated control ear (left) and treated ears with moderately (middle) and strongly (right) elevated SNR including the corresponding systemic S100A8/S100A9 level. Scale bar, 100 µm. (**g**) Application of a-S100A9-Cy5.5 or rabIgG-Cy5.5 to WT or S100A9$^{-/-}$ mice 24 h after the elicitation of ICD confirmed the specificity of optical imaging for S100A9 expression *in vivo*. Data are from five mice per group (mean ± s.d., $^{*}P<0.05$; *P*-values calculated using one-way analysis of variance with Bonferroni's post test). a.u., arbitrary units.

Cy5.5-labelled antibodies against S100A9 (a-S100A9-Cy5.5, 2 nmol of dye/mouse, spectral characteristics: $\lambda_{exc/em} = 680/700$ nm, band pass = 20 nm) were administered intravenously 24 h after croton oil application. Optical imaging was performed repeatedly 24–96 h after tracer application. Local tracer accumulation, as depicted by FRI, showed the highest level at 24 h (Fig. 1c,d). Fluorescence signals reflecting the high local release of S100A8/S100A9 correlated well with elevated systemic levels of

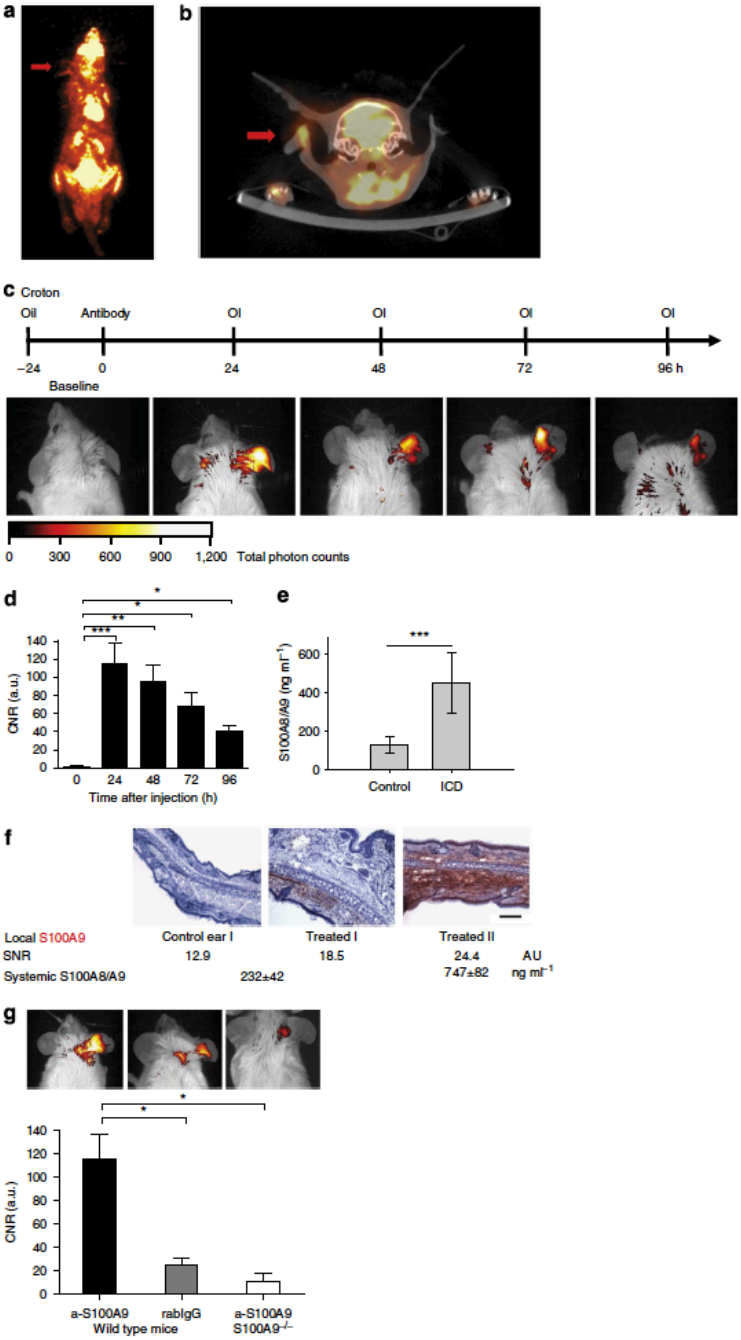

S100A8/S100A9 complex in the serum of mice 48 h after croton oil application, as quantified by ELISA (Fig. 1e, Supplementary Fig. 1). Local S100A9 expression could be confirmed using immunohistochemistry (Fig. 1f). In healthy animals, a-S100A9-Cy5.5 showed a biodistribution that is typical for macromolecular substances (Supplementary Fig. 2). To discriminate nonspecific tracer distribution, rabbit IgG of irrelevant specificity was labelled with Cy5.5 (rabIgG-Cy5.5) and injected into a control group of mice. S100A9-deficient mice ($S100A9^{-/-}$) served as additional controls for the specificity of tracer to target binding. Both sets of controls showed only a slight increase in fluorescence at local sites of inflammation, most likely reflecting hyperemia and $F_c\gamma$ receptor expression/binding in areas of inflammation (Fig. 1g). The distribution of rabIgG-Cy5.5 and a-S100A9-Cy5.5 in either healthy wild-type (WT) animals or non-involved organs was virtually identical (Supplementary Fig. 2).

Monitoring local inflammation in allergic contact dermatitis (ACD). To assess the capability of S100A9 imaging to reflect phagocyte activity in T-cell-dependent adaptive immune reactions, we analysed the expression of S100A9 in a model of ACD[13]. Two days after the allergen challenge of sensitized mice, a-S100A9-Cy5.5 or rabIgG-Cy5.5 was administered and fluorescence intensities were monitored for up to 48 h after tracer application. Disease progression was assessed by monitoring the ear swelling during ACD (Fig. 2a). Already after 3 h, the specific probe accumulated in the area of inflammation, peaking at 24 h (Fig. 2b). FRI data (Fig. 2b,c) were again in good accordance with increased S100A8/S100A9 serum levels of $258 \pm 116\ ng\,ml^{-1}$ at day 3 ($P<0.01$) and of $289 \pm 91\ ng\,ml^{-1}$ at day 4 ($P<0.001$) compared with control mice ($129 \pm 42\ ng\,ml^{-1}$, five mice per group (two independent experiments, mean ± s.d)) and clinical symptoms (ear swelling; Fig. 2a). Similar fluorescence intensities of specific and nonspecific antibodies were obtained in unaffected ears, representing a perfusion background signal (Fig. 2c). To further differentiate the accumulation of labelled specific versus unspecific antibody in the region of inflammation, 2 nmol of both Cy5.5-labelled anti-S100A9 and Cy7-labelled rabIgG were injected simultaneously *in vivo* during ACD. Fluorescence signals obtained after the separate excitation of both probes were acquired and compared with data derived *in vitro* under defined conditions. The Cy5.5/Cy7 (reflecting a-S100A9/rabIgG) ratio *in vitro* was constant (1.83 ± 0.15); however, we observed a significant increase to 4.73 ± 1.31 *in vivo* (Fig. 2d). To rule out the effects of the dye properties on probe distribution, a-S100A9-Cy5.5 and a-S100A9-Cy7 were used simultaneously. An identical biodistribution of the differently labelled probes could be observed. Although a direct comparison of absolute signal intensities was obviated by different emission wavelengths and different quantum yields, the signal ratios between the affected and unaffected ear were virtually identical (Fig. 2e). A parallel injection of a-S100A9-Cy5.5 and rabIgG-Cy5.5 did not result in a further increase in the local signal compared with the injection of a-S100A9-Cy5.5 alone. As the S100A9-specific probe is based on a polyclonal antibody and thus presumably contains only a relatively small fraction of antigen-specific antibodies, these data confirm the specificity of our findings (Supplementary Fig. 3a). Immunohistochemistry showed a significant infiltration by CD11b myeloid cells, Gr-1 granulocytes and F4/80 macrophages as a source of locally released S100A8/S100A9 (Supplementary Fig. 3b).

Monitoring local activity of inflammation in arthritis. S100A8 and S100A9 are highly expressed in synovial tissue in rheumatoid arthritis and serum concentrations have been shown to be reliable biomarkers reflecting local disease activity[10,11,15]. We performed optical imaging of S100A8 and S100A9 expression *in vivo* in a murine collagen-induced arthritis (CIA) model and correlated imaging data with the clinical scores of disease activity. CIA was induced by immunization of DBA/jdba1/j mice with type II collagen. Clinical manifestations of arthritis started around day 7 after the last collagen injection. Symptoms prevailed for up to 3 weeks to different degrees in the foot joints. Mice received labelled antibodies 1 week after the last collagen injection (day 28). Optical imaging was performed starting 24 h after dye application.

Owing to the highly variable inflammatory response of individual joints in CIA, we performed a clinical scoring for each individual foot on the basis of a three-point scale (CS0, CS1 and CS2) accounting for redness, swelling and deformation. S100A9 expression, as depicted by optical imaging, showed excellent correlation with clinical scoring, clearly discriminating clinically mild from severe joint inflammation (Fig. 3a) with a high signal-to-noise ratio (SNR) for severely inflamed joints (Fig. 3b). Even single affected small joints could be clearly identified (Fig. 3c). The cumulative disease activity score of all four feet (range 0–8) correlated well with optical imaging data presented as mean values for all four feet and systemic S100A8/S100A9 levels of $1{,}180 \pm 360\ ng\,ml^{-1}$ in mice with mild arthritis (CS2-3) versus $170 \pm 30\ ng\,ml^{-1}$ in healthy control mice and $2{,}700 \pm 380\ ng\,ml^{-1}$ in mice with high disease activity (CS4-6; Fig. 3d,e). To assess unspecific tracer distribution, we employed non-targeted Cy5.5-labelled rabIgG and observed only faint tracer signals, even in strongly inflamed joints (Fig. 3a). The simultaneous injection of Cy7-labelled antibodies against the S100A8 subunit of the S100A8/S100A9 heterodimer (a-S100A8-Cy7, 2 nmol dye/mouse, spectral characteristics: $\lambda_{exc/em}$ = 755/780 nm, band pass = 20 nm) and a-S100A9-Cy5.5 showed an almost identical *in vivo* distribution with equally specific accumulation in target areas (Fig. 3f,g). SNR of a-S100A8-Cy7 and a-S100A9-Cy5.5 showed excellent correlation with disease activity scores of individual feet (Fig. 3h). To further assess a potential prognostic value of the presented approach, we conducted the CIA model in C57BL/6 mice. Development of arthritis and outcome in this mouse strain is highly variable and unpredictable. Even during early disease, when first clinical signs of CIA could only just be detected, scans allowed for the safe delineation of areas of S100A9 expression. All four paws were scored daily and imaging was repeated when manifesting clinical signs of inflammation were present. We also demonstrated an excellent correlation between early and late imaging (Fig. 3i,j), as well as between early imaging and the clinical development of individual paws (Fig. 3k).

Phagocyte activity during *Leishmania major* infection. Experimental *leishmaniasis* is a well-established model for analysing the Th1/Th2-dependent immune response to infection. C57BL/6 mice show early activation of phagocytes within the first days after *Leishmania major (L. major)* inoculation, which results in an effective Th1-response and the clearance of parasites. In contrast, Balb/c mice lack the sufficient activation of phagocytes in the initial phase of infection, finally resulting in the development of a Th2-dominated, ineffective immune response and subsequent parasite dissemination. The consecutive granuloma formation is accompanied by an overwhelming yet inefficient phagocyte activation in the late phase of disease[16].

At day 28 after infection, in the late phase of disease, optical imaging of infected animals was performed, showing significantly higher fluorescence signals in the feet of infected Balb/c mice as

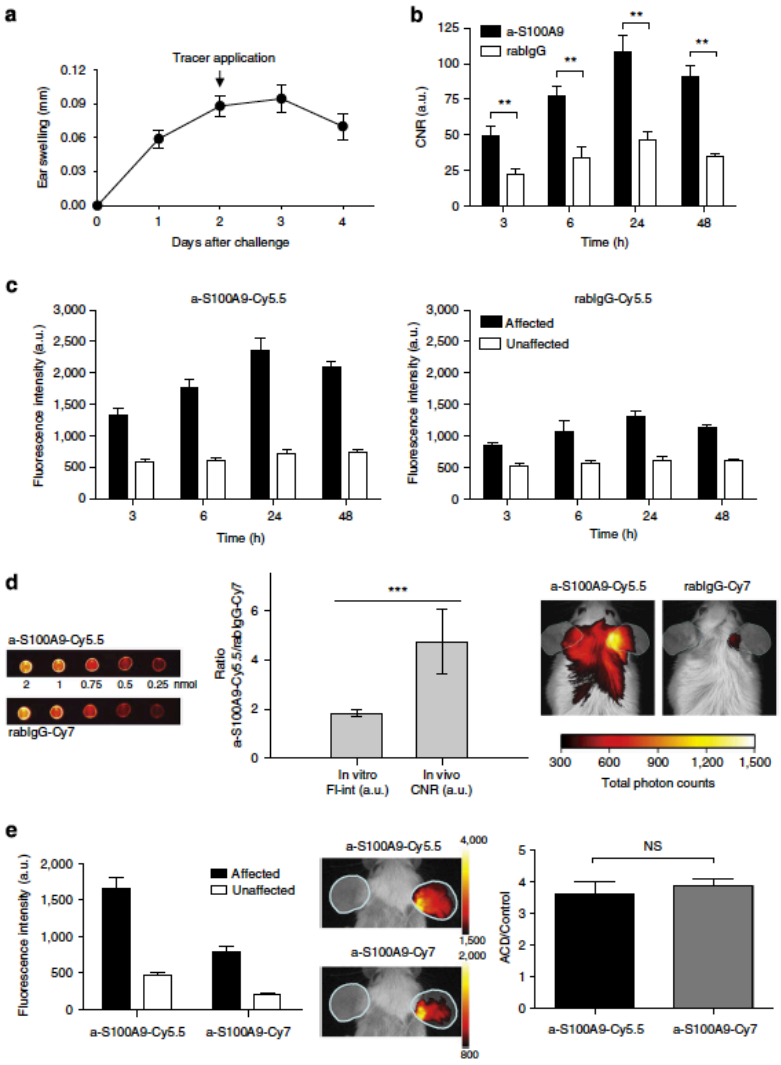

Figure 2 | Monitoring of S100A9 expression during ACD by fluorescence reflectance imaging (FRI) *in vivo*. (**a**) ACD was induced in mice and disease progression was assessed by the increase in ear swelling. (**b**) FRI was performed at different time points after the application of either a-S100A9-Cy5.5 or rabIgG-Cy5.5, as indicated in the figure. The optimal time point for optical imaging was found to be 24 h after tracer application. (**c**) Fluorescence intensities of the specific (left image) versus unspecific tracer (right image) of affected (black bars) versus unaffected (white bars) ears allowed for the estimation of $F_c\gamma$ receptor contribution to total FRI signals. (**d**) Comparison of the ratios of equal amounts of a-S100A9-Cy5.5 and rabIgG-Cy7 *in vitro* (FL-int = fluorescence intensities, left side) versus *in vivo* (CNR, right side). ACD was induced in mice and 2 nmol of Cy5.5-labelled anti-S100A9 and Cy7-labelled rabIgG were injected simultaneously. Optical imaging was performed 24 h after antibody injection and the region of interest (ROI) of data acquisition was labelled in cyan. Data are from five mice per group (two independent experiments each, mean ± s.d.) $^*P<0.05$, $^{**}P<0.01$, $^{***}P<0.001$; Student's *t*-test. (**e**) Comparison of the ratios of equal amounts of a-S100A9-Cy5.5 and a-S100A9-Cy7 during ACD. ACD was induced in mice and 2 nmol of Cy5.5- and Cy7-labelled anti-S100A9 each was injected simultaneously. Optical imaging was performed at 24 h after antibody injection and the ROI of data acquisition was labelled in cyan (data are from five mice, mean ± s.d. according to Student's *t*-test). a.u., arbitrary units; NS, not significant.

compared with C57BL/6 mice and untreated control feet (Fig. 4a, right images). RabIgG-Cy5.5 confirmed the specificity of S100A9-labelling (Fig. 4a, left images). We observed an excellent correlation of optical signals with systemic S100A8/S100A9 levels (Fig. 4b) and footpad swelling (Fig. 4c) as a clinical sign of inflammation. Moreover, in C57BL/6 mice, even at day 28 after infection, fluorescence-reflected macrophage activity allowed the grading of residual inflammation (Fig. 4d).

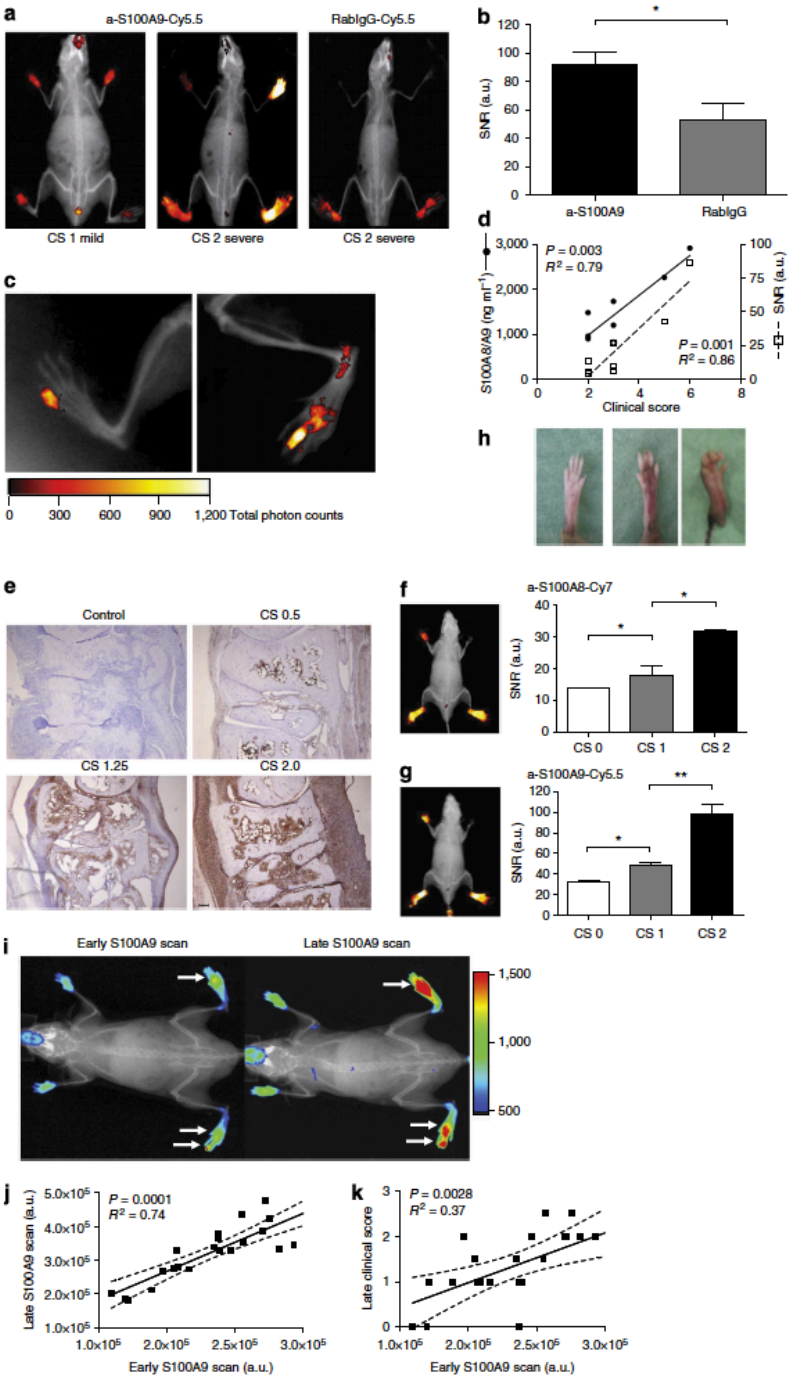

Using S100A9 imaging, even the critical, initial activation of the phagocyte system in *L. major*-resistant C57BL/6 mice could be detected during the very early phase at day four after infection. Measurements of S100A8/S100A9 expression in sera or local wash-outs by ELISA confirmed the detected imaging signals (Fig. 4e). In contrast, the failure of sufficient early phagocyte activation in Balb/c mice was associated with the absence of a significant increase in S100A9 expression (Fig. 4f). We could therefore demonstrate that locally expressed S100A9 is the first imaging marker predicting the development of a Th1 immune response, several weeks before the clinical outcome of infection.

Discussion

Inflammatory disorders like autoimmune diseases, allergies and acute or chronic infections are important challenges in health care. The continuously growing understanding of the biological basis of inflammation stimulates the development of targeted therapies, specifically addressing selected steps in the process of pathogenesis. This is accompanied by a growing demand for specific diagnostic approaches, which are capable not only of sensitive detection but also of characterization of the disease stages on a molecular level. Molecular biomarkers that meet the requirements as set out by current therapeutic developments—sensitive reflection of disease activity changes under therapy, safe visualization of subclinical disease activity as a sign of therapy failure and a prediction of the outcome—are still missing. However, these requirements are a prerequisite for the adaptation of personalized therapeutic approaches providing optimal therapy.

Analysing S100A8 and S100A9, two members of the DAMP family, our study comprises a novel diagnostic approach: DAMPs or alarmins are widely accepted to represent initial tissue signals in response to cell stress and tissue damage, thus representing ideal candidates for the early and sensitive detection of developing inflammation[3,5,17]. Both proteins are among the most upregulated genes in numerous inflammatory diseases[7,15]. S100A8/S100A9 complexes are secreted during the activation of immigrating phagocytes or released by necrotic cells because of tissue damage at local sites of inflammation, acting as endogenous triggers of Toll-like receptor-4 and inducing the expression of pro-inflammatory signalling molecules in phagocytes, lymphocytes, endothelial and epithelial cells and osteoclasts[8,10,18,19]. In this context, S100A8 and S100A9 show typical characteristics of alarmins or DAMPs. Targeting S100A8/S100A9, we therefore monitored an inflammatory mechanism that has been shown as highly relevant in different mouse models of inflammation like allergies, autoimmune diseases, arthritis and infection and has also proven to be a valuable marker for discrimination and grading of clinically relevant acute and chronic inflammation[7–10,13,18,19].

Targeted imaging of cytokines, for example, interleukin-1β or tumour necrosis factor-α revealed only limited sensitivity and/or specificity and a relatively low SNR[20–22], probably due to a low gradient of the cytokine concentration between local inflammatory exudates and systemic serum. In contrast to most cytokines, chemokines and other pro-inflammatory molecules, the local accumulation of S100A8 and S100A9 is very high (up to 100 μg ml^{-1} and about 50- to 100-fold higher than systemic concentrations), allowing the sensitive and specific detection of local changes in the expression of these molecules[15,23]. S100A8 and S100A9 comprise about 40% and 5% of the cytosolic proteins in granulocytes and monocytes, respectively. They are specifically released during the interaction of phagocytes with inflammatory activated endothelial cells and can subsequently bind to heparan sulfate of the endothelial glycocalyx[15,24–26]. The high abundance and matrix binding appear to be responsible for the high local accumulation of these proteins at sites of inflammation compared with other inflammatory molecules, which allows the detection of these molecules even by MRI[27] and accounts for the high target to background ratios that we observed in our *in vivo* imaging studies.

In contact dermatitis, as a model of local inflammation, we could demonstrate that the expression of S100A9 is a very sensitive marker for inflammatory processes and reflects disease activity independently of the underlying pathomechanism, for example, in toxic or in allergen-induced inflammation. In contrast to most imaging studies, we confirmed that our imaging data closely correlated not only to the local expression of S100 proteins by phagocytes in the dermal infiltrate, as determined by immunohistochemistry, but also to systemic levels of both proteins and clinical parameters. The specificity of our data was confirmed by the use of nonspecific antibodies (rabbit-derived IgG without relevant specificity) to determine perfusion and unspecific $F_c\gamma$-receptor binding. Parallel injection of the S100A9-specific probe and rabIgG labelled with different dyes ruled out *in vivo* competition for the specific target or dye-dependent effects. Moreover, we applied the specific probe a-S100A9-Cy5.5 in ICD in WT and S100A9$^{-/-}$ mice. SNR of a-S100A9-Cy5.5 in WT mice were significantly higher compared with nonspecific antibodies, as well as compared with data obtained from S100A9$^{-/-}$ mice. In this model, WT and S100A9$^{-/-}$ mice showed no differences regarding their inflammatory phenotype[13].

Figure 3 | Detection of single inflamed joints in collagen-induced arthritis by optical imaging. (**a**) CIA was induced in DBA/jdba1/j mice and optical imaging was recorded by FRI using a-S100A9-Cy5.5 or rabIgG-Cy5.5 at day 28. Individual feet were analysed and compared with clinical scores described in the Method section ($n=5$ mice per group, three independent experiments). (**b**) Comparison of imaging data of a-S100A9-Cy5.5 and rabIgG-Cy5.5 from mice feet with CS2 confirms the specificity of our findings (mean ± s.d., $^*P<0.05$, Student's *t*-test, $n=5$ mice per group, three independent experiments). (**c**) Enlarged view of only subclinical inflammation of single joints. (**d**) Correlation of imaging data and systemic S100A8/S100A9 levels of mice with clinical disease severity. Scoring of single feet were added up (maximum score 8 per mouse) and imaging data were calculated as mean values over all four feet. (**e**) S100A9 immunostaining of paw sections with CS of 0.5, 1.25 and 2 and control at day 28 confirmed correlation of local S100A8/S100A9 expression and severity of inflammation. Scale bar, 100 μm. (**f**,**g**) Simultaneous injection of a-S100A8-Cy7 (**f**) and a-S100A9-Cy5.5 (**g**) shows an almost identical distribution pattern in FRI. (**h**) Upper panel, representative pictures of paws for the different clinical scores. Lower panels, correlation of clinical scores with SNR for Cy7-labelled anti-S100A8 and Cy5.5-labelled anti-S100A9 ($n=5$ mice, mean ± s.d., $^*P<0.05$, $^{**}P<0.01$; one-way analysis of variance with Bonferroni's post test). (**i**) CIA was induced in C57BL/6 mice and a-S100A9-Cy5.5-driven FRI was performed at the first signs of arthritis (early time point) and for a second time where disease progression had occurred (late time point, 2 nmol of dye per mouse). All paws were analysed separately and compared with the clinical scoring as described in (**a**, $n=6$ mice). Representative images of an early (left image) versus late (right image) S100A9 scan are shown. White arrows indicate inflamed areas. Correlation of optical imaging data of early versus late time point (**j**) and early time point versus late clinical score (**k**). To correct for the variable areas of fore- and hind-paws, fluorescence intensities were normalized for the ROI size. Two fore-paws of one mouse were excluded from the analysis because of an incorrect position in the scanner (**j**,**k**). a.u., arbitrary units.

Analysing CIA, we confirmed an excellent correlation of S100A9 expression, as detected by optical imaging with local disease activity in individual joints. In addition, we demonstrated that the local expression of S100A9 and S100A8 is equally capable of uncovering sub-clinical disease activity, which is not reflected by established clinical parameters. Using blocking antibodies in arthritis models in WT and S100A9$^{-/-}$ mice revealed that this alarmin has a pivotal role in the inflammatory as well as in the

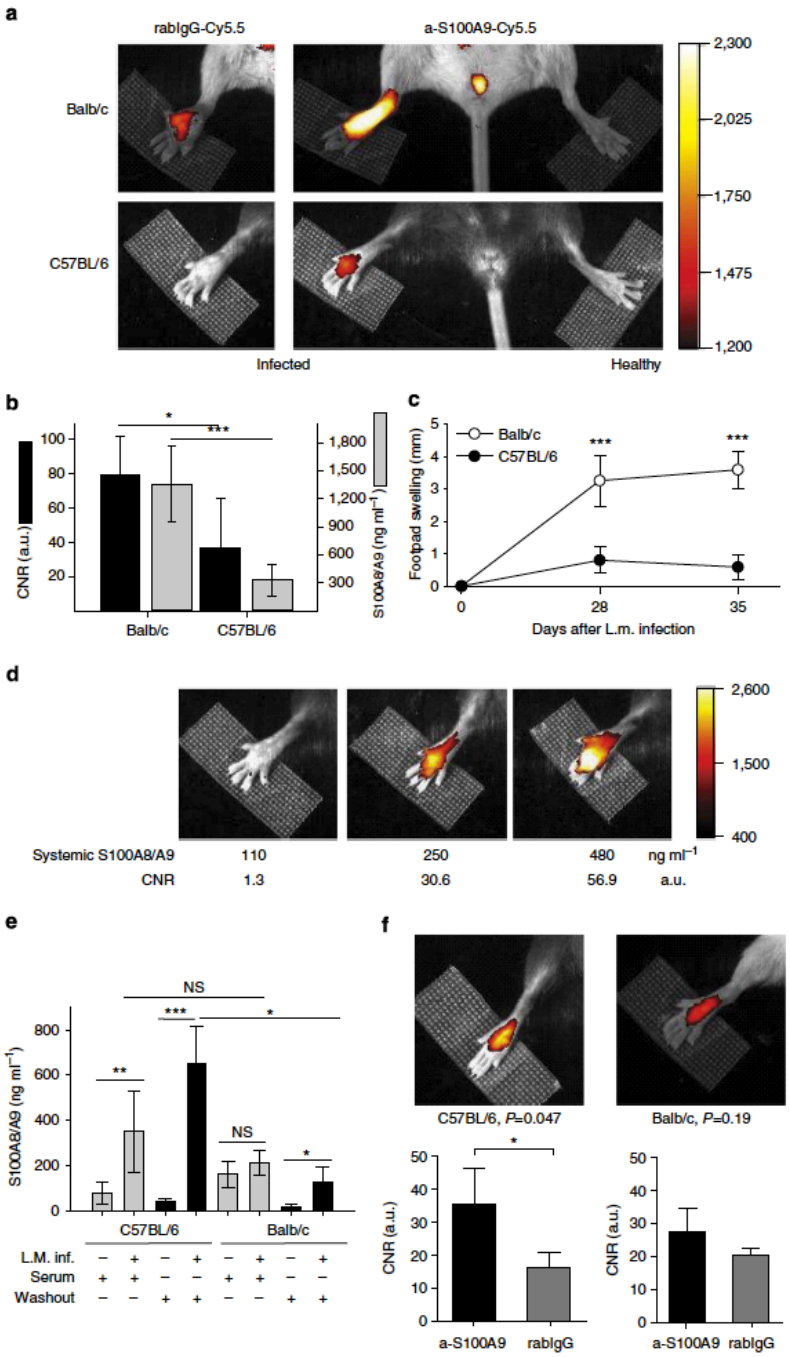

destructive process during arthritis[10,11,28], indicating that our imaging approach directly reflects major pathogenic aspects of arthritis.

In CIA, E-selectin-targeted optical imaging has been demonstrated to reflect inflammatory activity with similar SNR to our data[29]. Interestingly, S100A9 has been shown to induce the expression of E-selectin in endothelial cells[30], indicating that both methods address different target cells within closely linked inflammatory mechanisms. However, the high local level of S100A9 at sites of numerous inflammatory diseases makes this molecule more suitable for future imaging approaches in clinical practice. The detection of leukocyte populations with radiolabelled antibodies against macrophages (F4/80), T lymphocytes (CD4, CD3, CD40) or B lymphocytes (CD20), among others, and cell tracking studies with labelled cells have been used to monitor inflammatory processes in arthritis[31,32]. However, all of these approaches suffer from the disadvantage that the infiltration of significant numbers of these leukocytes takes a substantial amount of time and is not the initial event in the inflammation cascade. Moreover, leukocytes may persist during the resolution of inflammation, limiting the diagnostic value of these approaches for monitoring relapsing remitting courses of inflammation. Therefore, most of these studies have identified only low SNR and sometimes entirely failed to show a correlation of imaging results with disease activity[31,32]. The tissue destruction associated with phagocyte infiltration is reflected by protease activity and can be detected by small compounds targeting myeloperoxidase, cathepsin or matrix metalloproteinase activity[33–35]. However, these markers, in contrast to S100A8/S100A9, are not sensitive for the early inflammatory reaction, but reflect later stages of disease only.

Yet another interesting finding in our study was that the expression of S100A8/S100A9 during the initial phase of an inflammatory (infectious) process was the first early and sensitive marker for subclinical phagocyte activation known to be linked to the development of an effective Th1-response in this model. During the very early phase of *L. major* infection (day 4), we were able to visualize the effective activation of phagocytes in resistant C57BL/6 mice. In susceptible Balb/c mice, the lack of adequate, early phagocyte activation and differentiation into a pro-inflammatory M1-phenotype was reflected by low S100 expression in our imaging approach associated with priming a Th2 response, not sufficient to fight the infection. Hence, the imaging signal allowed for the prediction of a fatal outcome of disease, even weeks before full manifestation of the clinical phenotype and disease dissemination in this particular disease model.

Our data demonstrate for the first time that targeting members of the alarmin or DAMP family is a potent strategy for functional molecular imaging of inflammatory processes in general and independent of the underlying pathophysiology. Similar results of local expression of an alarmin family member could be demonstrated using a transgene reporter mice model for HSP-70 expression in ischemic brain injury. However, such transgenic approaches unfortunately only have limited potential for translation into clinical applications[36]. Owing to their specific mode of expression and release, S100A8 and S100A9 are sensitive biomarkers for the immediate response of innate immune mechanisms to disturbances of tissue homeostasis. The induction and release of S100A8/S100A9 have been shown to correlate very well with disease activity in many clinically relevant disorders, including rheumatoid arthritis, inflammatory bowel disease, autoimmune diseases, infections, allograft rejection or chronic processes like atherosclerosis, which underlines the translational potential and high impact of our findings for future basic research as well as clinical applications[3,7,12]. Optical imaging driven by fluorescently labelled antibodies has a growing translational potential beyond its impact on preclinical research and may be applicable for the examination of superficial lesions such as cutaneous inflammation. In addition, fluorescence endoscopy is gaining increasing interest and could foster the clinical use of fluorescent contrast agents[37]; for example, in the evaluation of inflammatory bowel disease, which is known to exhibit a very high local expression of S100A8/S100A9 (calprotectin)[38]. The potential of optical imaging of S100A8/S100A9 for regular clinical use is moreover underlined by the introduction of an optical scanner for visualization of the disease activity in rheumatoid arthritis, another inflammatory disorder with high local S100A8/S100A9 expression, currently driven by ICG fluorescence[39]. Finally, S100A8/S100A9 are highly upregulated during tumour development and even in the developing metastatic niche[40]. Therefore, another specific demand for optical molecular imaging of S100 proteins may arise in the context of intraoperative imaging for the safe delineation of malignant tissue during tumour resection[41].

For the translation of target-specific imaging approach into deep tissue imaging, other label strategies may have to be explored. Replacing the fluorescent dye with a radionuclide for either single photon emission computed tomography (SPECT) or PET imaging would allow for the examination of virtually all body compartments in humans, with specificity and sensitivity resembling that of optical imaging. With hybrid systems like PET/CT and PET/MRI increasingly applied in clinical imaging, targeted imaging of S100A8/A9 could be combined with high-resolution morphology. Targeted contrast agents for MRI, based on either superparamagnetic iron oxides or Gadolinium, suffer from the low sensitivity of MRI at clinical field strength and—in comparison to optical or radionuclide-driven imaging—large

Figure 4 | Mouse strain-specific responses during *L. major* infection monitored by S100A9 imaging *in vivo*. (**a**) Right hind legs of C57BL/6 mice and Balb/c mice (three independent experiments, each five mice per group) were infected with *L. major*, whereas the left hind legs served as controls. FRI was monitored during the late phase of infection at day 28 after receiving either a-S100A9-Cy5.5 or rabIgG-Cy5.5 (2 nmol of dye per mouse) 24 h earlier. (**b**) CNR was calculated for both mouse strains at day 28 after *L. major* infection. Significant strain-specific differences were found for both local (CNR) and systemic (S100A8/S100A9) parameters (three independent experiments, each five mice per group, mean ± s.d., $^{*}P<0.05$, $^{***}P<0.001$; Mann–Whitney *U*-test). (**c**) Footpad swelling of infected C57BL/6 mice and Balb/c mice at day 28 and 35 in relation to non-infected contralateral foot pads (mean ± s.d., $n=5$ for each mouse strain, $^{***}P<0.001$; *t*-test) demonstrates the different outcome in both mouse strains. (**d**) Individual comparison of representative optical imaging data (CNR) of infected C57BL/6 mice at day 28 after infection shows fairly good accordance, suggesting that systemic S100A8/S100A9 levels resemble disease activities. (**e**) During early *L. major* infection (day 4), sera (grey bars) and footpad washouts (black bars) of infected and non-infected mice were collected and analysed for S100A8/S100A9 by ELISA. Systemic and local S100A8/S100A9 levels were already significantly increased in infected C57BL/6 mice as compared with controls. In Balb/c mice, only a minor, nonsignificant increase in local S100A8/S100A9 expression was observed. Data are from fvie mice per group (mean ± s.d., $^{*}P<0.05$, $^{**}P<0.01$, $^{***}P<0.001$ and NS, not significant; Mann–Whitney *U*-test). (**f**) At day 4 already, local upregulation of S100A9 expression could be monitored in resistant C57BL/6 mice by optical imaging ($P=0.047$ by *t*-test) reflecting phagocyte activation. This was not detectable in susceptible Balb/c mice ($P=0.19$). Data are from five mice per group. a.u., arbitrary units.

amounts of the agent are required to incur a measurable change in relaxivity[42]. Although the visualization of tracer accumulation in areas of inflammation could be demonstrated for Gadolinium-loaded nanoparticles in selected experimental models[27], a convincing approach with translational potential has yet to be developed. Moreover, the combinatory application of contrast enhanced MRI and targeted imaging in hybrid systems to acquire even more diagnostic information in a single examination would be negated by the use of targeted MRI probes. As a paradigm for such future developments in molecular imaging, we provide the first fully integrated diagnostic approach on a member of the DAMP/alarmin family in various preclinical models of different modes of inflammation with clear potential for translation into clinical practice.

Materials and methods

Mice and reagents. C57BL/6 mice, Balb/c mice (Harlan Laboratories), DBA/jdba1/j mice (Janvier-Elevage) and S100A9-deficient mice (S100A9$^{-/-}$, back-crossed to C57BL/6 or Balb/c background (F10 generation))[43] were used at the age of 8–12 weeks, sex matched for each set of experiments and housed under specific pathogen-free conditions. All experiments with mice were performed with the approval of the State Review Board of Nordrhein-Westfalen (Germany) according to the German law for animal welfare (Permit Number: 84-02.04.2012.A058) or by the Ethics Committee of University Hospital Nijmegen (Permit Number: DEC 2014-044). All reagents were purchased from Sigma at the highest purity grade available, unless indicated otherwise.

ELISA. We used an in-house ELISA to determine the concentrations of S100A8/S100A9 in sera and washouts of footpads, as described earlier (Supplementary Fig. 1)[10]. We calibrated our ELISA against purified S100A8/S100A9 heterodimer as complexes have been shown to be the predominant form of these proteins.

Antibodies and antibody labelling. Rabbit-derived antibodies addressing S100A9 or S100A8 were purified via protein G-sepharose and labelled with the fluorochromes Cy5.5 or Cy7 according to the manufacturer's instructions (GE Healthcare). Cy5.5-labelled rabbit IgG without relevant specificity in mice served as a control. Briefly, 5 mg of the antibody was dialysed towards 100 mM Na_2CO_3 buffer, pH 8.0 and a 20-fold excess of the fluorochrome was added for 90 min at RT. The resulting tracer was purified from unbound dye using size exclusion chromatography (PD10 column). The labelling efficacy (dye/antibody ratio) was determined on the basis of ultraviolet-spectra of the purified dye-antibody compound using PBS as a reference buffer. Typically, the labelling resulted in 2.5–3.0 fluorochrome molecules per antibody, irrespective of the precursors.

***In vivo* imaging.** Mice were held under isoflurane inhalation anaesthesia for the duration of the scan and the imaging chamber was heated to 30°. As the total scan time was usually under 1 min, physiological effects due to a significant decrease of body temperature were not to be expected. Mice were intravenously injected with either the specific Cy5.5-labelled S100A9 antibody (a-S100A9-Cy5.5, 2 nmol of Cy5.5 ~100 µg antibody in total) or Cy5.5-labelled antibody of irrelevant specificity (rabIgG-Cy5.5), unless specified otherwise. In selected experiments, a-S100A9-Cy5.5- and Cy7-labelled S100A8 antibodies (a-S100A8-Cy7) or a-S100A9-Cy5.5- and Cy7-labelled S100A9 antibodies (a-S100A9-Cy7) or a-S100A9-Cy5.5 and rabIgG-Cy5.5 antibodies were administered in parallel in the same animal for simultaneous detection.

FRI. FRI was performed using the Carestream FX Pro Imaging Station (Carestream Health). For imaging of Cy5.5-labelled antibodies, excitation light was set to 630 nm using an appropriate bandpass filtre. Emission at 700 nm was recorded using a filtre-equipped high-sensitivity (4-million-pixel) cooled charge-coupled device camera. Acquisition time was 30 s for each image, followed by a photography-style white light image or conventional X-ray for image fusion and co-registration of anatomical information.

For the imaging of Cy7-labelled compounds, excitation and emission wavelengths were 730 and 790 nm, respectively; acquisition time was 30 s.

For the time of examination, mice were held under isoflurane inhalation anaesthesia (2.5% isoflurane in air).

For each region of interest measured for imaging analysis, the mean fluorescence intensity (SI) and resulting standard deviation (s.d.) were determined.

From the acquired fluorescence signals of the target region (SI_{target}), SNRs were calculated as $SNR = SI_{target}/s.d._{background\ signal}$.

If possible, the comparison of affected organs (target) and healthy organs (control) in the same animal CNRs were calculated as $CNR = (SI_{target} - SI_{control})/s.d._{background}$.

PET and CT scanning. Animals were anaesthetized with isoflurane, and 10 MBq of ^{18}F-FDG in 100 µl 0.9% saline was injected intravenously 1 h before each PET analysis. For PET acquisition, animals were placed on a heat-controlled multimodal scanning bed and PET list mode data were acquired for 15 min using the 32-module quadHIDAC scanner (Oxford Positron Systems), dedicated to small animal imaging. The scanner has an effective resolution of 0.7 mm (full-width at half-maximum) in the transaxial and axial directions when using an iterative resolution recovery reconstruction algorithm. Subsequently, the scanning bed was transferred to the computed tomography scanner (Inveon, Siemens Medical Solutions) and a medium resolution (25 µm) CT acquisition was performed for each mouse. PET data were reconstructed into a single image volume for each mouse with a voxel size of $0.4 \times 0.4 \times 0.4\,mm^3$. CT was reconstructed into a volume data set with a voxel size of $0.007 \times 0.007 \times 0.007\,mm^3$. Image data sets were co-registered using extrinsic markers attached to the multimodal scanning bed and commercially available image analysis software (Inveon Research Workplace, Siemens Medical Solutions).

Immunohistochemistry. Immunohistochemistry of ear sections (cryo) or paw sections (paraffin) was performed as described earlier using purified rabbit antisera against murine S100A9 (refs 10,13). Briefly, after inhibition of endogenous peroxidase activity in frozen tissue sections Fc receptors were blocked by incubating in PBS/1% BSA including 50% normal goat serum (NGS). Slides were immunostained in a two-step procedure of incubation of primary antibody or isotype control followed by a horseradish peroxidase-conjugated secondary antibody using AEC as chromogen. Images were acquired by using an upright microscope (Axioskop, Zeiss). Paws from arthritis experiments were fixed in 4% formaldehyde and joints were decalcified with 5% formic acid in PBS during 7 days. After dehydration and embedment in paraffin, sections of the paws were cut (7 µM) in a standardized manner and processed for S100A9 staining. Sections were treated with 1% H_2O_2 to inhibit endogenous peroxidase and 0.1% Triton/PBS for antigen retrieval and additionally incubated with rabbit anti-S100A9 antibodies followed by a goat-anti-rabbit biotinylated antibody and 3,3′ diaminobenzidine (DAB).

Eliciting irritant and ACD. ICD was induced by the application of 1% croton oil in olive oil-acetone (1:4) to the dorsal surface of the right ear of mice ($n = 5$ per group) for 24 h, whereas the left ear served as a control. FRI was performed at 24, 48, 72 and 96 h after tracer application, corresponding to 48, 72, 96 and 120 h after croton oil treatment, respectively. Subsequently, mice were killed and ears were snap-frozen in liquid nitrogen and transferred for immunohistochemistry.

To elicit ACD, C57BL/6 or Balb/c mice were sensitized by the application of 25 µl of 0.5% 2,4-dinitrofluoro-1-benzene (Sigma) in olive oil/acetone (1:4) to the shaved abdominal wall on two consecutive days. Six days later, mice were challenged with 15 µl of 0.4% 2,4-dinitrofluoro-1-benzene in olive oil/acetone on the dorsal surface of the right ear. At day 2, mice were injected with either a-S100A9-Cy5.5 or rabIgG-Cy5.5 or a combination of a-S100A9-Cy5.5/rabIgG-Cy7, a-S100A9-Cy5.5/a-S100A9-Cy7 or a-S100A9-Cy5.5/rabIgG-Cy5.5. FRI was performed at different time points after antibody application, as indicated in Fig. 2. The disease severity of ACD was monitored by measuring the ear swelling.

Induction and imaging of CIA. Arthritis was induced in DBA/jdba1/j or C57BL/6 mice by immunization using bovine collagen type II as described in detail earlier[44]. Briefly, bovine collagen type II (bCII, MD Biosciences) was dissolved in 0.05 M acetic acid at a concentration of 2 mg ml^{-1}. Mice were injected subcutaneously at the tail base with 100 µg bCII emulsified in Complete Freund's Adjuvant (Difco). The animals were boosted at day 21 with an intraperitoneal injection of 100 µg bCII. The onset of polyarthritis occurred around 4–5 days later. Mice were regularly inspected from day 14 after disease induction and scored for swelling, erythema and deformation of each joint three times a week (CS0 = no swelling, CS1 = slight swelling and erythema, CS2 = pronounced oedema including joint rigidity). Scoring of single joints was added up to a maximum possible score of eight per mouse (two per paw). Regarding the susceptibility of C57BL/6 mice, arthritis was evaluated using an extended scoring three-point scale: 0 = normal; 0.5 = erythema, light oedema; 1 = mild but definitely visible, erythema and oedema of one digit/toe or limb; 2 = erythema and moderate oedema of at least two digits/toe or limb; 3 = erythema, severe oedema of the entire paw and/or rigidity. Imaging was performed after arthritis was clinically detectable in the majority of treated animals 24 h after tracer application of either a-S100A9-Cy5.5 or rabIgG-Cy5.5 or a combination of a-S100A9-Cy5.5/a-S100A8-Cy7. At the end of the experiment, mice were killed and serum was collected for S100A8/S100A9 quantification by ELISA. Hindpaws were excised and processed for histology.

Experimental leishmaniasis. Cutaneous leishmaniasis was initiated in two different mouse strains (C57BL/6 and Balb/c) by the subcutaneous application of 2×10^7 promastigotes (stationary phase) of *L. major* in 50 µl PBS into the right hind footpad. Footpad thickness of the infected in relation to the healthy foot was assessed for clinical monitoring of disease. FRI was performed at days 4 and 28 after infection (representative for an early and a late phase immune response), 24 h after tracer injection. In separate experiments, sera and footpad washouts were

collected at days 4 or 28 after *L. major* inoculation for S100A8/S100A9 quantification by ELISA. Briefly, *L. major* infected and non-infected hindpaws were washed out by s.c. injection of 250 µl PBS. Without applying any force, in order to obtain secreted protein, approximately 250 µl of the draining liquid was collected and used for further analysis.

Statistical analysis. Results are presented throughout as mean values ± standard deviation (s.d.). *P*-values are given in the figure legends and values of $P > 0.05$ were considered not to be significant. Statistical analyses were performed by parametric tests (*t*-test or one-way analysis of variance) and the Mann–Whitney *U*-test.

References

1. Chan, A. C. & Behrens, T. W. Personalizing medicine for autoimmune and inflammatory diseases. *Nat. Immunol.* **14,** 106–109 (2013).
2. Gotthardt, M., Bleeker-Rovers, C. P., Boerman, O. C. & Oyen, W. J. Imaging of inflammation by PET, conventional scintigraphy, and other imaging techniques. *J. Nucl. Med.* **51,** 1937–1949 (2010).
3. Chan, J. K. *et al.* Alarmins: awaiting a clinical response. *J. Clin. Invest.* **122,** 2711–2719 (2012).
4. Harris, H. E., Andersson, U. & Pisetsky, D. S. HMGB1: a multifunctional alarmin driving autoimmune and inflammatory disease. *Nat. Rev. Rheumatol* **8,** 195–202 (2012).
5. Rock, K. L., Latz, E., Ontiveros, F. & Kono, H. The sterile inflammatory response. *Annu. Rev. Immunol.* **28,** 321–342 (2010).
6. Yang, D., de la Rosa, G., Tewary, P. & Oppenheim, J. J. Alarmins link neutrophils and dendritic cells. *Trends Immunol.* **30,** 531–537 (2009).
7. Ehrchen, J. M., Sunderkotter, C., Foell, D., Vogl, T. & Roth, J. The endogenous Toll-like receptor 4 agonist S100A8/S100A9 (calprotectin) as innate amplifier of infection, autoimmunity, and cancer. *J. Leukoc. Biol.* **86,** 557–566 (2009).
8. Vogl, T. *et al.* Mrp8 and Mrp14 are endogenous activators of Toll-like receptor 4, promoting lethal, endotoxin-induced shock. *Nat. Med.* **13,** 1042–1049 (2007).
9. Loser, K. *et al.* The Toll-like receptor 4 ligands Mrp8 and Mrp14 are crucial in the development of autoreactive CD8+ T cells. *Nat. Med.* **16,** 713–717 (2010).
10. van Lent, P. L. *et al.* Myeloid-related proteins S100A8/S100A9 regulate joint inflammation and cartilage destruction during antigen-induced arthritis. *Ann. Rheum. Dis.* **67,** 1750–1758 (2008).
11. van Lent, P. L. *et al.* Active involvement of alarmins S100A8 and S100A9 in the regulation of synovial activation and joint destruction during mouse and human osteoarthritis. *Arthritis Rheum.* **64,** 1466–1476 (2012).
12. Foell, D. *et al.* Methotrexate withdrawal at 6 vs. 12 months in juvenile idiopathic arthritis in remission: a randomized clinical trial. *JAMA* **303,** 1266–1273 (2010).
13. Petersen, B. *et al.* The alarmin Mrp8/14 as regulator of the adaptive immune response during allergic contact dermatitis. *EMBO J.* **32,** 100–111 (2013).
14. Haroon, A., Zumla, A. & Bomanji, J. Role of fluorine 18 fluorodeoxyglucose positron emission tomography-computed tomography in focal and generalized infectious and inflammatory disorders. *Clin. Infect. Dis.* **54,** 1333–1341 (2012).
15. Frosch, M. *et al.* Myeloid-related proteins 8 and 14 are specifically secreted during interaction of phagocytes and activated endothelium and are useful markers for monitoring disease activity in pauciarticular-onset juvenile rheumatoid arthritis. *Arthritis Rheum.* **43,** 628–637 (2000).
16. Sacks, D. & Noben-Trauth, N. The immunology of susceptibility and resistance to Leishmania major in mice. *Nat. Rev. Immunol.* **2,** 845–858 (2002).
17. McDonald, B. *et al.* Intravascular danger signals guide neutrophils to sites of sterile inflammation. *Science* **330,** 362–366 (2010).
18. van Zoelen, M. A. *et al.* Expression and role of myeloid-related protein-14 in clinical and experimental sepsis. *Am. J. Respir. Crit. Care Med.* **180,** 1098–1106 (2009).
19. Huckins, D. S. *et al.* A novel biomarker panel to rule out acute appendicitis in pediatric patients with abdominal pain. *Am. J. Emerg. Med.* **31,** 1368–1375 (2013).
20. Barrera, P. *et al.* Radiolabelled interleukin-1 receptor antagonist for detection of synovitis in patients with rheumatoid arthritis. *Rheumatology* **39,** 870–874 (2000).
21. Barrera, P., Oyen, W. J., Boerman, O. C. & van Riel, P. L. Scintigraphic detection of tumour necrosis factor in patients with rheumatoid arthritis. *Ann. Rheum. Dis.* **62,** 825–828 (2003).
22. Roimicher, L. *et al.* (99m)Tc-anti-TNF-alpha scintigraphy in RA: a comparison pilot study with MRI and clinical examination. *Rheumatology (Oxford)* **50,** 2044–2050 (2011).
23. Achouiti, A. *et al.* Myeloid-related protein-14 contributes to protective immunity in gram-negative pneumonia derived sepsis. *PLoS Pathog.* **8,** e1002987 (2012).
24. Rammes, A. *et al.* Myeloid-related protein (MRP) 8 and MRP14, calcium-binding proteins of the S100 family, are secreted by activated monocytes via a novel, tubulin-dependent pathway. *J. Biol. Chem.* **272,** 9496–9502 (1997).
25. Robinson, M. J., Tessier, P., Poulsom, R. & Hogg, N. The S100 family heterodimer, MRP-8/14, binds with high affinity to heparin and heparan sulfate glycosaminoglycans on endothelial cells. *J. Biol. Chem.* **277,** 3658–3665 (2002).
26. Teigelkamp, S. *et al.* Calcium-dependent complex assembly of the myeloic differentiation proteins MRP-8 and MRP-14. *J. Biol. Chem.* **266,** 13462–13467 (1991).
27. Maiseyeu, A. *et al. In vivo* targeting of inflammation-associated myeloid-related protein 8/14 via gadolinium immunonanoparticles. *Arterioscler. Thromb. Vasc. Biol.* **32,** 962–970 (2012).
28. Cesaro, A. *et al.* An inflammation loop orchestrated by S100A9 and calprotectin is critical for development of arthritis. *PLoS ONE* **7,** 18 (2012).
29. Gompels, L. L. *et al. In vivo* fluorescence imaging of E-selectin: quantitative detection of endothelial activation in a mouse model of arthritis. *Arthritis Rheum.* **63,** 107–117 (2011).
30. Viemann, D. *et al.* Myeloid-related proteins 8 and 14 induce a specific inflammatory response in human microvascular endothelial cells. *Blood* **105,** 2955–2962 (2005).
31. Gaal, J. *et al.* 99m Tc-HMPAO labelled leukocyte scintigraphy in patients with rheumatoid arthritis: a comparison with disease activity. *Nucl. Med. Commun.* **23,** 39–46 (2002).
32. Mountz, J. M., Alavi, A. & Mountz, J. D. Emerging optical and nuclear medicine imaging methods in rheumatoid arthritis. *Nat. Rev. Rheumatol.* **8,** 719–728 (2012).
33. Gross, S. *et al.* Bioluminescence imaging of myeloperoxidase activity *in vivo*. *Nat. Med.* **15,** 455–461 (2009).
34. Ntziachristos, V., Ripoll, J., Wang, L. V. & Weissleder, R. Looking and listening to light: the evolution of whole-body photonic imaging. *Nat. Biotechnol.* **23,** 313–320 (2005).
35. Peterson, J. D. *et al.* Optical tomographic imaging discriminates between disease-modifying anti-rheumatic drug (DMARD) and non-DMARD efficacy in collagen antibody-induced arthritis. *Arthritis Res. Ther.* **12,** R105 (2010).
36. de la Rosa, X. *et al. In vivo* imaging of induction of heat-shock protein-70 gene expression with fluorescence reflectance imaging and intravital confocal microscopy following brain ischaemia in reporter mice. *Eur. J. Nucl. Med. Mol. Imaging* **40,** 426–438 (2013).
37. Kim, S. Y. & Myung, S. J. Optical molecular imaging for diagnosing intestinal diseases. *Clin. Endosc.* **46,** 620–626 (2013).
38. Leach, S. T. & Day, A. S. S100 proteins in the pathogenesis and diagnosis of inflammatory bowel disease. *Expert Rev. Clin. Immunol.* **2,** 471–480 (2006).
39. Werner, S. G. *et al.* Inflammation assessment in patients with arthritis using a novel *in vivo* fluorescence optical imaging technology. *Ann. Rheum. Dis.* **71,** 504–510 (2012).
40. Hiratsuka, S. *et al.* The S100A8-serum amyloid A3-TLR4 paracrine cascade establishes a pre-metastatic phase. *Nat. Cell Biol.* **10,** 1349–1355 (2008).
41. Orosco, R. K., Tsien, R. Y. & Nguyen, Q. T. Fluorescence imaging in surgery. *IEEE Rev. Biomed. Eng.* **6,** 178–187 (2013).
42. Huang, C. H. & Tsourkas, A. Gd-based macromolecules and nanoparticles as magnetic resonance contrast agents for molecular imaging. *Curr. Top. Med. Chem.* **13,** 411–421 (2013).
43. Manitz, M. P. *et al.* Loss of S100A9 (MRP14) results in reduced interleukin-8-induced CD11b surface expression, a polarized microfilament system, and diminished responsiveness to chemoattractants *in vitro*. *Mol. Cell Biol.* **23,** 1034–1043 (2003).
44. Koenders, M. I. *et al.* Tumor necrosis factor-interleukin-17 interplay induces S100A8, interleukin-1beta, and matrix metalloproteinases, and drives irreversible cartilage destruction in murine arthritis: rationale for combination treatment during arthritis. *Arthritis Rheum.* **63,** 2329–2339 (2011).

Acknowledgements

We thank Eva Nattkemper, Heike Hater, Ina Winkler and Heike Berheide for their excellent technical support. This work was supported by Grants from the Interdisciplinary Center of Clinical Research of the University of Muenster (Vo2/014/09, PIX), the German Research Foundation (DFG) EI 878 1-1 to M.E., CRC 656 A09, CRC 1009 B8 and B9 from the European Union's Seventh Framework Program under EC-GA No. 305266 'MIAMI' to Th.V. and J.R., by the Federal Ministry of Education and Research (BMBF), project AID-NET to J.R. and CR-UK (C1519/A6906) and the KCL-UCL Comprehensive Cancer Imaging Centre CR-UK and EPSRC, in association with the MRC and DoH to M.E.

Author contributions

Th.V. designed and supervised the study and experiments, performed animal studies and wrote the manuscript. M.E. designed the study and the experiments, performed optical imaging and wrote the manuscript. T.V., B.P., S.Z., K.R. and P.v.L. performed animal experiments and analysed the data. S.H. and A.F. performed PET and PET/CT experiments and analysed the data. C.G. and C.B. designed and supervised the optical imaging experiments and edited the manuscript. M.S. supervised the PET imaging experiments

and edited the manuscript. J.R. designed the study and experiments and wrote the manuscript.

Additional information

Supplementary Information accompanies this paper at http://www.nature.com/naturecommunications

Competing financial interests: The authors declare no competing financial interests.

Reprints and permission information is available online at http://npg.nature.com/reprintsandpermissions/

How to cite this article: Vogl, T. *et al.* Alarmin S100A8/S100A9 as a biomarker for molecular imaging of local inflammatory activity. *Nat. Commun.* 5:4593 doi: 10.1038/ncomms5593 (2014).

10.2 Publication II – Becker, Große Hokamp et al

***In vivo* quantification of the alarmin S100A9 in tumor lesions allows for estimation of the individual malignant potential by evaluation of tumor host-cell interaction**

Becker A*, Große Hokamp N*, Flores-Borja F, Barzcyk K, Varga G, Roth J, Geyer C, Heindel W, Bremer C, Vogl T, **Eisenblaetter M**

Journal of Nuclear Medicine, 2015 Mar;56(3):450-6

Optical In Vivo Imaging of the Alarmin S100A9 in Tumor Lesions Allows for Estimation of the Individual Malignant Potential by Evaluation of Tumor–Host Cell Interaction

Anne Becker*[1], Nils Große Hokamp*[1], Stefanie Zenker[2], Fabian Flores-Borja[3,4], Katarzyna Barzcyk[2], Georg Varga[5], Johannes Roth[2,6], Christiane Geyer[1,6], Walter Heindel[1], Christoph Bremer[6,7], Thomas Vogl*[2,6], and Michel Eisenblaetter*[1,3,8]

[1]*Department of Clinical Radiology, University Hospital Münster, Münster, Germany;* [2]*Institute of Immunology, University Hospital Münster, Münster, Germany;* [3]*Richard Dimbleby Department of Cancer Research, King's College London, London, United Kingdom;* [4]*Breakthrough Breastcancer Unit, Guy's and St. Thomas' NHS Hospital Trust, London, United Kingdom;* [5]*Department of Paediatric Rheumatology and Immunology, University Hospital Münster, Münster, Germany;* [6]*Interdisciplinary Center for Clinical Research, Münster University, Münster, Germany;* [7]*Department of Radiology, St. Franziskus Hospital GmbH Münster, Münster, Germany; and* [8]*Division of Imaging Sciences and Biomedical Engineering, King's College London, London, United Kingdom*

Tumors recruit and reprogram immune cells to support tumor development and spread, the most prominent among them being of monocytic origin such as tumor-associated macrophages (TAM) or myeloid-derived suppressor cells (MDSC). The alarmin S100A8/A9 has been implicated in the induction of TAM and MDSC. We assessed S100A9 as a molecular imaging marker for the activity of tumor-associated immune cells in a syngeneic murine breast cancer model. S100A9 could serve as a surrogate marker for tumor immune crosstalk as a function of malignancy, providing a tool with the potential for both basic research in tumor immunology and clinical stratification of patients. **Methods:** BALB/c mice were inoculated with murine breast cancer cells of common origin but different metastatic capability. At different times during tumor development, optical imaging was performed using a S100A9-specific probe to visualize activated monocytes. To further explore the impact of tumor-educated monocytes, splenic myeloid cells were isolated from either healthy or tumor-bearing animals and injected into tumor-bearing mice. We analyzed the effect of the cell transfer on immune cell activity and tumor development. **Results:** We could prove S100A9-driven imaging to sensitively and specifically reflect monocyte activity in primary tumor lesions. The imaging results were corroborated by histology and fluorescence-activated cell sorting analyses. In a prospective experiment, S100A9 imaging proved indicative of the individual tumor growth, with excellent correlation. Moreover, we could show that the monocyte activity as depicted by S100A9 activity in the primary tumor lesion mirrored the tumor's metastatic behavior. Treatment with tumor-primed splenic monocytes induced increased tumor growth, accompanied by an augmented infiltration of activated myeloid cells (MDSC and TAM) into the tumor. The consecutive S100A9 expression as depicted by in vivo imaging was significantly increased. **Conclusion:** S100A9 proved to be a sensitive and specific marker for the activity of tumor-associated immune cells. To our knowledge, S100A9 imaging represents a first in vivo imaging approach for the estimation of recruitment and activity of tumor-associated myeloid immune cells. We demonstrated the potential value of this imaging approach for prediction of local and systemic tumor development.

Key Words: optical imaging; tumor immunology; monocytes; cancer; tumor-induced inflammation; MRP8/MRP14; calprotectin

J Nucl Med 2015; 56:450–456
DOI: 10.2967/jnumed.114.146688

The accumulation of activated immune cells in tumors in response to specific tumor signals has been recognized as a crucial driver of carcinogenesis, even marked one of the hallmarks of cancer in the latest edition of Hanahan and Weinberg's work (*1*). Among the cells infiltrating the tumor, macrophages and their precursors, monocytes, are the most abundant (*2*). A tumor-promoting role of so-called tumor-associated macrophages (TAMs) could be demonstrated, with TAM activity as an indicator of poor prognosis and reduced outcome for several types of malignant disease including breast cancer (*3,4*). TAMs secure tumor survival in various ways: their delivery of vascular endothelial growth factor and other angiogenic factors enhances neoangiogenesis. Their supply of different chemokines creates a tumor-permissive environment, maintained by myeloid-derived suppressor cells (MDSCs), suppressing the antitumor immune response (*5*) of natural killer and CD8+ cytotoxic T cells (*6*). Moreover, TAMs have been shown to support tumor growth and spread by degradation of extracellular matrix components and to be essentially involved in the development of metastasis with evidence for TAM action in multiple steps of this process (*7*).

The alarmin S100A8/A9 heterodimer seems to be a key molecule for TAM and MDSC action. S100A8/A9 is a member of the S100 protein family of calcium-binding proteins and under physiologic circumstances involved in calcium homeostasis and tubulin turnover (*8*). Secreted by activated phagocytes via a hitherto unknown mechanism, S100A8/A9 induces proinflammatory effects via binding to TLR4 or RAGE regulating migration, activation, and

Received Aug. 4, 2014; revision accepted Jan. 12, 2015.
For correspondence or reprints contact: Michel Eisenblaetter, Comprehensive Cancer Imaging Centre, Division of Imaging Sciences and Biomedical Engineering, and The Richard Dimbleby Department of Cancer Research, New Hunt's House, Guy's Hospital Campus, London SE1 1UL, U.K.
E-mail: michel.eisenblaetter@kcl.ac.uk
*Contributed equally to this work.
Published online Feb. 12, 2015.

TABLE 1
Summary of In Vivo Imaging Experiments

Experiment	Mouse strain	Tumor type	*n*	Tracer	Purpose	Fig.
I	BALB/c wt	4T1	28	1, 2	Proof of principle	1
II	S100A9−/−	4T1	5	1	Proof of specificity	1
III	BALB/c wt	4T1	6	1, 3	Parallel injection (tracer 2 labeled with Cy7)	1
IV	BALB/c wt	4T1	11	1	Correlation signal/growth	2
V	BALB/c wt	4T1; 67NR, 168FAR	32	1	Correlation signal/malignancy	3
VI	BALB/c wt	4T1	20	1	Cell transfer	4

wt = wild-type; 1 = tracer aS100A9-Cy5.5; 2 = tracer rabIgG-Cy5.5; 3 = tracer rabIgG-Cy7.

maturation of myeloid immune cells (*9*). In the tumor microenvironment, S100A8/A9 induces MDSC, promoting tumor-induced immunomodulation (*10,11*). S100A8/A9 is secreted by monocytes/macrophages (*12*) early during immigration into the tumor region and consecutive differentiation (*13*) hence reflecting their respective local activity. Therefore, S100A8/A9 appears to be an attractive target for visualization of monocyte/TAM activity in the tumor microenvironment, indicative of tumor tissue crosstalk.

In a recent publication, the principles of S100A9 imaging were successfully established in various models of inflammation, confirming sensitivity and specificity of the antibody-based tracer aS100A9-Cy5.5 for local changes of monocyte activity (*14*). On the basis of this experience, we aimed to prove the feasibility to visualize tumor-associated inflammation and assess this approach for estimation of the activity of tumor-educated immune cells in the tumor microenvironment.

MATERIALS AND METHODS

Tracer Synthesis

A polyclonal antibody against murine S100A9, harvested and purified from immunized rabbits in house, was labeled with Cy5.5 (aS100A9-Cy5.5, λ excitation [λ_{ex}] = 673 nm; λ emission [λ_{em}] = 692 nm; GE Healthcare Bio-Sciences Corp.) as described earlier (*14*). As control for unspecific tracer distribution, rabbit-derived IgG of irrelevant specificity was labeled with Cy5.5 or Cy7 (rabIgG-Cy5.5/Cy7, λ_{ex} = 747 nm; λ_{em} = 774 nm; GE Healthcare Bio-Sciences Corp.) for parallel injection experiments. All tracers were injected intravenously into the tail of mice in amounts of 2 nmol dye (~100 μg antibody) 24 h before imaging.

Tumor Models

In vivo experiments are summarized in Table 1.

All animal experiments in this study have been approved by the responsible authorities (reference of local government approval AZ 8.87-50.10.36.08.191) and performed according to the regulations set out by the institutional review committees.

Female BALB/c (Charles River Laboratories Deutschland) or S100A9 knock-out mice with genetic BALB/c background (age, 8–12 wk) were used.

Murine breast cancer cell lines 4T1, 168FAR, and 67NR share the genetic background of a common maternal cell line and were used for tumor induction as an established syngeneic model system of graded malignancy (*15*). Characteristics of the tumor cells are summarized in Table 2. Cells were cultured and harvested according to established protocols (*15*). Cells (1.5×10^6) in 50 μL of phosphate-buffered saline were implanted into mice either subcutaneously over the flank (experiments I–IV, VI) or orthotopically into the mammary fat pad (experiment V). Tumor size was measured daily.

To control for a contribution of the tumor cells to local S100A9 levels and to prove specific tracer to target binding, S100A9−/− mice (*16*) were inoculated with 4T1 cells accordingly and underwent the same imaging procedure.

All imaging experiments were performed tumor-size-dependent (4–6 mm) to reduce the influence of differences in tumor growth between cell lines or mouse strains (*17*). For experiment IV, animals were kept after in vivo imaging, and the tumor growth was monitored over the following 8–10 d.

Cell Transfer

From spleen tissue of either healthy or 4T1 tumor–bearing mice (10 d after tumor implantation), CD11b+ cells were isolated using magnetic cell separation and transferred into mice, which were subsequently inoculated with 4T1 tumors (amount of transferred CD11b+ cells, 1×10^6). In the spleens of tumor-bearing animals, this population of myeloid cells/monocytes should contain tumor-educated MDSC (*18*). Eight days after tumor implantation, all animals underwent S100A9 imaging as described below.

In Vivo Imaging

For in vivo optical imaging, a fluorescence-reflectance imaging (FRI) system (Bruker BioSpin) was used. Excitation light was adapted according to the dyes to 630 nm (Cy5.5) or 730 nm (Cy7), respectively. The resulting emission was recorded at 700 or 790 nm, using a filter-equipped, high-sensitive charge-coupled device camera. Signal acquisition time was 30 s (experiment V, 5 s) for fluorescence images. White-light images were acquired for anatomic orientation.

Fluorescence-mediated tomography (FMT) was used for 3-dimensional visualization of dye distribution in the target region. The free space flat panel FMT device (In-vivo Imaging System FMT 2500 and FMT 2500 Imaging Software, version 1.1.1.3; both Visen Medical) allowed for reconstruction of 3-dimensional data from fluorescence signals at 680 and 750 nm for visualization of Cy5.5 or Cy7 (*19,20*). Scanning time of the tumor region was around 4 min.

TABLE 2
Characteristics of Murine Breast Cancer Cells

Characteristic	4T1	168FAR	67NR
Shed cells	++	+	—
Invasion	+	—	—
Regional lymph node	—	+	—
Solid metastasis	++	—	—

++ = very strong; + = detectable; — = not detectable.

Mice were held under inhalation anesthesia (2.0% isoflurane in air) during examinations.

The region of interest (ROI) was placed to cover the whole tumor area as depicted on white light images. FRI data were presented as mean photon counts, normalized for the ROI area, in arbitrary units (AUs). From each dataset, mean values and SD were calculated.

For experiment VI, scans were performed immediately (0 h) and 24 h after tracer injection. From these values, a Δfluorescence intensity (ΔFI) was calculated as signal from the target ROI at 24 h minus signal from the target ROI at 0 h. After in vivo imaging, animals were sacrificed and organs were harvested for correlative ex vivo examination of dye-distribution using FRI; tumor tissue was harvested for fluorescence-activated cell sorting (FACS) or histology.

Validation Experiments

The resected tumors were divided, and equal amounts of tissue were processed for immunohistochemistry and FACS, respectively. For FACS, single-cell suspensions were produced from tumor tissue and stained for S100A9 and CD11b with corresponding isotype controls.

Monocyte specific staining was performed using an allophycocyanin-labeled ratCD11b antibody (eBioscience) and S100A9-specific staining with a polyclonal S100A9 antibody and fluorescein isothiocyanate–labeled goat-antirabbit secondary antibody (Jackson Immuno Research Europe). Nonspecific rabIgG and allophycocyanin-labeled rabIgG (eBioscience) were used as controls. FACS data were gated according to size and granularity to exclude cell detritus. Isotype controls served for adjusting individual FACS measurements. All FACS measurements were conducted using a FACSCalibur system and analyzed using the CellQuest Pro software (both BD Biosciences). Data were presented as cell frequency reduced by the individual isotype control to exclude unspecific staining.

For histology, tissue was paraffin-embedded and cut. Tumor sections were stained for S100A9 and F4/80 (macrophages) for direct correlation of imaging findings. All stainings were performed according to established protocols (*21,22*).

Moreover, lysates from resected tumors, tumor cells from tissue culture, and tissue culture supernatant were analyzed for S100A8/A9 using a specific, in-house–established enzyme-linked immunosorbent assay (ELISA) (*14,23*).

Statistical Analysis

Data were analyzed using the Student *t* test (experiments I, II, VI), 1-way ANOVA test with Bonferroni post test (experiment V), or linear regression (experiment IV). All analyses were performed using the GraphPad Prism software (version 4.03; GraphPad Software Inc.).

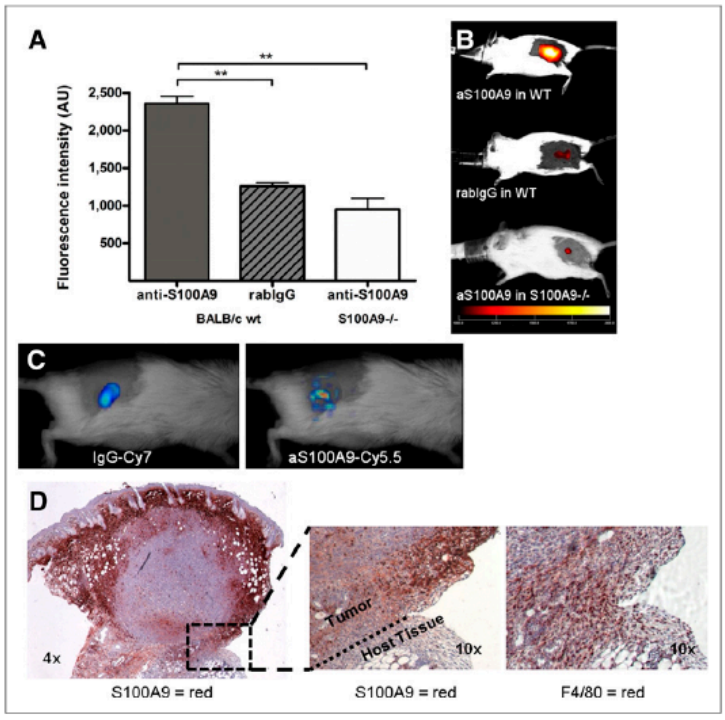

FIGURE 1. (A and B) S100A9 imaging specifically identifies tumor-associated immune cells. aS100A9-Cy5.5 injection in 4T1 tumor–bearing wild-type (wt) animals results in significantly higher specific fluorescence than unspecific rabIgG-Cy5.5 or injection of specific aS100A9-Cy5.5 in S100A9−/− knock-out mice. (C) FMT after parallel injection of rabIgG-Cy7 and aS100A9-Cy5.5 showed homogeneous distribution of rabIgG-Cy7 in tumor region, reflecting perfusion, whereas aS100A9-Cy5.5 accumulated in delineated regions only. (D) Histology confirmed S100A9+ cells (red) in corresponding, peripheral areas of tumor (left) with F4/80+ TAM detectable within clusters of S100A8/A9+ active monocytes (right).

RESULTS

In Vivo Imaging: Proof of Principle

To prove specificity of tracer to target binding and to control for unspecific tracer accumulation (e.g., perfusion-related or $F_c\gamma R$-mediated), 4T1 tumor–bearing mice were injected with aS100A9-Cy5.5 or rabIgG-Cy5.5. A significantly higher signal in FRI was detected after injection of the specific probe than after injection of equal amounts of rabIgG-Cy5.5 (2,430 vs. 1,240 AUs; $P < 0.001$, $n = 16/12$). In S100A9−/− mice, injection of aS100A9-Cy5.5 resulted in signals comparable to the rabIgG-Cy5.5–mediated signal in wild-type animals (950 AUs; $n = 5$) (Figs. 1A and 1B). In ex vivo biodistribution studies, resected organs were analyzed for fluorescence signals and a significantly higher fluorescence in the tumor after injection of aS100A9-Cy5.5 than rabIgG-Cy5.5 could be verified (Supplemental Fig. 1; supplemental materials are available at http://jnm.snmjournals.org). Tumor-to-nontarget tissue ratios (kidneys, muscle) were significantly higher for aS100A9-Cy5.5 (aS100A9-Cy5.5 vs. rabIgG-Cy5.5 tumor to kidney: 3.2 vs. 2.1; $P \leq 0.001$; tumor to muscle: 3.76 vs. 2.4; $P \leq 0.05$).

After parallel injection of aS100A9-Cy5.5 and rabIgG-Cy7, FMT allowed for simultaneous evaluation of the distribution of both tracers. Although rabIgG-Cy7 showed a homogeneous distribution over the whole vital tumor area, aS100A9-Cy5.5 accumulated in delineated hot-spot areas,

predominantly located in the periphery of the tumor (Fig. 1C). TAMs within clusters of S100A9+ cells could accordingly be defined by histology (Fig. 1D).

S100A9 Imaging Correlates with Tumor Growth

The development of 4T1 tumors was assessed longitudinally over 10 d, after imaging at an early stage of tumor development (tumor size, <5 mm).

A higher aS100A9-Cy5.5 signal in early FRI and the confirmatory detection of an increased presence of S100A9+ cells on tumor resection were found in fast-growing tumor lesions as compared with lesions with slower development and only mild aS100A9 accumulation (Figs. 2A and 2B). The S100A9 signal strongly correlated with the consecutive individual tumor growth ($R^2 = 0.86$; $P < 0.0001$, $n = 11$) (Fig. 2C).

S100A9 Signals Reflect Metastatic Potential

Targeted S100A9 imaging revealed significant differences between the 3 tumor entities, with 4T1 tumors exhibiting the highest aS100A9 accumulation (FRI signal, 427.3 AUs), followed by 168FAR (325.2 AUs) and 67NR (250.8 AUs) (Figs. 3A and 3B). The ex vivo analysis of the tumor immune cell infiltrate revealed the presence of CD11b+ cells in all tumors (Figs. 3C and 3D), with the amount of S100A9+ cells among the immune cell infiltrate confirming the in vivo imaging (4T1, 8.7% of total cell infiltrate; 168FAR, 2.0%; 67NR, 1.2%) and reflecting the specific grade of malignancy (Fig. 3D).

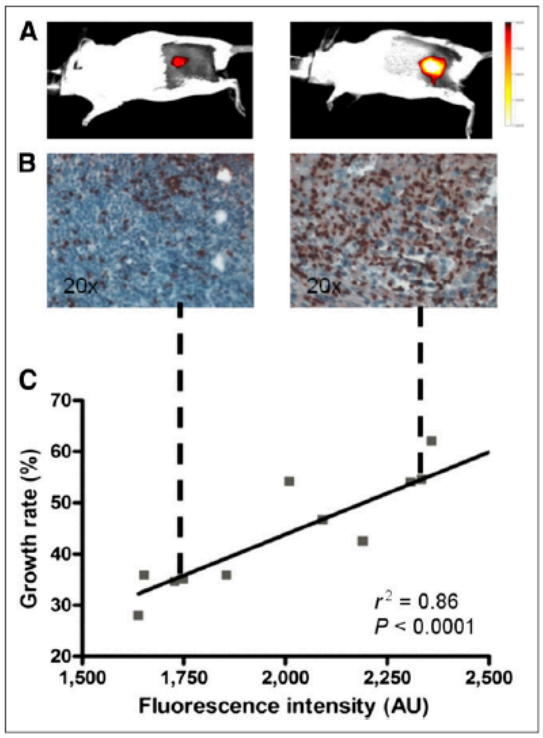

FIGURE 2. Correlation between tumor growth and S100A9 fluorescence intensity. S100A9 imaging at early time points during tumor development (lesion size < 5 mm; A) shows only low fluorescence signals in animals with subsequently only moderate tumor growth (left). Ex vivo, only few S100A9+ cells (red/brown) could be found in tumor specimens of these animals (B, left). High initial S100A9 signal (A, right) predicted more rapid tumor growth and reflected pronounced infiltration of tumor by S100A9+ cells (B, right). Developmental variation among 4T1 tumor lesions could be predicted by S100A9 imaging, correlating relative growth rate over 10 d, after imaging (C; $r^2 = 0.86$; $P < 0.0001$; $n = 11$).

Origin of S100A9 Expression

ELISA of both tissue culture supernatant and cell lysates of the different murine breast cancer cells was negative for S100A8/A9 protein expression, whereas resected tumor samples, comprising tumor cells and the immune cell infiltrate, showed high S100A8/A9 levels. 4T1 tumor samples exhibited significantly higher protein levels than 168FAR or 67NR samples (Table 3).

To specifically control for expression of S100A9 by tumor cells in vivo, FACS analysis of resected tumor tissue was performed. Tumor samples from 4T1, 168FAR, or 67NR regularly comprised less than 0.1% S100A9+ cells of other than monocytic (CD11b+) origin (Fig. 3C), screening out the presence of S100A9+ tumor cells.

In summary, tumor cells did not exhibit S100A9 protein expression in vitro or in vivo; the S100A9 expression as reflected by specific imaging is virtually exclusively indicative of tumor-associated monocyte/macrophage activity.

MDSC Promote Tumor Growth and S100A9 Expression

CD11b+ cells as an apparent source of S100A9 in the tumor microenvironment were isolated from the spleens of either tumor-bearing (including tumor primed MDSC [tMDSC]) or healthy mice (naïve, immature myeloid cells [IMC]) and transferred into animals, which were thereafter inoculated with 4T1 (schematic representation of the protocol in Supplemental Fig. 3).

The average tumor growth in animals, transferred with tumor primed CD11b+ cells including tMDSC, was significantly accelerated as compared with mice after transfer of monocytes from healthy controls (average relative tumor size on day 8 as compared with day 1 tMDSC vs. IMC: 316% vs. 228%; $P = 0.001$; Fig. 4A; growth curve in Supplemental Fig. 2). This was also reflected by in vivo imaging: S100A9 fluorescence was significantly higher in mice after transfer of tMDSC and consecutive accelerated tumor development than in the control group (tMDSC vs. IMC: 250.2 vs. 106.6; $P < 0.01$; Fig. 4B). The treatment with IMC had no significant effect as compared with untreated mice (relative size day 8, 249%; FRI, 98.5).

Ex vivo histology confirmed the in vivo imaging results and revealed a strongly increased infiltration of tMDSC-treated tumors by S100A9+ cells as compared with IMC-treated tumors (Fig. 4C).

DISCUSSION

Tumor-associated immune cells are critical for malignant disease. Numerous studies illustrated immune cells to be supportive of tumor development and spread on the one hand and the interference with the antitumor immune response on the other (*24*). Tumor immunotherapy, the strategy to inhibit the induction of tumor-promoting immune cells and consecutively increase the host ability to overcome the suppression of an effective antitumor immune response, has been hailed a turning point in cancer therapy (*25*). Striking results have been reported in patients with advanced, even metastatic disease including lung, renal, prostate, and breast cancer (*26*). Still, response varies largely among the selected patients, and surrogate markers as to which patient might

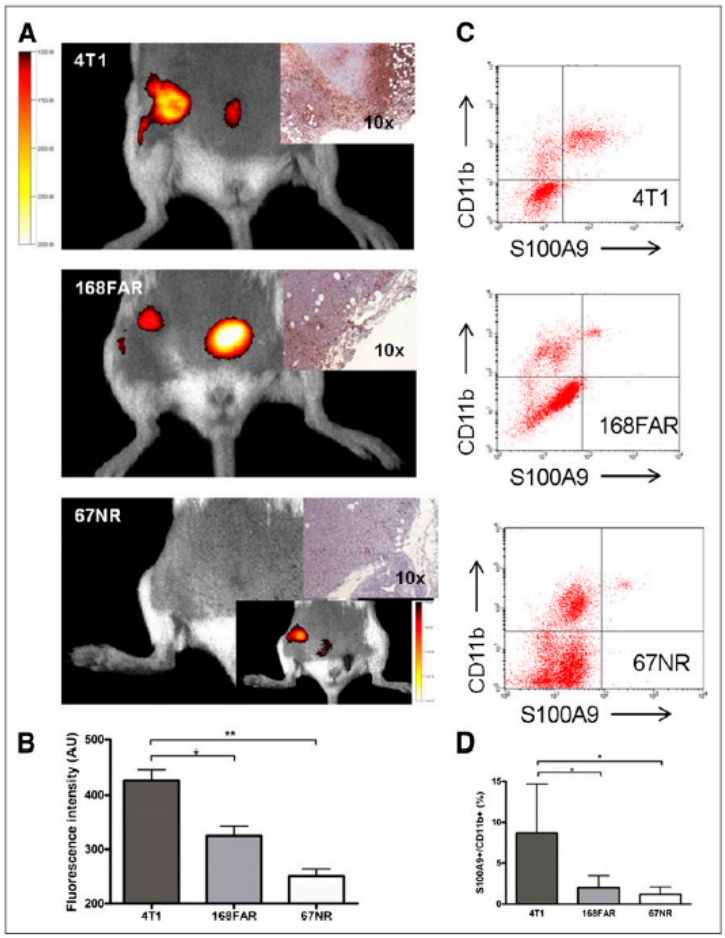

FIGURE 3. S100A9 imaging reflects metastatic capability. S100A9 in vivo imaging reveals significant differences between tumor entities of different metastatic capabilities (exemplary images in A; corresponding S100A9 histology; data in C). In vivo signal in 67NR tumors was visible only after threshold was reduced (insert). Ex vivo analysis of cellular tumor infiltrate revealed CD11b+ S100A9+ cells in all 3 tumors in amounts, confirming in vivo imaging results (B and D). Individual isotype controls and resulting gating are elaborated in Supplemental Figure 2.

benefit from the treatment are largely elusive (*27,28*). This specifically precludes monitoring of immunomodulatory cancer therapy because reliable diagnostic approaches for the determination of the biologic activity within the tumor microenvironment are still missing. For both clinical and preclinical applications, a method for sensitive monitoring of immune cell activity in malignant disease would be highly desirable. In clinical settings, it would enable patient stratification based on tumor-mediated inflammation whereas in preclinical settings it would facilitate further research in tumor biology.

We present an approach for visualization of S100A9+ monocyte activity in the tumor microenvironment as a surrogate marker for tumor-driven immune cell activity and indicator of the tumor ability to establish a supportive environment.

Within cell-tracking studies featuring either iron oxide–mediated MR imaging (*29,30*) or radionuclide imaging, for example, using ^{64}Cu-liposome labels for PET (*31*), the abundance of macrophages and other phagocytes in the tumor microenvironment could already be shown. Within this study, we present an approach for visualization of monocyte activity beyond sheer abundance in the primary tumor. With tumor-associated monocytes being discussed as prognostic indicators for tumor development (*4,24*), this technique could provide valuable information on ongoing tumor/immune cell crosstalk.

S100A8/A9 has been shown to mediate the crosstalk between tumor cells and monocytes, macrophages, and MDSCs (*6,32,33*). Local release closely reflects the monocyte/phagocyte activity (*34*), qualifying S100A8/A9 as an imaging target. The principle of S100A9-targeting for sensitive visualization of local monocyte activity in inflammatory processes has recently been established (*14*).

We now use this approach to address crucial components of the inflammatory tumor microenvironment using S100A9 as a marker for the activity of tumor-associated monocytes.

Although endogenous S100A9 expression has been proposed for several human tumor types (*35–37*) based on elevated systemic levels (*36*) and upregulation on the RNA level, expression on the protein level has not been well documented. The systemic levels, reported in human cancer patients and observed in tumor-bearing animals, are in this context also likely to represent activated monocytes. Although further evaluation of this hypothesis will be necessary, we could safely prove that none of the tumor cell lines we used for this study shows measurable S100A9 expression and thus, in these experimental tumor models, measured signals were mediated by tumor-invading monocytes.

The rabIgG-Cy5.5–mediated, unspecific background signal can be attributed to local hyperemia and binding of $F_c\gamma$ receptor, expressed on resident and invading immune cells (*38*) as well as, for example, endothelial cells (*39*). $F_c\gamma$ receptor expression can equally affect both rabIgG and aS100A9-Cy5.5 accumulation and increase immune cell infiltration via immune complex formation (*40*). The superiority of aS100A9-Cy5.5 over the unspecific isotype control has been extensively documented (*14*). In histology, we could detect S100A9 in colocalization with immune cells of monocytic heritage (TAM and MDSC), indicating a mutual relationship as recently suggested (*41*). Specific sites of monocyte activity could be identified in vivo using S100A9-driven FMT.

It is well established that monocytes, recruited to the tumor, support local tumor growth and invasion (*6,17,34,42*). In vivo imaging of S100A9 expression allowed for stratification of tumor lesions according to the activity of tumor-associated monocytes.

TABLE 3
ELISA Results

Parameter	TC supernatant			TC cell lysates			Resected tumor lysates		
	4T1	168FAR	67NR	4T1	168FAR	67NR	4T1	168FAR	67NR
S100A8/A9 (ng/mL)	0	0	0	0	0	0	86,897	4,665	1,927
SD	Not applicable	Not applicable	Not applicable	Not applicable	Not applicable	Not applicable	50,044	3,513	1,348

An established supportive microenvironment, reflected by a high S100A9 in vivo imaging signal, favors the consecutive tumor growth as suggested by our results and may be interpreted as an indicator of reduced prognosis.

Monocytes have also been reported to support the first steps toward distant metastasis at primary tumor level (*7,43*). In a murine model of graded malignancy (*15*), the different activity of tumor-associated monocytes, potentially supporting the systemic shed of cells from the primary tumor, was reflected by S100A9 imaging.

We artificially increased the number of tumor-primed MDSCs in tumor-bearing animals. In tumor lesions of identical size, the transfer of tumor-educated splenic monocytes including MDSC resulted in an increased recruitment of S100A9+ cells to the tumor and significantly higher S100A9 signal in the tumor and stimulated a more aggressive tumor development in accordance with recent data (*6,17*). An increase in naive monocytes, however, had virtually no effect on the activity of tumor-associated immune cells as reflected by S100A9 imaging and tumor growth.

Our findings support reports about the crucial importance of tumor-associated monocytes—including MDSC—for tumor development and fit with reports on them mutually promoting their respective activity and accumulation in the tumor (*44,45*). We could demonstrate that S100A8/A9 expression as measured by in vivo imaging reflects TAM and MDSC abundance and the malignant development in individual tumors and may thus function as a surrogate marker for the tumor's ability to recruit and activate immune cells to induce a supportive microenvironment.

Future studies will have to elucidate the relevance of S100A9 expression in the context of other tumor models and the potential for S100A8/A9 to serve as a marker for response to immunomodulatory therapy.

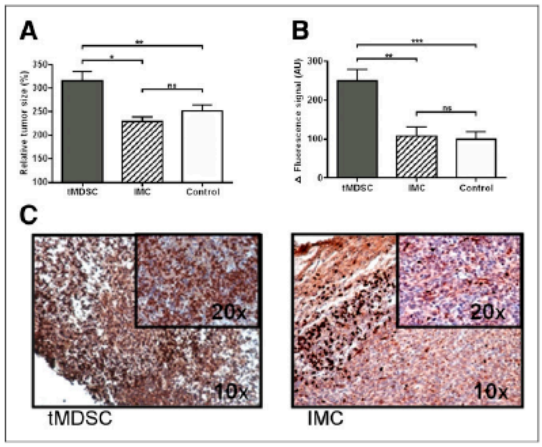

FIGURE 4. (A) tMDSC promote tumor growth. Splenic monocytes (1 × 10^6) from either tumor-bearing (tMDSC) or healthy animals (IMC) were injected intravenously into mice, inoculated with 4T1 (scheme in Supplemental Fig. 3). Accelerated growth resulted in relatively increased tumor size (% of size compared with d1) in tMDSC-treated animals. (B) S100A9-specific imaging revealed significantly higher immune cell activity in tMDSC-treated tumors as compared with controls. (C) Immunohistochemistry for S100A9 confirmed increased infiltration of S100A9+ cells into tMDSC-treated tumors as compared with IMC-treated controls.

CONCLUSION

Optical imaging of S100A9 allows for the estimation of TAM and MDSC activity in tumors and thus for stratification of tumor lesions with regard to local tumor–host interactions and the potential development. For basic research, this technique will offer the opportunity to study the role of TAMs in malignant progression in more detail. With regard to clinical cancer research, the importance of tumor-associated immune cells as promoters of malignant progression and thus as potential targets for diagnostics and therapy is emphasized and a potential route suggested.

DISCLOSURE

The costs of publication of this article were defrayed in part by the payment of page charges. Therefore, and solely to indicate this fact, this article is hereby marked "advertisement" in accordance with 18 USC section 1734. This work has been supported by funding from the Interdisciplinary Center of Clinical Research of the University of Muenster (Vo2/014/09, PIX); the German Research Foundation (DFG) CRC 1009 B8, B9, and EI 878 1-1; the Medical Research Council (MR/L001640/1); and CRUK (C1519/A6906) within the KCL-UCL Comprehensive Cancer Imaging Centre CRUK and EPSRC in association with the MRC and DoH. No other potential conflict of interest relevant to this article was reported.

ACKNOWLEDGMENTS

We thank Heike Berheide, Eva Nattkemper, Klaudia Niepagenkemper, Ingrid Otto-Valk, Claudia Terwesten-Solé, and Ina Winkler for excellent technical support. Tumor cells have been kindly provided by Frank Miller, Karmanos Cancer Center.

REFERENCES

1. Hanahan D, Weinberg RA. Hallmarks of cancer: the next generation. *Cell.* 2011;144:646–674.
2. Goswami S, Sahai E, Wyckoff JB, et al. Macrophages promote the invasion of breast carcinoma cells via a colony-stimulating factor-1/epidermal growth factor paracrine loop. *Cancer Res.* 2005;65:5278–5283.

3. de la Cruz-Merino L, Barco-Sanchez A, Henao Carrasco F, et al. New insights into the role of the immune microenvironment in breast carcinoma. *Clin Dev Immunol.* 2013;2013:785317.
4. Obeid E, Nanda R, Fu YX, Olopade OI. The role of tumor-associated macrophages in breast cancer progression. *Int J Oncol.* 2013;43:5–12.
5. Condeelis J, Pollard JW. Macrophages: obligate partners for tumor cell migration, invasion, and metastasis. *Cell.* 2006;124:263–266.
6. Cheng P, Corzo CA, Luetteke N, et al. Inhibition of dendritic cell differentiation and accumulation of myeloid-derived suppressor cells in cancer is regulated by S100A9 protein. *J Exp Med.* 2008;205:2235–2249.
7. Quail DF, Joyce JA. Microenvironmental regulation of tumor progression and metastasis. *Nat Med.* 2013;19:1423–1437.
8. Vogl T, Ludwig S, Goebeler M, et al. MRP8 and MRP14 control microtubule reorganization during transendothelial migration of phagocytes. *Blood.* 2004;104:4260–4268.
9. Markowitz J, Carson WE 3rd. Review of S100A9 biology and its role in cancer. *Biochim Biophys Acta.* 2013;1835:100–109.
10. Talmadge JE. Pathways mediating the expansion and immunosuppressive activity of myeloid-derived suppressor cells and their relevance to cancer therapy. *Clin Cancer Res.* 2007;13:5243–5248.
11. Sinha P, Okoro C, Foell D, Freeze HH, Ostrand-Rosenberg S, Srikrishna G. Proinflammatory S100 proteins regulate the accumulation of myeloid-derived suppressor cells. *J Immunol.* 2008;181:4666–4675.
12. Ghavami S, Chitayat S, Hashemi M, et al. S100A8/A9: a Janus-faced molecule in cancer therapy and tumorgenesis. *Eur J Pharmacol.* 2009;625:73–83.
13. Mukhtar RA, Moore AP, Tandon VJ, et al. Elevated levels of proliferating and recently migrated tumor-associated macrophages confer increased aggressiveness and worse outcomes in breast cancer. *Ann Surg Oncol.* 2012;19:3979–3986.
14. Vogl T, Eisenblätter M, Völler T, et al. Alarmin S100A8/S100A9 as a biomarker for molecular imaging of local inflammatory activity. *Nat Commun.* 2014;5:4593.
15. Aslakson CJ, Miller FR. Selective events in the metastatic process defined by analysis of the sequential dissemination of subpopulations of a mouse mammary tumor. *Cancer Res.* 1992;52:1399–1405.
16. Manitz MP, Horst B, Seeliger S, et al. Loss of S100A9 (MRP14) results in reduced interleukin-8-induced CD11b surface expression, a polarized microfilament system, and diminished responsiveness to chemoattractants in vitro. *Mol Cell Biol.* 2003;23:1034–1043.
17. Källberg E, Vogl T, Liberg D, et al. S100A9 interaction with TLR4 promotes tumor growth. *PLoS ONE.* 2012;7:e34207.
18. Gabrilovich DI, Ostrand-Rosenberg S, Bronte V. Coordinated regulation of myeloid cells by tumours. *Nat Rev Immunol.* 2012;12:253–268.
19. Ntziachristos V, Tung CH, Bremer C, Weissleder R. Fluorescence molecular tomography resolves protease activity in vivo. *Nat Med.* 2002;8:757–760.
20. Soubret A, Ripoll J, Ntziachristos V. Accuracy of fluorescent tomography in the presence of heterogeneities: study of the normalized Born ratio. *IEEE Trans Med Imaging.* 2005;24:1377–1386.
21. Frosch M, Strey A, Vogl T, et al. Myeloid-related proteins 8 and 14 are specifically secreted during interaction of phagocytes and activated endothelium and are useful markers for monitoring disease activity in pauciarticular-onset juvenile rheumatoid arthritis. *Arthritis Rheum.* 2000;43:628–637.
22. Foell D, Wulffraat N, Wedderburn LR, et al. Methotrexate withdrawal at 6 vs 12 months in juvenile idiopathic arthritis in remission: a randomized clinical trial. *JAMA.* 2010;303:1266–1273.
23. Vogl T, Tenbrock K, Ludwig S, et al. Mrp8 and Mrp14 are endogenous activators of Toll-like receptor 4, promoting lethal, endotoxin-induced shock. *Nat Med.* 2007;13:1042–1049.
24. Allavena P, Mantovani A. Immunology in the clinic review series; focus on cancer: tumour-associated macrophages: undisputed stars of the inflammatory tumour microenvironment. *Clin Exp Immunol.* 2012;167:195–205.
25. Couzin-Frankel J. Breakthrough of the year 2013: cancer immunotherapy. *Science.* 2013;342:1432–1433.
26. Brahmer JR, Tykodi SS, Chow LQ, et al. Safety and activity of anti-PD-L1 antibody in patients with advanced cancer. *N Engl J Med.* 2012;366:2455–2465.
27. Merelli B, Massi D, Cattaneo L, Mandala M. Targeting the PD1/PD-L1 axis in melanoma: biological rationale, clinical challenges and opportunities. *Crit Rev Oncol Hematol.* 2014;89:140–165.
28. Simeone E, Ascierto PA. Immunomodulating antibodies in the treatment of metastatic melanoma: the experience with anti-CTLA-4, anti-CD137, and anti-PD1. *J Immunotoxicol.* 2012;9:241–247.
29. Daldrup-Link HE, Golovko D, Ruffell B, et al. MRI of tumor-associated macrophages with clinically applicable iron oxide nanoparticles. *Clin Cancer Res.* 2011;17:5695–5704.
30. Shi Q, Pisani LJ, Lee YK, et al. Evaluation of the novel USPIO GEH121333 for MR imaging of cancer immune responses. *Contrast Media Mol Imaging.* 2013;8:281–288.
31. Locke LW, Mayo MW, Yoo AD, Williams MB, Berr SS. PET imaging of tumor associated macrophages using mannose coated ^{64}Cu liposomes. *Biomaterials.* 2012;33:7785–7793.
32. Chen H, Xu C, Jin Q, Liu Z. S100 protein family in human cancer. *Am J Cancer Res.* 2014;4:89–115.
33. Burke M, Choksawangkarn W, Edwards N, Ostrand-Rosenberg S, Fenselau C. Exosomes from myeloid-derived suppressor cells carry biologically active proteins. *J Proteome Res.* 2014;13:836–843.
34. Ehrchen JM, Sunderkotter C, Foell D, Vogl T, Roth J. The endogenous Toll-like receptor 4 agonist S100A8/S100A9 (calprotectin) as innate amplifier of infection, autoimmunity, and cancer. *J Leukoc Biol.* 2009;86:557–566.
35. Ichikawa M, Williams R, Wang L, Vogl T, Srikrishna G. S100A8/A9 activate key genes and pathways in colon tumor progression. *Mol Cancer Res.* 2011;9:133–148.
36. Kawai H, Minamiya Y, Takahashi N. Prognostic impact of S100A9 overexpression in non-small cell lung cancer. *Tumour Biol.* 2011;32:641–646.
37. McKiernan E, McDermott EW, Evoy D, Crown J, Duffy MJ. The role of S100 genes in breast cancer progression. *Tumour Biol.* 2011;32:441–450.
38. Hogarth PM, Anania JC, Wines BD. The FcγR of humans and non-human primates and their interaction with IgG: implications for induction of inflammation, resistance to infection and the use of therapeutic monoclonal antibodies. *Curr Top Microbiol Immunol.* 2014;382:321–352.
39. Ryan US. The endothelial surface and responses to injury. *Fed Proc.* 1986;45:101–108.
40. Heyman B. Regulation of antibody responses via antibodies, complement, and Fc receptors. *Annu Rev Immunol.* 2000;18:709–737.
41. Grebhardt S, Muller-Decker K, Bestvater F, Hershfinkel M, Mayer D. Impact of S100A8/A9 expression on prostate cancer progression in vitro and in vivo. *J Cell Physiol.* 2014;229:661–671.
42. Balkwill F, Charles KA, Mantovani A. Smoldering and polarized inflammation in the initiation and promotion of malignant disease. *Cancer Cell.* 2005;7:211–217.
43. DeNardo DG, Johansson M, Coussens LM. Immune cells as mediators of solid tumor metastasis. *Cancer Metastasis Rev.* 2008;27:11–18.
44. Gabrilovich DI, Nagaraj S. Myeloid-derived suppressor cells as regulators of the immune system. *Nat Rev Immunol.* 2009;9:162–174.
45. Mantovani A, Schioppa T, Porta C, Allavena P, Sica A. Role of tumor-associated macrophages in tumor progression and invasion. *Cancer Metastasis Rev.* 2006;25:315–322.